DIELECTRIC PROPERTIES OF CHLORAPATITE

A THESIS

Presented to

The Faculty of the Graduate Division

by

Ekkehart O. Rausch

In Partial Fulfillment

of the Requirements for the Degree

of Doctor of Philosophy in the School of Physics

Georgia Institute of Technology

August, 1976

DIELECTRIC PROPERTIES OF CHLORAPATITE

Approved:

R.A. Young, Chairman

James C. Elliott

James R. Stevenson

Date approved by Chairman: MAR 7 1977

ACKNOWLEDGEMENTS

Rarely is an experimental research project the sole accomplishment of a single individual. It is, therefore, appropriate and most gratifying to thank those who have contributed so much of their effort, talent and ideas.

I am primarily indebted to Professor R. A. Young for his ideas and excellent constructive criticism. His comments, quite often, led to a clear insight into many of the problems that were encountered.

Much gratitude is also extended to Dr. P. E. Mackie and Dr. K. Sudarsanan. Without their aid and months of effort some parts of this thesis would not have materialized. Dr. Mackie is remembered for his continuous encouragement and interest in this thesis and, in particular, for his efforts devoted to the collection of data with the computer controlled diffractometer. Dr. Sudarsanan is remembered especially for his assistance with structure refinements and photographic techniques in x-ray diffraction. Also, I would like to thank Dr. J. C. Elliott for his helpful comments and suggestions, and Dr. C. O. Pollard for his assistance during the initial phases of this work.

Many people have contributed to the technical aspects of this thesis. However, among this group there were certain individuals who contributed much more than others. They are as follows.

First, I would like to express my sincere appreciation to Mr. W. Hicklin for his year-long assistance in preparing specimens. Next, I would like to thank Mr. J. Cagle and Mr. J. Callahan for constructing some of the electronic instruments; Mr. K. Springfield, Mr. R. Bell and Mr. R. W. Gryder for machining, with excellence, many of the components which were used in the experimental system; Mr. V. Mallett for providing some of the photographs in this work; and Mr. T. Mackrovitch, Mr. B. R. Livesay and Professor E. W. Thomas for providing an assortment of instruments, vacuum equipment and ceramic components.

I acknowledge financial support from the National Institute of Dental Research (NIDR Grant # DE 01912) and I would like to thank Dr. G. Walker and Dr. O. P. Puri (both at Clark College, Atlanta, Ga.) for providing encouragement and partial financial support.

Last, but certainly not least, I would like to thank my parents for their continuous encouragement throughout this project.

TABLE OF CONTENTS

TABLE OF CONTENTS (Continued)

TABLE OF CONTENTS (Continued)

TABLE OF CONTENTS (Concluded)

LIST OF TABLES

LIST OF TABLES (Concluded)

LIST OF ILLUSTRATIONS

LIST OF ILLUSTRATIONS (Continued)

LIST OF ILLUSTRATIONS (Continued)

LIST OF ILLUSTRATIONS (Continued)

LIST OF ILLUSTRATIONS (Concluded)

SUMMARY

Most dielectrics found in nature have dielectric constants between 1 and 10 and rarely greater than 100. Nearly stoichiometric chlorapatite ($Ca_5(PO_4)_3Cl$) is, therefore, a material with unusual dielectric properties because it exhibits a dielectric constant $> 10^4$, a dielectric anisotropy $> 10^3$, an apparent ferroelectric character and time-dependent d.c. conductivity. At 1000 Hz and 25°C the real part of the dielectric constant (ε') is $\sim 10^4$ and the imaginary part (ε'') is $\sim 10^3$ parallel to the c axis while < 10 and < 0.01, respectively, perpendicular to c.

The purpose of this research was first to measure and then to explain these dielectric properties on the basis of a detailed atomic scale mechanism. Both dielectric and x-ray measurements of several kinds were employed.

Dielectric Studies

Measurements of the dielectric constants, ε' and ε'', as a function of frequency (10^2-10^6 Hz), temperature (25-400°C) and applied-field dependence were explored in "pure" and fluorine-doped forms of chlorapatite. The substitution of only 4% of the Cl by F ions reduced both ε' and ε'' parallel to c (at 26°C and 1000 Hz) by a factor of 100. This evidence verified that the high dielectric constant is directly associated with the Cl ions.

A vacancy defect model is advanced which successfully accomodates all of the above phenomena. It involves (a) the migration of Cl vacancies along the Cl chain and (b) field reversible shifts (~ 0.8 Å) of Cl ions along the chain direction in double wells made available by the occurrence of Cl ion vacancies. The activation energy of the Cl shift (< 0.2 eV) and the dipole density (e.g., < 1 per 100 cells) were also determined from the data.

Although the D versus E hysteresis loop observed in chlorapatite is suggestive of a ferroelectric character, the structure of the bulk of this material is centrosymmetric, which symmetry is not consistent with the occurrence of ferroelectricity. As a result the hysteresis loop was not identified as a bulk property of chlorapatite but instead it was associated with the Cl shift which in turn is indirectly associated with the small number of vacancy defects in the crystal. The term pseudo-ferroelectric is therefore used for this chlorapatite material.

The d.c. conductivity was ascribed to vacancy migration and the subsequent neutralization of the vacancies near the electrodes.

X-Ray Studies

In order to better understand, both, the nature of the dielectric properties in ClAp and the mechanism of the transition occurring near 200°C x-ray studies were initiated to investigate the temperature dependence of (a) the r.m.s. thermal vibrational amplitude of the Cl ion in the c direction, (b) the equilibrium position of the Cl ion, and (c) the intensities and breadths of some of the "monoclinic" x-ray

reflections to determine the persistence of monoclinic ordering and the domain size for it. The transition reported by others near 200°C has been shown not to be, as they thought, the monoclinic to hexagonal phase transition. Instead, that transition is herein predicted to occur at a temperature between 400 and 500°C. The 200°C transition appears to be associated with the breaking up of the monoclinic long-range ordering of the crystal into microdomains perhaps no larger than 60 Å.

On the basis of these results for chlorapatite, a possible mechanism is proposed for the reversal of OH dipoles in hydroxyapatite involving an O^{2-} defect and leading to possibly similarly interesting dielectric properties in that material.

CHAPTER 1

INTRODUCTION

Background

Apatite is the name given to a class of compounds having the chemical formula $Ca_{10}(PO_4)_6X_2$ where X represents F, Cl, or OH ions. Some apatites are important to the fertilizer industry because of their phosphate content and natural abundance, others are used in fluorescent lighting. Hydroxyapatite ($Ca_{10}(PO_4)_6(OH)_2$), in particular, generates considerable widespread interest because it is closely related to the principal inorganic component of bone and tooth enamel[1,2,3,4,5,6]. Impurities, such as CO_3^{2-}, Cl^-, F^-, etc., constitute some of the significant differences between the synthetic material, $Ca_{10}(PO_4)_6(OH)_2$ (henceforth referred to as OHAp) and biological apatite. This crystalline "impure" OHAp makes up about two thirds of the mineral phase in bone and 99% of the hard tissue in tooth enamel[1]. The remaining mineral phase in bone generally consists of amorphous or poorly crystallized calcium phosphates which may well be the building blocks for the biological apatites[7]. A detailed review of the problems of the composition and structure of the mineral components of the biological hard tissues was recently published by Elliott[3].

Purpose of Research

Bioelectric Effects in Bone and Tooth Enamel

The fact that bone structure and growth are related to mechanical stress was recognized by Wolff in 1892[18]. A possible element in the interaction between stress and bone growth was found in 1956 by Fukada and Yasuda[19] who demonstrated not only the piezoelectric properties of bone (the production of electric charges in bone due to applied stress), but also the indirect or converse properties (production of strain due to an applied electric field). Subsequently, it was found that bone growth could be electrically stimulated[20,21,22]. This effect was used with success in 1971 to enhance the healing of a bone fracture[23]. Thus, the importance of understanding both the origin of the piezoelectric effect in bone and the influence of electric currents on bone growth is generally recognized. A recent review on piezoelectricity in bone from a physical point of view was published by Williams[24]. Early investigators[25] considered attributing the piezoelectric behavior to biological apatite, because piezoelectricity is a well known property of crystalline materials such as quartz. However, Cochran, Pawluk and Bassett[26] soon showed that demineralized bone gave piezoelectric signals similar in magnitude to those from whole bone. As a result, it appeared that the piezoelectric effect is totally due to the fibrous protein material in bone and not to biological apatite. This conclusion, however, does not explain the effects of electric current on bone growth. For that, one should also consider the effect of electric fields on the apatites,

for it is the apatite that is, basically, the principal material that is deposited and remodeled in bone healing.

The polarization P of a dielectric is dependent upon the dielectric constant ($P_i = \varepsilon_0 \sum_j (\varepsilon_{ij} - 1)E_j$). Therefore, for a dielectric immersed in an electric field, the greater the dielectric constant along a particular direction, the greater the torque which tends to align that direction with the electric field lines. If the field is non-uniform, the dielectric will experience in addition a transport force $\vec{F} = (\vec{P} \cdot \vec{\nabla})\vec{E}$, which is again a function of the dielectric constant and the electric field. Because ClAp possesses a large anisotropy in its dielectric constant ($\varepsilon_{\parallel C} \sim 10^4$ and $\varepsilon_{\perp C} \sim 10$) small, free ClAp crystallites of microscopic dimensions will be readily transported in a non-uniform field and oriented such that their c axis align with the field. Furthermore, because ClAp is structurally very similar to OHAp[5,10,27,28], this fact may have considerable biological implications in relation to artificially or biologically induced electrical fields due to collagen. For example, the OH^- ions ordered in columns along the c axis constitute dipoles which may be reversible under special conditions (see Chapter VII) in the presence of low frequency electrical fields and thus may lead to a large anisotropy in the dielectric constant similar to that observed in ClAp. Dielectric measurements on natural "OHAp"[14,29], which contains impurities such as CO_3^{2-}, Mg^{2+}, Cl^-, and also F^-, revealed a low dielectric constant ($\varepsilon' \sim 10$) parallel to the c axis direction. As a result, the rate of bone regeneration and the

properties of newly formed bone at a fracture site may be influenced not only by the strength and direction of an applied electric field but also by the amount and type of impurities present in the biological apatites. Clearly, dielectric studies of OHAp as a function of direction and impurities within the crystal structure are important to the understanding of the fundamental bone growth and regenerative processes.

Fluorine Impurity Effect

Numerous experiments have clearly demonstrated an increased resistance to caries attack due to small concentrations (e.g. a few hundred ppm) of F^- ions in tooth enamel (for example see Ref. 8). In addition, it is known that the apatitic crystallites in tooth enamel are formed with their c axes approximately aligned perpendicular to the tooth enamel surface[4]. Structure analyses of nearly stoichiometric and F^- contaminated OHAp indicated that OH^- groups form linear columns along the c axis[11] and that F^- ions can substitute for OH^- ions[9,10,12]. Thus, if F^- ions are bound very strongly to the apatite structure they could inhibit the diffusion of OH^- ions along the c axis direction[12]. Because one of the theories of enamel caries regarded as most probable involves anisotropic disolution of enamel by acids, it was suggested that the blocking of the diffusion of OH^- ions may be the mechanism by which the caries attack is prevented[12,13]. Some authors[14,15] have challenged the F^- ion blocking concept on grounds that the migration energy for the F^- ion is less than that for the OH^- ion. Their conclusion, however, is based on

calculations made with a rigid polarizable point ion model. In fact, some experimental evidence suggests the opposite is true. For instance, the lattice heat of formation is known to be greater for $Ca_5(PO_4)F$ than for OHAp[16]. The electronegativity of the F ion is greater than that of the OH^- ion[17]. Also conversion of chlorapatite and fluorapatite to OHAp carried out for this work both with single crystals and with powders showed that fluorapatite (henceforth referred to as FAp) is more stable at high temperatures in steam than is chlorapatite (henceforth referred to as ClAp), which indicates that F^- ions cannot be as easily replaced by hydroxyl groups. The activation energies for migrating ions in crystals can be extracted from dielectric data[14] and are affected by the behavior of impurities which block the ion migration. It was, thus, recognized that dielectric investigation of Cl migration in chlorapatite and fluor-chlorapatite (henceforth referred to as (F,Cl)Ap) could provide experimental data on the blocking role of F impurities which could also have relevance to the blocking role of F in F-doped OHAp.

Dielectric Investigations of Chlorapatite

Dielectric investigations of synthetic apatites are interesting not only from a biological, but also from a purely physical point of view. For instance, ClAp possesses some unusual solid state properties in addition to the anisotropy of its dielectric constant. In order to understand these peculiarities, a detailed knowledge of the ClAp structure is needed. A projection of the ClAp structure onto the a, b plane is shown in Figure 1. Unfortunately, this type of representation does not allow for easy visualization of the structure in

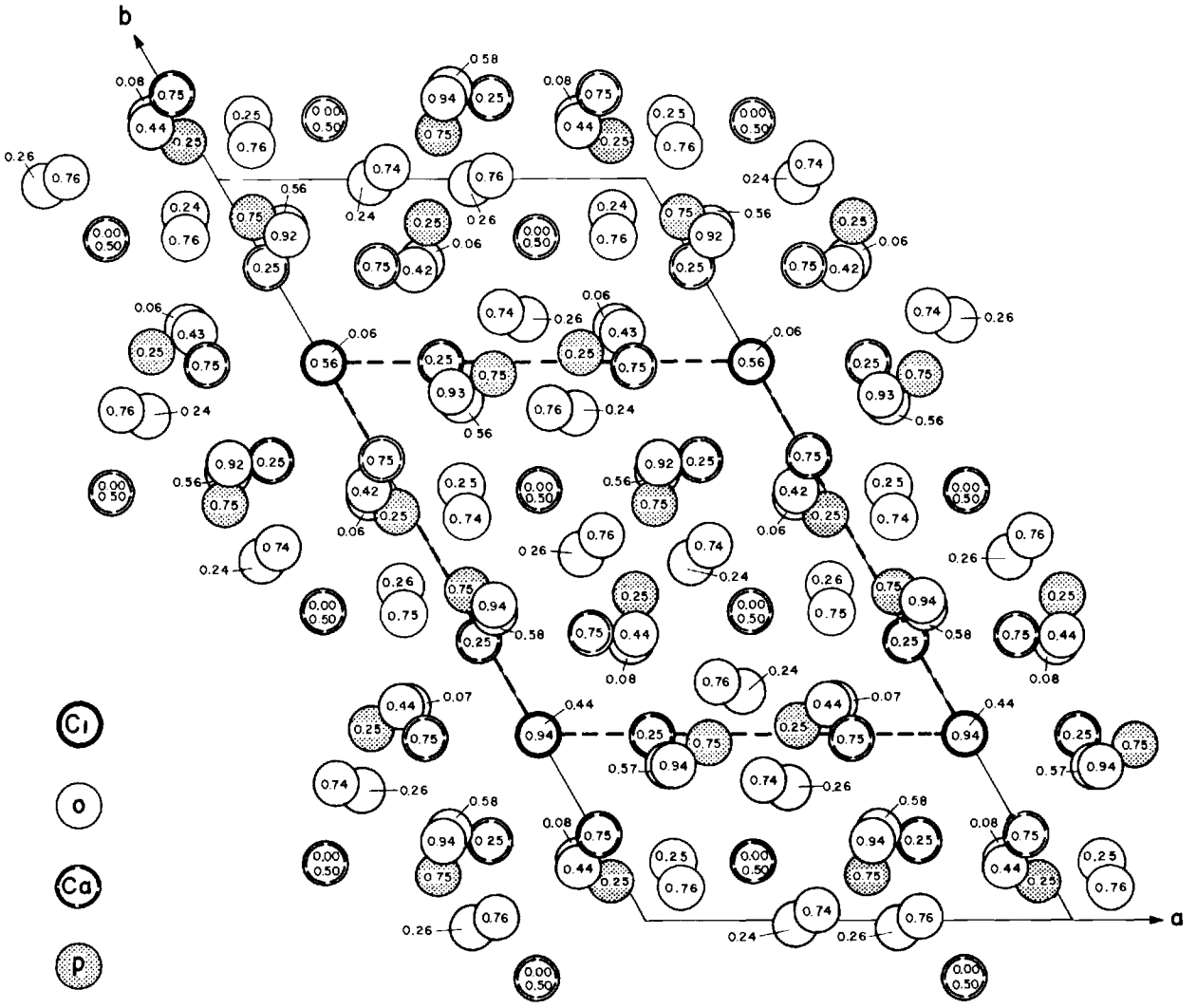

Figure 1. Projection of Chlorapatite Structure onto the a, b Plane. The numbers within the circles give the z-coordinate of the atoms. (After P. E. Mackie, J. C. Elliott, and R. A. Young, Acta Cryst. B28, 1840 (1972)).

three dimensions. However, one may gain a simplified view of the structure by regarding[3] the phosphate ions as rigid spheres with a diameter of about 3.7 Å. The spheres are close packed into layers which form a regular array of depressions. It is possible to stack several layers on top of each other such that the spheres in the 1st, 3rd, 5th sheet, etc., are vertically aligned and fall into one of two sets of depressions in the 2nd, 4th, 6th layers, etc. which are also vertically aligned. This leaves the other set of depressions (holes) in the 2nd, 4th, etc. layers vertically aligned over similar depressions (holes) in the 1st, 3rd, etc layers. In this way, channels are formed which are occupied with columns either of Cl or Ca ions. The Cl ions are closely packed along the c axis direction such that the Cl-Cl distance within the columns (3.38 Å) is less than the sum of the ionic radii (3.62 Å). There are two crystallographically equivalent positions for each Cl ion along the c axis (channel) direction[27] as shown in Figure 2. Site A is located 0.4 Å above and site B 0.4 Å below the z = 0 or 1/2 position. In stoichiometric ClAp with the monoclinic space group $P2_1/b$, all Cl ions along the a axis occupy either site A or B whereas along the b axis the ions form an ABAB arrangement, which is associated with the glide plane, a symmetry element occurring in this space group. The stoichiometric cell is centro-symmetric. Consequently, the center of negative charges coincides with the center of positive charges and, therefore, the cell has a zero net dipole moment. However, the cell can be divided into four sections. Each one contains a single identical

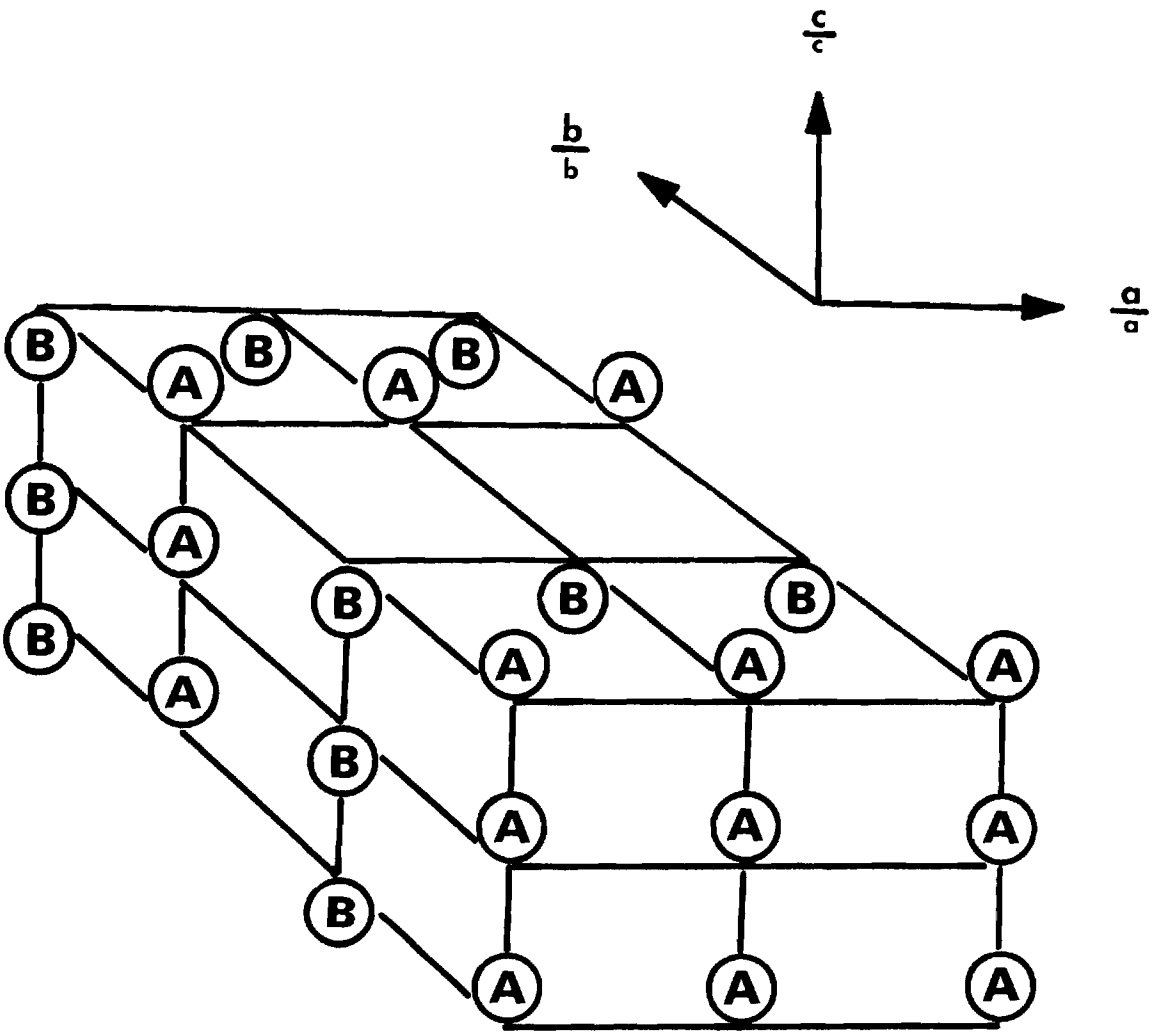

Figure 2. Arrangement of Cl Ions in Monoclinic ClAp. A, Cl Ions 'above' the z = 0 or 1/2 position; B, Cl Ions 'below' the z = 0 or 1/2 position. The relationship between the b and a lattice parameter is given by $|b| = 2\,|a|$.

dipole which is associated with the Cl ion position. These are directed along $\pm \bar{c}$ and are arranged antiparallel to each other along the b axis, but parallel to each other along the a axis. The antiparallelism is characteristic of an antiferroelectric. On the basis of this information and the fact that the $P2_1/b$ space group is nonpolar, Elliott and Young[30] and Young and Elliott[31] investigated whether there might be antiferroelectric[32] behavior in ClAp. However, a plot of the polarization versus the applied electric field revealed an apparent ferroelectric character, which can occur only in a polar space group. It was considered[30] that the Cl ions might be shifted between sites A and B under the influence of strong fields such that all Cl ions would be located either above or below the z = 1/2 plane. If this were true, the center of symmetry and the glide plane would disappear and all h k_{odd} ℓ reflections with $\ell \neq 0$ would also vanish, since their presence depends on the existence of the glide plane. However, when the intensities of the strongest h k $2(k_{odd})$ x-ray reflections of a ClAp sample were monitored with a diffractometer system as a function of an applied d.c. electric field parallel to the c direction, as suggested by Elliott[33], no changes in the intensities were found, although fields up to 10,000 V/cm were applied. Furthermore, the same crystal did exhibit an apparent ferroelectric character when subjected to fields of the order of 3,000 V/cm.

In summary, crystal structure studies suggested that an antiferroelectric behavior might occur in ClAp. On the other hand dielectric measurements revealed the existence of an apparent ferroelectric

character and the possibility that some ions, presumably Cl ions, are easily shifted under the influence of an electric field. Thus, the ultimate objective of this thesis was to develop a detailed atomic scale mechanistic model which can explain both quantitatively and qualitatively the dielectric properties of ClAp, F-ClAp and Cl-deficient ClAp. This information may then be applied to problems in industry or to the problems of the biological apatites of tooth enamel and bone, such as the effect of electric currents on bone growth, or it may be combined with solid state theory to further explore the relationship between material properties and atomic structure.

Experiments were, therefore, designed to measure both the real and imaginary part of the dielectric constants in ClAp, including the conductivity, as a function of frequency (0 to 10^6 Hz), temperature (25°C to 300°C), orientation, impurity content and Cl deficiency.

Literature Survey on Dielectric Measurements in Apatite

To date, little has been published on the dielectric properties of apatite. In fact, FAp is the only material in the apatite group for which detailed experimental and theoretical investigations have been carried out[14,29]. Siegel[29] reported measurements on the temperature and frequency dependence (4°K to 400°K and 30 Hz to 150 KHz) of the dielectric constant and loss for naturally occurring OHAp and for synthetic ClAp. However, in this work his ClAp data will be shown to be incorrect. Some later publications[34,35,36], for the most part,

were abstracted from the theses of Siegel[29] and Tse[14]. Other workers have concentrated mostly on one or another aspect of the dielectric properties of apatite. Elliott and Young[30] made some preliminary investigations of the dielectric constant and hysteresis loops of ClAp; and Pollard[37], among others, suggested that OHAp could exhibit a possible $\bar{D}$ versus $\bar{E}$ hysteresis due to OH^- dipole reversal. Kautz[38] made dielectric loss measurements on FAp with known fluoride vacancy concentrations of 0.4, 1.5 and 3.9 atomic percent at temperatures from 110°K to 500°K. Thus, before this work was initiated few data were available on the dielectric properties of synthetic ClAp. No data were available on stoichiometric OHAp or on any of the apatites doped with known quantities of impurities, for example (F,Cl)Ap, (F,OH)Ap, and (OH,Cl)Ap, nor on any apatites other than calcium apatites.

CHAPTER II

INSTRUMENTATION AND EQUIPMENT

Crystal Growth Apparatus

The synthetic ClAp crystals were grown from solutions of chlorapatite in molten $CaCl_2$ according to Prener's[39] method with the equipment and procedures used by Mackie et al.[27]. A Lindbergh type 54233 furnace (maximum temperature 1500°C) was used to raise the temperature of the mixture to its melting point. Within the crystal growth range (1280°C to 1040°C) the furnace temperature could be reduced at the rate of 1°C/h with a locally designed and built electronic controller. The output voltage from the furnace thermocouple was compared with the controller generated d.c. signal and the differential voltage was amplified and used as a feed back signal to a solid state regulator (R. I. Research Incorporated LABAC Model 20-12) which directly controlled the current for the heating elements. The sample was placed inside a one meter long Zr doped alumina tube in which the atmosphere could be controlled (primarily to exclude CO_2). In order to exclude unwanted gases a constant positive pressure was maintained inside with an inert gas, such as Ar or He. The inert gas leaving the tube was bubbled through a beaker filled with glycerin which served as a flow detector. The sample itself was located at the hottest region, near the center of the furnace, where the temperature gradients were at a minimum. In order that the

crystals not be contaminated with impurities the reaction vessel was made of platinum.

Chlorapatite to Hydroxyapatite Conversion System

Recently, Elliott and Young[40] were able to convert spheres (up to 0.4 mm in diameter) of single crystals of ClAp to OHAp through the exchange of Cl^- ions for OH^- ions in single crystals. Their method was to pass steam over ClAp crystals held at about 1200°C for a period of 2 weeks. That technique was used in this work to convert thin platelets (3 mm x 3 mm x 0.2 mm) of ClAp to OHAp. The equipment specially built for the present work is shown schematically in Figure 3. A boiler from a Corning Distilling Apparatus Type AG-1b supplied the steam, which was superheated to about 200°C (to eliminate condensation) in a ~ 70 cm long Pyrex tube wrapped with asbestos, 0.038 cm thick nichrome wire, and asbestos, in that order. The electrical heating element for the crystal consisted of a boat-shaped platinum foil which was silver-soldered to the ends of two 0.64 cm thick brass rods. The assembly was held together by a plug manufactured from "lava," a naturally occuring aluminum silicate compound. The temperature of the conversion chamber was kept above 100°C to eliminate condensation and was transparent (Pyrex) to allow the temperature of the crystal to be monitored with an optical pyrometer (Leeds and Northrup Co., Cat. No. 8626-C). A step-down transformer coupled to a Variac served as a power supply to heat the crystal. In order to avoid cracking of the crystal by thermal shocks, the Variac was operated with an electric motor and worm gear transmission capable of changing the

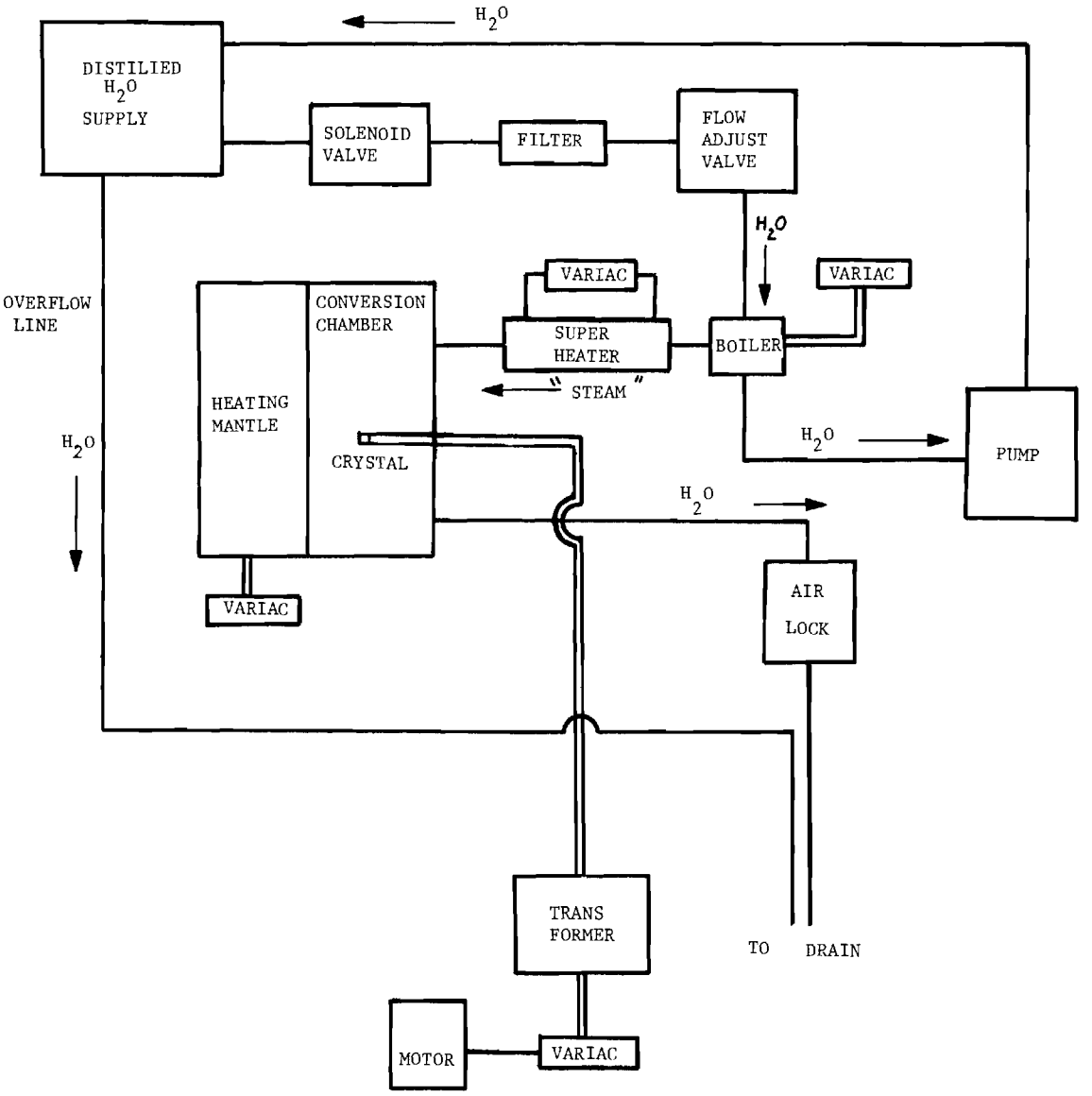

Figure 3. Schematic Diagram of System for Converting ClAp to OHAp in Single Crystal Form.

sample temperature at the rate of 3°C per minute. An air lock prevented gases other than H_2O from entering the system. Continuous operation over long periods of time required the installation of a filter (glass wool) and the use of distilled water. The apparatus also contained some safety features such as a solenoid valve and a thermal switch near the boiler to protect the system and to shut down its operation in case of a power or water loss.

Chlorapatite to Cl Deficient Chlorapatite Conversion System

Prener[41] has shown that ClAp powder can be made Cl deficient through loss of $CaCl_2$ in vacuum at temperatures greater than 900°C. The ClAp powder is simply heated in vacuum for approximately 16 hours. His technique was adapted for single crystals in this work. A silica tube of about 2 mm wall thickness, 10 mm inside diameter and 30 cm long was sealed at one end and placed in a tubular furnace (Hoskins Electric Furnace Type FD 303). The open end was connected to a diffusion pump, which in turn discharged to a mechanical fore-pump. An ionization gauge monitored the pressure within the system. Operating pressures within the 10^{-6} Torr range could easily be achieved. A liquid N_2 trap was placed between the diffusion pump and the sample to prevent the contamination of the sample with diffusion pump oil.

Dielectric Properties Measurement System

Dielectric Cell

Because of limited size of intact crystals available, limited

with respect both to area and to minimum thickness without cracking, a dielectric measurement cell was needed that would permit measurement of capacitances in the picofarad range. In addition, it was found necessary to minimize the environmental influences encountered in the measurement of the dielectric properties of ClAp. For example, water vapor adsorbed on the ClAp crystal specimen markedly increased the measured capacitance, especially when the electric field was parallel to the c axis; sometimes by a factor of 10. The final cell design (Figures 4 and 5) owes some features to that of Gravel and Kestigian[42]. The contact electrode configuration, however, was modified to gain fast thermal response when the capacitor was heated. Each electrode was heated separately. The crystal was sandwiched between two copper electrode disks and, to prevent the formation of an insulating layer of CuO, each electrode was electroplated with silver. The electrodes were held in position by two thin (0.16 cm diameter) alumina rods T_1 and T_2 (Figure 4) which were also used as thermocouple supports. The lower rod was stationary whereas the upper one was free to move in a vertical direction. The thermocouple junctions were countersunk into the alumina rod and, thus, were insulated from the electrodes. If they had been allowed to touch the copper, the electrodes would have been shorted to ground, because the grounding of at least one lead from each thermocouple was necessary to reject unwanted a.c. noise in the temperature control circuit. The upper electrode was backed by a spring to ensure good thermal and electrical contact with the crystal. The lower electrode could not move, and therefore,

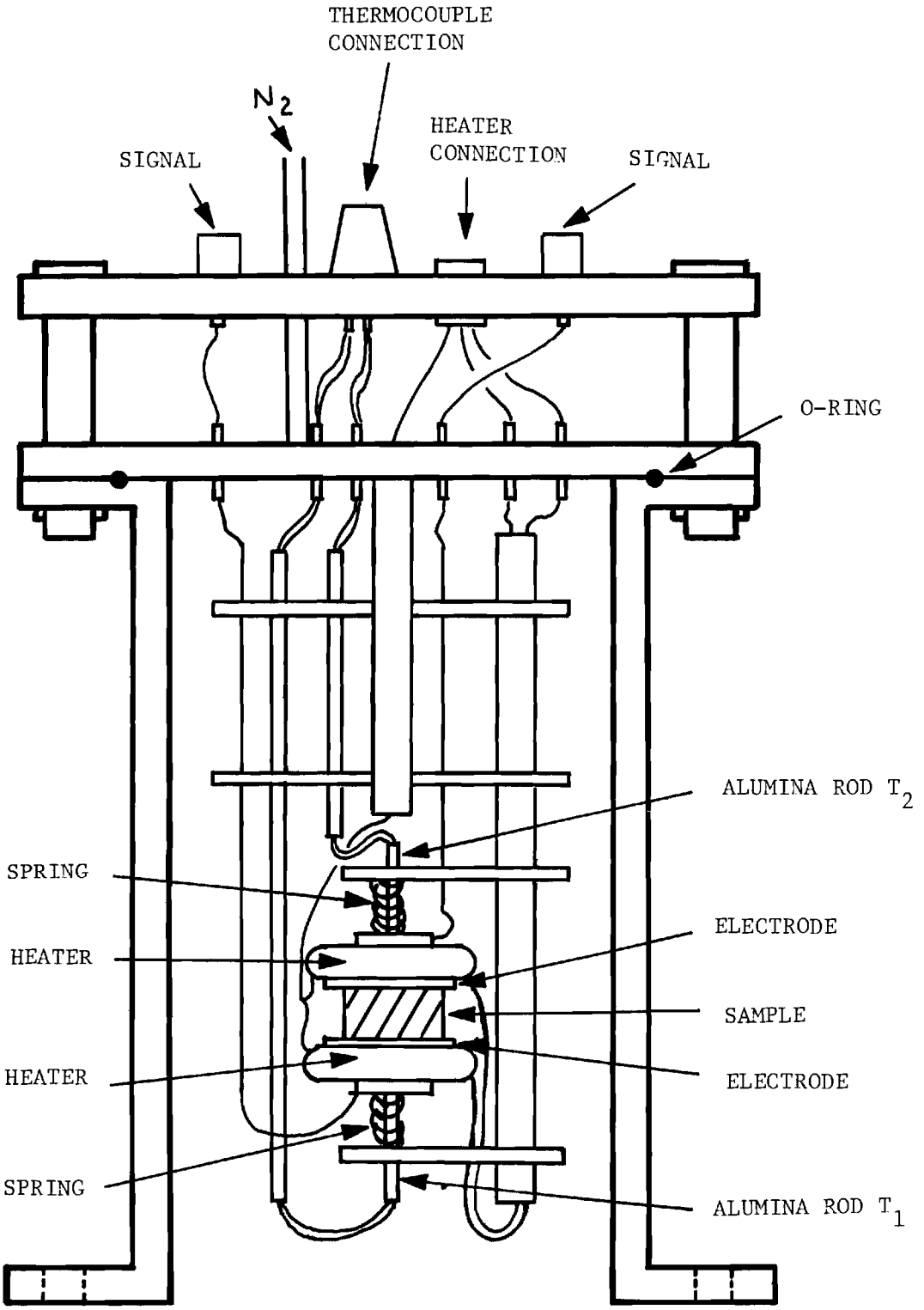

Figure 4. Electrode Arrangement within the Dielectric Cell.

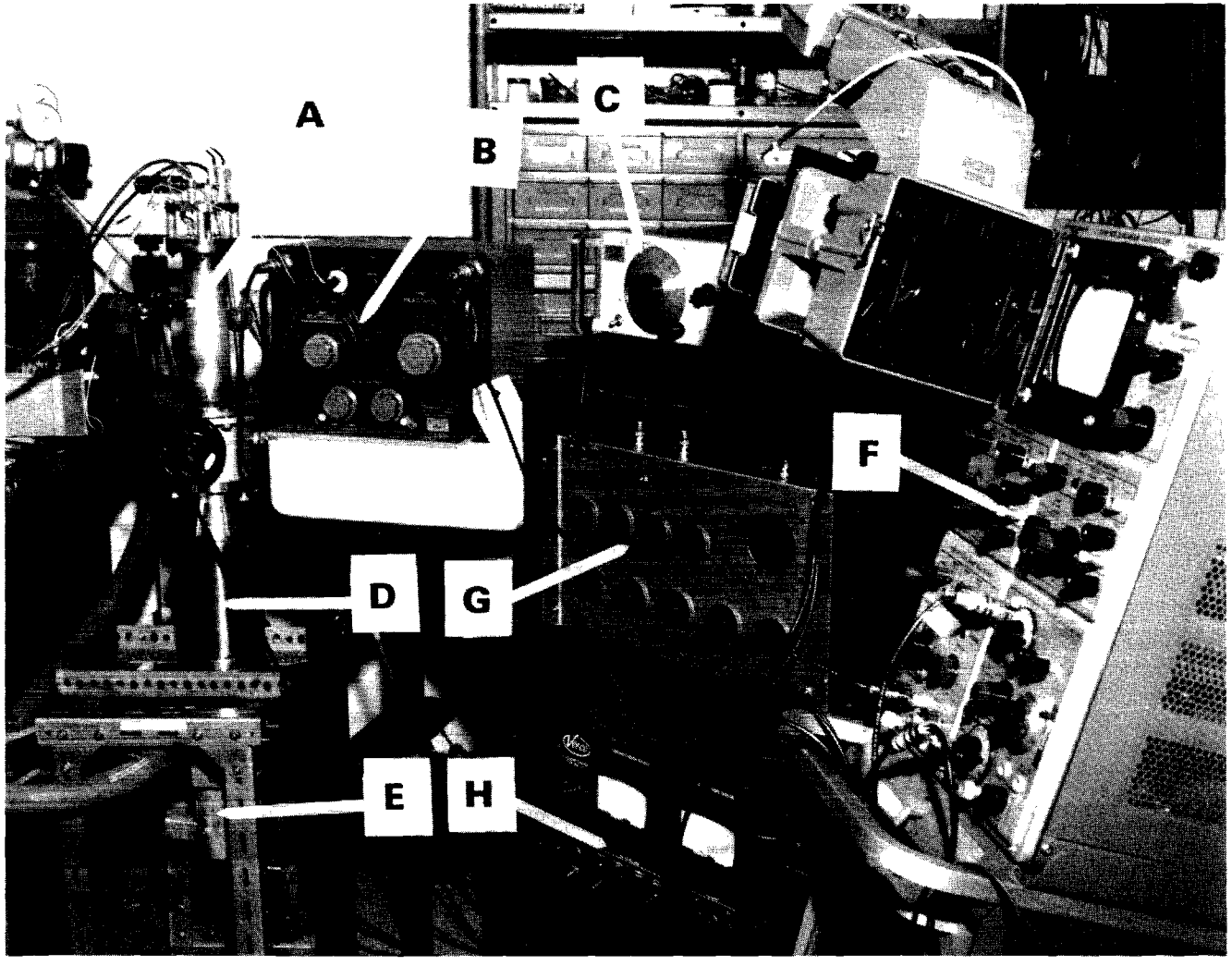

Figure 5. Partial View of Dielectric Measurement System. A, Cell; B, R. F. bridge; C, R. F. oscillator; D, Liquid N_2 trap; E, Diffusion pump; F, Oscilloscope used as R. F. detection system. Also shown are: G, Compensator for hysteresis loop tracer; H, Ion gauge controller.

the lower spring was used for an entirely different purpose. Its function was to equalize the thermal leak-off to the surrounding gas and support structure with respect to the upper electrode. As a result, fine balancing of the dissipated wattage in the heaters was easily accomplished by varying either the R_a or R_b resistor (Figure 6). The goal, of course, was to create a uniform temperature environment for the crystal. When the thermocouple outputs were equal, the temperature gradients across the crystal were taken to be at a minimum. It appeared that the fast thermal response and the relatively low residual capacitance (4.5 pf for a 0.2 mm electrode separation) made the cell an excellent system for investigating the dielectric properties of many samples. Unfortunately, the dual heating system may cause errors in the measured loss tangent and capacitance, particularly at high temperatures, due to electrical leakage from one electrode to the other through the heating system. A detailed drawing of the electrode arrangement and of the various leakage paths is shown in Figure 7. R_s was a shunt resistance in parallel with C_x. R_H and R_L were resistances from both electrodes to ground. Typical values of R_s, R_L, and R_H are found in Table 8 of Appendix B. The heaters were constructed of coiled nichrome wire (0.04 cm in diameter) and cemented with a mixture of sodium silicate and #30 Sauereisen into a doughnut. This cement is highly conductive when not baked out properly. Therefore, to insure proper insulation a (0.0025 cm thick) sheet of mica was used to isolate the heater electrically from the electrode disk and an alumina cylinder

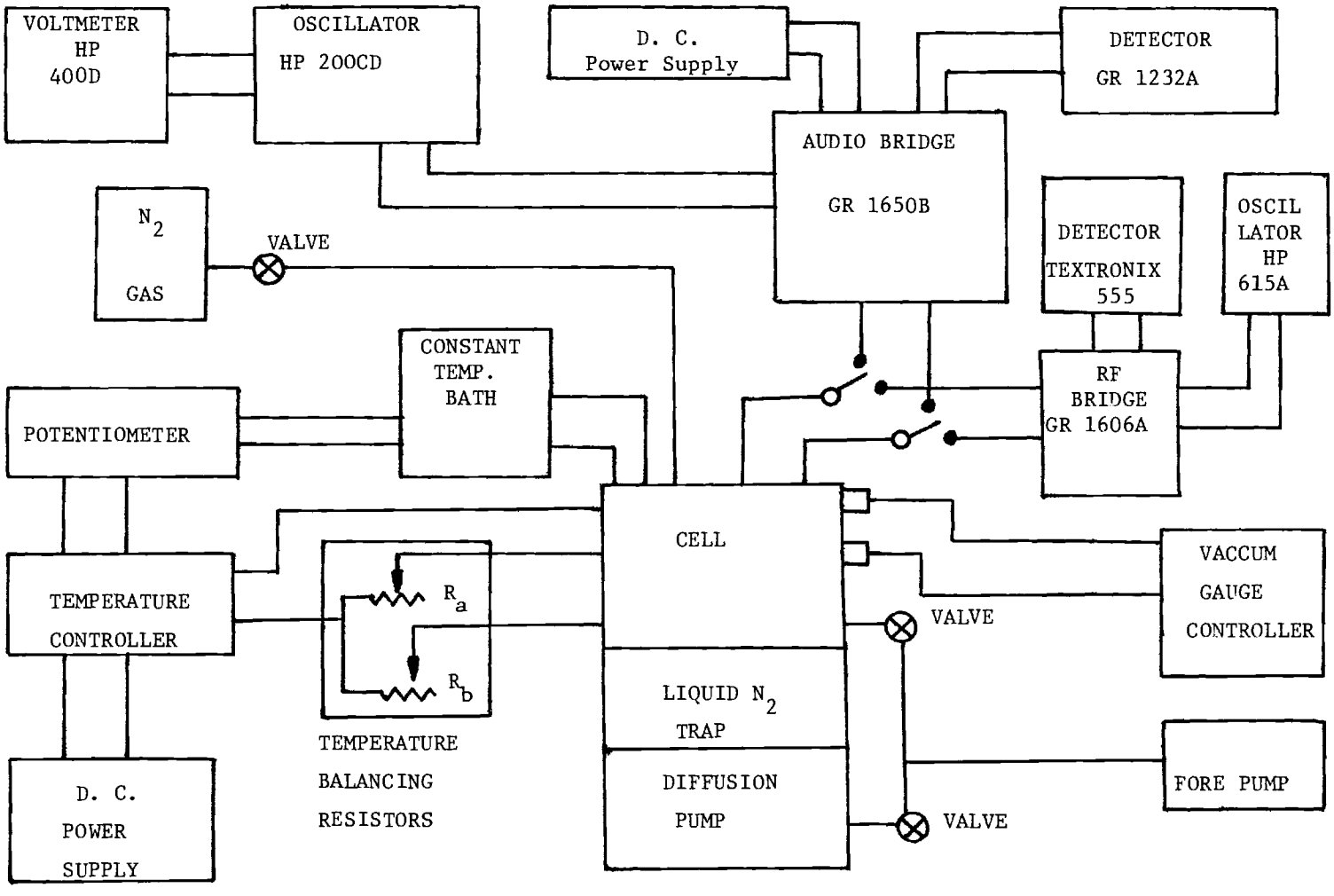

Figure 6. Schematic Diagram of Dielectric Measurement System.

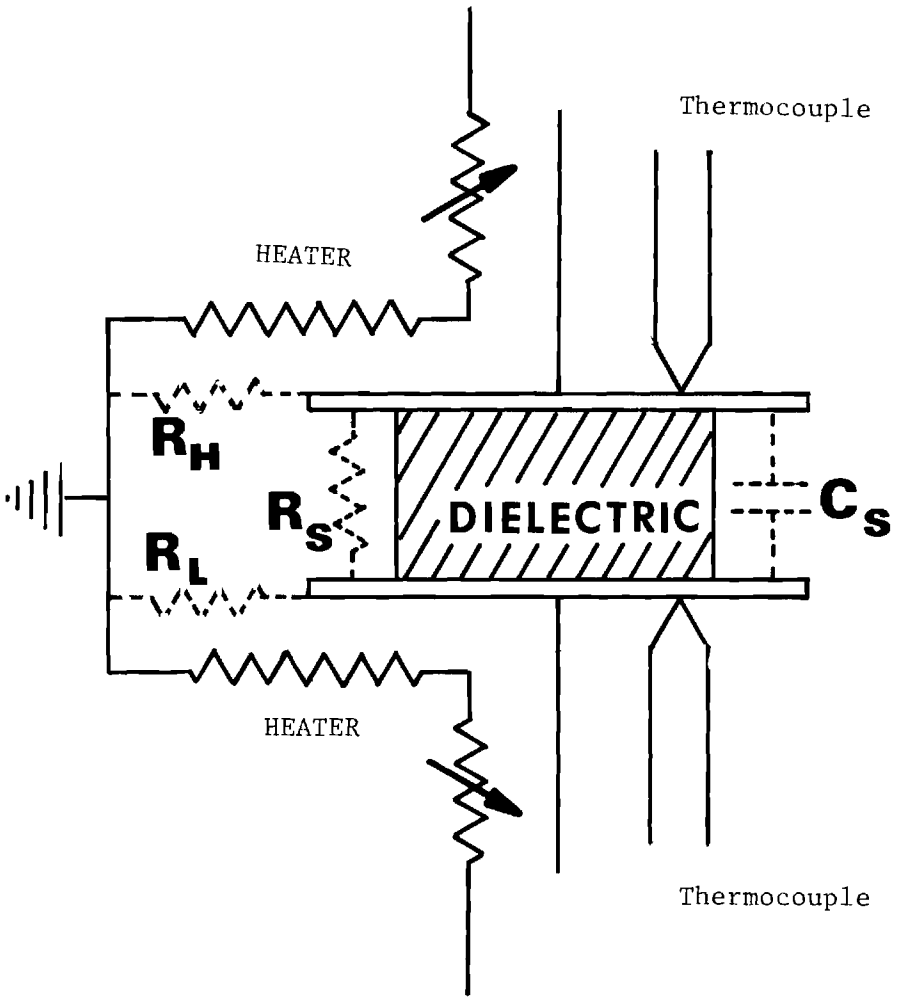

Figure 7. Schematic Diagram of Dielectric Cell Showing Stray Capacitances and Resistances.

(American Lava Corporation, Alsimag 753) was used to separate it from the electrode stem. Again, one lead of each heater was grounded to minimize a.c. noise. The cell was mounted directly onto the throat of a 2 inch diffusion pump. This controlled the environment and eliminated errors in the dielectric constant due to water adsorption on the ClAp specimen. With the forepump a pressure of 10^{-3} Torr could be obtained within minutes. The two-inch mercury diffusion pump in conjunction with a liquid nitrogen trap could lower the pressure to 10^{-6} Torr within a half hour. The limit was 6×10^{-7} Torr.

Bridge, Vacuum and Heating Systems

A thorough analysis of the dielectric constant of any material requires a number of specialized systems to cover the frequency range from 0 to 10^{15} Hz. The actual frequencies used for measurements are usually determined by the region of interest or the onset of the lowest and highest dielectric constants of the material. For this work, the region of interest was between 10^{2} and 10^{7} Hz.

The two instruments required to cover this range were an audio bridge (General Radio type 1650-B, range:20 hz to 20,000 hz) and a radio frequency bridge (General Radio type 1606-A, range:400K Hz to 10^{7} Hz). It was possible to extend the frequency range of each bridge until the audio and r.f. measurements overlapped at 10^{5} Hz. However, the bridge accuracies were reduced between 20,000 Hz and 400,000 Hz. The capacitance accuracy for the audio bridge at 10^{5} Hz is +1%, -3.5% instead of the $\pm$1% below 2×10^{4} Hz. The amount of

reduction in accuracy for the r.f. (radio frequency) bridge was not supplied by the General Radio Corporation. However, a typical plot of the real part ε' versus the imaginary part of the dielectric constant ε'' (Figure 25) shows the scatter of points at 10^5 Hz. The estimated precision for the r.f. capacitance on that basis is $\pm$10%.

The audio-bridge was connected to the cell be means of two 1 m long coaxial cables with a capacitance of 150 pf/m. The outer conductor of each cable and the bridge casing were grounded to remove the capacitance between the ungrounded signal leads (~ 300 pf) which otherwise would have been in parallel with the sample capacitance. This three terminal method, however, introduced stray capacitances elsewhere in the bridge circuit. A detailed analysis of the influence of stray resistance and capacitance on audio bridge measurements is given in Appendix B.

In contrast to the audio bridge, the r.f. bridge did not indicate the capacitance and loss tangent (tan δ) directly, but instead measured the reactance and resistance of the sample. Therefore, it was important to examine all stray reactances, especially the inductive reactance, as possible sources of errors. In fact, if the measuring frequency is increased beyond the audio range (10^5 Hz), the lead capacitive reactance ($X_c = 1/2\pi fC$) becomes negligible, whereas the lead inductive reactance ($X_L = 2\pi fL$) increases. The latter reactance can not be removed simply by using the same three terminal connection method which was employed for audio bridge measurements. For this reason 18 gauge, unshielded, solid wire

leads were used. Their stiffness and a one inch minimum spacing between them ensured a constant stray capacitance. In addition, the leads were made as short as possible (about 50 cm) to reduce their inductive effect on the measurements. Elaborate calculations which correct for inductive errors are given in Appendix B, Section 4.

The audio bridge was coupled with a Hewlett Packard (henceforth abbreviated HP) 200CD sinusoidal signal generator and a General Radio Corporation (henceforth GR) type 1232 A detector to obtain the best possible signal to noise ratio. Because the detector could be tuned to each frequency at which measurements were taken, the bridge circuit-noise was virtually eliminated. A HP type 400 D volt meter indicated the output voltage of the oscillator. A three volt signal was applied to the audio bridge transformer for routine capacitance measurements. The three to one step down transformer ratio ensured that only 1 volt or less was applied to the sample. Typical electric fields between the sample's electrodes were of the order of 10 V/cm. By means of a switch the bridge would be connected to a d.c. power supply (100 V max.) for d.c. conductivity measurements. The r.f. bridge was operated with a HP type 651 A test oscillator and a Tektronix type 555 dual beam oscilloscope, with a type 1A1 plug-in unit, which served as a detector. The sensitivity was better than 0.001 volt. A 2 volt input signal was applied to the bridge. Thus, as was the case with the audio bridge, the potential difference across the sample was always less than or equal to 1 volt, because the r.f. bridge transformer had a 2 to 1 step down ratio. Also, it was

possible to ground one lead and, therefore, to eliminate much noise in the circuit. Other components (for details see Figure 6) associated with the system included the 2 inch mercury diffusion pump (Edwards Company Ltd.), a mechanical forepump, a liquid nitrogen trap and an ion gauge with its associated controller. The heating system for the sample consisted of the temperature balancing resistors, a d.c. power supply (maximum voltage: 15VDC, maximum amperage: 10 amps), a temperature controller, a Barber-Coleman millivolt potentiometer (model #PA-10-1), and a constant temperature bath. The combination of d.c. power to the heater and grounding of the negative terminal of the power supply helped to reduce circuit noise. The temperature controller was specially designed and built for this work by J. R. Cagle and J. Callahan (Georgia Institute of Technology). It was capable of raising the temperature of the electrodes from 25°C to 200°C within approximately 2 minutes. By means of the balancing resistors (see Figure 6), the temperature difference between the electrodes could be reduced to less than 0.5°C of the set temperature. The constant temperature bath consisted of a 100 ml flask of forepump oil placed inside a dewar, which was covered with a one inch thick styrofoam disk. The temperature variation of the bath did not exceed about 0.5°C while the data were being collected.

D versus E Hysteresis Loop Tracer

The plot of the displacement field of a ferroelectric sample versus the applied electric field shows a hysteresis loop which is usually exhibited directly on an oscilloscope. If the sample is a

low loss material, the use of a Sawyer-Tower circuit[43] (see Figure 8) is the best and simplest way to display the hysteresis loop. However, if the sample if very lossy, other circuits[44,45] are available which compensate for the conductivity within the material. A recent design[46] utilizing the special characteristics of operational amplifiers was chosen for this work. Figure 9 shows the schematic for the circuit. The power supply consisted of a HP type 200 CD oscillator, an audio amplifier and a step up audio transformer. The compensator was designed and built for this work by J. R. Cagle, Georgia Institute of Technology. The resistance could be varied between 10 K and 600 MΩ in steps of 10 KΩ. The capacitance had a range between 1 pf and 10,000 pf and could be varied in steps of 1 pf. The Tektronix type 0 and Z plug-in units contained the operational and differential amplifiers, respectively. Both were inserted into the Tektronix type 555 oscilloscope to make up the bulk of this circuit. The arms containing the operational amplifiers were initially balanced by: a) removing the sample; b) setting $R_c = \infty$; c) adjusting the operational amplifiers #1 and #2 for equal amplification (C_1 and C_2 were always kept equal to each other); and d) final adjustment of the trimmer capacitor for zero output of the differential amplifier (set for maximum amplification). As a result, the d.c. resistance and the linear capacitance of the sample (due to the polarization current which is in phase with the applied field) could be obtained directly from the compensator after the compensation was executed. In order to understand the operation of this compensating circuit it is necessary to consider

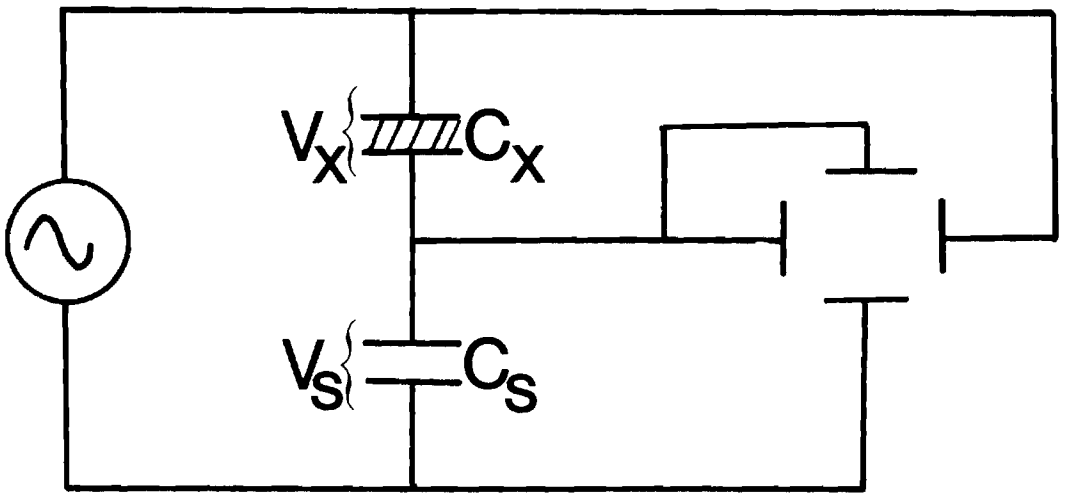

Figure 8. Sawyer - Tower Circuit. (After C.B. Sawyer and C.H. Tower Phys. Rev. 35, 269 (1930)).

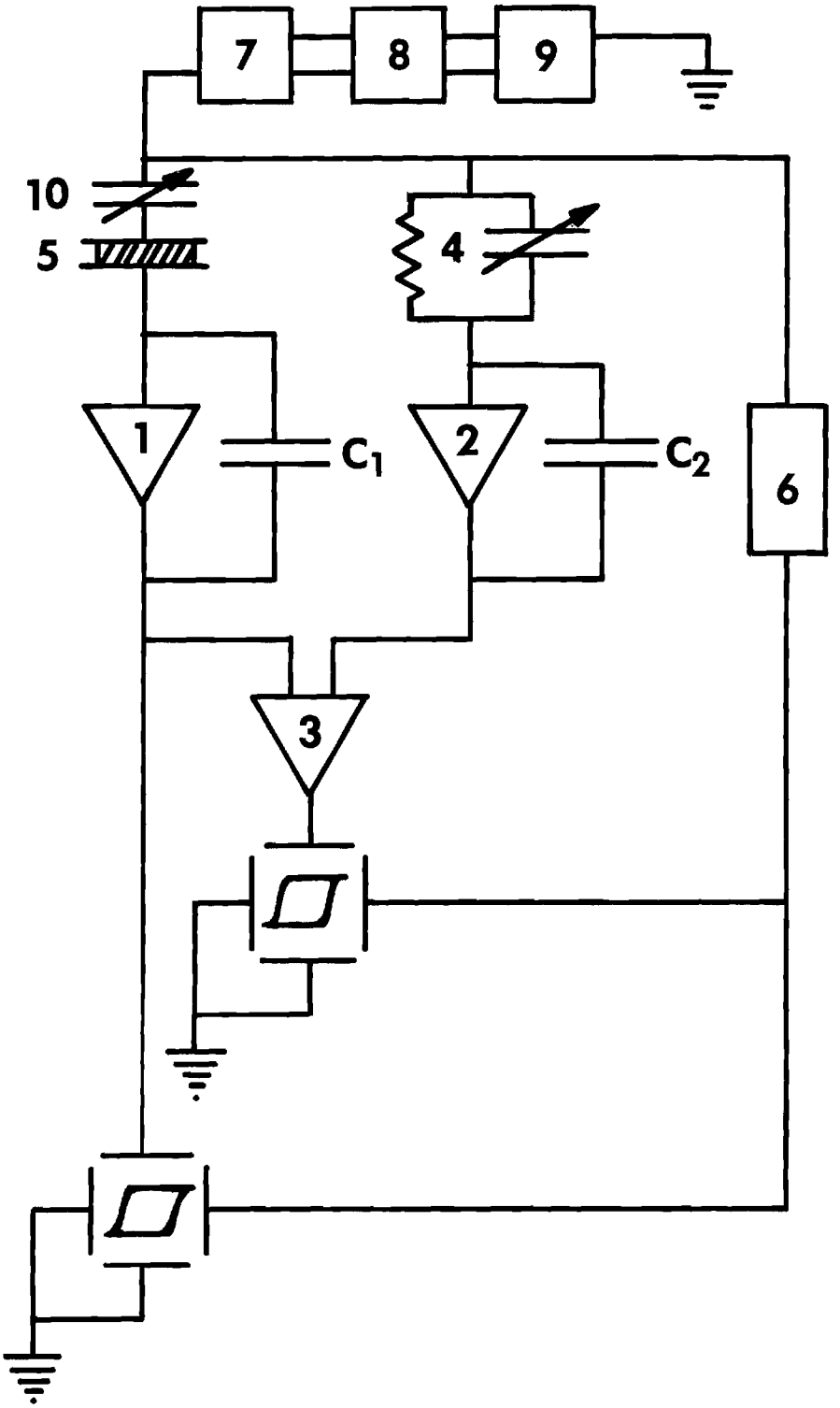

Figure 9. Schematic Diagram of D versus E Hysteresis Loop Tracer. 1, 2, Operational amplifiers; 3, Differential operational amplifier; 4, Compensator network; 5, Sample; 6, Voltage attenuator; 7, Audio transformer; 8, Audio amplifier; 9, Audio oscillator; 10, Trimmer capacitor; C_1 and C_2 are feedback capacitors.

first the basic Sawyer-Tower circuit (Figure 8) and to understand the distortion of the capacitances of the sample and the standard capacitor respectively. Likewise, V_x and V_s are the potential drops across the sample and the standard capacitor, respectively. Therefore, the horizontal axis on the oscilloscope displays V_x, which is proportional to the applied electric field E, where

$$|\vec{E}| = \frac{V_x}{d}$$

and d is the crystal thickness. V_s is displayed on the vertical axis and is proportional to the polarization in C_x. This is shown as follows. The free charge Q on C_x is equal to Q on C_s and thus, $V_s C_s = C_x V_x = Q$ where C_s is a constant. V_s becomes

$$V_s = \frac{\varepsilon_o \varepsilon' A |\vec{E}|}{C_s} \tag{2.1}$$

where

$$C_x = \frac{\varepsilon_o \varepsilon' A}{d}$$

and

$$V_x = |\vec{E}| d$$

Equation 2.1 is related to the polarization by

$$\varepsilon' = 1 + \frac{\vec{P}}{\varepsilon_o \vec{E}} \tag{2.2}$$

If $\varepsilon' >> 1$, as in the case of ClAp and many ferroelectrics, equation 2.2 becomes $\varepsilon' \simeq \frac{\vec{P}}{\varepsilon_o \vec{E}}$. Equation 2.2 is strictly true for a homogenous, isotropic (Class A) dielectric medium. However, in Appendix C it is shown that the same equation is applicable to ClAp with $\vec{E}$ parallel to c, where c is the "ferroelectric" direction. Substitution of equation 2.2 into 2.1 yields

$$|\vec{P}| \simeq \frac{V_s C_s}{A} = \frac{Q}{A}$$

where A is the surface area of the sample capacitor. If C_x is replaced by a resistor R, then the potentials across C_s and R are given by

$$V_{c_s} = V_{c_{so}} \sin(\omega t - 90°)$$

$$V_R = V_{R_o} \sin(\omega t)$$

Since C_{cs} and V_R are out of phase by 90° with respect to each other, the oscilloscope will show an ellipse or a circle (Figure 10a). If C_x is replaced by a standard capacitor C'_s the equations become

$$V'_{c_s} = V'_{C_{so}} \sin(\omega t - 90°)$$

$$V_{cs} = V_{c_{so}} \sin(\omega t - 90°) .$$

V'_{cs} and V_{cs} are in phase. The resultant curve is a straight line (Figure 10b). A combination of resistive and capacitive components will usually produce a rotated ellipse (Figure 10c). A ferroelectric

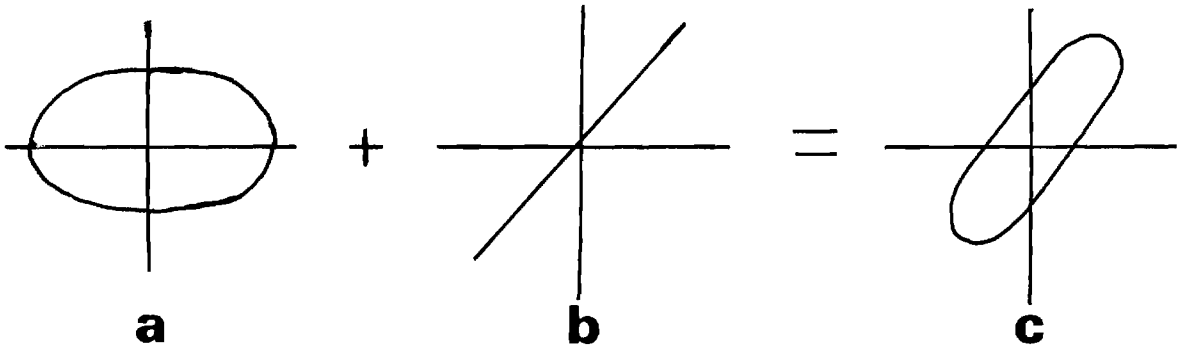

Figure 10. Oscilloscope Traces of Linear Resistance and Capacitance Replacing the Sample in the Sawyer-Tower Circuit. A; Pure resistance; B, Pure capacitance; C, Resistance and capacitance in parallel.

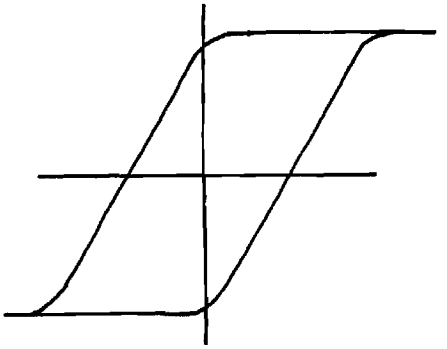

Figure 11. Typical Ferroelectric Hysteresis Loop Without D. C. Conductance.

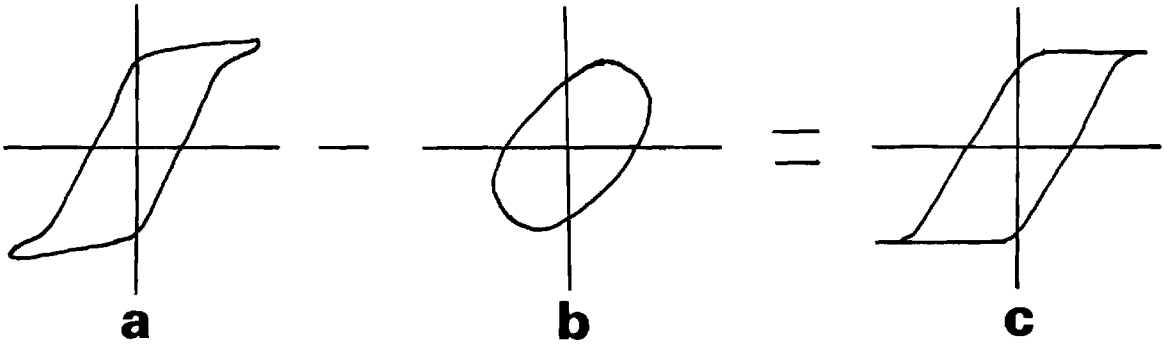

Figure 12. Compensation of Ferroelectric Hysteresis Loop. A, Uncompensated loop; B, Compensating Loop for linear capacitance and resistance; C, Compensated Loop.

material, however, will produce a characteristic hysteresis loop (Figure 11). The complex circuit of the hysteresis loop tracer (Figure 9) can now be easily understood. The feedback capacitors C_1 and C_2 have the same function as the standard capacitor C_s in the Sawyer-Tower circuit. Also, due to the operational amplifier inverted-signal feedback mechanism, the input junction is maintained at virtually zero, or ground potential. Consequently, the potential drop across the sample is equal to the power supply output voltage which is, therefore, directly fed to the horizontal plates of the dual beam oscilloscope.

The current flowing through the ferroelectric sample can now be thought of as a superposition of three distinct components: a) the capacitive or polarization current which is linear with respect to the applied field (I_{cx}); b) the non-linear polarization current (I_p); and c) the resistive current (I_R). The magnitudes of I_{cx} and I_R are matched by the compensator. As a result, only I_p is transmitted by the differential amplifier. The compensation process is shown in Figure 12. A typical, uncorrected, saturated hysteresis loop of a very lossy sample is shown on the left side. By subtracting a rotated ellipse due to I_{cx} and I_R one obtains the corrected loop due to I_p on the right hand side.

Computer Controlled Single Crystal X-Ray Diffractometer System

The automatic selection and scanning of Bragg reflections and print out of information facilitates the collection of large quantities of data. For this reason, the bulk of the X-ray data was collected

with a computer controlled single-crystal diffractometer system (FACS-1 Picker Corporation, Cleveland), whose control program had been developed by Mackie[47]. Details on the PDP-8 computer, the diffractometer interface, the type of diffractometer, the counting chain and the input-output devices are given in Chapter II of the Ph.D. thesis by Mackie[47].

Manually Operated Single Crystal X-Ray Diffractometer System

In order to collect certain of the data (measurement of the lattice parameters) a manually operated diffractometer system was employed. The available θ - 2θ diffractometer carried a four circle goniostat which had previously been designed and built at the Georgia Institute of Technology[48] and mounted on the commercially produced base. The counting chain consisted of an X-ray photon detector (scintillation detector with photomultiplier tube), pulse height discriminator, scalar and a timer. The data were printed on paper tape.

Crystal Heater

Most of the X-ray intensity data were collected at temperatures above 25°C with the Picker FACS-1 4-axis single crystal diffractometer. The gas-stream method was used to heat the crystal because it fulfilled the following requirements best: a) The crystal must be heated uniformly such that the temperature gradient between any two points within the crystal is small (<1°C/mm). b) The temperature must be maintained within $\pm$1°C. c) There should be no obstructions in the primary

or reflected X-ray beam which would require additional absorption corrections. A detailed analysis of the gas-stream method applied to small (~ 0.5 mm) spherical crystals and the description of an operational unit were given by Young[49]. The essential features of Young's design, such as a base which provides support for power and gas inlets, heating elements made of coiled high resistance wire, and a gas mixer at the exit nozzle were incorporated into this heater (see Figure 13) specially designed for this work.

The dimensions of the heater had to be selected carefully because it was mounted onto the χ circle of the FACS-1 diffractometer, directly opposite to the goniometer head, so that the gas stream was always coaxial with the ϕ axis. A bulky unit with an exit nozzle too close to the crystal would severely restrict the accessability of the 2θ, χ field. On the other hand the unit had to be large enough to supply sufficient power in order to maintain a continuous exit nozzle temperature of 700°C at the selected airflow rate, in this case 3 cubic feet per minute. Figure 14 shows the temperature distribution in the gas stream existing at the nozzle at 476°C. The maximum temperature at which data were collected was 450°C. Figure 15 shows the 2θ, χ field accessible with this heater in place. The variation in temperature at the crystal position with the heater operating at 457°C was less that $\pm$1°C over periods of several hours. Three thermocouples were used to control the unit and to protect it and the diffractometer. One (alumel-chromel 30 ga.) was affixed to the heater base to sense the temperature of the goniostat χ circle. The second thermocouple

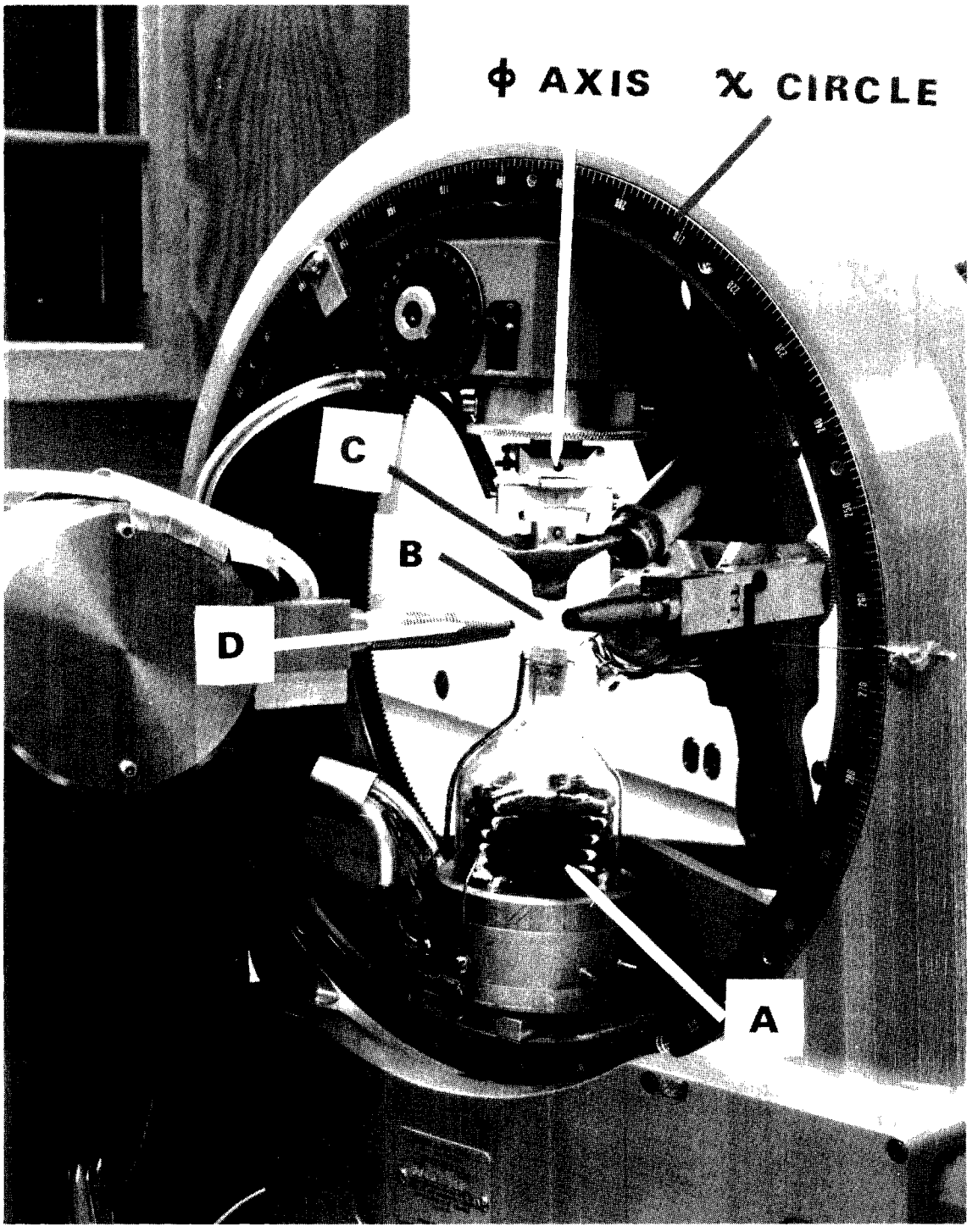

Figure 13. Heater Mounted on χ Circle of Computer Controlled Diffractometer. A, Heater; B, Crystal; C, Deflection shield; D, Incident beam collimator.

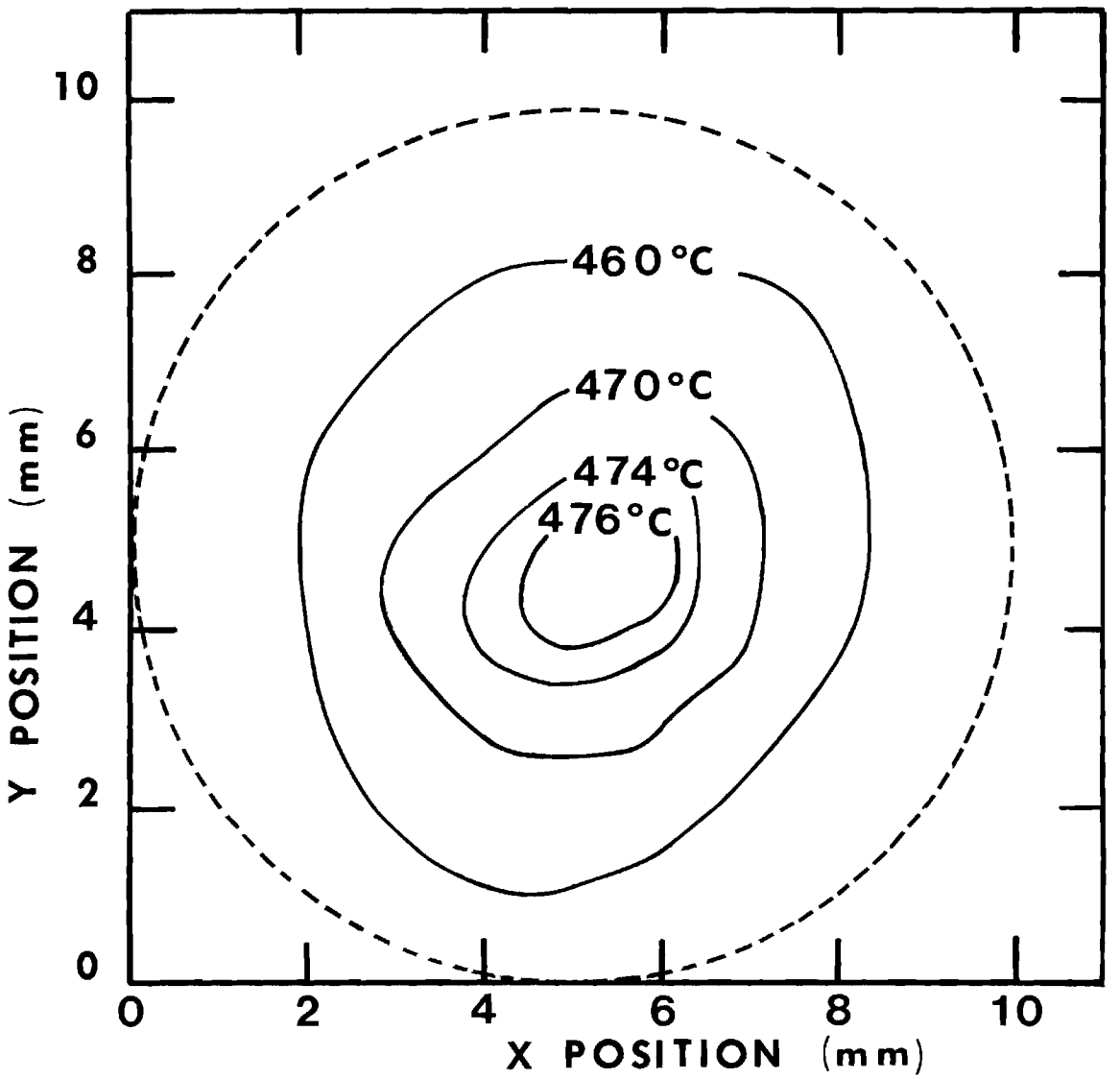

Figure 14. Isotherms at Nozzle Exit of Heater with Nominal Gas-Stream Temperature of 476°C. Dashed line represents inner diameter of nozzle exit.

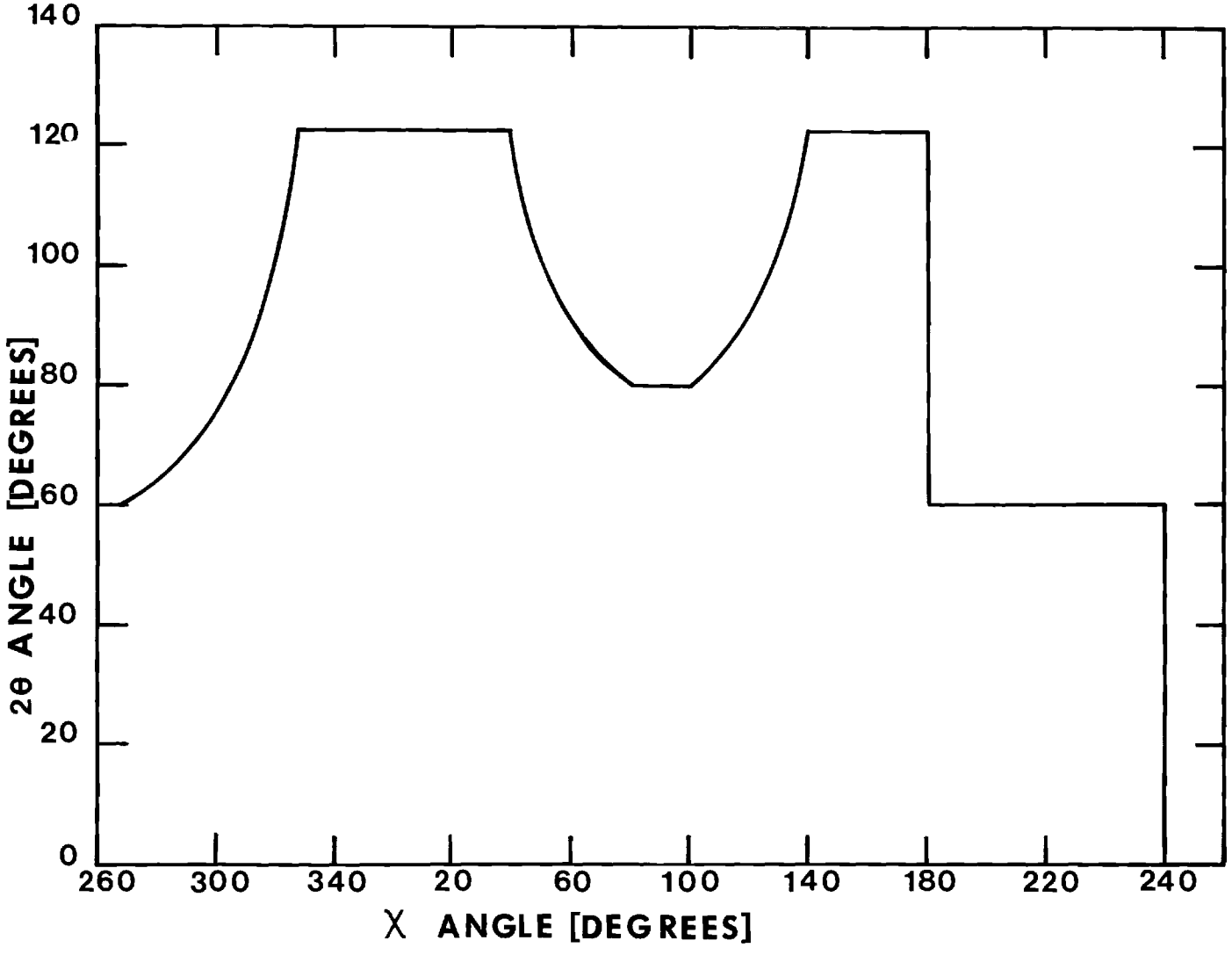

Figure 15. Accessible 2θ, χ Field with Heater Mounted on the Diffractometer. That under the curve is the accessible area.

(Platinum + Platinum -10% Rhodium, 40 ga.) was attached to the uppermost heating element where burn-out is most likely to occur. The heater was automatically shut off whenever the base temperature exceeded 30°C or the top heater element reached 800°C. The third thermocouple helped to regulate the gas stream temperature and therefore, was located at the center of the nozzle exit. A fourth alumel-chromel, 40 gauge thermocouple was used to measure the temperature in the air stream near (e.g. within < 1 mm) the crystal. A control unit especially designed and built by J. R. Cagle of the Georgia Institute of Technology supplied the power, controlled the over-temperature relays and maintained the temperature at the set value.

CHAPTER III

EXPERIMENTAL APPROACH

Chlorapatite Growth

Flux growth of large (3-4 mm) ClAp crystals, from a $Ca_{10}(PO_4)_6$ Cl_2-$CaCl_2$ solution, was reported by Prener[39]. This same technique was used for this work, but with one exception. It was found that dehydration of $CaCl_2.2H_2O$ in a stream of HCl at 500°C was difficult to achieve. After the drying process, the $CaCl_2$ usually consisted of rock like lumps, which were extremely difficult to remove from the drying bottle and, furthermore, had to be ground again into a powder. Besides, HCl is a poisonous and very corrosive gas. To avoid these difficulties the mixture was heated directly in an argon atmosphere in the furnace at 500°C for 24 hours. Because the melting temperature was dependent on the weight ratio of $CaCl_2$ to ClAp powder, slightly more $CaCl_2$, about 5 gm more than the 60 gm suggested by Prener[39], was mixed with ClAp powder to compensate for the weight loss due to water. Upon completion of the dehydration period the temperature was increased to 1280°C and crystal growth was initiated by decreasing the temperature at the rate of 1°C/hr. Crystals with dimensions up to 4 mm x 4 mm x 5 mm were obtained.

Chlorapatite to Hydroxyapatite Conversion

Data from ClAp to OHAp converted crystals were not analyzed because the cracks, which developed within the sample during the

conversion, will distort the measurements of the material's true dielectric constant and loss and render the data analysis meaningless. Nevertheless, it is instructive to discuss the experimental technique used so that similar errors may be avoided in the future.

The conversion process was initiated by preheating the conversion chamber, the steam superheater and the boiler. The crystal's temperature was raised to 1200°C over a period of approximately 6 hours. The system was allowed to operate for a two week period. Shut-down occurred in reverse order.

Examination of converted crystals under a 10 power microscope revealed many cracks both perpendicular and parallel to the $\underline{c}$ axis. The immediate inclination is to attribute this problem to thermal gradients which can arise because of nonuniform temperature distributions in the platinum boat or because of cold steam passing over a hot crystal surface which is hundreds of degrees centigrade above the steam temperature. The former argument must be excluded because no thermal gradients were observed with the optical pyrometer which is sensitive within $\pm$ 10°C. The latter reason is not valid either, because crystals heated in vacuum or with the steam flow temporarily removed were also cracked. A tenable conclusion is that cracking results from stresses which are directly related to lattice dimension changes during the conversion process.

The lattice parameters of ClAp ($\underline{a}$ = 9.645 Å, $\underline{c}$ = 6.763 Å) will be changed to those of stoichiometric OHAp ($\underline{a}$ = 9.421 Å, $\underline{c}$ = 6.881 Å) if conversion takes place. Because single crystals remain single

crystals during the process, the conversion must progress from the surface to the interior of the crystal by diffusion of OH ions along the Cl columns. Thus, it is expected that at any time during the conversion one would find a continuous distribution of cell dimensions between the surface and the interior of the crystal. This conclusion has been supported with X-ray data. The Bragg reflection profiles from incompletely converted crystals were nearly flat at the top and extended over a 2θ range of approximately 0.5° (2θ). This profile can be interpreted as a superposition of Bragg reflections from many crystallites with a small spread in cell dimensions about a mean value. Such a mismatch of cells within a crystal will produce stress. Because the a and c axes are changing during the conversion, it is reasonable to expect the formation of cracks.

Conversion of Chlorapatite to Cl-Deficient Chlorapatite

Single crystals of Cl-deficient ClAp were wanted for the dielectric studies. Efforts to produce them were only partially successful.

The conversion chamber (Chapter II, part 2) was first evacuated to a pressure of 10^{-6} Torr. The crystals were then heated to 1200°C and kept at that temperature for 10 days. Shutdown occurred in reverse order. Approximately a dozen crystals were converted during 3 runs. All crystals developed cracks both parallel and perpendicular to the c axis, although no thermal gradients were observed with an optical pyrometer (sensitivity $\pm$ 10°C) during the conversion. Prener[41] reported $CaCl_2$ loss from ClAp powder annealed in a vacuum for 16 hours

at temperatures between 900°C and 1200°C and corresponding a and c lattice parameter changes. Thus, presumably, the cracks are caused by stresses due to differences in cell parameters arising from $CaCl_2$ loss.

Specimen Preparation for Dielectric Measurements

Slicing and Polishing

Stoichiometric ClAp, FAp and (F,Cl)Ap grown from the flux usually occur as hexagonally shaped needles with the c axis parallel to the needle axis. The crystals were oriented by aligning a well-formed hexagonal face with the edge of a glass slide (c axis parallel to edge) and were mounted with a thermosetting plastic. The glass slide was glued to a machined metal block and the whole assembly transferred to the magnetic chuck of an automated precision slicing machine. Water served as a cooling medium. The crystals were generally sliced into slabs about 0.5 mm thick with the c axis either parallel to or perpendicular to the large faces of the platelet. The alignment of the c axis ($\perp$ or $\parallel$) was checked with orientation photographs on a Buerger precession camera. The slabs were subsequently polished with 600 grit emery paper and 3 different grades (7 μm, 3 μm, 1 μm) of diamond paste to a maximum surface roughness of 1 micrometer. To maintain parallelism of the face during the polishing procedure the crystal was glued to a specially-made hand-held jig. At this point some inclusions or cracks could be easily identified under a 10 power microscope. The occurrence of visible channels parallel to the c axis was a very common feature of these chlorapatites and fluorapatites. In such cases, the section which contained the channel was

either removed or the whole crystal was discarded.

To form a capacitor one normal procedure is to evaporate on each face of the slab a circular gold electrode with an area smaller than the crystal area. In this work this method was not practical because the crystal dimensions were generally very small (2 mm x 2mm x 0.2 mm). Instead, the slab was polished into a rectangular shape and covered completely with the evaporated electrode material. The conductive layer on the sides was then removed with 1 micrometer diamond paste. The electrode area could then be easily determined.

Specimen Characterization

Stoichiometric ClAp has the monoclinic space group $P2_1/b$. Impure or highly Cl-deficient ClAp is usually hexagonal with the space group $P6_3/m$. These two forms are easily distinguished from each other with x-ray methods because, except for $\ell = 0$, the monoclinic reciprocal lattice contains additional points which are located halfway between the normally occurring hexagonal lattice points along the b axis. Precession photographs of the h k 2 reciprocal lattice layers of all ClAp specimens were made, because the h k 2 layer contains some of the strongest "monoclinic" reflections. In addition, the a and c lattice parameters of all crystals were measured by the Bond method with the manual goniostat to determine, via Vegard's law, the F/F+Cl ratio in (F,Cl)Ap and the amount of $CaCl_2$ loss in ClAp. The most nearly stoichiometric ClAp crystals had a lattice parameters which were generally between 9.645 ± 0.001 and 9.648 ± 0.001. A 1 percent change in F or vacancy concentration[41] would have changed the a

lattice parameter by 0.002 Å or 0.003 Å, respectively.

Electrode Preparation

Although conductive epoxy paints are commonly used as electrodes in dielectric measurements and had been used for the earlier experiments in this laboratory, they were demonstrated to be unsatisfactory for this work. Evaporated metal films had to be used. The question of electrode placement, contact closeness, and composition of the electrodes is often crucial to the accurate determination of dielectric constants if they are high. In the case of ClAp with the applied field $\vec{E}$ parallel to the c axis an order of magnitude difference in the capacitance of the same sample was found when the evaporated gold film was replaced with a conductive silver epoxy paint. Evidently, with these electrodes, the capacitance representative of the bulk dielectric properties of the crystal was not the only thing contributing to the measurement. Evaporated aluminum and gold-chromium films were also employed as electrode materials. All the evaporated films gave similar results, but a major difference existed between results with conductive paints and those with evaporated films. In general, a reduced capacitance value was observed for those crystals having a conductive paint as electrode material. This difference can be understood if one considers the dielectric medium between the electrodes as a 3-layer material with dielectric constants ε'_1, ε'_2, and ε'_3 and thicknesses d_1, d_2 and d_3 respectively. ε'_1 and ε'_3 can correspond to the surface impurity layers which are usually present on any dielectric. For

equivalent impurity or extraneous layers 1 and 3, so that $\varepsilon'_1 = \varepsilon'_3$ and $d_1 = d_3$, the capacitance of the three layer dielectric becomes (see Appendix D)

$$C = \frac{\varepsilon'_1 \, \varepsilon'_2 \, \varepsilon_0 \, A}{\varepsilon'_2 \, \Delta t + \varepsilon'_1 \, d_2} \quad , \tag{3.1}$$

where

A is the electrode area,

ε_0 is the permittivity of free space (8.85×10^{-12} fd/m)

ε'_2 is the dielectric constant of the material to be measured,

and Δt is equal to the combined thickness of the impurity layers $(d_1 + d_3)$.

In order for C to be within 1% of the correct value, assuming A and d ($d = d_1 + d_2 + d_3$) can be measured with negligible error, it is required that

$$\Delta t \leq \frac{1}{\varepsilon'_2} \left(\frac{\varepsilon'_1 \, d_2}{0.99} - \varepsilon'_1 \, d_2 \right)$$

Let $d_2 = 0.02$ cm (typical thickness of a ClAp sample) and $\varepsilon'_1 = 85$, the dielectric constant of water at room temperature and 1000 Hz. Then,

$$\Delta t < \frac{0.017}{\varepsilon'_2} \quad .$$

If $\varepsilon'_2 = 1000$ $\qquad$ $\Delta t \leq 1700$ Å

If $\varepsilon'_2 = 10{,}000$ $\qquad$ $\Delta t \leq 170$ Å

If the assumption is made that $\varepsilon'_1 = 1$, the dielectric constant of air, and $d_2 = 0.02$ cm, then

for $\varepsilon'_2 = 1000$ $\quad \Delta t \leq 20$ Å ;

for $\varepsilon'_2 = 10{,}000$ $\quad \Delta t \leq 2$ Å .

Conductive paints usually consist of silver or gold flakes mixed with a film-forming binding material. It might be expected that the surface of the film would be much more nearly composed of the film-forming material alone than would the bulk of the painted-on electrode. Scanning electron microscope studies of our conductive epoxy paints did indicate, in fact, that the binder itself may form a several thousand Å thick interface which possibly could act as a dielectric impurity layer.

It is interesting to reverse the problem and to find an effective thickness Δt given the following information on ClAp. The assumption is made that the dielectric constant is equal to 10,000 ($\varepsilon'_2 = 10{,}000$), d_2 is equal to 0.02 cm and C is reduced by a factor of 2, which factor was obtained from the experimental determination of capacitance on crystal thickness. The effective thickness of Δt was found to be about 200 Å, or $d_1 = d_3 = 100$ Å. This number is quite reasonable in view of the previous discussion and it supports the idea that the dielectric constant of ClAp parallel to the c direction (hereafter written as $\varepsilon'_{\parallel c}$) is of the order of 10^3 to 10^4 at room temperature. To remove as many impurities (mainly H_2O molecules) as possible prior to the evaporation of the metal electrode film, each crystal was washed in hot trichloroethylene vapor and left in a vacuum

at 10^{-6} Torr for approximately 1 hour. Only gold electrodes were used, because this element is chemically inert.

The thickness of the crystal with gold film (< 1% of crystal thickness) was measured with a micrometer. The slab's surface was then covered with silver paint to protect the gold film from being rubbed off or damaged (no differences were observed in the measurements with and without the silver paint applied). Finally, the capacitor's total thickness (including the silver paint) was measured to be used in the capacitance correction procedure.

Specimen Preparation for X-Ray Measurements with the FACS-1 System

For least squares structure refinements the X-ray intensity data usually need to be corrected for absorption. That is greatly simplified if the specimen is ground to a spheroidal shape. Then, the absorption correction is a function of μr and θ, where μ is the absorption coefficient (for ClAp μ = 28.6 cm^{-1} for Mo Kα radiation), r the radius of the crystal and θ is the diffraction angle. To minimize the errors introduced by uncorrected absorption, the crystal should be as spherical as possible. However, this requirement is often not realized in practice. For the particular ClAp crystal used in this experiment the average radius was 0.511 mm and μr was equal to 0.731, ensuring that the absorption correction factor varies slowly with successive values of θ. All radii agreed within 0.006 mm. The intensity attenuation in the crystal is given by

$$I = I_0 e^{-\mu r}$$

Since the maximum difference in radii $\Delta r = 6 \times 10^{-4}$ cm leads to only a 2% difference in I, corrections for a sphere were used. The crystal was mounted on a silica fiber with the c axis nearly perpendicular to the ϕ axis. With this mounting χ could be restricted to the angles $-30° \leq \chi \leq +30°$, because data from only those reciprocal lattice points which are confined to an 8° cone about the c* axis were required. With this orientation all 2θ angles up to 120° were accessible (see Figure 15).

Finally, a Laue photograph of the specimen was made and examined for features such as polycrystallinity which would make the crystal unsuitable for quantitative diffraction measurements.

Data Collection Strategy

Dielectric Data

The dielectric measurements of ClAp, in particular, appeared to be easily influenced by the ambient environment and permanently changed by large electric fields. Reproducibility of the data, therefore, could not be achieved until two questions were answered. First, exactly which environmental component(s) is (are) involved? Second, what electric field strength will permanently distort the dielectric constants?

In 1970, Siegel[29] reported that air greatly influenced the dielectric measurements of ClAp. Elliott[33] observed that electrical measurements on compressed OHAp powder were very dependent on moisture. In order to check and to firmly establish the influence of absorbed

water molecules on the dielectric measurements of ClAp the following experiment was carried out at room temperature. A ClAp crystal with $E_{\parallel c}$ was placed inside the cell. A pyrex tube filled with water and a dry N_2 source were connected with Tygon tubing to the gas inlet of the cell according to Figure 16. The system was first purged with dry N_2 with valve #2 closed. Valve #1 was then shut, the cell evacuated, and the bridge readings recorded.

At 2×10^{-5} Torr pressure

$C_s = 6.95$ nf

$\tan \delta = 0.25$

The Tygon lines were depressurized by temporarily opening valve #1 and bleeding the excess N_2 into the vacuum chamber. The cell was again evacuated to slightly less than atmospheric pressure. Valve #2 was now opened and the water heated to fill the tygon tubing with water vapor. When valve #1 was opened, both the capacitance and loss tangent increased rapidly. The bridge values recorded after several minutes were as follows:

At nearly atmospheric pressure

$C_s = 13$ nf

$\tan \delta = 0.37$

Final readings

$C_s = 19.3$ nf

$\tan \delta = 0.41$

When the same procedure was repeated with H_2, Ar and He gas, only very small changes (~ 10 pf) were observed. In the thought that these small changes may have been caused by water vapor mixed with the gases, a drying agent was inserted between the N_2 gas supply and the

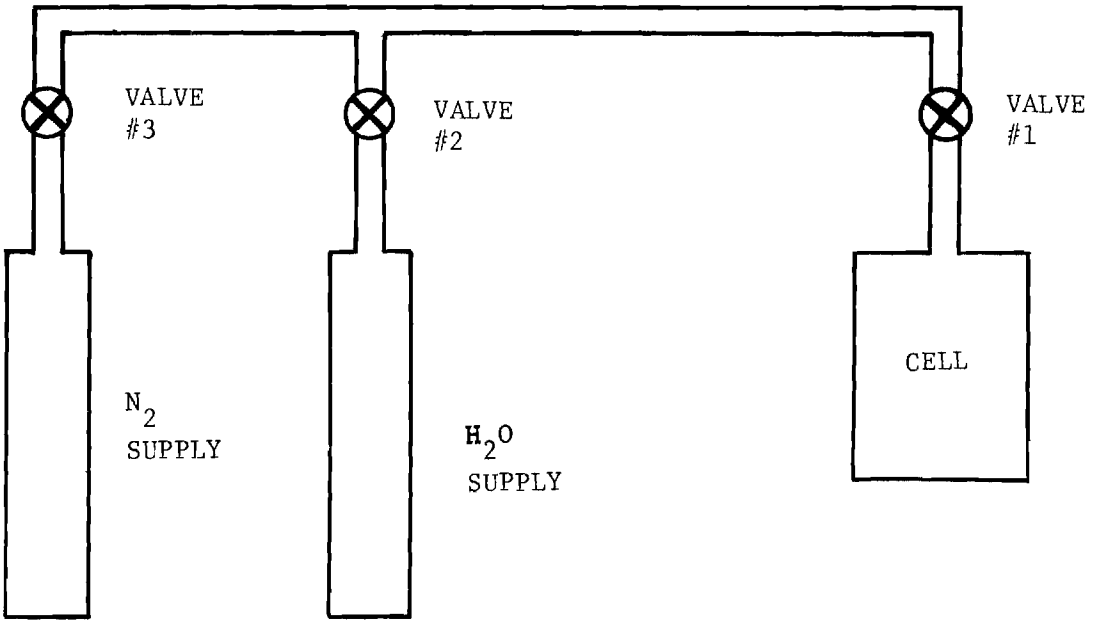

Figure 16. Schematic Diagram of System Used for Assessing the Effect of H_2O on Electrical Properties of ClAp.

cell. The changes were thereby eliminated. All subsequent measurements were taken in an N_2 environment at a constant pressure. Abundant literature is available on dielectric measurements of materials with adsorbed gases[51,52,53]. (These references are only a representative sample.) Figures 17 and 18 show the dependence of the capacitance on temperature for ClAp with $E_{\perp c}$ in air and dry nitrogen respectively at 1,000 Hz. The cooling and heating curves coincide with the crystal in an N_2 environment, but in air they do not. The plots in Figures 17 and 18 were typical of many samples tested in each case.

Before dielectric measurements were attempted with any crystal, the cell which contained the sample was evacuated to 10^{-6} Torr and recharged with N_2 gas. The crystal was then heated to 200°C. At this temperature, the chamber was once again evacuated, then refilled with dry nitrogen and allowed to cool to room temperature. This process was repeated several times until the capacitance and loss tangent readings for the heating and cooling cycle coincided. All measurements were carried out in a nitrogen atmosphere, which facilitated rapid thermal conduction in heating and cooling of the sample. Measurements were found to be reproducible when the crystal was removed from and returned to the cell several times.

The question of whether the dielectric constant, the d.c. conductivity or the hysteresis loop should be measured first was ignored until it was found that the application of large fields (~ 10,000 V/cm) to ClAp with $E_{\perp c}$ distorted the measured values of

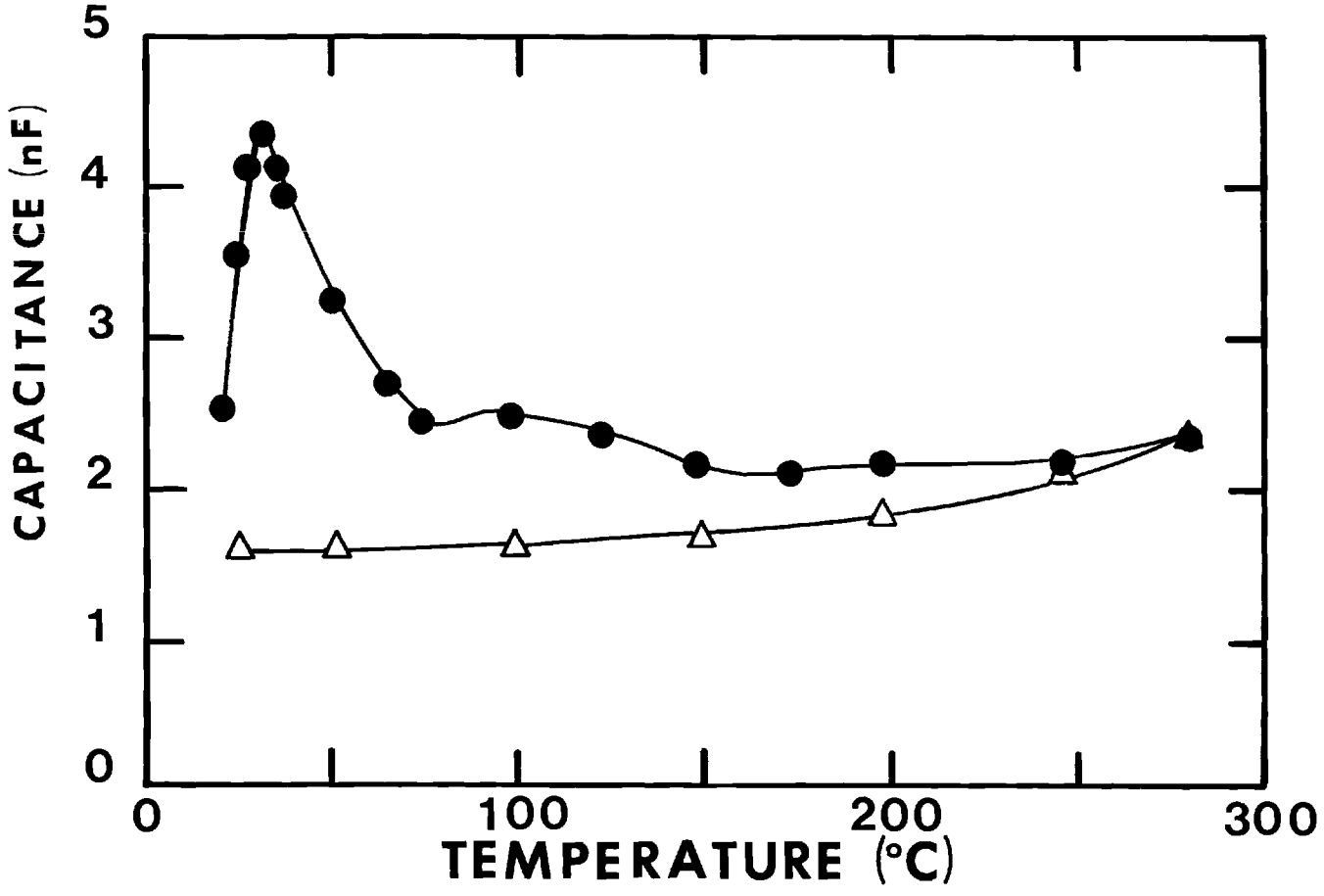

Figure 17. Temperature Dependence of Capacitance of ClAp in Air (E parallel to c, Sample CN7PE). The heating run is represented by solid circles, the cooling run by triangles.

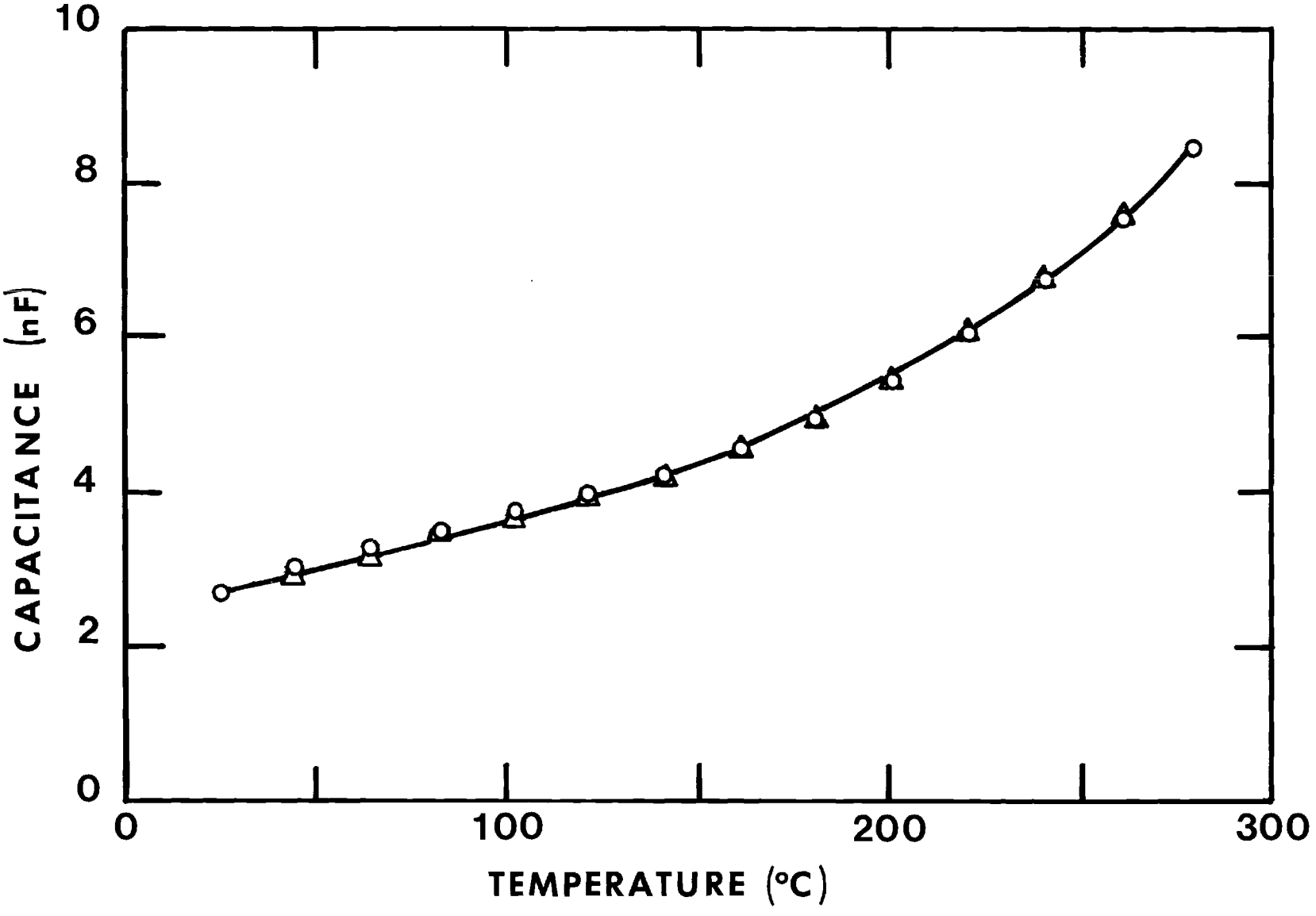

Figure 18. Temperature Dependence of Capacitance of ClAp in Dry N_2 (E parallel to c, Sample CN7PE). The heating run is represented by circles, the cooling run by triangles.

the sample. The readings were always less after the field was applied. A 30% drop in capacitance and tan δ was not unusual. For this reason, all of the measurements employing only small fields (10 V/cm) were completed first. Hysteresis loop measurements were carried out next. At this stage some samples became highly conductive (fields up to 10^4 V/cm were applied) so that an entirely different group of samples had to be used for d.c. conductivity measurements.

Only after these problems of reproducibility were solved could the data collection proceed. The measurements were taken as a function of frequency at constant temperature. A 30°C step between each set from 25°C to a maximum of 300°C was selected.

The hysteresis loops were photographed at various frequencies, temperatures and applied fields.

X-Ray Data

Three distinct sets of x-ray data on ClAp were collected. These were two intensity data sets, the "β_{33} set" and the "phase transition set," and one reflection-position set. The β_{33} data set was used for least squares structure refinements and consisted of seven subsets, each one collected at a different temperature (25°C, 50°C, 100°C, 150°C, 200°C, 250°C, 300°C). Because the apparent ferroelectric effect and the apparent transition at 200°C were tentatively attributed to the Cl ion movements, interest was primarily focused on the motion of these ions along the c axis as a function of temperature. Both their positions and their mean square thermal vibrational amplitudes

along $\bar{c}$ ($\overline{u^2_{33}}$), were the parameters of interest. $\overline{u^2_{33}}$ is related to the parameter β_{33}, obtained from least squares structure refinements[54], through the following equation

$$\overline{u^2}_{33} = \frac{c^2 \beta_{33} c\ell}{2\pi^2}$$

hence, the name "β_{33} data."

The specimen used for this experiment was monoclinic and triply twinned mimetically. Hence, the direct approach would be to refine the structure in the monoclinic space group $P2_1/b$. However, the required information can also be obtained from a refinement in the hexagonal space group $P6_3/m$, because the monoclinic form is so strongly pseudo-hexagonal that a previous refinement of monoclinic ClAp in the $P6_3/m$ space group had shown[47] that the Cl positional parameters, z, and the β_{33} parameters agree within the third decimal place, which is sufficient to give the required precision of $\pm$ 0.001 Å for z and $\sqrt{\overline{u^2_{33}}}$. The latter approach was used to avoid computational difficulties such as the calculation of twin volume ratios and scale factors for each crystal orientation in the twin. Therefore, all k_{odd} ("monoclinic") reflections were simply eliminated from the β_{33} data set. The refinement starting parameters for each set were always obtained from the least squares results of the set collected at the next lowest temperature. The exception, of course, was the room temperature set. As it was not expected that the composition of the crystal, formed under high temperature conditions, would be changed

by this comparatively mild heating to 400°C the atomic multipliers were not allowed to vary in the refinement.

Intensities were collected of only those reflections whose reciprocal lattice points were confined to a half cone centered about the c axis with its apex at the origin of reciprocal space. The cone angle was adjusted until each data set contained about 600 reflections. The details of data collection are discussed both in Chapter IV and Appendix C of Mackie's thesis[47]. A minor addition to the computer control program was made to limit data collection to reciprocal lattice points within the previously described half-cone and within the χ limits determined in Chapter II of this thesis. The addition to the control program is indicated in Figure 19, where α is the cone angle (about 8°). The limits on h, k, ℓ and 2θ were: $-8 \leq h \leq 8$, $0 \leq k \leq 16$, $1 \leq \ell \leq 16$, $0.5° \leq 2\theta \leq 115°$. Upon completion of each set, the 2θ, ω, χ and ϕ angles of 12 reflections were determined with a peak-centering program. These data were processed with a least-squares[88] technique to calculate the lattice parameters at that temperature.

The transition set of x-ray intensity data were collected for the following reason. According to Prener[39] all h k_{odd} ℓ reflections disappear whenever nearly stoichiometric ClAp is heated above the transition point (~ 200°C). Our x-ray intensity data, however, clearly indicated that this was not the case; some h k_{odd} 2 reflections were observed even at 300°C. Hence, the integrated intensity, the peak intensity and the ratio of integrated to peak intensity of

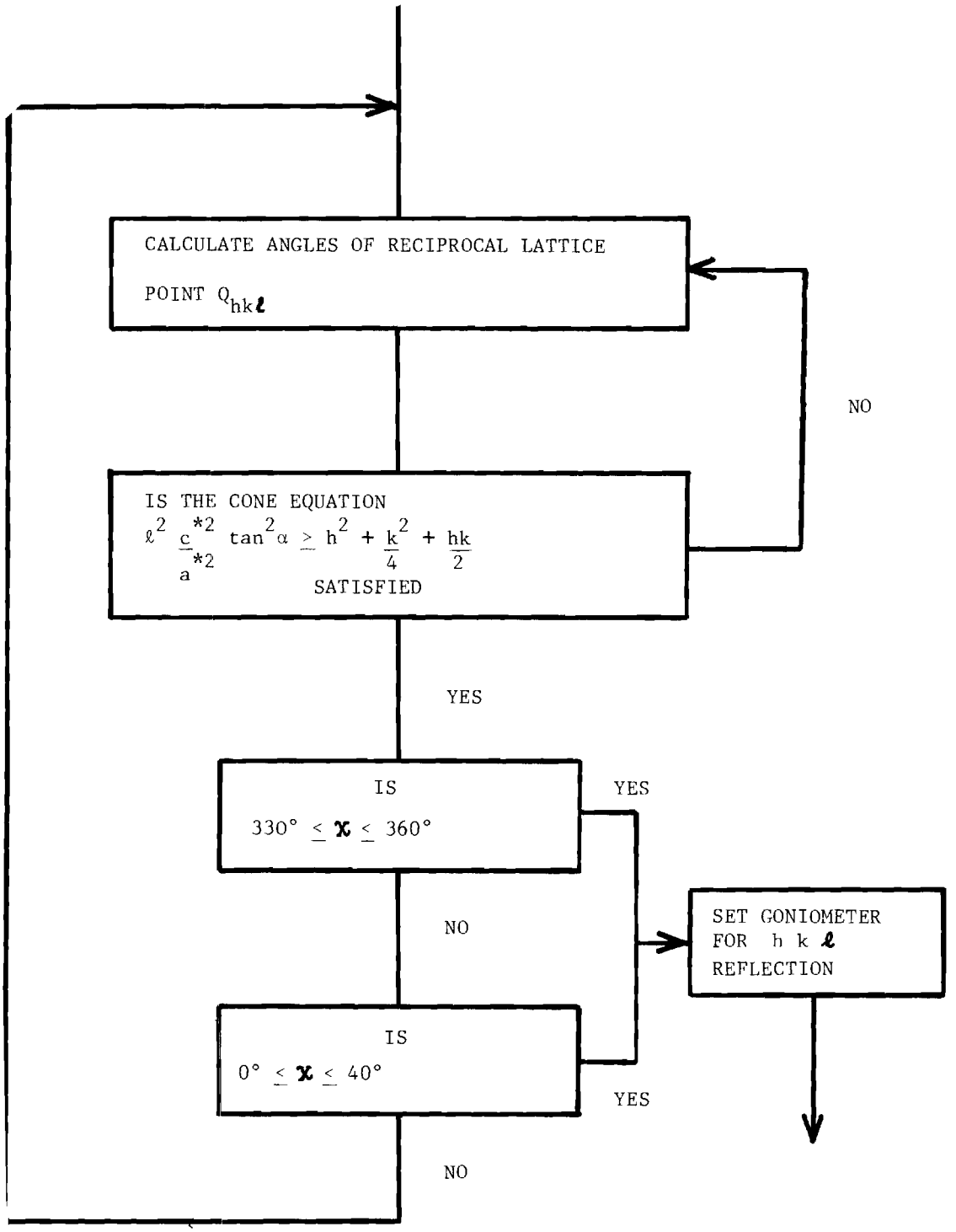

Figure 19. Subroutine of Computer Program Which Controls the Diffractometer.

several h k_{odd} ℓ reflections were collected and plotted as a function of temperature in order to reveal more information on the nature of the transition. This second data set (the transition data set) consisted of 15 subsets; each one collected at a different temperature (25°C, 100°C, 150°C, 170°C, 180°C, 196°C, 203°C, 210°C, 220°C, 230°C, 250°C, 300°C, 350°C, 408°C). Each subset contained 20 reflections. To monitor any changes in twinning, 12 of these 20 reflections were collected from the first "crystal" of the triple twin (the sample being that used for the β_{33} data) and four from each of the other two "crystals." The four were selected so that the same four reflections were measured for each of the three crystals in the twin. (Here the triple twin is defined as the composite of three crystals each having a different orientation about the c axis.) The 12 reflections were selected on the basis of strength and falling within the imposed χ limits.

The salient features of the data collection procedure were as follows. The k h ℓ indices of all 20 reflections were stored on disk memory. The computer calculated the 2θ, ω, χ and ϕ angles of the first reflection and set the detector to $2\theta° - 1.5°$. A 2θ step scan was then carried out over a 3° (2θ) scan range centered on the peak. The step size was 0.05° (2θ) and the counting time for each step lasted 10 seconds. Upon completion of the scan, the next h k ℓ was selected and the above process repeated. At the beginning, every hour thereafter, and at the end, the h k ℓ sequential selection routine was interrupted to step scan over the standard reflection, the 008, in

order to monitor any changes in the primary beam intensity or crystal orientation. After all required reflections were scanned, the temperature of the crystal was set to the next value and the data collection procedure repeated.

The third set of X-ray data, those on reflection positions, was for lattice parameter determination. The lattice parameters of all specimens with the exception of the β_{33} specimen were determined with the manually operated diffractometer. For the precise lattice parameter measurements needed ($\pm$ 0.001 Å) the Bond[50] method was used. Bond[50] took advantage of the fact that if the photon detector window is large (~ 2 cm in our case) then θ can be measured between the two diffraction positions of the crystal shown in Figure 20 irrespective of the exact position of the detector. To obtain the lattice parameters the angles R_1 and R_2 in Figure 20 were measured for a number of h 0 0 and 0 0 ℓ reflection pairs and the average angle ($\theta = (R_1 + R_2)/2$) for each was substituted in the Bragg equation, $2d \sin \theta = n\lambda$. Typical results are shown in Table 1. Although not all known corrections[67,68] were taken into account the required precision of $\pm$ 0.001 Å was achieved. This conclusion was derived from Figure 30, which basically is a demonstration that Vegard's law is rather strictly obeyed in the intersubstitution of F and Cl in (F,Cl)Ap. Important, however, is the fact that the scatter of points in Figure 30 about the line is so small that the precision in lattice parameter measurements is in fact shown to be better than $\pm$ 0.001 Å.

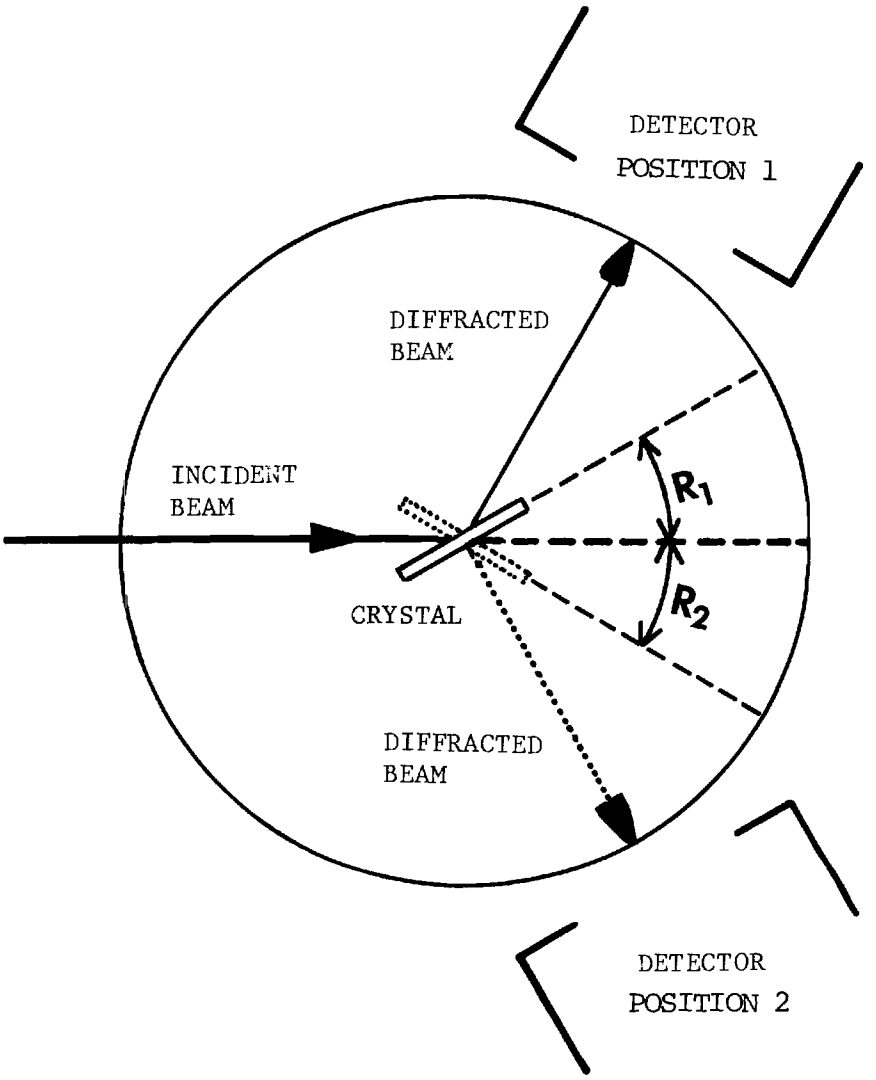

Figure 20. Schematic Diagram of a Diffractometer Employing the Bond Method. Solid lines represent diffraction condition with crystal and detector in position 1 (R_1 is the measured angle). Dotted lines represent diffraction condition with crystal and detector in position 2 (here R_2 is the measured angle).

Table 1. Lattice Parameters of ClAp and (F,Cl)Ap Samples Measured with the Bond Method (λ=0.70926 Å)

Sample	Reflection h k ℓ	a(Å)	c(Å)
CLAP	0 0 16		6.7649
C5PE	0 0 12		6.7656
	15 0 0	9.6488	
	12 0 0	9.6499	
	0 0 16		6.7646
CLAP	0 0 12		6.7650
C16PE	15 0 0	9.6468	
	12 0 0	9.6477	
	0 0 16		6.8855
FAP	0 0 12		6.8859
F3PE	17 0 0	9.3711	
	15 0 0	9.3724	
	0 0 16		6.7786
(F, Cℓ)Ap	0 0 12		6.7796
FC1PE	15 0 0	9.6315	
	12 0 0	9.6325	

Data Reduction

Audio Bridge Data

The equivalent electrical circuit of a parallel plate capacitor is usually represented as an ideal capacitor in parallel with an ideal resistor. However, at times, measurements had to be made with the series capacitance bridge, because its loss tangent range was different from that of the parallel bridge. Here, the sample is represented as an ideal capacitor in series with an ideal resistor. All such measurements of apparent series capacitances must, then, be converted to the actual, parallel capacitances. The equation to be used is

$$C_p = C_s \left(\frac{1}{1 + \tan \delta^2}\right) \tag{3.4}$$

and is derived in Appendix B, section 1. The loss tangent need not be converted, since its value is the same for the series or parallel combination, as shown in Appendix B, section 1. The raw value ((tan δ)/M), however, had to be multiplied by a scaling factor M dependent on the operating frequency and given in the instruction manual[55].

A correction was made to the loss tangent in accordance with Appendix B, section 3. The residual corrections were condensed into equation 3.5 developed for use with a computer program. These corrections were determined on the basis of bridge performance and served to improve the accuracy of the measured loss tangent.

$$D_x = -X\ (0.00022F - 0.0002) + 0.00116F \tag{3.5}$$

where F is the frequency in kilohertz and X the capacitance dial reading. D_x is a number which must be subtracted from observed tan δ values to improve the accuracy of tan δ to $\pm$ 5% $\pm$ 0.001. This correction was found to be valid only when F exceeded 1,000 hz, X was less than 6.3, and the capacitance bridge was set to the picofarad range.

The three terminal method[55] effectively removed all stray capacitances except the cell electrode capacitance, which was in parallel with the sample and had a typical value of about 4 pf. This capacitance (C_{err}) was calculated with equation 3.6 and simply subtracted from the measured value.

$$C_{err} = \frac{\varepsilon_0 A}{d_0} - \frac{\varepsilon_0 A_s}{d_0} \tag{3.6}$$

A is the cell electrode area and A_s is the area of the dielectric. The cell electrodes had a disk-shaped form with a 0.25 inch radius. Thus, the area A is fixed, whereas the electrode gap, d_0, and the area A_s are functions of the sample's geometry. The second term represents the cell electrode capacitance under the sample area, which must be subtracted from the first term, the total cell electrode capacitance.

Capacitance corrections for the fringing field were found to be negligibly small. This is shown as follows. A ClAp specimen ($E_{\parallel_c}$) with evaporated gold electrodes (diameter of crystal = diameter of electrodes) was used. The capacitance of this specimen was measured first between the electrode disks of the dielectric cell in air

(electrode area 1.27 cm^2, crystal face area $\lesssim$ 0.05 cm^2). Wires (<< area of crystal face) were then attached to both faces and the capacitance measured again by attaching the wires directly to the bridge input terminals. Because the fringing field capacitance for the latter method (here the diameter of electrode = diameter of crystal) can be calculated (~ 0.1 pf) and because no difference in the capacitance between the two types of measurements were observed, it was concluded that the fringing field capacitance could be neglected for ClAp with the electric field parallel to the c axis.

The dielectric constant (i.e., real part) and dielectric loss were obtained with equations 3.7 and 3.8,

$$\varepsilon' = \frac{C_p d}{\varepsilon_0 A_s} \tag{3.7}$$

$$\varepsilon'' = \varepsilon' \tan \delta \tag{3.8}$$

where C_p is the corrected parallel capacitance and d, the sample thickness.

R. F. Bridge Data

The r. f. bridge corrections were more intricate for two reasons: i) Only the two terminal method could be used, thus, corrections had to be made for the cell's stray capacitance to ground. ii) The inductive impedance of the leads becomes increasingly important in the megacycle range and its influences on the measurements must be eliminated.

At times, the cell was shunted with a standard capacitor to bring the reactance and resistance into direct reading range. Corrections for this capacitor were made first with equations B-43 and B-44 of Appendix B, section 4. The resistance of the standard capacitor was extremely high and, thus, for all practical purposes could be ignored.

The circuit may now be represented by an inductive impedance in series with two capacitive impedances themselves in parallel as shown in figure 61. The next step was to correct for the inductive impedance of the leads with the following equations.

$$X_C = X_M + X_L$$

$$R_C = R_M - R_L$$

where X_M and R_M are the measured capacitive reactance and resistance to be corrected; X_L and R_L are the inductive reactance and resistance, respectively. X_C and R_C are the partially corrected capacitive reactance and resistance.

The remaining components in parallel with the sample impedance were the residual capacitive cell impedance Z_{c1} and the cell electrode impedance Z_{c2}. The two capacitive impedances were added vectorially with the aid of equations 3.11 and 3.12.

$$R_A = \frac{-X_1 X_2 R_2 + X_1 R_2 (X_1 + X_2)}{R_2^2 + (X_1 + X_2)^2} \qquad (3.11)$$

$$X_A = \frac{X_1 R_2^2 + X_1 X_2 (X_1 + X_2)}{R_2^2 + (X_1 + X_2)^2} \tag{3.12}$$

X_2 and R_2 were the series capacitive reactance and resistance of the cell electrode and X_1 is the residual capacitive cell reactance. R_1, the residual capacitive cell resistance, was assumed to be infinite and, therefore, was not included in the calculation. R_A and X_A were then subtracted from X_C and R_C with equations B.43 and B.44 of Appendix B, section 4 (here $R_S = R_A$, $X_S = X_A$, $X_M = X_C$, $R_M = R_C$) to obtain, finally, the reactance X_x and resistance R_x of the sample. It is important to realize that the sample was treated as a reactance and resistance in series with each other. Therefore, the capacitance and resistance calculated from the final corrected values X_x and R_x were converted to the equivalent parallel capacitance. The required data were obtained with the following equations.

$$\tan \delta = R_x / X_x \tag{3.13}$$

$$C_p = \frac{1}{2\pi f X_x (1 + \tan^2 \delta)} \tag{3.14}$$

$$\varepsilon' = \frac{d C_p}{\varepsilon_0 A_s} \tag{3.15}$$

$$\varepsilon'' = \varepsilon' \tan \delta \tag{3.16}$$

f is the frequency, A_s is area of the sample and d is its thickness. The conversion equation for series R_x to parallel R_x is derived in Appendix B, section 1.

X-Ray Data

Normalization of intensities of the β_{33} data followed the guidelines set down by Mackie[47]. Standard corrections were made for adsorption, Lorentz and polarization factors and anomalous dispersion[57]. Isotropic extinction[56] corrections were incorporated in the least squares refinement program[54].

The corrections for the transition data were distinctly different. Three parameters were extracted from the step-scan data. These are the peak intensity, the integrated intensity and the ratio of the integrated to peak intensity. Before these variables were calculated, the data were normalized with respect to the intensity of the first standard reflection (0 0 8) in each subset and corrected for background. Normalization was accomplished by fitting a second degree polynomial to the series of standard reflections.

The background was approximated by a least-squares fitted straight line between the last five points on both ends of the diffraction profile.

The integrated intensity was obtained after the background was subtracted point by point from the diffraction profile.

To find the peak intensity a five-point parabola was fitted to the central section of the diffraction profile.

Experimental Errors

Although some errors presented in this section are large, even the maximum possible errors are tolerable, because the significance of this work does not lie in the accurate determination of ε' of ClAp,

but rather in the discovery of the fundamental processes which give rise to the anomalous electrical properties. However, it is useful to go through some error analysis to assure ourselves that the errors are in fact never so large as to vitiate the interpretations made.

Audio Bridge Accuracy

The audio bridge accuracy for capacitance as specified by the General Radio Corporation is $\pm$ 1% $\pm$ 1 pf except at frequencies between 20 K hz and 100 K hz where it decreases to +1%, -3.5%. The maximum percent error in ε' is determined from

$$\Delta\varepsilon' = \%\text{ error in } d + \%\text{ error in } C_p + \%\text{ error in } A_s \qquad (3.19)$$

or $\Delta\varepsilon' = \pm\ (10\% + 1\% + 2\%) = \pm\ 13\%$

at 100 hz $\Delta\varepsilon' \simeq \pm\ 15\%$

The thickness and length of one side of the crystal were determined with an uncertainty of $\pm$ 0.01 mm. Hence, the percent error for the thickness is

$$\Delta d \simeq \pm\ 10\%$$

where the average thickness of a crystal is 0.1 mm. The percent error for the area is

$$\Delta A \simeq \pm\ 2\%$$

where the average area of a crystal is 1 mm. The error $\Delta\varepsilon''$ in ε'' for ClAp is given by

$$\Delta\varepsilon'' = \Delta\varepsilon' + \Delta \tan \delta$$

Because corrections were made for the residual loss tangent error inherent in the bridge as outlined in this chapter, section 7 and appendix B, section 3, the accuracy of tan δ was always maintained within $\pm$ 0.001 $\pm$ 5%. This was determined by standard capacitors having known loss tangent values. Tan δ never fell below 0.01 for ClAp (E''_c) and (FClAp) (E''_c) specimen so that the uncertainty in tan δ for these specimens (the most important data are derived from these samples) is $\pm$ 10% $\pm$ 5% or a total of $\pm$ 15%. Thus, the maximum percent error in ε'' for frequencies $\leq$ 100 KHz was always less than

$$\Delta\varepsilon''_{max} < \pm (15\% + 15\%) = \pm 30\% \quad .$$

R. F. Bridge Accuracy

The accuracy specifications for the r. f. bridge are given below. The uncertainty in resistance is equal to

$$\Delta R = \pm (2\% + 1\Omega + 0.008\ Rf)$$

where f is the frequency in megahertz and R is the resistance. The last term is important only at 10 MHz. R at that frequency was found to be always less than 320Ω. Therefore, the resistance error is generally less than

$$\Delta R \leq \pm (2\% + 2.56\Omega)$$

$$\Delta R \leq \pm 3\%$$

since 2.56 is roughly 1% of 320 . The uncertainty in the reactance is given

$$(\Delta X) = \pm (1\% + 0.0024\ f^2\ (1 + \frac{R}{1{,}000})\% \pm \frac{10^{-4}x}{f}\ \Omega + 0.1\Omega)$$

where X is the measured reactance. At very low frequencies (~ 100 KHz) only the 1/f term is important. The reactance was generally less than 250Ω at 100 KHz. Thus

$$\Delta X \leq \pm (1\% \pm 10^{-3}\ (250) + 0.1\Omega)$$

or

$$\Delta X \leq \pm 1\%$$

The last two terms amount to about 0.1% and, therefore, have been neglected. The f^2 term is important only at high frequencies. Thus, at 10 MHz the reactance error is

$$(\Delta X) \leq \pm (1\% + 0.0024\ f^2\ (1 + \frac{R}{1{,}000})\% + 0.1\Omega)$$

When the previous value of 320Ω is substituted for R, the error becomes

$$\Delta X \leq \pm (1\% + 0.32\%) \simeq \pm 1.3\%$$

Because $\tan \delta = \frac{X}{R}$, the percent error is given by

$$\Delta \tan \delta \leq \pm (1\% + 1.3\%) \leq \pm 2.3\%$$

The change in capacitance due to a small change in tan δ and X is obtained from the total differential of equation 3.14. The percent error in C_p is

$$\Delta C_p = \left(\frac{\Delta X}{X}\right) 100 + \left[\frac{2 \tan \delta}{1 + \tan^2 \delta}\right] (\Delta \tan \delta) \ (100)$$

Where $\left(\frac{\Delta X}{X}\right) 100$ is the percent error in the reactance and $\left(\frac{\Delta \tan \delta}{\tan \delta}\right) 100$ the percent error in tan δ. The factor $\frac{2 \tan^2 \delta}{1 + \tan^2 \delta}$ is always less than 2 for any value of tan δ.

Therefore,

$$\Delta C_p \leq \pm (1.3\% + 4.6\%) \simeq 6\%$$

The percent error in ε' is given by

$$\Delta \varepsilon' = \Delta d + \Delta C_p + \Delta A$$

$$\Delta \varepsilon' = \pm (10\% + 6\% + 2\%) = \pm 18\%$$

The percent error in d and A were determined previously. Finally, the possible error in ε'' is given by

$$\Delta \varepsilon'' = \Delta \varepsilon' + \Delta \tan \delta$$

$$\Delta \varepsilon'' = \pm (18\% + 2.3\%) = 20.3\%$$

Significance of Scatter in Dielectric Constant in Chlorapatite

When repreducibility or certain trends of plotted data are examined the absolute accuracy, at times, becomes much less important than the precision. It could be argued that the variation in the complex dielectric constant among the four ClAp samples ($E_{\perp c}$) would provide a measure of precision for ε' and ε''. This is not the case, however, since ε^* ($\varepsilon^* = \varepsilon' - i\varepsilon''$) at low frequencies depends on the orientation of large dipole moments, the number of which, in turn, depend on the number of defects (Cl vacancies) within the dielectric (to be discussed in Chapter IV). The number of vacancies vary from specimen to specimen, so that differences in ε^* (which were observed experimentally) are expected. Clearly, data of this type do not represent precision. However, the reproducibility of temperature dependent data for each ClAp specimen, as in figure 18, does yield a precision for capacitance of $\pm$ 100 pf and for tan δ of $\pm$ 0.01. An estimated accuracy of ε' due to the change in the number of defects can be obtained from figure 28 in Chapter IV which yields $\pm$ 17% at 1,000 Hz. This must be added to a value of $\pm$ 15% (derived previously) to give a total accuracy of approximately $\pm$ 32% for ε' parallel to the c axis.

X-Ray Data

A detailed discussion on the limiting factors of precision and accuracy in measuring single crystal Bragg intensities is given in Chapter III of the Ph.D. thesis by Mackie[47].

CHAPTER IV

EXPERIMENTAL RESULTS AND THE VACANCY MODEL

Introduction

This chapter is devoted to the development of a vacancy model consistent with the crystal structural details which is capable of explaining the experimental results for the dielectric properties of ClAp and (F,Cl)Ap. The model itself has been subdivided into two broad categories, the Cl shift and vacancy migration. The basic building blocks of the applicable dielectric theory, upon which a coherent theoretical approach to the dielectric behavior of ClAp rests, are set forth in Appendix A.

The Chlorine Shift

The Shift Model

Table 2 summarizes the experimental facts discussed so far. The conclusion to be drawn from this information is that each type of data, x-ray and dielectric, seems to point to a different model. To resolve the apparent inconsistencies, it must be remembered that the x-ray diffraction measurements made probe the average properties of the crystal whereas dielectric measurements often depend on the behavior of isolated defects in the structure. Therefore, the first step toward the development of a dielectric model requires that the structural defects in ClAp be taken into consideration. Furthermore, one requires that the model's predicted behavior be consistent, both

Table 2. X-Ray and Dielectric Results that at First Appeared to be Inconsistent

X-Ray Experiments	Results	Dielectric Experiments	Results
Structure Refinement of ClAp	Antiferroelectric but not ferroelectric behavior possible for ClAp with E field parallel to $\underline{c}$	Dynamic dependence of $\bar{D}$ field on applied $\bar{E}$ field ($\bar{E} \parallel \underline{c}$)	Hysteresis Loop shows ClAp may be ferroelectric ($\bar{E} \parallel c$) but not antiferroelectric
Dependence of intensities of $hk_{odd}\ell$ ($\ell \neq 0$) reflections for ClAp on applied $\bar{E}$ field parallel to $\underline{c}$ axis	No change in intensities observed hence no change to a polar space group as needed for ferroelectric character	Dynamic dependence of $\bar{D}$ field on applied $\bar{E}$ field ($\bar{E} \parallel c$)	Possible ferroelectric character requires removal of glide plane which changes the space group and requires $hk_{odd}\ell$ ($\ell \neq 0$) intensities to be zero
Temperature dependence of intensities of $hk_{odd}\ell$ ($\ell \neq 0$) reflections for ClAp	Rapid approach to near zero intensities at ~ 200°C suggests partial or pseudo phase transition which, in turn, leads to expectation of dielectric anomaly in $\varepsilon''_{\underline{c}}$ at ~ 200°C	Temperature dependence of ε''_c	No anomaly observed near 200°C

quantitatively and qualitatively, with dielectric and x-ray diffraction data. A least squares structure refinement carried out by Mackie al.[27] on a synthetic ClAp crystal confirmed that about 5% of the total stoichiometric amount of Cl was missing. In fact they showed that these vacancies apparently contributed strongly to the easy shifting of Cl ions. Prener[41] also indicated that flux-grown ClAp crystals have a tendency to be Ca and Cl deficient through loss of $CaCl_2$. Similar defects (vacancies) were found in other crystals and were used to explain the high dielectric constants associated with these materials. For example, Tse[14] measured dielectric constants of the order of 10^4 in FAp at about 1 KHz and temperatures greater than 500°C. He associated the large values with F vacancies migrating along the c axis. In a second example, the dielectric constant of HF contaminated ice was found to vary greatly with impurity concentration[59]. Values as high as 10^4 were obtained at 1 Hz and a temperature of -10°C for nearly pure ice crystals (with HF substituted in the range of 10^{-7}M). Since each HF molecule replaces one molecule of H_2O, the number of H vacancies depends directly on the HF concentration. The large dielectric constant was explained on the basis of H vacancy migration or proton transfer.

Could a similar mechanism be responsible for the dielectric properties of ClAp? The answer to this question requires a detailed study of the structural features of this material, expecially the Cl environment. These ions are arranged in columns along the c axis and, thus, Cl jumps or vacancy migration would most likely occur

along these columns.

A view of the Cl environment in ClAp prepared by Mackie et al.[27] is reproduced in Figure 21 (the ellipsoids represent r.m.s. thermal vibrational amplitudes, not ion sizes). The Cl ions are nearly coplanar with and located at the center of an oxygen triangle. For example, Cl(a) is associated with the O(a) triangle. This position does establish a normal Ca-Cl distance with the Ca(b) triangle. But the symmetry of the rest of the structure about the z = 0 and 1/2 planes also permits an alternate site for Cl(a) at the center of the O'(a) triangle which would establish a normal Ca-Cl bond length with the Ca(a) triangle. For a stoichiometric crystal, however, once the Cl(a) position is fixed (for example, in the lower O(a) triangle as in Figure 21) all other Cl ions within this column (for a stoichiometric crystal) on either side of Cl(a) must also occupy their respective lower oxygen triangles (i.e., Cl(b) must also be at the center of the O(b) triangle, etc.). This is the case because the Cl ions are tightly packed within the linear Cl chains such that the Cl-Cl distance along the columns (3.38 Å) is less than the sum of the ionic radii (3.62 Å). No translational movement (except thermal vibrations) is expected along the c direction within columns unless a vacancy exists. A possible plot of the potential energy for a Cl ion along a column of Cl ions near a vacancy is shown in Figure 22.

There are certain processes within the Cl column which would be expected if Cl(a) were suddenly removed. For example, Cl(b) would probably jump to its crystallographically equivalent (in the

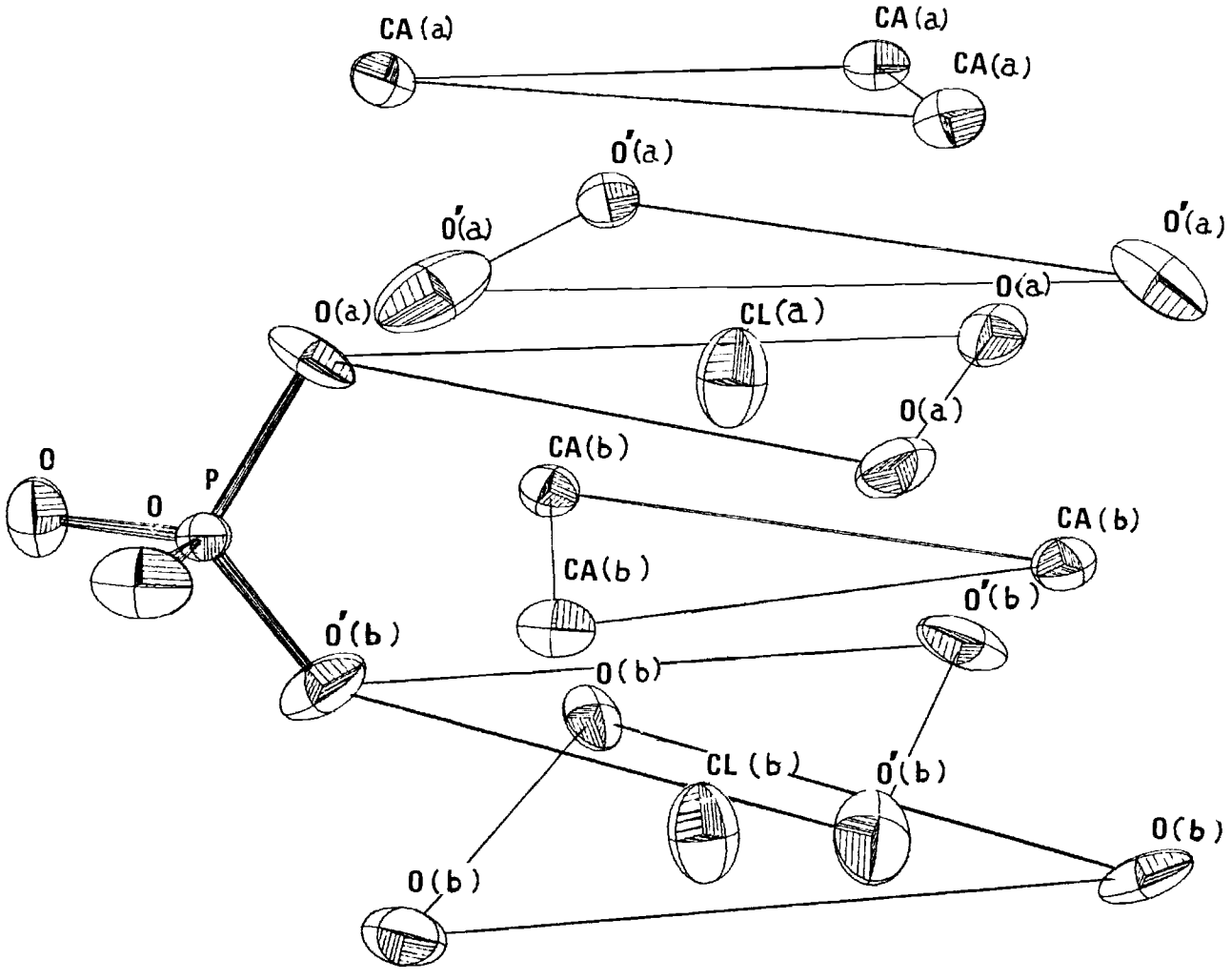

Figure 21. Chlorine Environment in ClAp. The ellipsoids represent r.m.s. thermal vibrational amplitudes, not ion sizes. Adapted from Mackie et al.[27]

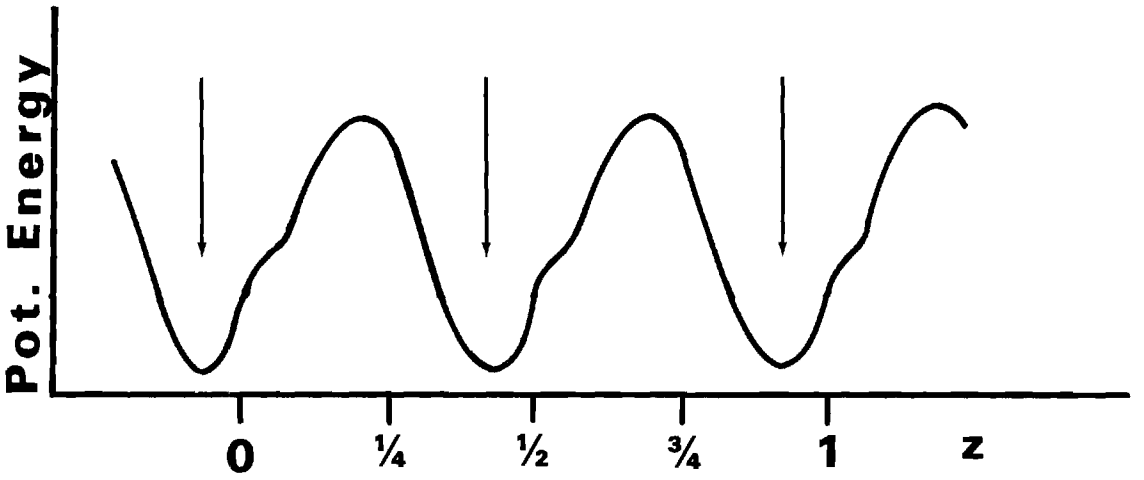

a) Without vacancy

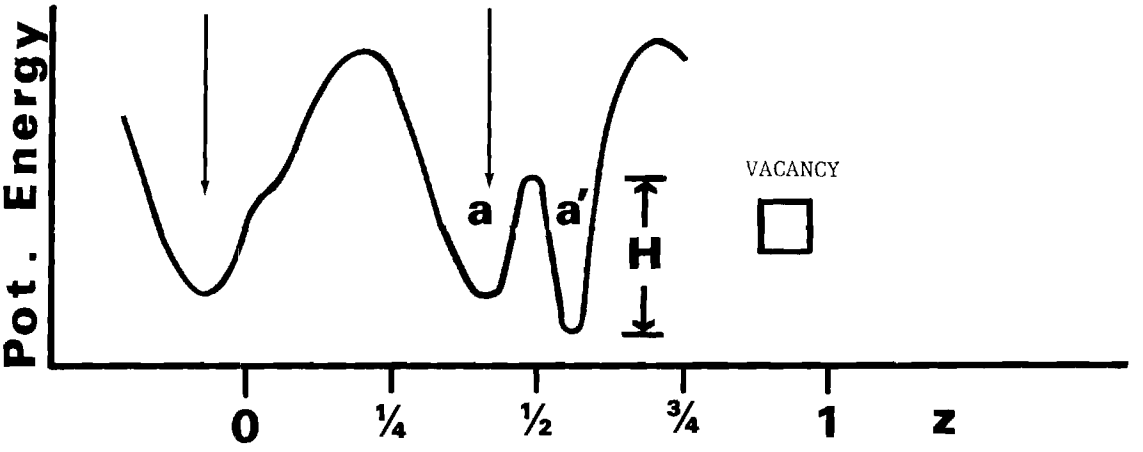

b) With vacancy

Figure 22. Possible Potential Energy Distribution Along a Cl Chain. The arrows represent the positions of the Cl ions. z is the positional parameter along the c axis within a unit cell. H represents the energy barrier for the double well.

hexagonal form) site at the O'(b) triangle, a distance of 0.8 Å away. In fact the tight packing within the column would promote such displacements. The next ion Cl(c) immediately below Cl(b) (refer to Figure 23) would relax, but not quite so far, to establish a more normal Cl-Cl distance; a similar thing would occur with Cl(d) and so on. While Cl(b) is expected to remain bound to the positive vacancy, under the action of an applied field Cl(c) would be able to move between Cl(b) and Cl(d) etc. However, Cl(d) can not move unless Cl(c) has shifted previously and thus made room for Cl(d). After Cl(c) has shifted Cl(d) would be located in a double potential well (as in Figure 22) and ready to jump from well a to a'. The whole process would resemble the "domino effect," where a tilt or displacement of the first initiates a similar action in all succeeding blocks. This process would occur at low frequencies of the applied field where sufficient time might be available for short segments within the columns to shift back and forth. However, our model assumes no interaction between Cl ions. As a result it is only applicable at high frequencies where the shift is confined to only one Cl ion, probably the one (perhaps Cl(c)) which relaxed near to (not at) the z = 1/2 position upon removal of Cl(a). For this ion it would be particularly easy to shift from well a to a'. Mathematical treatment of the high frequency case given in Appendix A, section 5, adequately accounts for the behavior of the real and imaginary dielectric constant and the activation energy of the shift process in that frequency region.

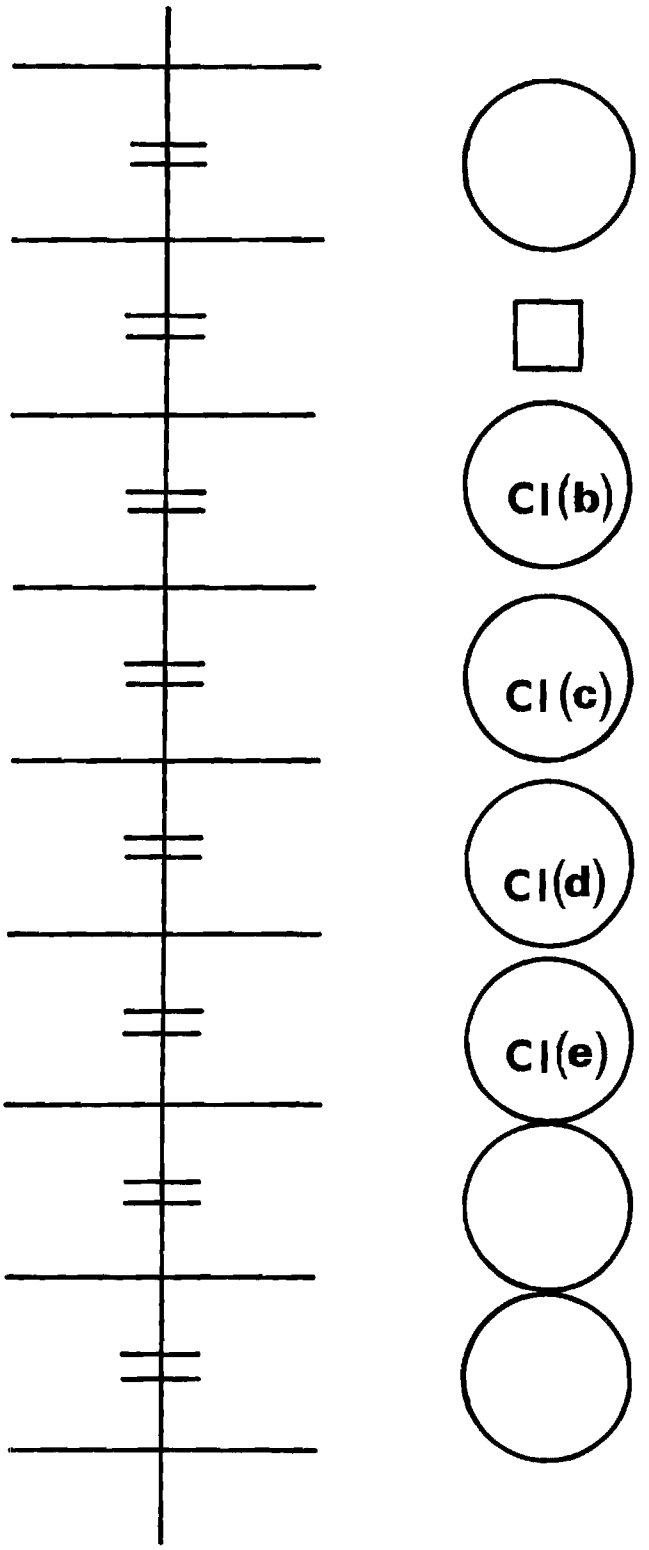

Figure 23. Schematic Diagram of Probable Relaxation Process within a Cl Column Near a Vacancy. The long and short horizontal bars represent Ca and O triangles, respectively.

In order to simplify the model two assumptions were made: i) the density of the shifting particles must be sufficiently dilute so that interaction terms can be neglected, and ii) the energy barrier of the double well must be greater than the thermal energy, kT, of the particle. The experimental data will show that both assumptions are justified.

Dielectric Dispersion

Due to slight differences in the local environment (i.e., the position of the nearest Cl neighbor) within the structure, the barrier H is probably not the same for each particle; rather, a distribution of the heights of the energy barriers about a mean value is expected. It was found that the data for ε' and ε'' at frequencies greater than 10^5 hz can be well fit by a Cole-Cole plot (due to K. S. Cole and R. H. Cole[60], see Appendix A, section 4), the physical model for which is a superposition of Debye oscillators each having its own characteristic relaxation time τ_n. The distribution of τ_n about a mean τ_m is given by the function F(s) below. ε' and ε'' are given by

$$\frac{\varepsilon' - \varepsilon_\infty}{\varepsilon_s - \varepsilon_\infty} = \frac{1 + (\omega\tau_m)^{1-\alpha} \sin(\pi\alpha/2)}{1 + (\omega\tau_m)^{2(1-\alpha)} + 2(\omega\tau_m)^{1-\alpha} \sin(\pi\alpha/2)} \tag{4.3}$$

$$\frac{\varepsilon''}{\varepsilon_s - \varepsilon_\infty} = \frac{(\omega\tau_m)^{1-\alpha} \cos(\pi\alpha/2)}{1 + (\omega\tau_m)^{2(1-\alpha)} + 2(\omega\tau_m)^{1-\alpha} \sin(\pi\alpha/2)} \tag{4.4}$$

where ε_∞ is the dielectric constant at $\omega = \infty$

ε_s is the dielectric constant at $\omega = 0$,

τ_m is the relaxation time of the macroscopic polarization,

and α is the spread parameter ($0 \leq \alpha \leq 1$). α is related to the spread in relaxation times[60] according to

$$F(s) = \frac{\sin \alpha\pi}{2\pi\{\cos h[(1 - \alpha)s] - \cos \alpha\pi}$$

where s is defined by

$$s = \ln \frac{\tau}{\tau_m}$$

and ω is the angular frequency. At 27°C the FWHM of F(s) extends from $\tau = 3.49 \times 10^{-6}$ sec to $\tau = 2.32 \times 10^{-5}$ sec. The values of α ($\alpha = 0.24$) and τ_m($\tau_m = 9 \times 10^{-6}$ sec) at 27°C, which were used in this calculation, were derived from the experimental data of the same sample that is associated with Figures 24, 25, and 26. The frequency dependence of ε'_c and ε''_c is shown in Figure 24. It must be emphasized that equations 4.3 and 4.4 are valid for ε'_c and ε''_c only at frequencies > 10^5 Hz. By eliminating $\omega\tau$ from equations 4.3 and 4.4, ε' can be related to ε'' by

$$\{1/2(\varepsilon_s + \varepsilon_\infty) - \varepsilon'\}^2 + \{\varepsilon'' + 1/2(\varepsilon_s - \varepsilon_\infty) \tan (\pi\alpha/2)\}^2 \qquad (4.5)$$

$$= 1/4(\varepsilon_s - \varepsilon_\infty)^2 \sec^2 (\pi\alpha/2)$$

The resulting (Cole-Cole plot (ε' vs. ε'') is a semicircle with its center depressed below the $\varepsilon'' = 0$ axis (Figure 25). The Cole-Cole plot was primarily used to extract the spread parameter, α, (α = 2 (measured angle in Figure 25) / π) which in turn was needed to obtain τ_m. The

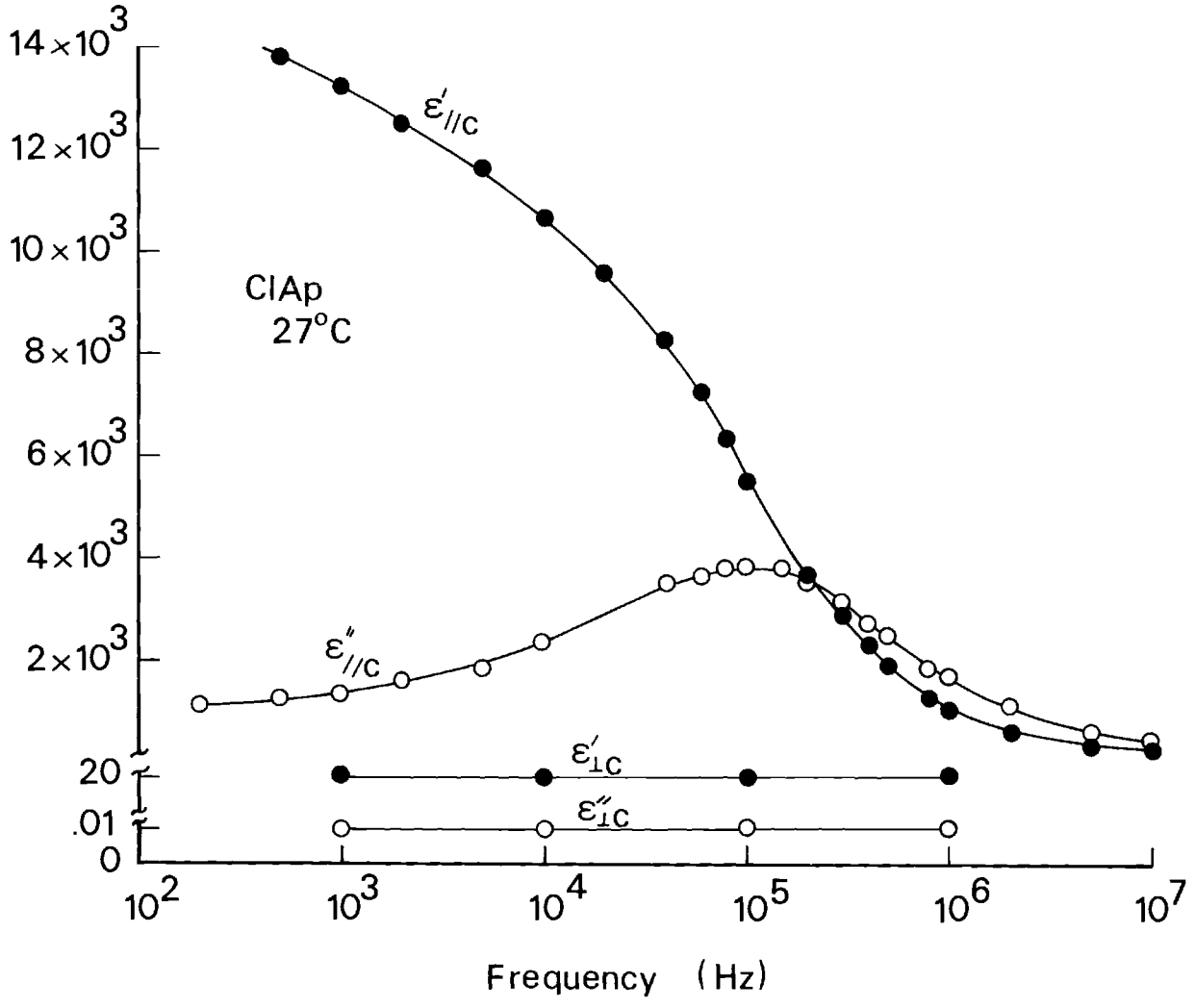

Figure 24. Frequency Dependence of the Real and Imaginary Dielectric Constant with the Electric Field Both Parallel and Perpendicular to the c Axis.

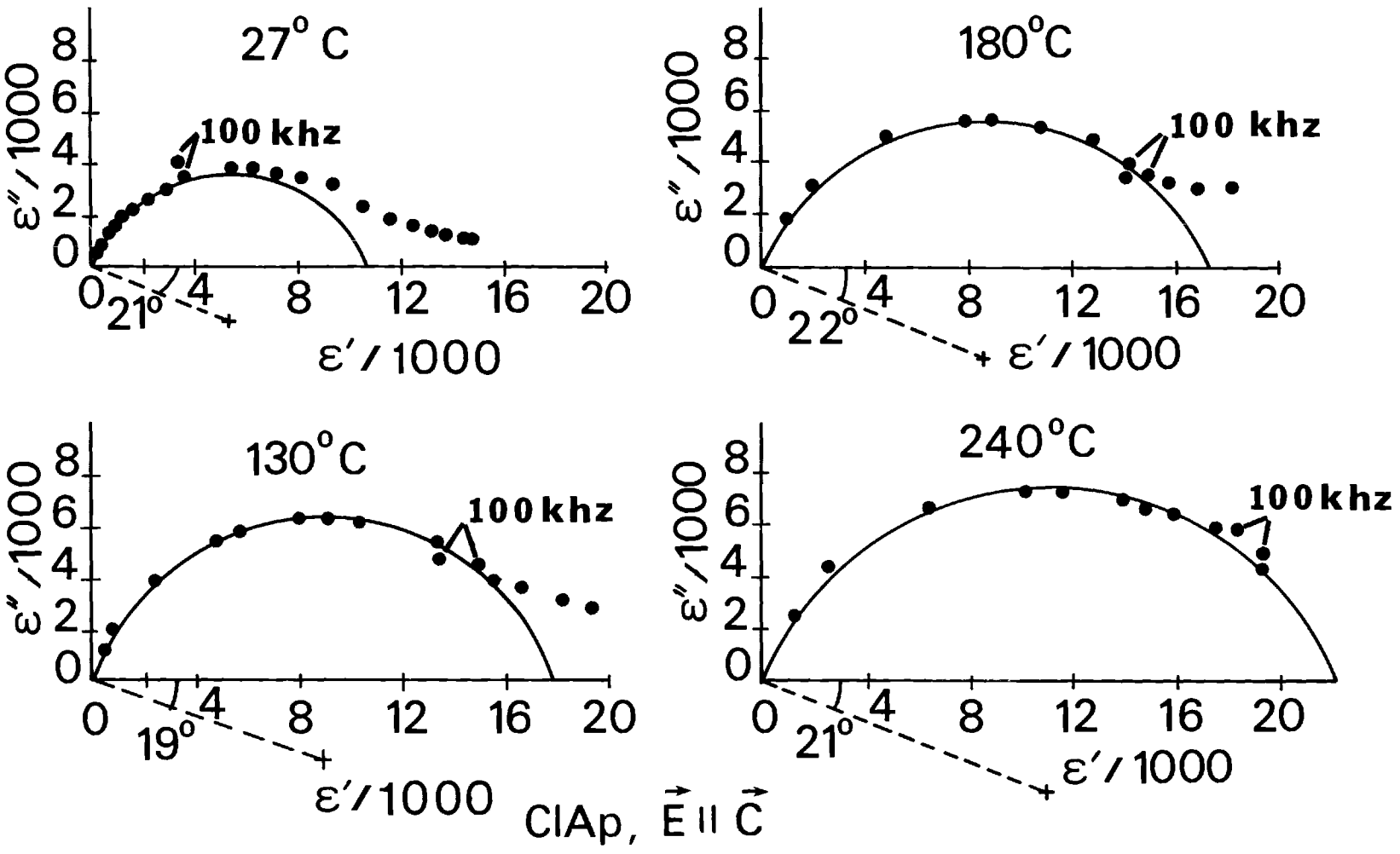

Figure 25. Dielectric Constants of ClAp at Four Temperatures Plotted in the Complex Plane (Cole-Cole Plot) (Sample C2PE, E parallel to c). The cross marks the center of the Cole-Cole circle, the spread parameter α is the depression of the center expressed as $\frac{2}{\pi}$ times the angle shown.

mean relaxation time at a particular temperature was obtained from a plot of equation 4.6, which is the result of substituting equation 4.3 into 4.4.

$$\frac{\varepsilon'}{\varepsilon''} - \frac{\varepsilon_\infty}{\varepsilon''} = \frac{1}{\omega^{(1-\alpha)}\,\tau^{(1-\alpha)}\cos(\pi\alpha/2) + \tan\frac{\pi\alpha}{2}} \qquad (4.6)$$

A plot of $\frac{\varepsilon' - \varepsilon_\infty}{\varepsilon''}$ versus $\frac{1}{\omega^{(1-\alpha)}}$ (Figure 26) gives a straight line with the slope given by

$$a = \frac{1}{\tau_m^{(1-\alpha)}\cos(\pi\alpha/2)} \qquad (4.7)$$

To obtain the activation energy the required parameter, τ_m, was extracted from equation 4.7, the α value having been first obtained from the Cole-Cole plot shown in Figure 25. A plot of log τ_m versus 1/T (Figure 27) shows that the temperature dependence of experimental values of τ_m can be described by an exponential law given by

$$\tau_m = \tau_o\, e^{H/kT} \qquad (4.8)$$

in accordance with the equation derived from the double well model in Appendix A, Section 5. Here τ_o is the mean period of vibration of the Cl ion in either well. Its value obtained by extrapolation to $\tau = \infty$ in Figure 27 is 6.0×10^{-8} sec. The slope yields an activation energy of 0.125 eV. The 0.120 eV, 0.117 eV and 0.170 eV were derived values from three other samples. The data can be found in Appendix G. These

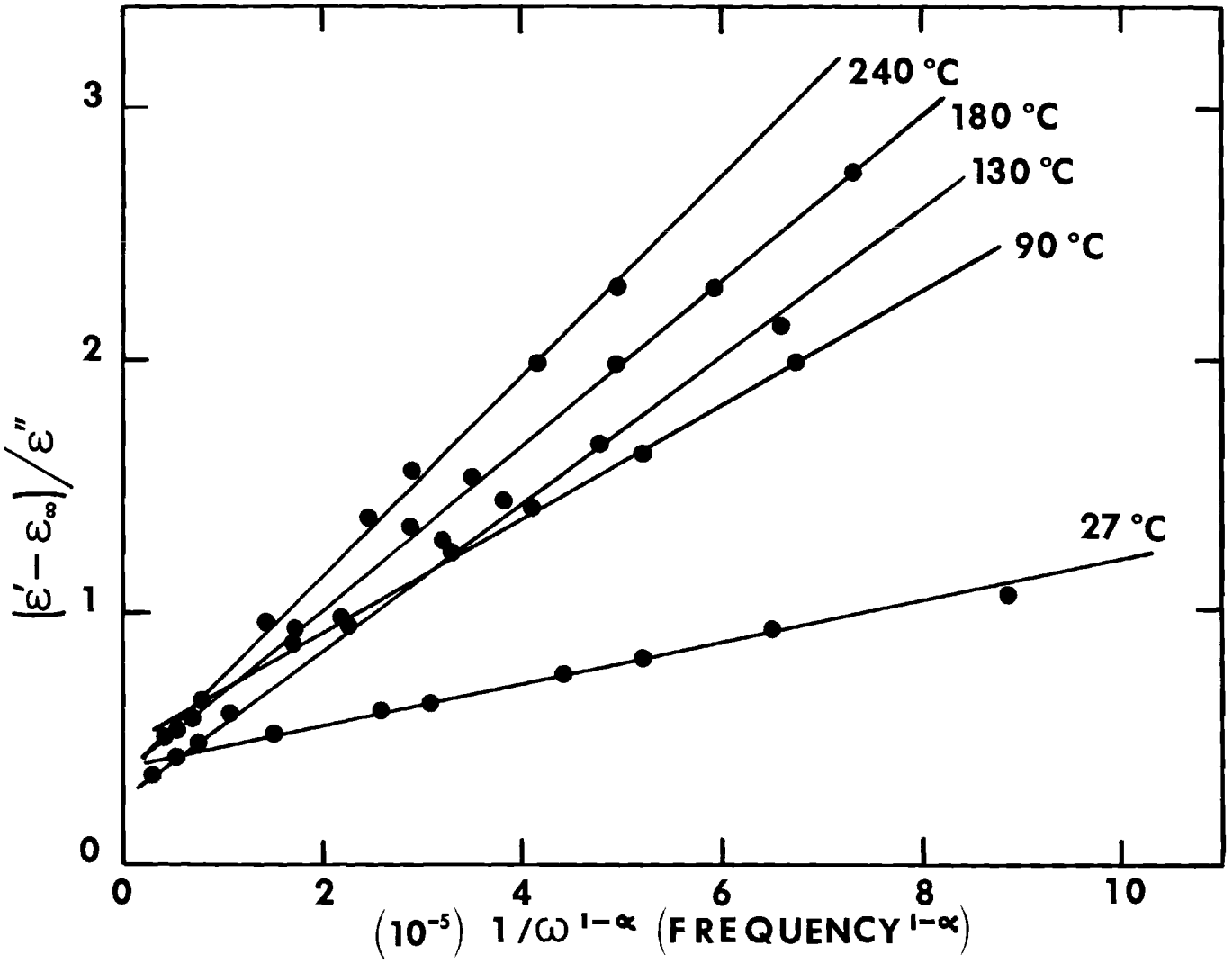

Figure 26. Plots for Determining Relaxation Times in ClAp at Various Temperatures.

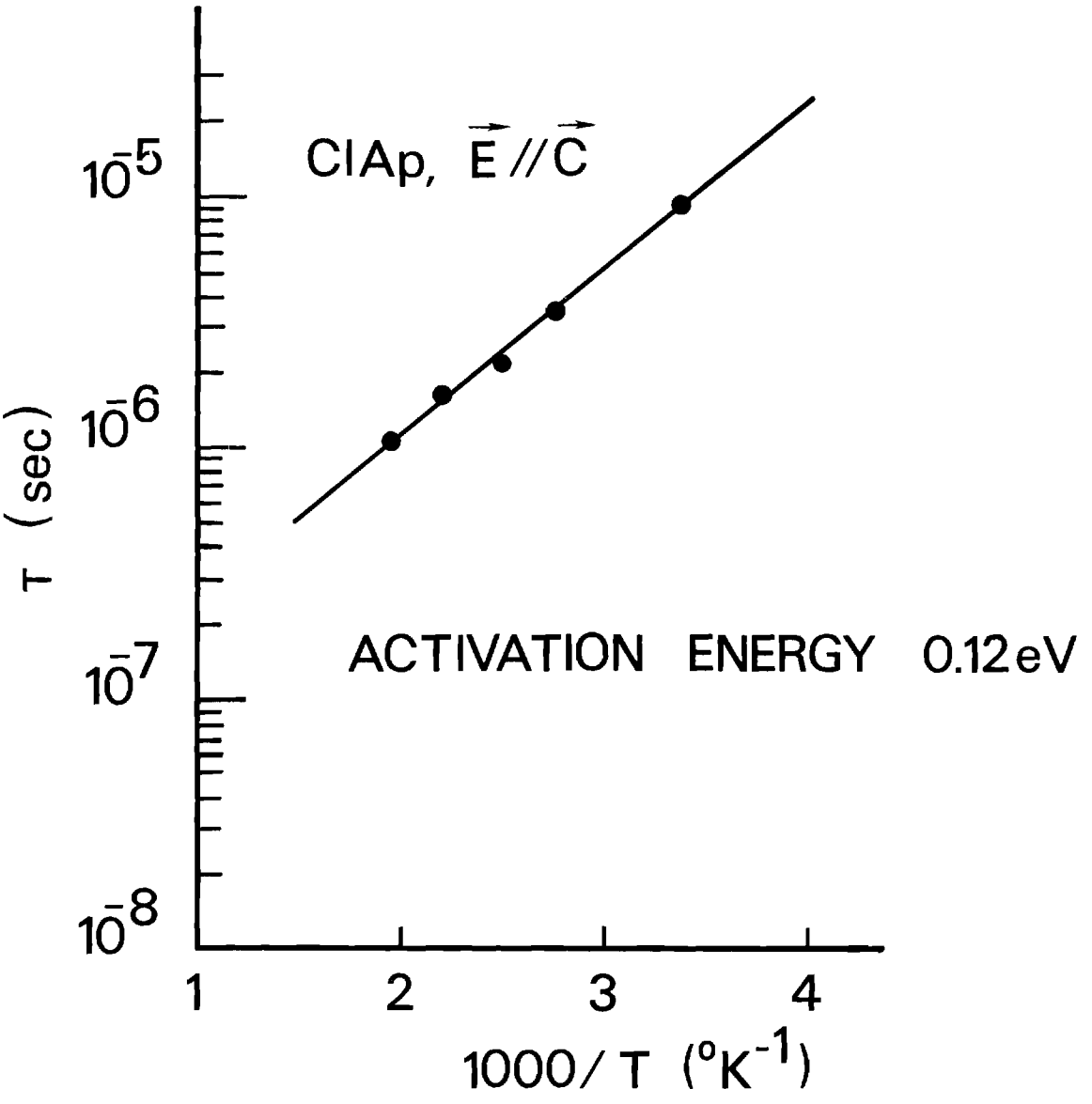

Figure 27. Relaxation Times of ClAp (Sample C2PE) as a Function of Reciprocal of Absolute Temperature.

together give an average of 0.14 $\pm$ 0.03 eV. A comparison of H with the approximate thermal energy of Cl ions at 23°C (kT ~ 0.025 eV) confirms (i) the previous assumption H > kT where k is the Boltzmann constant and T ~ 300°k and (ii) the easy shifting ($e^{-H/kT} \approx 0.4\%$) of Cl ions from well a to a' or vice versa.

So far only the shift in the high frequency region ($10^5 < f < 10^7$ hz) has been discussed. At low frequencies ($< 10^5$ hz), on the other hand, the shift of entire segments of Cl ions, not just one, might occur. However, to account for the frequency dependence of ε'_c and ε''_c over the full range of frequencies would require a much more sophisticated mathematical treatment which would take into consideration the effect of the nearest neighbors, primarily, the change in the potential well of one Cl where an adjacent Cl undergoes a shift.

Dipole Density

High dielectric constants greater than 100 are not ordinarily found in nature. Some ferroelectric materials, for example $BaTiO_3$, do exhibit values in the 10^4 range, but only near their phase transition temperatures. Most dielectrics have dielectric constants between 1 and 10 (see Appendix A, section 3). The fact that the dielectric constant of ClAp can be as high as 10^4 is, therefore, an unusual property of this material. However, it can be explained in terms of the vacancy model.

We proceed now, first to estimate the dipole density required to account for the observed dielectric constant and, second, to compare

this density with the expected density of defects (Cl vacancies). In a symmetric double well even though kT < H (but not << H), a number of particles N_1 will jump from well A to B (see Appendix A, section 5) as a result of fluctuations in their thermal energy and a number N_2 will jump from B to A such that at any instant of time the population in either well must be identical. Therefore, the macroscopic polarization is equal to zero. But the application of an external electric field causes a population difference given approximately by (see Appendix C)

$$N_1 - N_2 = n \simeq \frac{\varepsilon_o E \varepsilon''_c}{p} \tag{4.9}$$

where ε_o is the permittivity of free space, E is the applied electric field ($\sim 10^3$ V/m), p is the dipole moment and ε''_c is the dielectric constant in the c direction. Of course, equation 4.9 gives only an order of magnitude estimate of the dipole density since the dipole moment is not known precisely. However, the significance is that the dipole density need be only of the same order of magnitude as, or less than, the number of vacancies in order to account for the dielectric constant at high frequencies ($\sim 10^5$ Hz) where only one Cl ion per vacancy is expected to shift. For this estimate, take ε''_c to be $\sim$ 4,000 (Figure 24). The shift distance is of the order of 0.8 Å, which is the difference between the Cl equilibrium position above and below the glide plane at Z = 1/2. The charge on the Cl ion is equal to that of an electron. Thus, the dipole moment is equal to 1.28×10^{-29} coul-m. Substituting these values into equation 4.9 yields

$$n \simeq \frac{(8.85 \times 10^{-12} \text{ fd/m})\ (4{,}000)\ (10^{3} \text{ V/m})}{(1.6 \times 10^{-19} \text{ coul})\ (0.8 \times 10^{-10} \text{ m})}$$

$$\simeq 2.8 \times 10^{24} \text{ dipoles/m}^3$$

The volume of a hexagonal ClAp cell is approximately 545 Å so the number of cells per cubic meter is 1.84×10^{27}. There are 2 Cl ions per cell, so that the total number of Cl ions per m^3 is 3.67×10^{27}. Thus, the number of dipoles which must reorient to yield a dielectric constant of 4,000 is 0.08%. This appears to be a reasonable number considering that there are about 5% vacancies available. Thus, the second assumption of the model which considers the sample as a solution of isolated dipole moments has now been shown to be justified since roughly only 1 out of every 1250 Cl ions (0.08%) need be an active dipole.

However, it is not known how small fields (~ 1000 V/m) could cause a sufficiently large number of Cl shifts to account for the large dielectric constant ε'_{c} in ClAp. Of importance here is the ratio of the potential energy edE (the increase in potential energy of a Cl ion in an electric field E) to the thermal energy kT of the Cl ion at room temperature (see Appendix A, section 5). For electric fields ~1000 V/m that ratio is approximately

$$\frac{edE}{kT} = \frac{(1.6 \times 10^{-19} \text{ coul})\ (0.8 \times 10^{-10} \text{m})\ (1000 \text{ V/m})}{0.025 \text{ eV } (1.6 \times 10^{-19} \text{ joules/eV})} \simeq 3 \times 10^{-6}$$

which appears to be too small to provide the required polarization.

Although there appears to be no interaction between shifting dipoles at frequencies > 10^5 hz, the fact that τ_o is equal to 6.0 x 10^{-8} sec instead of the usual value of ~ 10^{-12} sec or less (for lattice vibrations) suggests that the vibrational frequencies of the Cl's are severely perturbed by adjacent Cl ions. Because the perturbation is probably not the same for each Cl ion at any instant in time, one would expect a spread in relaxation times .

Anisotropy

In general the ionic conductivity with E $\perp$ c is 4 orders of magnitude lower than the corresponding conductivity with E || c. Tse[14] found an analogous 2 to 4 orders of magnitude difference in FAp, but only at high temperatures (~ 1000°C) where F vacancy migration is dominant (at room temperature FAp with E || c, FAp with E $\perp$ c and ClAp with E $\perp$ c have approximately the same value of ionic conductivity).

In constrast to the high $\varepsilon'_{\parallel c}$ and $\varepsilon''_{\parallel c}$ values, the dielectric constant and loss perpendicular to the c axis is orders of magnitude lower ($\varepsilon'_{\perp c}$ ~ 20, $\varepsilon''_{\perp c}$ ~ 0) and effectively constant for frequencies between 10^2 and 10^7 hz and at temperatures up to 300°C (Figure 24). Unfortunately, no data on the potential energy distribution and activation energy of the Cl ions perpendicular to the c axis is available. Therefore, an explanation of the existing anisotropy in ClAp can only be based on available structural data[27]. The significant features of the structure perpendicular to the c axis are i) the

large intercolumnar Cl-Cl distance (9.6 Å) and ii) the many intervening atoms (such as the phosphate groups) between the Cl columns. A Cl shift analogous to the double well model is, therefore, could not occur perpendicular to the c axis, because this direction is blocked by these intervening atoms.

Fluor-Chlorapatite

A drastic reduction in $\varepsilon'_{\perp c}$ and $\varepsilon''_{\perp c}$ at room temperature occurs when even small amounts of Cl in ClAp are replaced by F (see Figure 28). This evidence clearly indicates that the high $\varepsilon'_{\perp c}$ is directly associated with the Cl ions. Based on the vacancy model, the conclusion is that the number of Cl vacancies diminished by orders of magnitude during the growth process, the vacancies being filled by F ions. In fact, both the atomic multipliers obtained from x-ray least squares structure refinements[61] and chemical analysis[62] revealed an excess of halogen in the (F,Cl)Ap specimens studied by Mackie et al.[61] (F/(F + Cℓ) = 0.15, 0.43). All F ions were found to be centered on the hexad-axis, some located at their normal FAp sites (the center of the Ca triangles at z = 1/4 and 3/4) and others not. No high frequency dispersion, similar to that of ClAp, was observed for any (F,Cl)Ap samples used in this work (Figure 29 shows two (F,Cl)Ap having F/F + Cl ratios of 0.04 and 0.3 respectively). However, at least one sample (FClPE, F/(F + Cl) = 0.04) did exhibit a weak hysteresis loop at 100°C (Figure 31) which indicated that some Cl ions were able to shift in (F,Cl)Ap, but only in those samples which have a low F content.

The $\frac{F}{F+Cl}$ ratios of the samples used in this work were determined

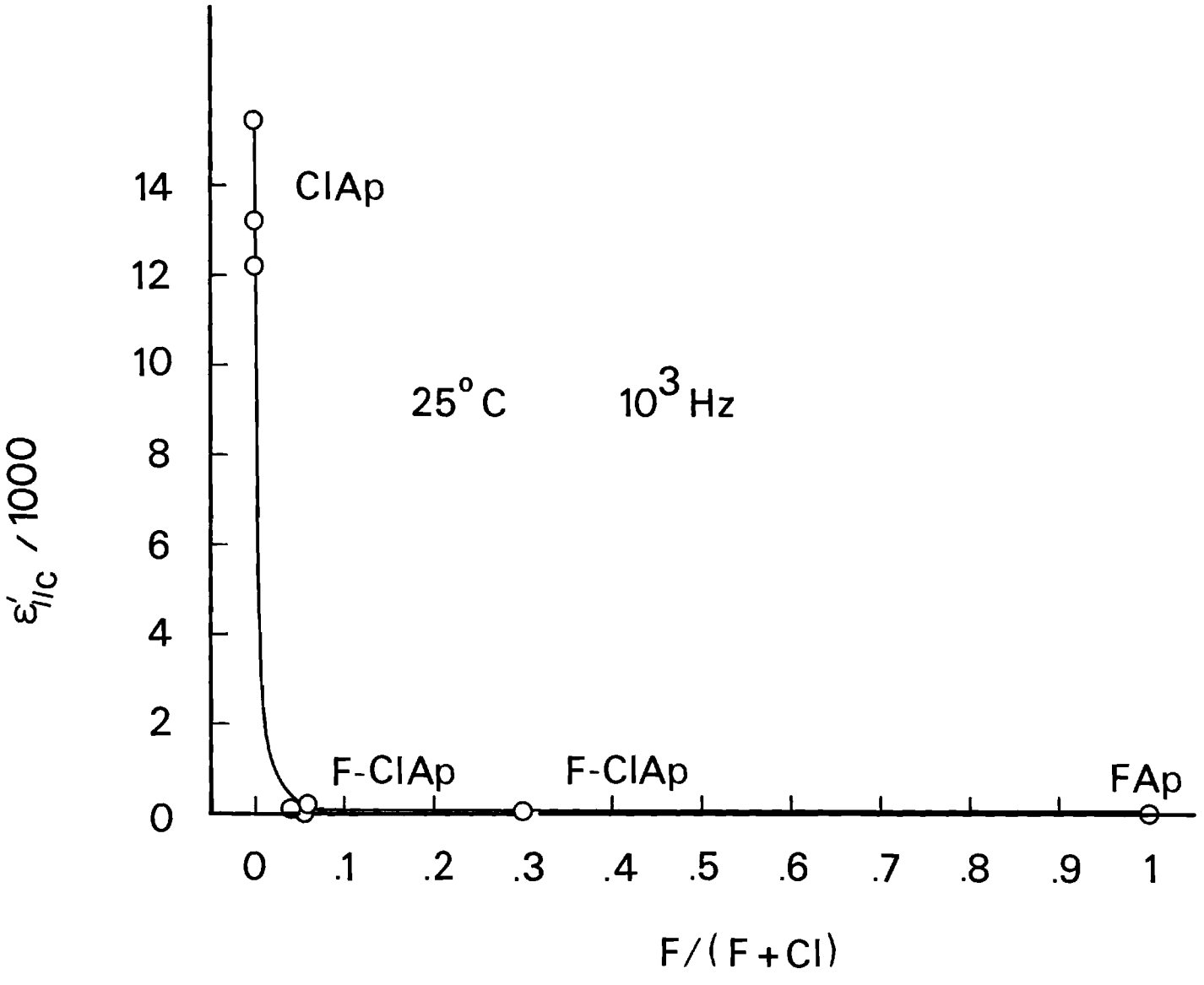

Figure 28. Dependence of Dielectric Constant on F Content in (F,Cl)Ap.

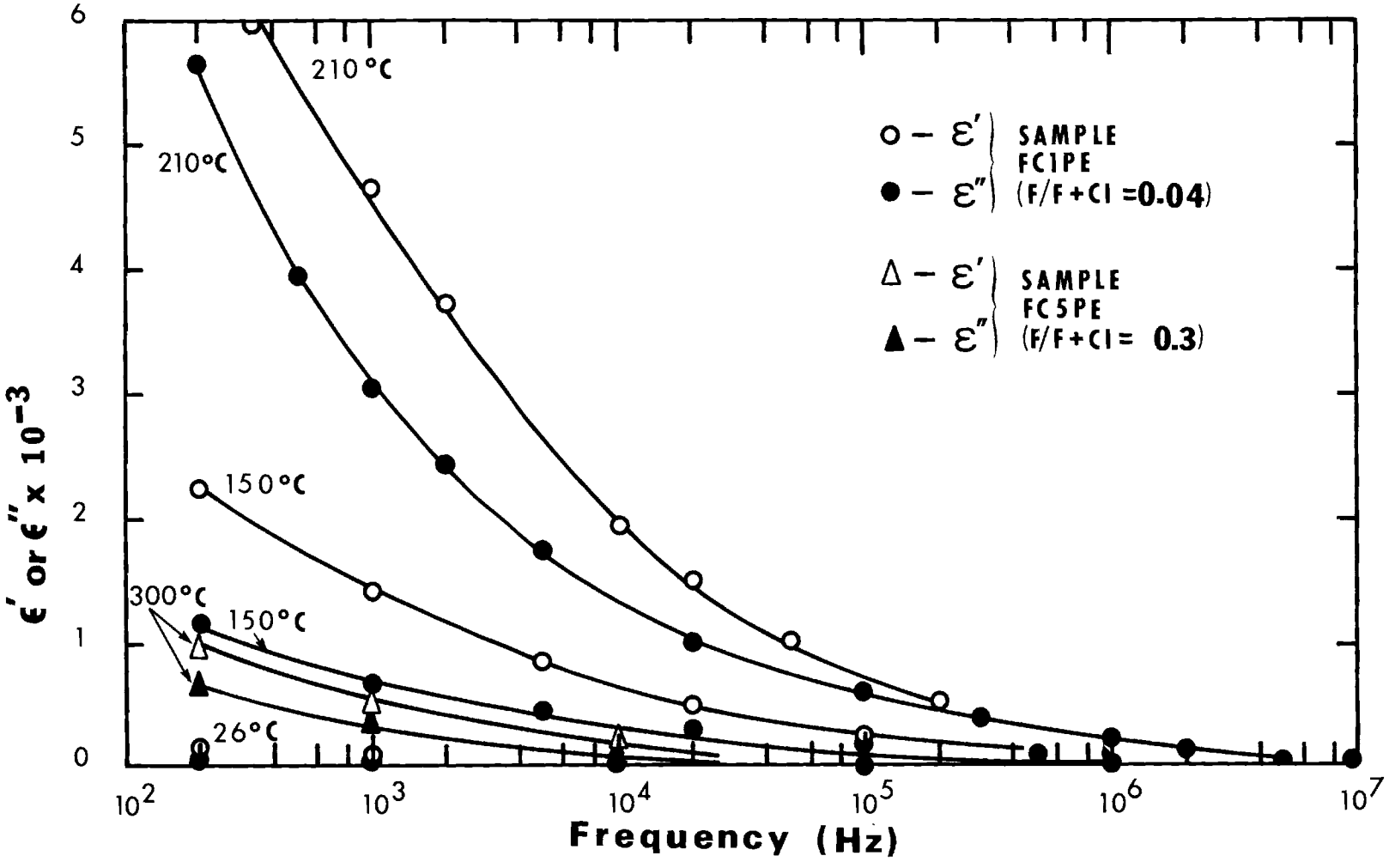

Figure 29. Frequency Dependence of Dielectric Constant and Dielectric Loss for Two (F,Cl)Ap Samples.

by two methods, (1) chemical analysis done in 1970 by N. V. Braun[62] with the Willard-Winter steam distillation method followed by titration with thorium nitrate and (2) lattice parameter measurements made during this work. The a lattice parameter is especially sensitive to changes in chemical composition in the apatites and varies linearly with the $\frac{F}{F+Cl}$ ratio. Figure 30 shows the dependence of $\frac{F}{F+Cl}$ ratios on the a lattice parameters of available samples.

Cl Deficient Chlorapatite and Hydroxyapatite

If the number of Cl vacancies determines to a large extent the value of ε''_c, then an increase in these vacancies should be accompanied by an increase in the dielectric constant. For this reason, an attempt was made to investigate Cl deficient ClAp. Unfortunately, all of the ClAp crystals converted to OHAp and all of those made Cl deficient (by heating in a vacuum) contained cracks both perpendicular and parallel to the c axis. Since dielectric measurements will be affected by the thickness and the complex dielectric constant of the material inside the crack, the cracking perpendicular to c rendered this approach ineffective. Although a detailed calculation of the capacitance of a three-layer dielectric can be carried out (Appendix D and Chapter III), the effective gap thickness can not be determined unless the complex permittivity of the particular apatite, which is itself an objective of the investigation, is already known. Without some measure of the gap (e.g., cracks perpendicular to c) thickness, the dielectric data could not be interpreted with sufficient precision to permit any quantitative

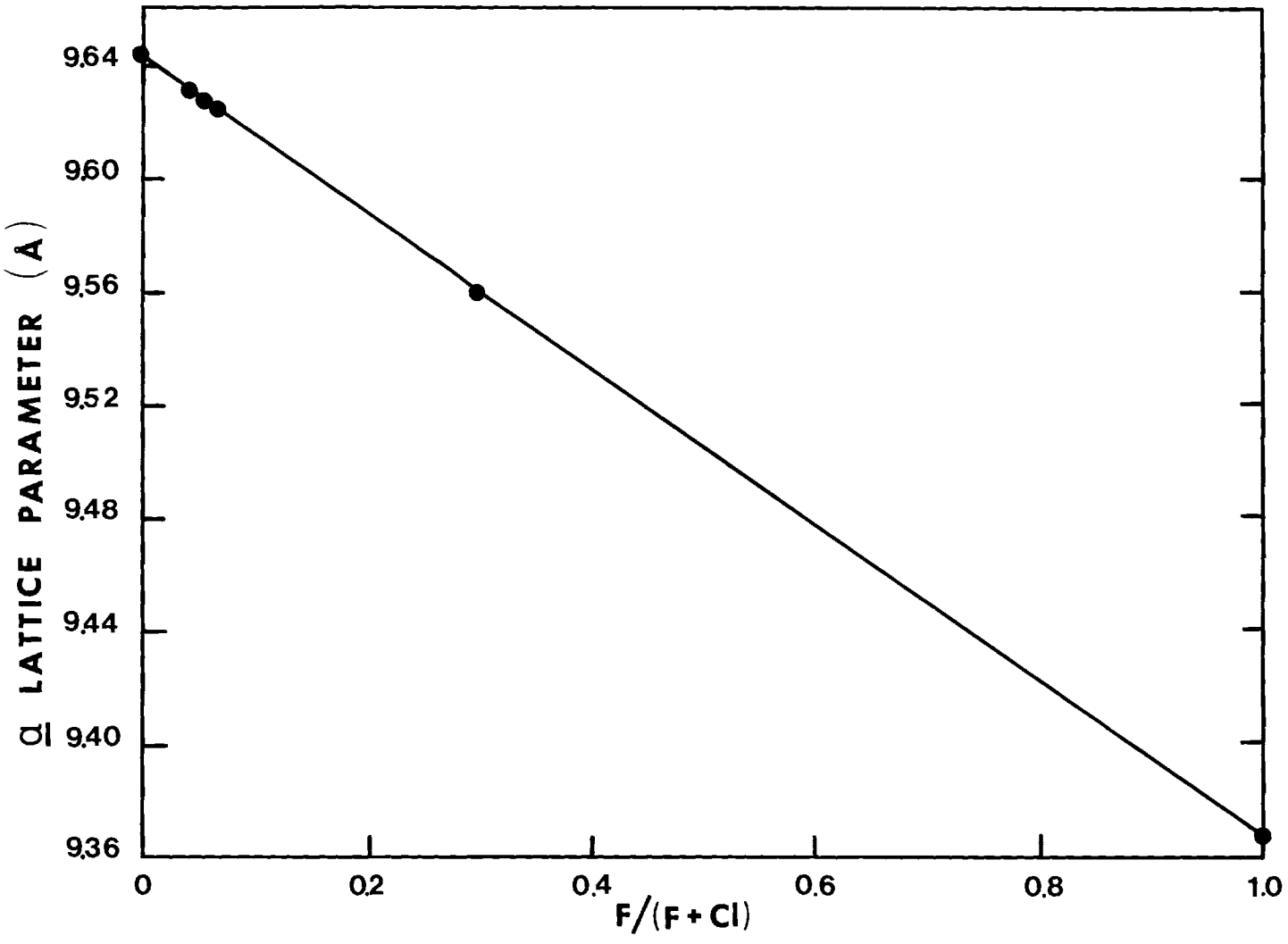

Figure 30. Dependence of a Lattice Parameter of Some Samples on F Content in (F,Cl)Ap.

assessment of the effect of the induced Cl vacancies. Typical values of apparent $\varepsilon'_{\parallel_c}$ and $\varepsilon''_{\parallel_c}$ of our Cl-deficient samples at 26°C were generally of the order of 100 or less, depending on the measuring frequency used. The degree of Cl deficiency was in the range of 0 to 20% (deficiency was determined from lattice parameters, Vegard's law and Prener's[41] results for $CaCl_2$ deficient ClAp in powder form).

There are other ways to produce Cl-deficient single crystals of ClAp than by heating them in a vacuum. For example, Johnson[63] grew ClAp crystals from the melt at 1650°C which were highly Cl deficient due to rapid loss of $CaCl_2$ by vaporization. Whether or not these crystals would be suitable for dielectric measurements depends entirely on the size and the degree of induced strain due to the presence of large temperature gradients during growth. It would probably be well to consider crystals prepared by his method for extension of the present work along these lines. That, of course, would require setting up a crystal growth procedure and apparatus not now on hand.

Although they were not available for this work, OHAp crystals of adequate size (e.g., 1 mm) for dielectric measurements are now reported to have been successfully grown by two different groups (Mengeot et al.[64] and D. Roy[65]). Thus, dielectric measurements on OHAp should be possible either now or in the near future.

D versus E Hysteresis Effect

An electric field E applied along a direction $\vec{u}$ in a dielectric will give rise to a polarization $\vec{P}$. If the material has dipoles which

orient in jumps then the relationship between $\vec{P}$, $\vec{u}$, and $\vec{E}$ will not be linear and a plot of $\vec{P} \cdot \vec{u}$, versus $\vec{E}$ will exhibit a hysteresis loop (see Figure 11). Some materials have, in addition to non-linear polarization, a linear component. Some, for example ClAp, may also be highly conductive. Both phenomena, especially conduction, can distort or even mask the hysteresis behavior displayed on an oscilloscope. The larger the conductivity, the more elliptical the hysteresis loop will become. Figure 31 shows the hysteresis loop of a (F,Cl)Ap sample ($\frac{F}{F+Cl} = 0.04$) at 100°C, where the non-linear behavior was almost completely disguised by the linear polarization. With the compensator, a special feature of the hysteresis loop tracer used in this work, it was possible to eliminate the distortions from conductivity and linear polarizability and to display only the non-linear polarization component. As a result, the existence of hysteresis loops showing dipole effects in ClAp, which were originally reported by Elliott and Young[30], and of some (F,Cl)Ap has now been firmly established (see Figures 31 and 32).

When non-linear polarization effects are absent, after the sample's capacitance and conductance are compensated for the resulting trace is a horizontal straight line. This point is illustrated in Figure 33 with a $BaTiO_3$ sample at 123°C. The crystal is ferroelectric below 120°C, the transition temperature, and paraelectric above[70]. Although ClAp appears to undergo a phase transition at 200°C, non-linear effects were still observed at 250°C (see Figure 39). This phenomenon is explained in Chapter V. No hysteresis loops were

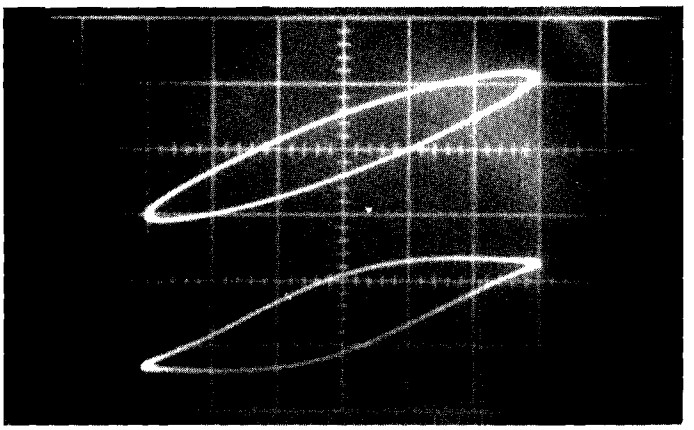

Figure 31. Hysteresis Loop of (F,Cl)Ap at 100°C and 100 Hz with E Field Parallel to c Axis. Lower loop is compensated version of upper. Specimen is FClPE for which F/(F + Cl) = 0.04 (applied field is 17600 V/cm). Vertical sensitivity was 0.5 V per large division for upper loop, 0.1 V per large division for lower loop.

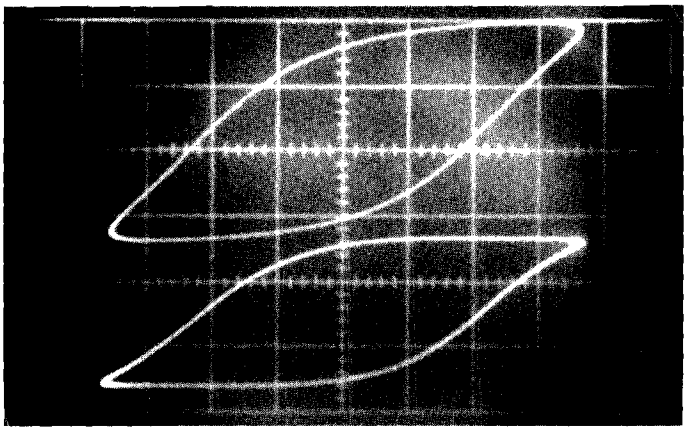

Figure 32. Hysteresis Loop of ClAp at 26°C and 100 Hz with E Field Parallel to c Axis. Lower loop is compensated (see Chapter II, part 5) version of upper loop (applied field is 6000 V/cm). Vertical sensitivity was 5 V per large division for upper and lower loop.

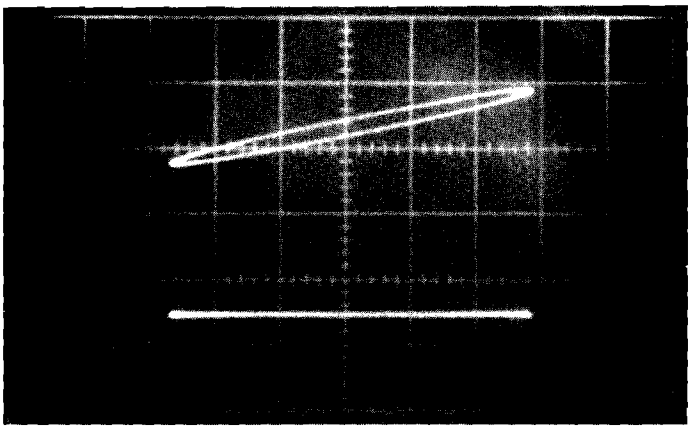

Figure 33. Hysteresis "Loop" of Barium Titanate at 123°C and 100 Hz. Lower "loop" is compensated version of upper (applied field is 10000 V/cm). Vertical sensitivity was 1 V per large division for upper and lower loop.

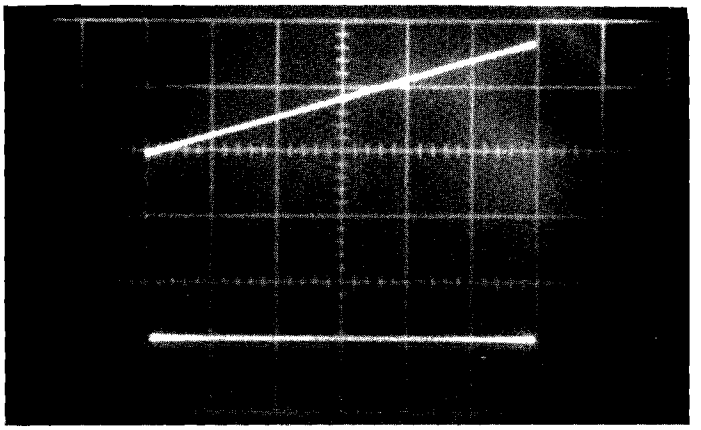

Figure 34. D versus E Trace for ClAp at 26° C and 100 Hz with E Field Perpendicular to c Axis. Lower trace is compensated; upper is not (applied field is 12500 V/cm). Vertical sensitivity was 0.5 V per large division for both loops.

observed if the field was applied perpendicular to the c axis (see Figure 34). Most interesting is the effect of fluorine on the ferroelectric character in ClAp (E || c). Among all the (F,Cl)Ap specimens tested, only the one with the lowest F/F+Cl ratio (~ 0.04) displayed a hysteresis loop at temperatures between 25°C and 300°C (Figure 31). No hysteresis loops were observed at all in FAp, not even at 300°C where some vacancy migration occurs[14]. Again, this evidence indicates that the apparent cause of the hysteretic behavior in ClAp must be attributed to the Cl ions.

Because of possible bioelectrical implications (see Chapter I), a search for a D,E hysteresis loop behavior in sections of tooth enamel was initiated by Elliott and Young[30]. Present investigations have led to the same experimental results, i.e., none was found. The samples were cut so that the c axes of the enamel crystallites, which are essentially perpendicular to the exterior enamel surface[4], were aligned with the electric field. Although maximum instrument sensitivity was used, no hysteresis loops similar to ClAp's were observed (see Figure 35), perhaps because tooth enamel crystallites contain many impurities (impure OHAp). Their effect on the dielectric properties of OHAp and, even, the dielectric properties of OHAp itself have not yet been determined.

Pseudo-Ferroelectricity

Although the hysteresis loops in Figure 32 strongly suggest that ClAp is ferroelectric, its space group[27] is not compatible with a ferroelectric character. By definition, true ferroelectricity and

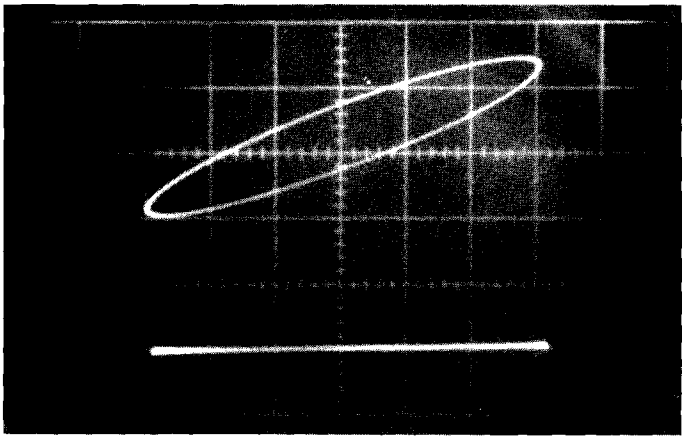

Figure 35. D versus E Trace for Human Tooth Enamel at 25°C and 100 Hz with E Field Perpendicular to Enamel Surface. Upper trace is compensated; lower is not (applied field is 6000 V/cm). Vertical sensitivity was 5 V per large division for both loops.

antiferroelectricity can only occur in noncentrosymmetric (polar) and centrosymmetric (non-polar) space groups, respectively. Thus, the best approach toward a solution of the problem is to describe the properties of both antiferroelectrics and ferroelectrics and then to correlate these properties with available experimental data on ClAp.

A Kittel[32,71] antiferroelectric consists of two equivalent sublattices having oppositely directed "spontaneous" subpolarizations consistent with a centro-symmetric structure. Whether or not the anti-parallel dipoles can be reversed depends on a number of parameters. Usually, with increasing temperature and field, switching is more likely to occur. If it does, the antiferroelectric becomes temporarily ferroelectric. The $\bar{D}$ vs. $\bar{E}$ plot then exhibits hysteresis loops in the high $\bar{E}$ region, where the crystal is antiferroelectric. Figure 36 gives an example of such a "butterfly loop" for $PbZrO_3$, a material that is antiferroelectric normally, but in which a ferroelectric character can be induced under high electric fields. Some materials can not be switched, within the temperature range where the structure is antiferroelectric, before electrical breakdown occurs. These materials exhibit a linear D, E relationship. In general, the plot is a rotated ellipse if electrical conduction exists; otherwise it is a straight line.

Ferroelectrics usually contain domains of spontaneous polarization of differently oriented opposite polarity[72,73]. However, within each domain all dipoles are oriented or at least contribute a component

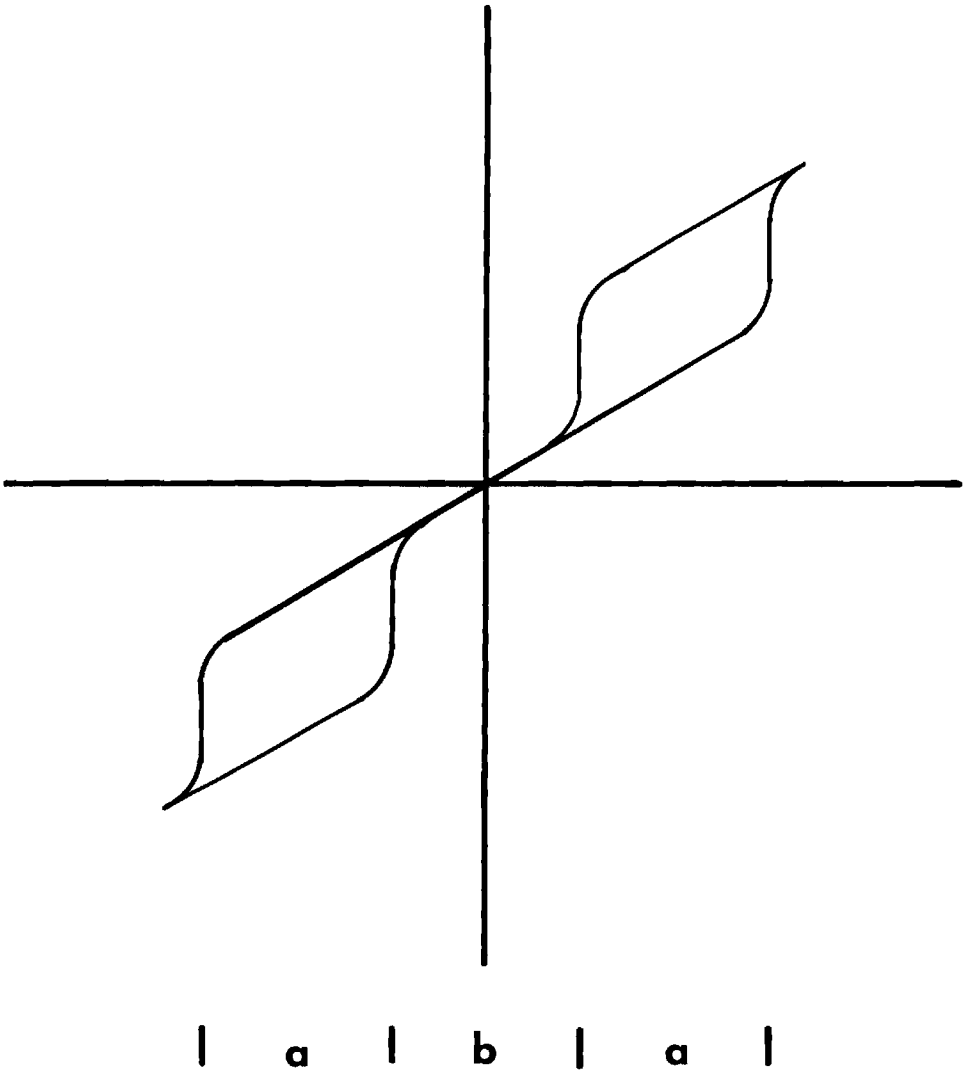

Figure 36. Antiferroelectric Hysteresis Loop for $PbZrO_3$ (from Reference 70). (a) Ferroelectric region; (b) Antiferroelectric region.

all in the same direction consistent with the non-centrosymmetric (polar) space group of the material. When the ferroelectric is immersed in a strong field the dipoles tend to align themselves spontaneously with the field. This phenomenon can be observed as D, E hysteresis loops. Ferroelectrics also exhibit a discontinuity in the temperature derivative of the dielectric constant at their ferroelectric-to-paraelectric transition temperature (Curie point)[73]. The abrupt changes in the polarization properties of the material are accompanied by a symmetry transformation and the disappearance of the hysteresis loop[73]. For example, $BaTiO_3$ has cubic symmetry in the paraelectric state above the 120°C transition temperature, whereas in the ferroelectric state below 120°C it has tetragonal symmetry.

Now, consider the ClAp studied here. This material appears to be ferroelectric ($E \parallel \underline{c}$)[30] and seems, by optical measurements, to undergo[39] a monoclinic to hexagonal phase transition at about 200°C. These facts suggested that ClAp might also exhibit an anomaly in ε' at 200°C. Unfortunately neither a Curie point nor the disappearance of the hysteresis loop was observed up to 400°C, the upper temperature limit for current experiments. Thus, these ferroelectric indicators could not be used for identification purposes here.

Approximately 95% of the cells in a typical crystal used for this work are stoichiometric (subscribe to the centosymmetric space group $P2_1/b$) and seemingly do not contribute to the high ε' nor to the hysteresis loops. This hypothesis is supported by the lack of electric field dependence of h k_{odd} ℓ ($\ell \neq o$) reflections which indi-

cates that the glide plane on the average is not destroyed by electric fields of the strength used for the dielectric measurements. As shown in Chapter I, section 2, the dipole moments associated with Cl ions and adjacent Ca triangles form two equivalent sublattices having oppositely directed "spontaneous" subpolarizations consistent with antiferroelectric requirements. Thus on the basis of the $P2_1/b$ space group, the field dependence of h k_{odd} ℓ reflections and the polarization sublattices this group of cells should be classified as antiferroelectric.

However, because the Cl ions are tightly packed within the structural columns, reorientation of the dipoles (i.e., Cl shift) does not appear to be possible within the range of temperatures and applied electric field strengths used in this work. Thus, the D versus E response of these cells should be a straight line making an angle with the E axis. The polarization and, hence, the dielectric constant should be very small, as in FAp.

The remaining ~5% cells in the ClAp studied are Cl deficient. The Cl ions near the vacancies can shift between the z = 0.44 (or 0.04) and z = 0.56 (or 0.06) sites, which corresponds to reversal of dipole moments. Because the net dipole moments persist temporarily even in the absence of a field, the P versus E plot is similar to a typical ferroelectric hysteresis loop. A superposition of D versus E behavior due to all the cells will be equivalent to the superposition of a linear D versus E curve from the 95% stoichiometric cells and the hysteresis curve from the few cells containing a moveable Cl ion. The

resultant response will again be a hysteresis loop as discussed in Chapter II. Therefore, the conclusion is that even though the bulk of a ClAp crystal is structurally ordered as an antiferroelectric material its dielectric behavior is masked by a strong ferroelectric effect arising from the defects. Thus, perhaps,the name pseudo-ferroelectric would be appropriate for ClAp.

Non-Dependence of X-Ray Reflections on Electric Fields

In the monoclinic structure, $P2_1/b$, the mirror plane of the hexagonal structure is replaced by a glide plane, which is associated with the doubling of one axis and the h k_{odd} ℓ ($\ell \neq 0$) reflections in nearly stoichimetric ClAp. Therefore if, for any reason, the glide plane reverts to a mirror plane all h k_{odd} ℓ ($\ell \neq 0$) reflections must also vanish.

It was suggested by Elliott and Young[30] on the basis of the observed hysteresis loops that the action of large electric fields ($\sim 10^4$ V/m) might allow about half of the Cl ions to reverse their sense of displacement from the z = 1/2 position. As a result, the glide plane and hence all h k_{odd} ℓ ($\ell \neq 0$) reflections should disappear. This model would be consistent with the hysteresis loops, but would not explain the lack of electric field dependence of "monoclinic" reflections. A study of the 1 9 2, 4 3 2, 0 11 2, 0 9 2 and $\bar{2}$ 11 2 reflections clearly indicated no change in the observed intensitites, although fields up to 10,000 V/cm were applied. For example, the intensity of the $\bar{2}$ 11 2 reflection had a value of 2850 cps (counts per second) with a fluctuation of $\pm$ 200 cps. The background intensity

did not exceed 1,100 cps. Although, a 1% change in the intensity would have amounted to about 29 cps it probably could have been detected by inspecting the general trend of the curve. This suggests that less than 1% of the Cl ions were undergoing a shift. As a result, this experimental fact not only provides support for the shift model, but reinforces the previous suggestion that most Cl ions are essentially "locked" into a fixed position at room temperature.

Vacancy Migration

Under certain conditions (high temperatures, large electric fields) impurity ions and/or vacancies within a solid may acquire considerable mobility which results in an ionic conduction process. On the basis of the columnar arrangement of the halogen ions, of the existence of about 5% Cl vacancies, and of the careful preparation of synthetic ClAp to avoid impurities, it is assumed that the dominant conduction process at temperatures between 25°C and 300°C is based on vacancy migration. In order to maintain electro-neutrality throughout the volume of the crystal, Ca vacancies must also exist. Prener[41] has shown that ClAp can be made Cl deficient at temperatures above 900°C through loss of $CaCl_2$. Thus, it is important to know under what conditions the Cl and Ca vacancies can become active and contribute significantly to the dielectric properties of ClAp, if at all, by migrating (by means of a Cl or Ca jump process) toward the electrodes under the influence of an applied electric field.

D.C. Conductivity

At elevated temperatures ($\geq$ 200°C) and low electric field

strength (~10 V/m) or at low temperatures (< 200°C) and high electric field strength (~ 10^4 V/cm) some charge carriers such as Cl or Ca vacancies can be expected to reach the electrode-dielectric interface and to be neutralized. As a result, an apparent dielectric loss ($\varepsilon''_{d.c.}$) will be measured. The additional term (discussed in Appendix A, section 6) which contributes to ε'' is

$$\varepsilon''_{d.c.} = \frac{\sigma}{\varepsilon_o \omega} \tag{4.8}$$

where σ is the d.c. conductivity of ClAp, ε_o is the permittivity in free space, and ω is the frequency of the applied field. The d.c. conductivity parallel to the c axis was measured on four ClAp samples and was found to be less than $10^{-9}\ \Omega^{-1}\ cm^{-1}$ in the temperature range 25°C to 200°C with an applied field of 60 V/cm. The substitution of $\sigma = 10^{-9}\ \Omega^{-1}\ cm^{-1}$ into equation 4.8 yields a maximum value of about 100 for $\varepsilon''_{d.c.}$ at the lowest frequency at which measurements were made (f = 100 Hz). The total dielectric loss (E || C) at 100 hz is usually greater than 10^4, which shows that $\varepsilon''_{d.c.}$ is negligible within the temperature range and magnitude of electric fields discussed above. This was no longer true if the field was increased by a factor of about 10. An increased d.c. conductivity (~ $10^{-8}\ \Omega^{-1}\ cm^{-1}$) appeared around 200°C. It decreased exponentially with time (Figure 37). The time constant was 78 sec. The current of a capacitor being charged with electron, rather than ionic, flow also follows an exponential decay with a time constant τ given by

$$\tau = RC$$

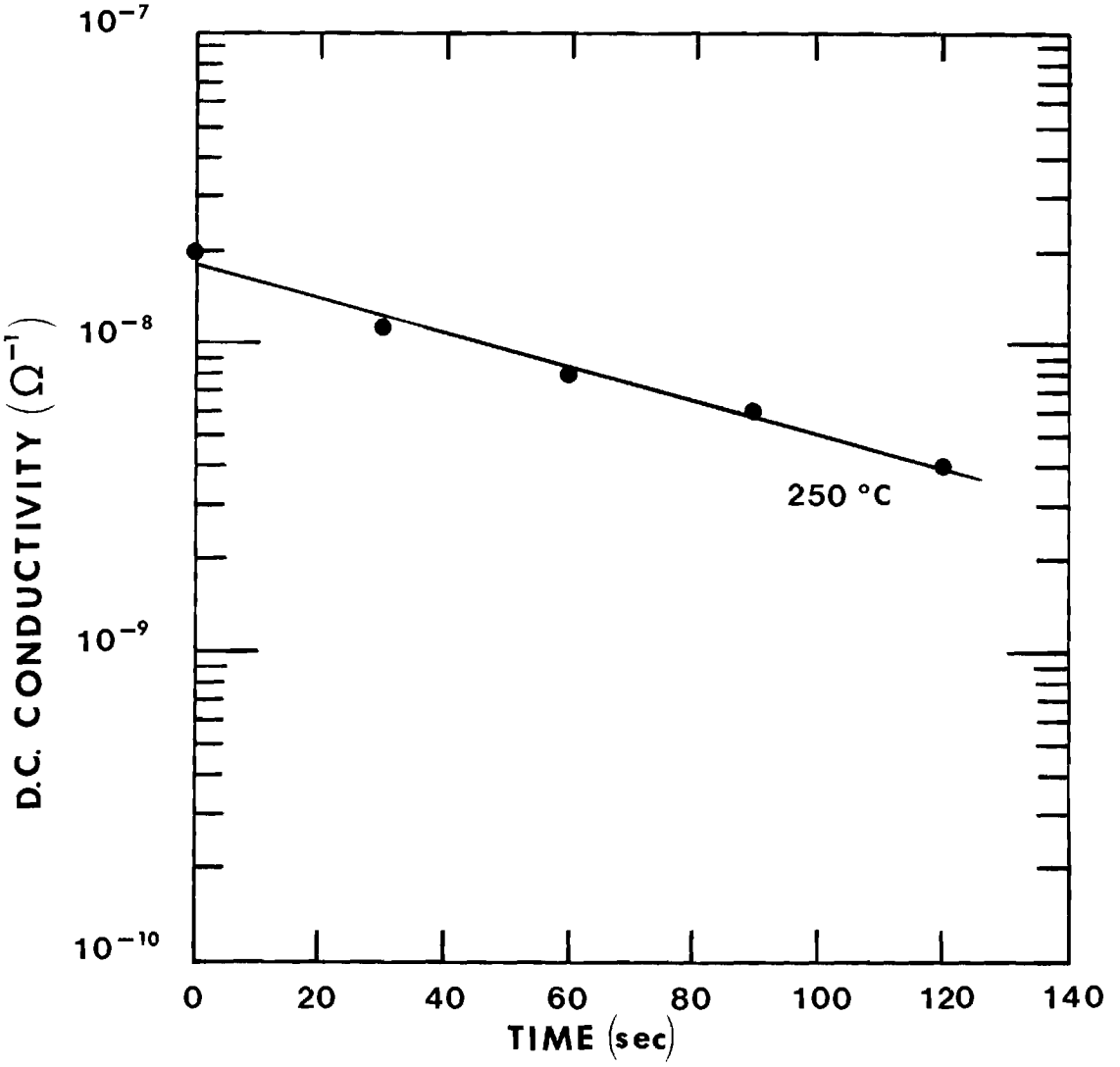

Figure 37. Time Dependence of D. C. Conductivity in ClAp (Sample C8PE) Immediately After the Removal of the Applied Field. Applied field was $\geq$ 1000 V/cm. Measuring Field was < 1 V/cm.

The substitution of experimental values for R(~ 10^8 Ω) (estimated from Figure 37) and the measured C(~ 5 x 10^{-10} fd) using the specimen of Figure 37 yielded τ ~ 0.05 sec, which should apply if the conductivity arose from electron migration. Clearly, the observed phenomenon must be ascribed to a different charge build-up process, presumably, neutralization of Cl^- and Ca^{2+} vacancies near the negative and positive electrodes, respectively. If the polarity is reversed the vacancies should migrate in the opposite direction and the process of charge accumulation and neutralization should repeat itself at the opposite electrodes. As predicted, when this was tested experimentally a time dependent d.c. conductivity was again observed similar to that in Figure 37. When the field was turned off, the Cl vacancies should redistribute themselves within the dielectric, presumably until the centers of positive and negative charges coincide . Therefore, this "space-charge" capacitance due to ions piling up near the electrodes should slowly decay. In fact, an exponential decay was observed experimentally with a time constant τ ~ 10^3 sec.

Due to electronic neutralization of Cl vacancies, Ca vacancies, or both, at the electrodes, the total number of these charge carriers within the material should temporarily diminish. This must result in a lower capacitance and hence, a lower dielectric constant. Therefore, it is suggested that ClAp crystals can be made temporarily highly stoichiometric by repeatedly heating the material to 200°C under the influence of a moderate d.c. field (~ 1000 V/cm). Through lattice parameter measurements after each heating and cooling cycle the dielectric constant at room temperature could be correlated with the

vacancy concentration in the crystal. Thus, it appears that the dielectric constant of ClAp could be controlled or modified. No d.c. conductivity data were collected for (F,Cl)Ap or ClAp ($E \perp c$).

Tunneling Mechanism

The activation energies and the migration mechanisms of Cl and Ca vacancies in ClAp were not known and could not be determined from the available experimental data. Nevertheless, a model for Cl vacancy migration along the c axis is proposed which is based on the available structural data for ClAp.

The shortest inter-columnar distance between Cl ions is 9.645 Å, in contrast to a 2.57 Å jump distance along the column. Thus, due to the many intervening atoms between the columns and the short columnar Cl-Cl distance, migration along the columns is much more likely than between them. However, before the Cl ions can jump into adjoining vacancies they must pass through one of the Ca triangles. The distance from the center of a Ca ion to the center of the triangle is 2.48 Å. Compared to the Ca-Cl bond length (2.73 Å) given by Sutton[74] it appears that at room temperature the Ca triangle would pose a formidable barrier against Cl passage. However, an exceptionally large thermal vibrational amplitude (~ 0.25 Å) of the Ca ions in the a, b plane (the usual thermal vibrational amplitude, $\sqrt{u_{11}^2}$ or $\sqrt{u_{22}^2}$ is ~ 0.1 Å) could lead to a momentary expansion just large enough to give, for example, a distance of 2.73 Å (Ca-Cl distance[74] in $CaCl_2$) from the center of a Ca to the center of the triangle and to allow a Cl ion to pass through.

Space Charge Polarization

Those charge carriers which are not neutralized near the electrode will either accumulate at the dielectric-electrode interface and form a space charge or will be blocked by crystal defects in the interior of the dielectric. Either case can result in enormous apparent dielectric constants. It is this process which can mask weak dielectric behavior. Therefore, it can account for the large linear polarizations which were observed during hysteresis loop measurements. This pehnomenon was extensively investigated by MacDonald[75,76] and by Jaffe[77,78]. MacDonald derived an expression for the admittance of a space charge layer. The treatment takes into account any degree of dissociation and recombination of charges and any ratio between the mobilities of positive and negative charge carriers.

In the present work, it was not considered crucial that a thorough investigation of the space charge polarization in ClAp be carried out.

CHAPTER V

TRANSITIONS IN CHLORAPATITE

Introduction

The monoclinic structure of ClAp differs from an hexagonal structure primarily by the alternation along the b axis of the z-coordinates of the Cl ions, identified with a particular symmetry element, a b-glide plane. If, for some reason, the Cl ions were to become statistically disordered the glide plane would transform into a mirror plane and the structure associated with the monoclinic space group $P2_1/b$ would change to the hexagonal space group $P6_3/m$. These changes can be readily observed with x-ray diffraction techniques, since the monoclinic structure gives rise to "extra" reflections which are absent for the hexagonal case. Because these reflections appear halfway between the "normally" occurring "hexagonal" reflections along the b* axis in reciprocal space they are labelled as h k_{odd} ℓ, where $\ell \neq 0$ and henceforth referred to as "monoclinic" reflections. All "hexagonal" reflections, of course, are labelled as h k_{even} ℓ. Prener[39], who investigated the temperature dependence of ClAp properties by optical means (examination of the crystal between crossed polaroids) and with x-ray diffraction cameras, noticed an apparent absence of the "monoclinic" reflections above 200°C and a disappearance of the crystal's birefringence perpendicular to the c axis at the same temperature. As a result of his findings he concluded that ClAp

undergoes a reversible monoclinic-to-hexagonal phase transition in the neighborhood of 200°C. However, recent and more precise measurements of the intensity of 20 different "monoclinic" reflections above 200°C have shown that these reflections persisted up to ~400°C (see Figure 42 and also Figure 65). On the basis of detailed structural data of the monoclinic phase, and because the pseudo-ferroelectric effect requires the existence of a low potential energy barrier to dipole reorientation, it was suggested by Elliott and Young that both the pseudo-ferroelectric effect[31] and the transition[30] in ClAp may be caused by the Cl ion shift. It was this idea which caused the experimental efforts in x-ray diffraction to be focused on the behavior of the Cl ions. Thus, the purpose of the work reported in this chapter was to identify the mechanism of the ~200°C transition by investigating the temperature dependence of (a) the r.m.s. thermal vibrational amplitude of the Cl ion in the c direction, (b) the equilibrium position (z-coordinate) of the Cl ion and (c) the intensities and breadths of some of the monoclinic x-ray reflections.

Transition Near 200°C

The most important results of the least-squares partial structure refinements and lattice parameter measurements of ClAp obtained in this work are shown in Table 3.

Both the observed and calculated structure factors of the least squares structure refinements can be found in Appendix H. At 25°C, good agreement was obtained with the refined values found by Mackie et al[27]. The r.m.s. thermal vibrational amplitude $\left(\sqrt{\overline{u_{33}^2}}\right)$

Table 3. Results of Least Squares Structure Refinements for ClAp

Temp. (°C)	Lattice Parameter (Å) c	a	β_{33}	$\sqrt{\overline{u_{33}^2}}$ (Å)	δ (Å)	Z(Cℓ)	R_2	wR_2	Cl Multiplier
			0.00955(5)*			0.4438(60)	0.022*	0.031*	0.159(100)*
25	6.761**	9.637**	0.00808(25)	0.137	0.390	0.44232(16)	0.0228	0.0306	0.158(200)
50	6.764	9.640	0.00935(24)	0.147	0.384	0.44327(19)	0.0247	0.0333	0.158
100	6.770	9.645	0.01179(29)	0.165	0.370	0.44537(21)	0.025	0.0353	0.158
150	6.776	9.651	0.01408(32)	0.181	0.356	0.44750(26)	0.0288	0.0265	0.158
200	6.778	9.656	0.01755(42)	0.202	0.318	0.45310(24)	0.0285	0.0357	0.158
250	6.785	9.659	0.01860(42)	0.208	0.305	0.45512(23)	0.0278	0.0357	0.158
300	6.790	9.659	0.02026(114)	0.218	0.291	0.45707(56)	0.0469	0.0873	0.158
350	6.790	9.661							

NOTE: Standard deviations (multiplied by 10^5) are shown in parentheses for those parameters varied.

*Results of Mackie et al.[27] Multiplier deduced from monoclinic structure refinement result.

**Values in this column were not subjected to 2θ zero corrections. This results in an error in the absolute but not in the relative values of these parameters.

$\overline{U_{33}^2}$ is the r.m.s. thermal vibrational amplitude of the Cℓ ion in the z direction. z (Cℓ) is the equilibrium position of the Cℓ ion (z-coordinate). δ is the distance between the Cℓ ion position and the mid-point (z = 1/2). w, the weight assigned, is the reciprocal of the variance estimated on counting statistics for the net reflection intensity.

$$R_2 = \frac{\Sigma \left| |F_o|^2 - |F_c|^2 \right|}{\Sigma |F_o|^2} \quad \cdot \quad wR_2 = \frac{\left[\Sigma w \left(|F_o|^2 - |F_c|^2\right)^2\right]^{\frac{1}{2}}}{\left[\Sigma w |F_o|^4\right]^{\frac{1}{2}}}$$

of the Cl ion along the c direction and its distance, δ, from the $z = 1/2$ position has been plotted as a function of temperature in Figure 38. It shows that the Cl ion shifted about 0.1 Å closer to $z = 1/2$ as the temperature was raised from 25°C to 300°C while the r.m.s. thermal vibrational amplitude increased to nearly 0.2 Å. But the combined effect still lacks about 0.1 Å of letting the Cl ion, on the average, reach and cross over the $z = 1/2$ position. This fact combined with the existence of the $\vec{D}$ versus $\vec{E}$ hysteresis loops both in ClAp and (F,Cl)Ap ($F/F + Cl \approx 0.04$) at 250°C (Figures 39 and 40) clearly indicates that even substantially above 200°C (a) a moveable Cl ion still experiences a double potential well and (b) that the Cl thermal vibrations are not able to carry the Cl freely past the potential barrier of the double well (In Figures 39 and 40 the upper uncorrected loops are almost masked by high conductivity and a large linear polarization arising, possibly, from space charge polarization (discussed in Chapter IV, section 3), but the hysteresis loops do exist). It was, thus, concluded that the changes occuring near 200°C do not constitute a true monoclinic to hexagonal phase transition. However, that some structurally related change does indeed occur near 200°C is demonstrated by the change in the slope of the a lattice parameters (Figure 41), the change in slope of the mean square thermal vibrational amplitude of the Cl ion, the abrupt change in the z position (shown in Figure 38 by δ), and the strong changes in the intensities of $h\ k_{odd}\ \ell$ ($\ell \neq 0$) reflections (Figure 42). What processes could account for these changes?

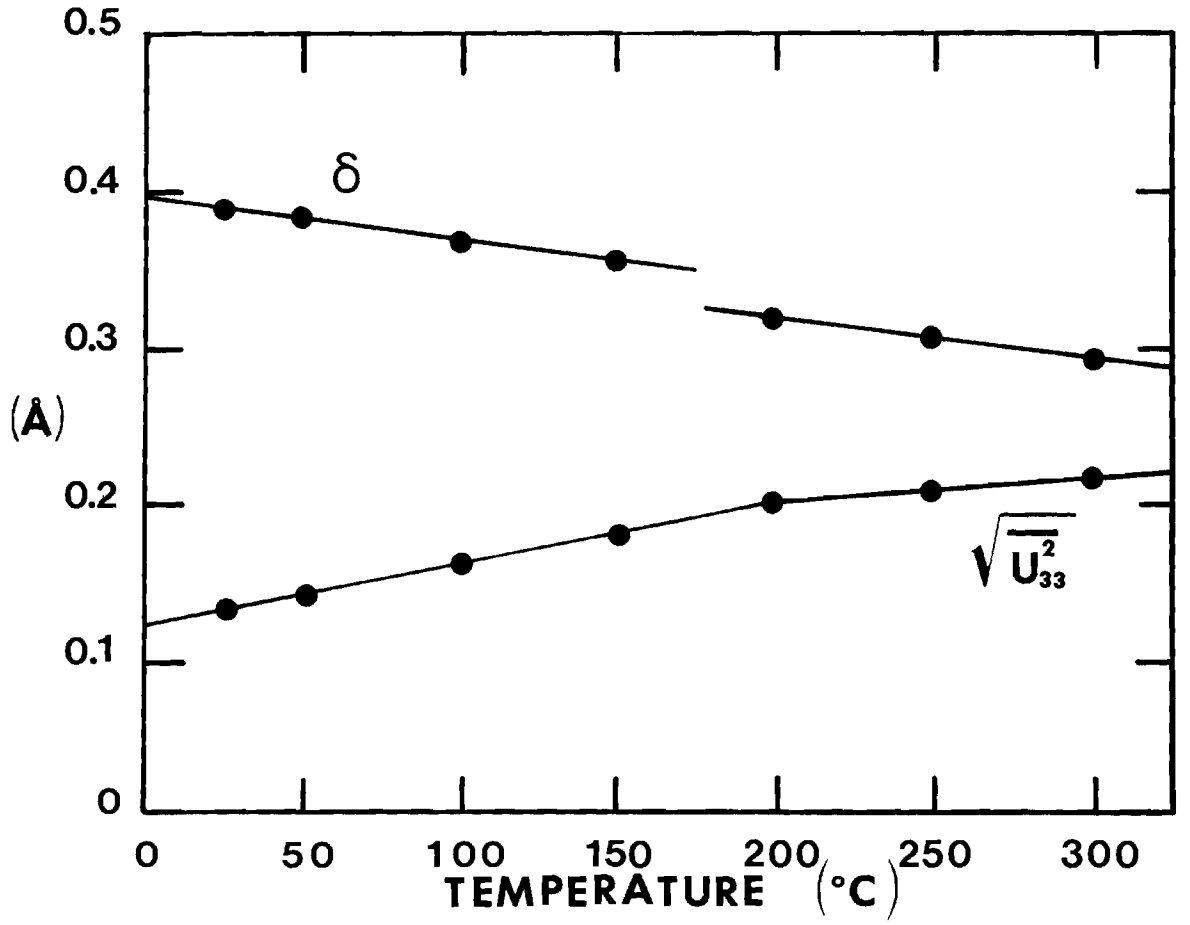

Figure 38. Temperature Dependence of Both the Root Mean Square Thermal Vibrational Amplitude $\sqrt{\overline{u_{33}^2}}$ of the Cl Ion and Its Distance from the z = 1/2 or z = 0 Position.

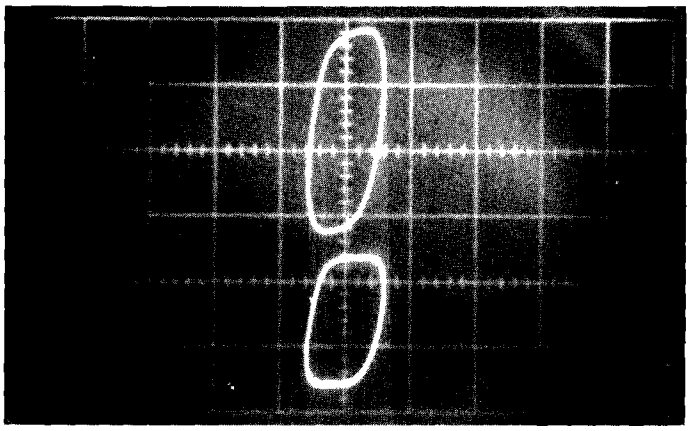

Figure 39. D versus E Hysteresis Loop of ClAp at 250°C and 100 Hz with the E Field Parallel to the c Axis. Lower trace is compensated; upper is not (applied field is 3300 V/cm). Vertical sensitivity was 5 V per large division for both loops.

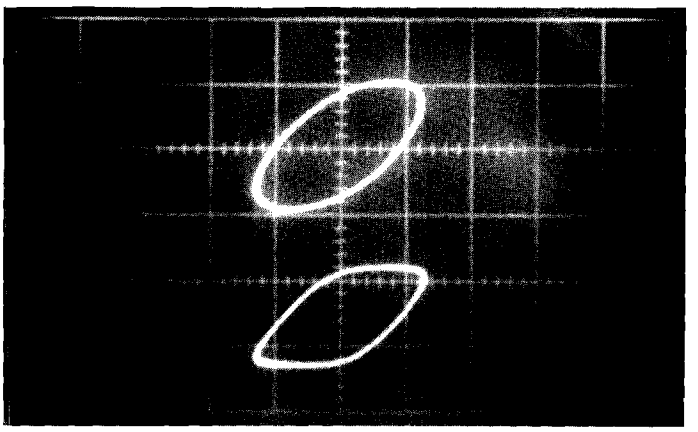

Figure 40. D versus E Hysteresis Loop of (F,Cl)Ap at 250°C and 100 Hz with the E Field Parallel to the c Axis. Lower trace is compensated; upper is not (applied field is 7000 V/cm). Vertical sensitivity was 10 V per large division for upper loop, 2.5 V per large division for lower loop.

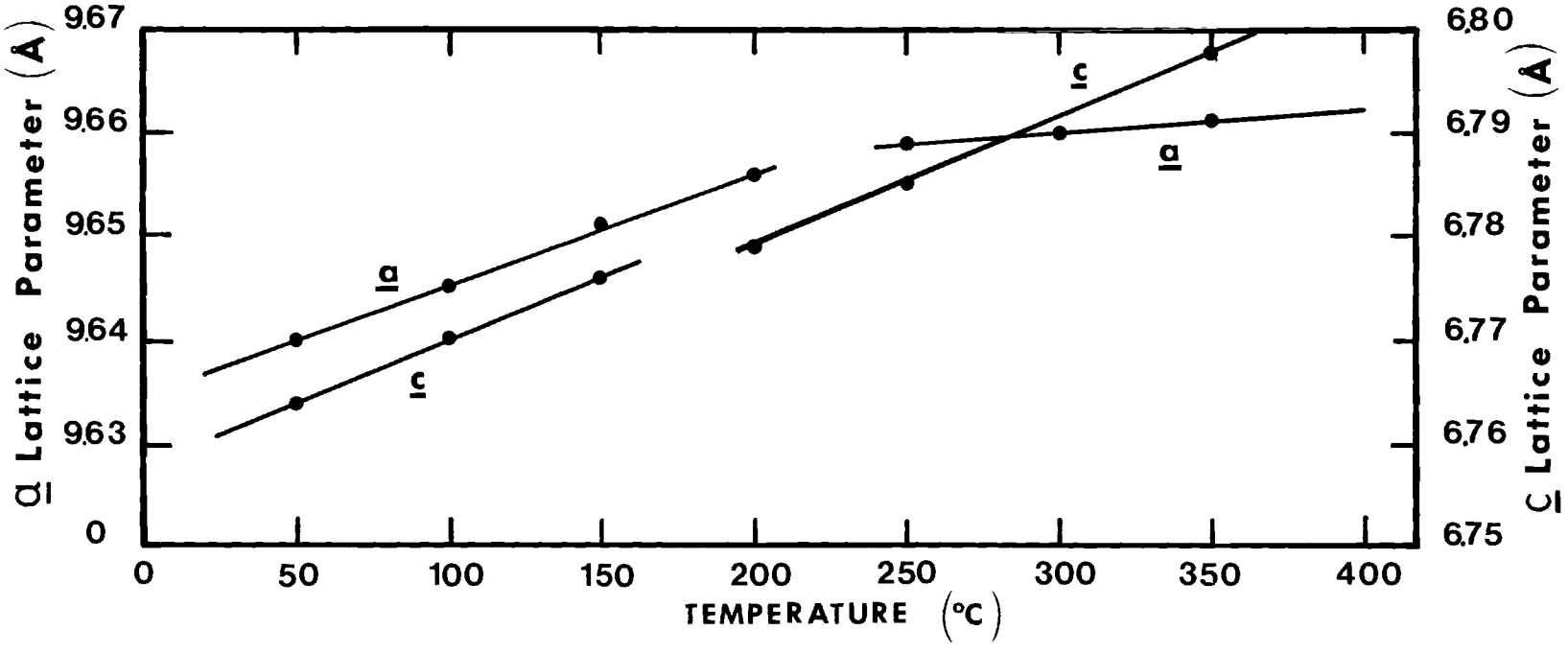

Figure 41. Temperature Dependence of a and c Lattice Parameters of ClAp.

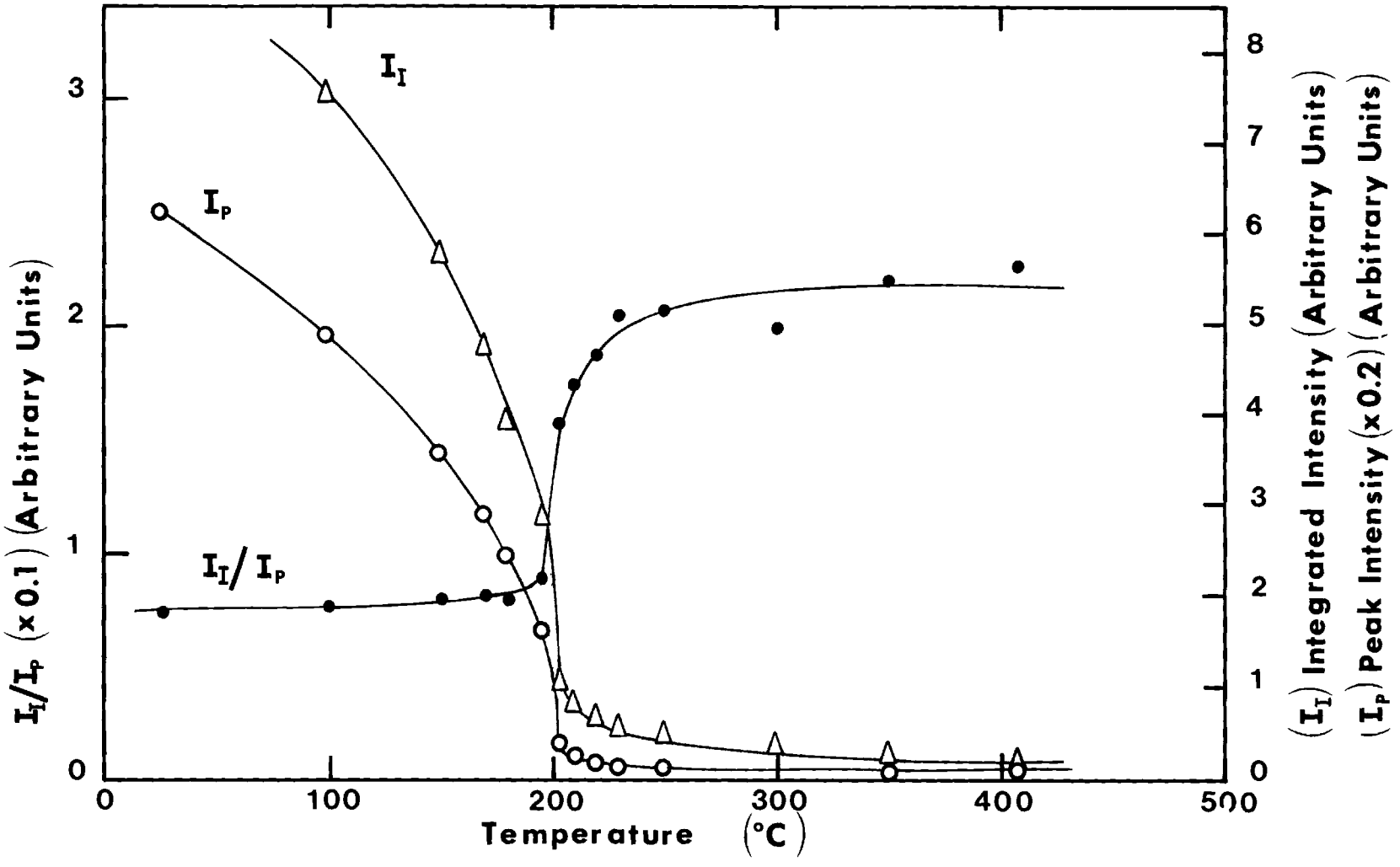

Figure 42. Temperature Dependence of the Integrated Intensity, I_I, Peak Intensity, I_P, and the Ratio, I_I/I_P, of the $\bar{4}$ 1 4 Reflection of ClAp.

Prener[39] suggested two processes which could bring about the hexagonal symmetry. Either most Cl atoms shift to the z = 0 or 1/2 position (which is clearly not the case according to the experimental data) or they become statistically disordered about these positions. However, due to the short Cl-Cl distance along the columns, complete statistical disordering is possible (with the aid of Cl vacancies) between and not within the columns. There is little doubt that impurities and the density of Cl vacancies, and probably, the Cl shift are intimately involved with the transition since Prener[39] reported a decrease in the transition temperature for Cl-deficient ClAp samples which were heated in vacuum at 800°C for 15 to 85 hours and an increase in the transition temperature for initial substitution of F in (F,Cl)Ap. The Cl deficiency occurs through loss of $CaCl_2$[41]. Prener[39] reported a transition temperature of 143°C for the 85 hour specimen. Another sample, a (F,Cl)Ap with a F/(F + Cl) ratio of 0.16, had a transition temperature of 310°C. The atomic scale mechanism by which the substituting F interacts with the Cl to produce this increase has been reported by Mackie and Young[61].

A plausible model which would account for these changes near 200°C is as follows. Thermal activation forces Cl ions near vacancies to move back and forth between equilibrium positions on opposite sides of z = 1/2 (or 0). With increasing temperature the shifting becomes increasingly probable and, consequently, the domain size in which the original inter-column monoclinic ordering is preserved becomes smaller. Finally, above 200°C most columns should be statistically

disordered with respect to each other along the b axis and only small regions retain their monoclinic character and give rise to weak h k_{odd} ℓ ($\ell \neq 0$) reflections. This, then, constitutes our model for ClAp between the temperatures of the optically observed transition (ca. 200°C) and the temperature (> 400°C) of the true monoclinic-to-hexagonal transition yet to be shown by x-ray data. It may be thought of as an optically uniaxial aggregation of x-ray monoclinic sub-microscopic domains, the orientation of each domain being a statistical choice of one of the three possible mimetic twin orientations (hence the uniaxial optical character). To accomodate the temperature induced strong reduction of the intensity of h k_{odd} ℓ ($\ell \neq 0$) reflections relative to h k_{even} ℓ reflections it is necessary to postulate that either (i) much of the material becomes hexagonal with monoclinic domains occuring here and there or (ii) the strains at the boundaries of these small domains causes atoms shifting closer to the hexagonal positions with consequent reduction of the h k_{odd} ℓ ($\ell \neq 0$) intensities. Both models are plausible and the change of δ with temperature (see Figure 38) is somewhat in accord with (ii). However, at this point we can not make a clear choice between those two possibilities.

The question arises then of how the micro-domains, intially all similarly oriented and indistinguishable parts of the overall single crystal, become independent of each other to take up different choices of the possible three orientations. A detailed discussion of the ordering mechanism by which ClAp is made monoclinic rather

than (statistically) hexagonal has been given by Mackie et al[27]. Basically, the mechanism involves a rumpling in the structure which in turn involves small displacements from the mirror plane positions of the hexagonal structure and slight shifts of the columnar Ca off the column axes. The end result is a rotation of the PO_4 tetrahedra, expansion of alternate oxygen triangles (centered on the 2_1 axis) and contraction of the others. The Cl ions normally occur in the expanded triangle. The Cl ions in the stoichiometric region of the crystal are in unusually close contact (3.38 Å compared to 3.62 Å for the sum of the ionic radii). The occurrence of a Cl vacancy invites a neighboring Cl ion to relax toward it by moving into the "wrong" oxygen triangle, thus violating the stoichiometric ordering scheme. Sufficient isolated exceptions to the ordering interfer with the propagation of the ordering information from column to column with the result that the ordering within one column no longer depends on its vacancy-affected neighbor. The crystal then becomes statistically hexagonal rather than monoclinic while yet retaining monoclinic micro-domains of defect-free or nearly defect-free material.

Another marked change that takes place near 200°C is that in the breadths of the "monoclinic" (i.e., k-odd) reflections (Figure 42). The "hexagonal" reflections (k-even) do not show a similar change of breadth (Table 31). It is not known whether the actual diffraction peak broadening is due to inhomogeneous strain broadening or a crystallite size effect. However, if the microdomain model discussed previously is correct and inhomogeneous strain is not important, then the size of these

micro-domain regions of the monoclinic form should be estimatable from the breadth of the h k_{odd} ℓ ($\ell \neq 0$) diffraction peaks with the Scherrer equation[79]

$$< t > = \lambda/\beta \cos \theta$$

where β is the full width at half maximum (FWHM) of the intrinsic diffraction profile expressed in radians 2θ. λ is the wavelength (0.709 Å) and $< t >$ is the volume average dimension of the monoclinic regions normal to the reflecting planes. To obtain β the observed reflection profile must first be deconvoluted from the observed profile which also contains the instrumental profile. This requires that both the observed reflection and the instrumental profiles be known. Usually the profile forms are approximately intermediate between Lorentzian and Gaussian functions. Thus it is useful to make calculations with both, since they are simply handled, and to hope that the truth lies somewhere between in this case. (The correct results, if desired enough, could be obtained from carrying through the deconvolution of the actual profiles expressed in Fourier series form after the instrumental profile had been determined by separate experiments.) It is known[79] that, if the Lorentzian function is used, $\beta = B - b$ where B is the FWHM of the reflection profile (from data) and b is the FWHM of the instrumental profile. For the Gaussian function β is given by $\beta^2 = B^2 - b^2$. If the ordinate of I_I/I_B scale in Figure 42 is multiplied by an appropriate scale factor (in this case 0.05) then both B and b can be read directly from the graph since I_I/I_B has the units of degrees. The scale factor was

chosen so that the I_I/I_B values times the scale factor reflected approximately the FWHM of the reflection profile. B was then obtained from the I_I/I_B values above 250°C (~1.1 degrees 2θ) and b from the values below ~100°C (~0.4 degrees 2θ). Because the b value, so chosen, is a composite of the instrumental profile with the intrinsic diffraction profile before the transition to microdomains, b is an overestimate of the actual value. As a result, β was underestimated and $< t >$ must be considered an upper limit (i.e., the size of the regions were always smaller than $< t >$) on the assumption that only size broadening was present.

The values of $R = I_I/I_B$ for the various k_{odd} reflections are given in Appendix I. Since they show little increase with increasing (h, k, ℓ) it appears that there is little broadening from strain, and hence, for our approximate calculation we may treat the diffraction broadening as all arising from small crystallite size.

The calculations were performed for the $\bar{4}$ 1 4 reflection as follows:

Peak position: $2\theta = 25.79°$

$\cos \theta = 0.97$

With the Lorentizian function used:

$\beta = B - b = 1.1 - 0.14 = 0.7$

$< t > = (0.709)/[(0.7/57.3)(0.97)] \simeq 60\text{Å}$

With the Gaussian function used:

$\beta^2 = B^2 - b^2 = (1.1)^2 - (0.4)^2 = 1.02$

$< t > = (0.709)/[(1.01/57.3)\ (0.97)] \simeq 41\ \text{Å}$

Thus, the actual crystallite size should be less than 60 Å. This conclusion does indeed support our model of ClAp between the ca. 200°C transition temperature and the temperature (> 400°C of the true monoclinic-to-hexagonal transition. Data on the other h k_{odd} ℓ reflections observed can be found in Appendix I. They lead to similar results.

Temperature Dependence of the Dielectric Constant Parallel to the c Axis in Chlorapatite Near 200°C

Since ε' is related to the polarization P by

$$\varepsilon'_{\parallel c} \approx \frac{P_{\parallel c}}{\varepsilon_0 E_{\parallel c}} \qquad (5.2)$$

(E is the electric field strength along the c axis), an anomaly in $\varepsilon'_{\parallel c}$ at a particular temperature (such as is observed in $BaTiO_3$ at 120°C) implies a similar behavior for the polarization. Theoretically, a discontinuity of $P_{\parallel c}$ could occur if the active dipole moments would spontaneously align or disalign at a phase transition point. Because of the nature of the ca. 200°C transition, just discussed, however, such an abrupt change should not be observed in ClAp. With increasing temperature, the ions in ClAp acquire more thermal energy. The expected result is a rise in the number of ions involved in the shift process, which implies an increase in $\varepsilon'_{\parallel c}$ and statistical disordering. Since the ions are not abruptly 'locked' into new positions above the point of maximum disorder, no discontinuity in the dielectric constant is expected to be, nor is, observed. Instead, $\varepsilon'_{\parallel c}$ is expected to increase continuously with rising temperature. Such behavior is shown in Figure 43 (which only extends to 250°C). In all such experiments an increase in

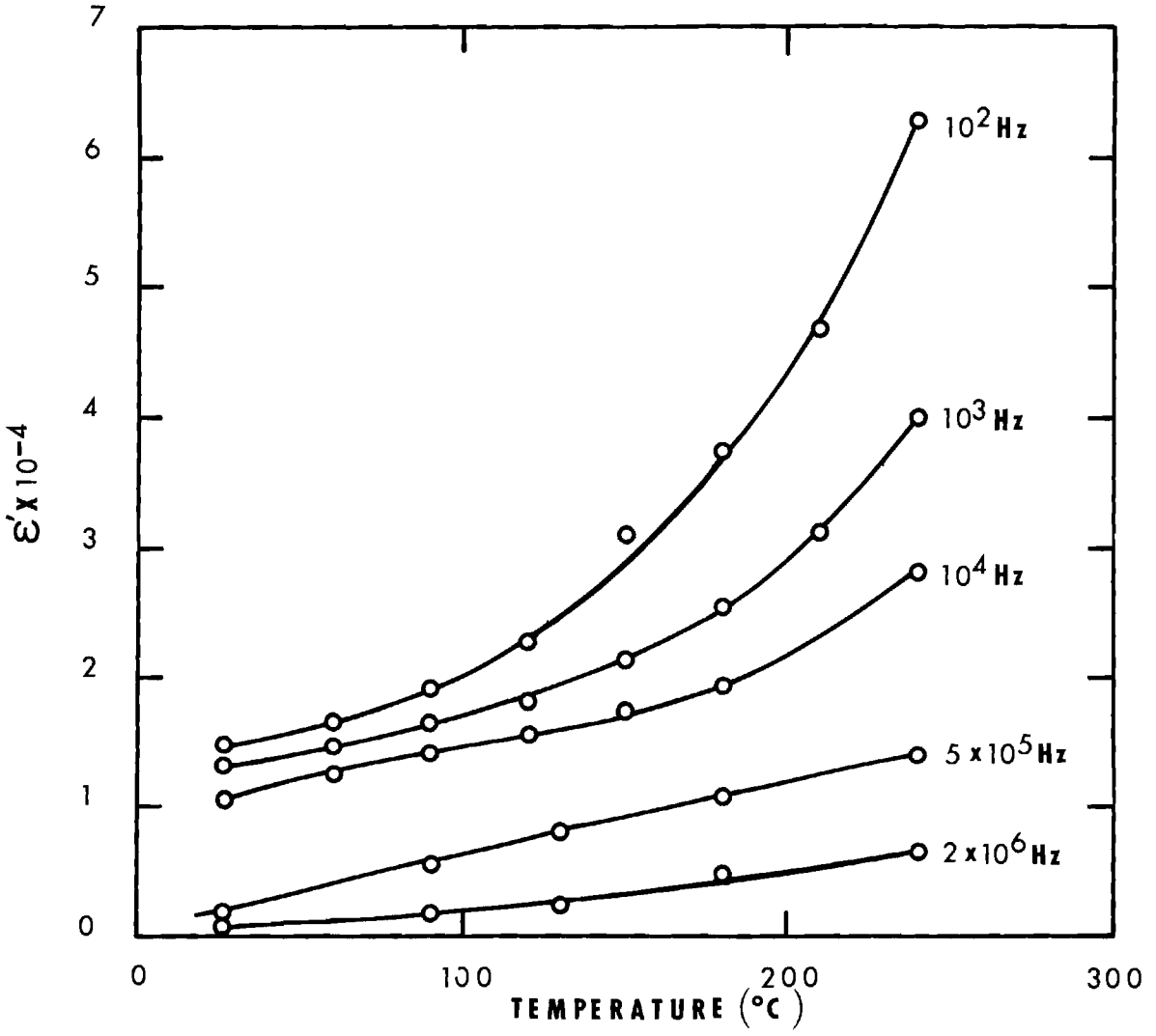

Figure 43. Temperature Dependence of the Real Part of the Dielectric Constant of ClAp at Audio Frequencies.

ε''_c was observed up to the maximum temperature used. In some cases that was 400°C.

True Monoclinic-to-Hexagonal Phase Transition

At 300°C the equilibrium position of the Cl ion is still 0.29 Å away from the z = 1/2 position. At the same time the Cl ion's mean square thermal vibrational amplitude is only 0.215 Å, insufficient to carry it past z = 1/2 into the neighboring potential well. These data suggest that the Cl ion is still, at 300°C, confined to one particular well. Linear extrapolation of the plot of δ and of $\sqrt{\overline{u_{33}^2}}$ (Figure 38) above 200°C causes them to meet in the neighborhood of 400-500°C. The implication is that at 400-500°C the root mean square vibrational amplitude $\sqrt{\overline{u_{33}^2}}$ in the $\underline{c}$ direction will become equal to δ (0.25 Å), and therefore will be sufficient to carry the ion over the potential barrier between the double well (Figure 22), producing a true hexagonal structure. This constitutes a true monoclinic-hexagonal transition. One should be able to detect the transition, because at this transition point δ should drop to zero and $\sqrt{\overline{u_{33}^2}}$ should abruptly increase with strong effects on at least some of the x-ray reflection intensities. To date no experiment testing the prediction of a true monoclinic-hexagonal transition at 400-500°C has yet been carried out.

CHAPTER VI

CONCLUSION ON CHLORAPATITE

All of the observed unusual dielectric properties in ClAp and its approximate 200°C transition have been explained on the basis of a Cl vacancy model. The salient features of this model and the transition mechanism are the following.

A defect free, stoichiometric ClAp crystal in an alternating electric field should have a low dielectric constant and dielectric loss, because all the ions are essentially "locked" into permanent positions. It is the Cl vacancy which both allows the Cl ions to shift their positions and lowers the barrier between some neighboring potential wells. The amount of shift and the number of Cl ions involved in the transport mechanism are essentially determined by the frequency of the electric field, the temperature and the type and number of defects. There are actually two distinct transport mechanisms, designated as Cl shift and as vacancy migration. The Cl shift refers to that process by which a Cl ion is able to shift between potential wells in the double well model (Figure 22). The Cl shift within segments involves the transport of a Cl ion over a distance of 0.8 Å. Only the Cl ions adjacent to a vacancy can initiate the shift. In this process the vacancies remain stationary. It is this mechanism which is in part responsible for the dielectric anisotropy and the high dielectric constant in the audio and r.f. frequency range. The apparent phase transition reported by others[39]

to occur near 200°C has been shown not to be a true monoclinic to hexagonal phase transition. Instead the changes near 200°C appear to be associated with the breaking up of the monoclinic ordering of the crystal into mimetically twinned microdomains perhaps no larger than 60 Å. The true monoclinic to hexagonal phase transition is predicted to occur in a range from 400 to 500°C, at which point it would be expected that the k_{odd} reflections and the dielectric hysteresis loops would finally cease to exist.

It has been concluded that although ClAp exhibits ferroelectric properties, as reported earlier[30], it is not a true ferroelectric because the stoichiometric structure is not involved. Rather, it has been shown that the shifting of a small fraction of Cl ions near Cl vacancies can account for the experimental D versus E hysteresis loop below and above 200°C and that the majority (e.g., 95% or more) of ClAp cells do not change to a polar space group. ClAp is therefore termed a "pseudo-ferroelectric."

Cl or Ca (or both) vacancy migration in ClAp, which is the second charge transport mechanism to be considered, appears to be operative at temperatures above 200°C in small (~ 10 V/cm) electric fields or at low temperatures ($25°C \lesssim T \lesssim 200°C$) in large (~ 10^4 V/cm) fields. Because Cl and Ca vacancies effectively constitute positive and negative charges, respectively, in the otherwise stoichiometric crystal, accumulation of vacancies near the electrodes must be considered an effective polarization which can contribute very large apparent dielectric constants and dielectric losses (also known as

space charge polarization). It is this process which may mask weak dielectric behavior. The fact that the inclusion of only 4% of F ($\frac{F}{F+Cl} = 0.04$) in the Cl column of ClAp eliminates the unusual dielectric behavior at low temperatures and low electric fields clearly suggests that it is mainly the Cl ion which is responsible for the unusual electrical phenomena.

No analysis was carried out on ClAp to OHAp converted crystals and on ClAp heated in vacuum (Cl deficient ClAp) because these crystals contained cracks which could vitiate the dielectric measurement results.

CHAPTER VII

POSSIBLE DIPOLE ORIENTATION MECHANISM IN HYDROYYAPATITE

One of the motivations for undertaking this work on ClAp was the possibility of developing results and models that might also be applicable to hydroxyapatite. We discuss here one possible extension of the ClAp result to OHAp.

OHAp is in many ways similar to ClAp. For example, the basic calcium phosphate structure is essentially the same in both materials, except that the chlorine ions are replaced by hydroxyl groups[11]. In each column the O-H dipole moments are aligned, whereas between the columns along the b axis their directions are alternately reversed (see Figure 44). As a consequence of the + - + - dipole orientation sequence, stoichiometric OHAp belongs to the same space group $P2_1/b$ as ClAp. Even more important is the fact that OHAp also undergoes an apparent phase transition around 200°C[80], again analogous to ClAp. Thus, only a small amount of thermal energy is necessary to destroy the strict intercolumn ordering information. Perhaps, a small electric field would be sufficient to reverse the hydroxyl groups. The possibility, therefore, exists for OHAp to exhibit a large complex dielectric constant and a relaxation dispersion at audio or r.f. frequencies, which would allow one to obtain the activation energy for dipole reversal.

Some papers were published on dielectric properties in OHAp by Pollard[37], Cockbain[81] and Tse[14,15], but no detailed atomic scale

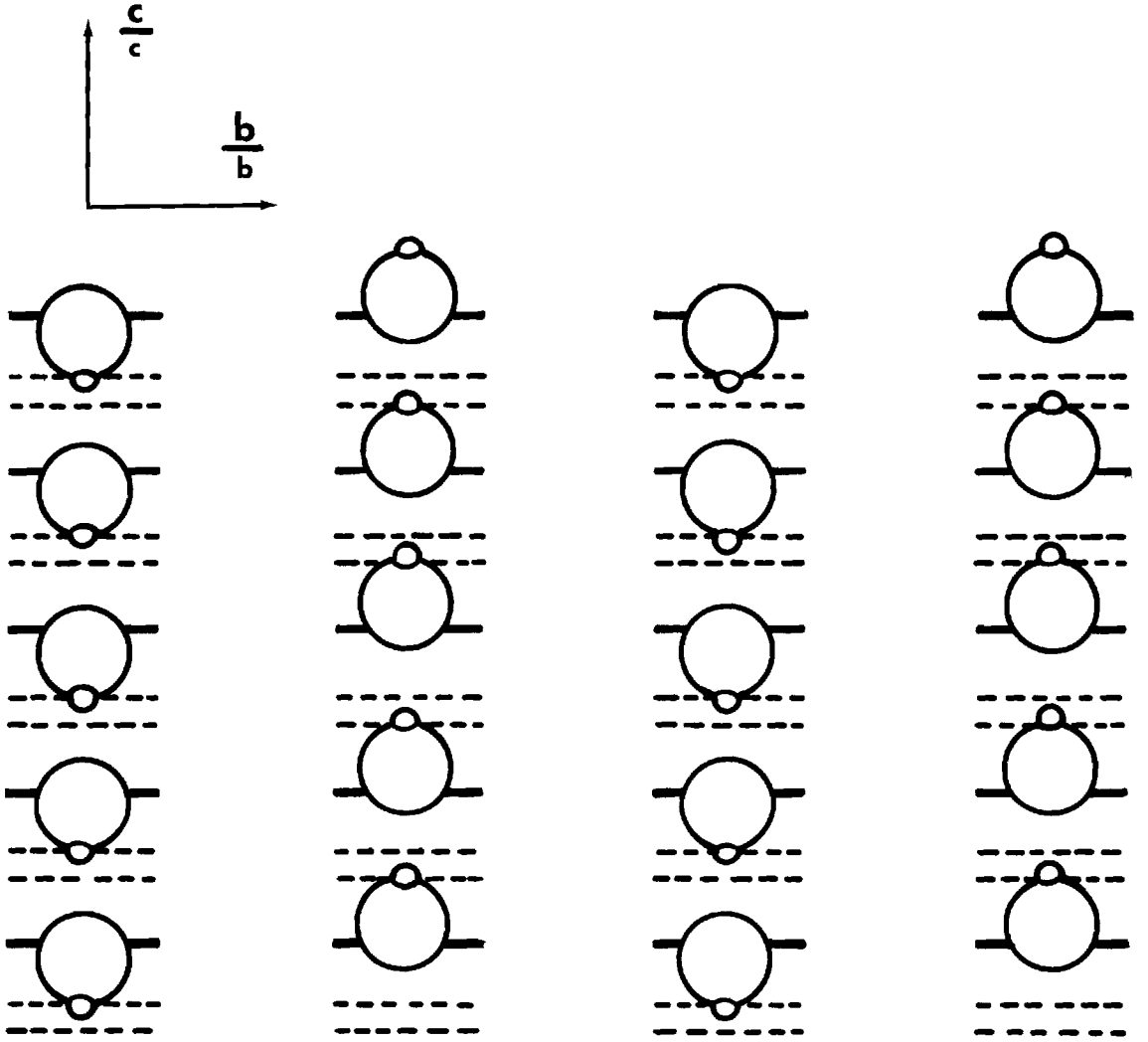

Figure 44. Arrangement of Hydroxyl Ions in OHAp. The long and short horizontal bars represent Ca and O triangles respectively. The small and large circles represent the hydrogen and hydroxyl oxygen ions respectively.

mechanism was suggested for OH reversal. This is now possible, by analogy with the ClAp case.

It is highly improbable that the H^+ ion can rotate about the O^{--} ion and transfer through the Ca^{++} ion triangle, as the $Ca^{++} - H^+$ electrostatic repulsion is probably much too large. The breaking of the O-H bond which would allow the O^{--} ion to move through the Ca triangle and bind with the next H^+ ion (the first step toward OH reversal) is also unlikely in a weak electric field, because the bond energy is very large, ~ 101.5 K cal/mole (4.4 eV). One must look, therefore, for a defect-activated reversal mechanism analogous to that in ClAp with a much smaller activation energy. There are many defects which can occur in OHAp. Some, such as the F ion or the OH vacancy can act as permanent reversal centers within a column during the growth of the crystal. However, none of these favor dipole reversal in a weak electric field once the crystal is in a solid state form. A particular promising defect, which has been observed in ClAp grown in air is the single O^{2-} impurity ion[82]. Such a defect could occur in OHAp in conjunction with an H_2O molecule to preserve charge balance. The O(1) could easily move through the Ca triangle (the Ca - O bond length in OHAp[10] is 2.38 Å which is nearly the same as the distance from a Ca nucleus to the center of the triangle, ~ 2.35 Å) and establish an H bond with the adjacent hydroxyl group. The migration distance is only 0.6 Å which is less than the Cl shift in ClAp. Once the O(1) ——— H — O(2) group is formed the H ion, enticed by an electric field, could possible shift toward

the guest O(1) ion to form the O(1)—H ——— O(2) group (see Figure 45).

If the frequency of the electric field is low, enough time may be available for the host O(2) ion to disassociate itself and migrate through the next calcium triangle. Of course, disassociation is thermally activated. The applied electric field only increases the probability of this process. This type of dipole reversal is known to occur in ice[59] and is only partly responsible for the dielectric constant of that material. On the basis of this information, however, it is wrong to conclude that the dielectric constant of OHAp is similar to ice (~ 100). On the contrary, ε' depends not only on the magnitude of the dipole moment, but also on the concentration of defects in various materials. It is also likely that the dielectric measurements of OHAp exhibit a Cole-Cole or Debye dispersion which would yield the activation energy of the OH reversal process. In fact, the transition temperatures and the shift process for CLAp and the one postulated for OHAp are so similar that one would expect similar dielectric behavior. Some experimental evidence is already available which does indeed support this suggestion. Dielectric relaxation studies in OHAp[34,29] show two dispersions. There is one near a frequency of 10^5 Hz at 300°K (as in ClAp) which could be associated with the H shift mechanism discussed previously since the activation energy corresponding to this peak was reported as 0.2 eV. The other dispersion, which occurs around 500Hz, could be associated with the OH shift or other defect shift mechanisms

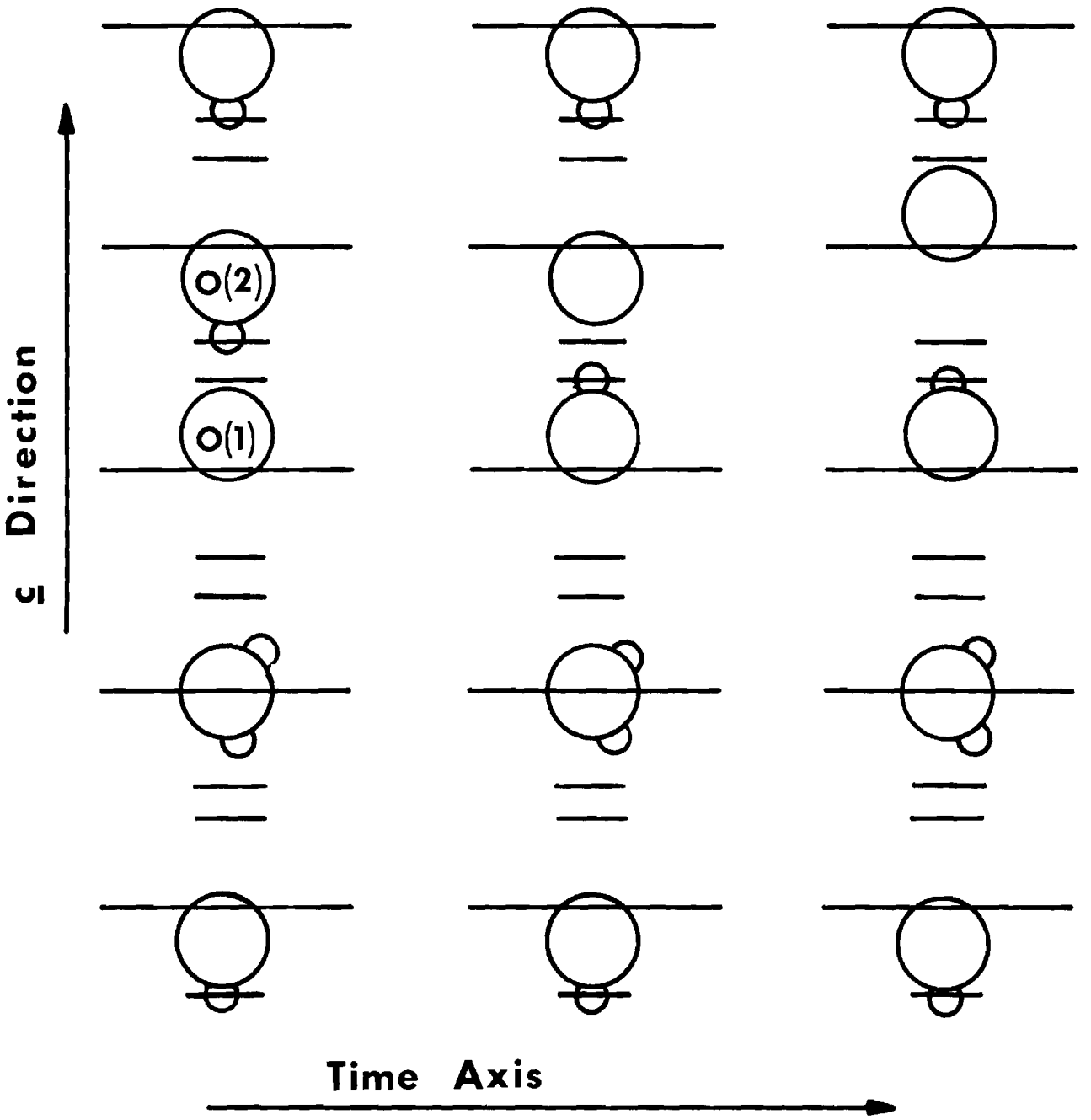

Figure 45. Possible Mechanism of Hydroxyl Dipole Reversal in OHAp. The long and short horizontal bars represent Ca and O triangles respectively. The small and large circles represent the hydrogen and hydroxyl oxygen ions respectively.

since these samples were cut from natural (Holly Springs, Georgia) OHAp. Most interesting is the experimental finding by Tang et al.[83] who investigated the motions of protons in OHAp with nuclear magnetic resonance techniques. They reported an activation energy of 0.1 eV (again this energy is essentially identical with that of ClAp) which they did not associate with the motion of whole hydroxyl ions along the columns. No other mechanism was provided as an explanation. It is now suggested that this low activation energy (0.1 eV) might be associated with the H shift, proposed in this work, between the $z = 0.44$ and $z = 0.56$ sites.

In summary, the dipole reversal process in OHAp is postulated to be similar to the mechanism in ClAp, except that the Cl shift is activated near a Cl vacancy whereas the OH reversal may be initiated by a different kind of defect. Experiments to confirm or reject the proposed mechanism will be worthwhile when suitably large and undamaged crystals of OHAp become available.

APPENDIX A

THEORY FOR LOSSY DIELECTRICS WITH DOUBLE WELLS AND IONIC CONDUCTIVITY

The purpose of this section is to discuss the fundamental theories on the behavior of solid dielectrics in electric fields. Examples of materials which fulfill the predictions of the theory are given.

Capacitor in a Static Field

Consider two parallel plates in a vacuum a distance d apart containing charges +Q and -Q respectively. The potential difference between the plates is given by

$$V = |\vec{E}_0|d \qquad d \ll \text{area of plates} \tag{A.1}$$

where E_0 is the electric field and the capacitance is

$$C_0 = \frac{Q}{V} \tag{A.2}$$

A dielectric may be thought of as a collection of positive and negative charges arranged in such a manner that the center of all the positive charges coincides with the center of all the negative charges. If the dielectric is inserted between the plates, the positive and negative charges separate to form dipoles which in turn generate an electric field E_p opposing the field E_0 (Figure 46). E_0 is reduced to E' in the dielectric and consequently V is also decreased to V'. Let the charge Q remain constant, then $C = \frac{Q}{V}$, and the static dielectric

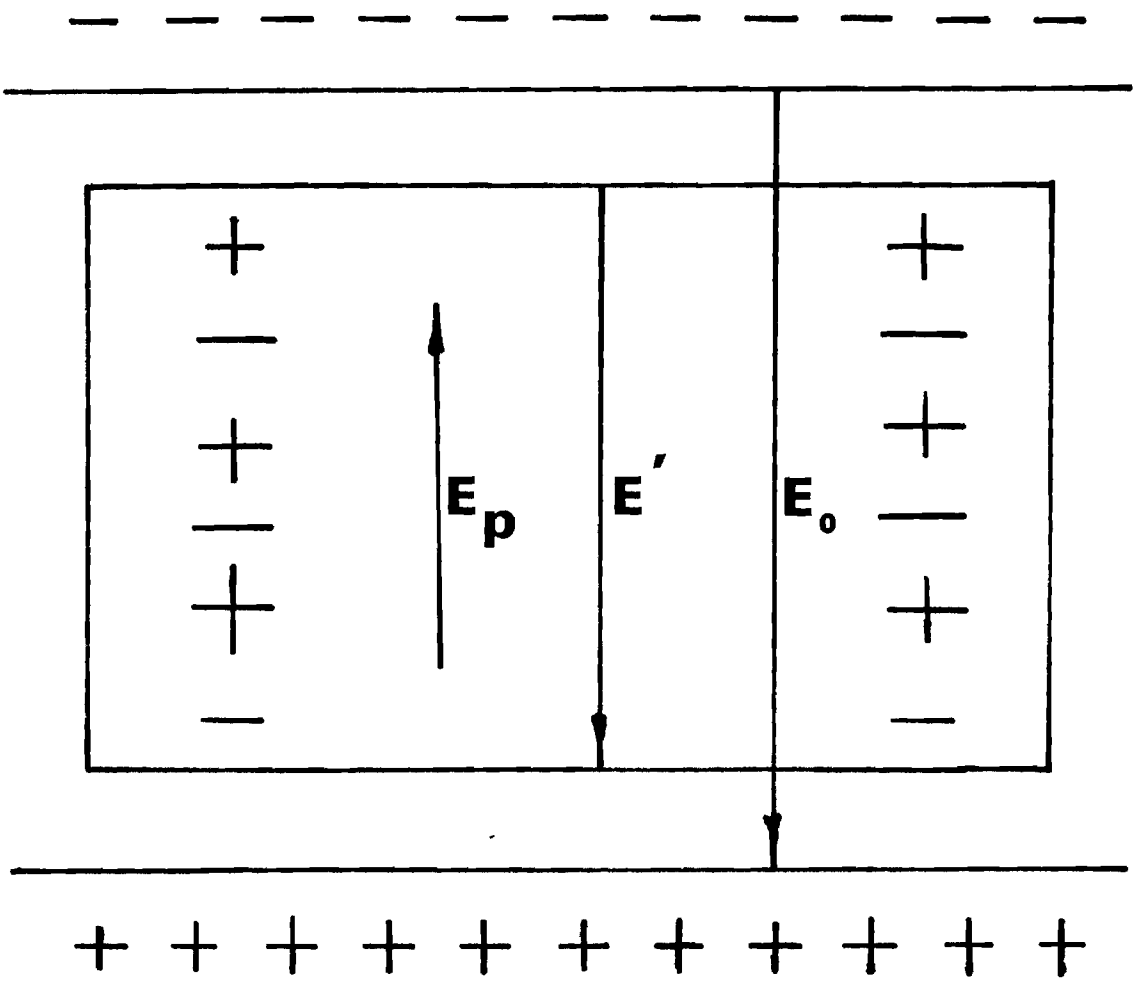

Figure 46. Electric Fields in a Capacitor Filled with a Dielectric.

constant of this ideal capacitor is

$$\varepsilon_S = \frac{C}{C_0} = \frac{V}{V'} \tag{A.3}$$

Some solid materials contain weakly bound charge carriers, which can move about within the dielectric especially at high temperatures and under the influence of strong electric fields. These charges may accumulate at structural imperfections thereby changing the potential V' and hence ε_S.

Capacitor in an Alternating Field

For sinusoidal oscillations of the free charges on the plates, the electric field E can be written as

$$\vec{E} = \vec{E}_0 \, e^{i\omega t}$$

where t is the time and $\frac{\omega}{2\pi}$ the frequency. Due to the inertia of the charge carriers the polarization $\vec{P}$ and the displacement field $\vec{D}$ will be out of phase with $\vec{E}$. The general relationship between these components in the m.k.s. system is

$$\vec{D} = \varepsilon_0 \vec{E} + \vec{P}$$

The phase shift between $\vec{E}$, $\vec{D}$ and $\vec{P}$ is mathematically expressed as

$$\vec{D}_0 \, e^{i(\omega t - \delta)} = \varepsilon_0 \vec{E}_0 \, e^{i\omega t} + \vec{P}_0 \, e^{i(\omega t - \phi)} \tag{A.4}$$

where $\vec{E}_0$, $\vec{D}_0$ and $\vec{P}_0$ are independent of time and ε_0 is a constant equal to 8.85×10^{-12} fd/m. Expansion of the left hand side of equation A.4 yields

$$\begin{aligned}
\vec{D}_0\, e^{i(\omega t - \delta)} &= \vec{D}_0 \cos(\omega t - \delta) + i\, \vec{D}_0 \sin(\omega t - \delta) \\
&= \vec{D}_0 (\cos \omega t \cos \delta + \sin \omega t \sin \delta) + \\
&\quad i\, \vec{D}_0 (\sin \omega t \cos \delta - \cos \omega t \sin \delta) \qquad (A.5) \\
&= \vec{D}_1 \cos \omega t + \vec{D}_2 \sin \omega t + i\, \vec{D}_1 \sin \omega t - i\, \vec{D}_2 \cos \omega t \\
&= \vec{D}_1\, e^{i\omega t} - i\, \vec{D}_2\, e^{i\omega t}
\end{aligned}$$

where $\vec{D}_1 = \vec{D}_0 \cos \delta$ and $\vec{D}_2 = \vec{D}_0 \sin \delta$

In general, $\vec{P}$ may be written as

$$P_i = \varepsilon_0 \sum_j X_{ij}\, E_j \qquad (A.6)$$

where the subscripts i and j represent the three coordinate directions x, y, and z and x_{ij} is the susceptibility tensor. Then $\bar{D}$ is given by

$$D_i = \varepsilon_0 \sum_j \varepsilon_{ij}\, E_j \qquad (A.7)$$

where the dielectric constant is also a tensor and given by

$$\varepsilon_{ij} = 1 + X_{ij} \qquad (A.8)$$

Three dielectric constants may now be defined

$$D_{1i} = \varepsilon_0 \sum_j \varepsilon'_{ij}\, E_{0j} \qquad (A.9)$$

$$D_{2i} = \varepsilon_0 \sum_j \varepsilon''_{ij}\, E_{0j} \qquad (A.10)$$

$$D_{1i} - i\, D_{2i} = \varepsilon_0 \sum_j \varepsilon^*_{ij}\, E_{0j} \qquad (A.11)$$

Thus

$$D_0\, e^{i(\omega t - \delta)} = (D_{1i} - i\, D_{2i})\, e^{i\omega t} = \varepsilon_0 \sum_j \varepsilon^*_{ij}\, E_{0j}\, e^{i\omega t} =$$

$$\varepsilon_0 \sum_j \varepsilon'_{ij} E_{0j} e^{i\omega t} - i\,\varepsilon_0 \sum_j \varepsilon''_{ij} E_{0j} e^{i\omega t}$$

$$\text{or} \quad \sum_j \varepsilon^*_{ij} E_{0j} = \sum_j \varepsilon'_{ij} E_{0j} - i \sum_j \varepsilon''_{ij} E_{0j} \tag{A.12}$$

Let the field E be applied along the direction z then E_x and $E_y = 0$ and dropping the subscripts equation A.12 becomes

$$\varepsilon^* = \varepsilon' - i\,\varepsilon'' \tag{A.13}$$

The new dielectric constant ε^* is complex and a function of frequency, because the phase angle ϕ will also depend on frequency. The quantities which are measured experimentally are ε', the real part of the complex dielectric constant, and the loss tangent defined as

$$\tan\delta = \frac{\vec{D}_0 \sin\delta}{\vec{D}_0 \cos\delta} = \frac{D_{2i}}{D_{1i}} = \frac{\varepsilon''}{\varepsilon'} \quad . \tag{A.14}$$

Clearly ε'' and ε' are not independent. So far, ε'' has not been identified. We suspect, however, due to its connection with the inertia of the charge carriers that ε'' is associated with the energy loss in the dielectric. To obtain an equation between ε'' and the phase angle ϕ we expand the right hand side of equation A.4.

$$\varepsilon_0 \vec{E}_0 e^{i\omega t} + \vec{P}_0 e^{i(\omega t - \phi)} = \varepsilon_0 \vec{E}_0 e^{i\omega t} + \vec{P}_0 (\cos\omega t - \phi) + i\,\vec{P}_0 \sin(\omega t - \phi)$$

Let $\vec{P}_0 \cos\phi = \vec{P}_1$ and $\vec{P}_0 \sin\phi = \vec{P}_2$

$$= \varepsilon_0 \vec{E}_0 e^{i\,t} + \vec{P}_1 (\cos\omega t + i \sin\omega t) - i\,\vec{P}_2 (\cos\omega t + i \sin\omega t)$$

$$= \varepsilon_0 \vec{E}_0 e^{i\omega t} + \vec{P}_1 e^{i\omega t} - i \vec{P}_2 e^{i\omega t} \tag{A.15}$$

Equating A.12 with A.15 when $E_0 = E_{0z}$ yields

$$\varepsilon_0 \varepsilon' \vec{E}_{0z} e^{i\omega t} - i \varepsilon_0 \varepsilon'' \vec{E}_{0z} e^{i\omega t} = \varepsilon_0 \vec{E}_{0z} e^{i\omega t} + \vec{P}_1 e^{i\omega t} - i \vec{P}_2 e^{i\omega t}$$

Equating real parts and imaginary parts yield

$$\varepsilon_0 \varepsilon' \vec{E}_{0z} = \varepsilon_0 \vec{E}_{0z} + \vec{P}_1$$

or
$$\vec{P}_0 \cos \phi = \varepsilon_0 \vec{E}_{0z} (\varepsilon' - 1) \tag{A.16}$$

and
$$\varepsilon'' \varepsilon_0 \vec{E}_{0z} = \vec{P}_0 \sin \phi \tag{A.17}$$

$$\tan \phi = \frac{\vec{P}_0 \sin \phi}{\vec{P}_0 \cos \phi} = \frac{\varepsilon'' \varepsilon_0 \vec{E}_{0z}}{\varepsilon_0 \vec{E}_{0z} (\varepsilon' - 1} = \frac{\varepsilon''}{\varepsilon' - 1} \tag{A.18}$$

and the relationship between ϕ and δ is

$$\tan \phi = \frac{\varepsilon' \tan \delta}{\varepsilon - 1} \tag{A.19}$$

The rate of energy dissipated in the dielectric is calculated as follows[84]. A change in the polarization of the dielectric leads to a displacement current i, where

$$i = \frac{d |\vec{P}|}{dt}$$

and
$$\frac{d |\vec{P}|}{dt} = - |\vec{P}_0| \sin (\omega t - \phi) \tag{A.20}$$

where
$$\vec{P} = \vec{P}_0 \cos (\omega t - \phi)$$

The rate of energy loss per unit volume due to heating is

$$H = \left|\vec{E}\right|_i = -E_{0z}\, P_0\, \omega \cos \omega t \sin (\omega t - \phi) \qquad (A.21)$$

where $\left|\vec{E}\right| = E_{0z} \cos \omega t$

using trigonometric relations

$$\cos \omega t \sin (\omega t - \phi) = \cos \omega t \sin \omega t \cos \phi - \cos 2 \omega t \sin \phi$$

$$= 1/2 \sin 2 \omega t \cos \phi - 1/2 \cos 2 \omega t \sin \phi - 1/2 \sin \phi$$

$$= 1/2 \left[\sin (2 \omega t - \phi) - \sin \phi\right]$$

So,

$$H = -1/2\, E_{0z}\, P_0\, \omega \left[\sin (2 \omega t - \phi) - \sin \phi\right]$$

Averaging over a complete cycle, yields

$$H_{av} = -1/2\, E_{0z}\, P_0\, \omega \left\{\frac{1}{t'}\int_o^{t'} \sin(2\omega\tau - \phi)\, dt\right\} + \frac{1}{2} E_{oz} P_o \omega \sin \phi \, \frac{1}{t'} \int_o^{t'} dt$$

$$H_{av} = 1/2\, E_{0z}\, P_0\, \omega \sin \phi$$

Substituting equation A.17 into equation A.22 yields

$$H_{av} = \left(1/2\right) E_{0z}^2\, \omega\, \varepsilon_0\, \varepsilon''$$

So, for any frequency ε'' determines the rate of energy loss per unit volume of the dielectric averaged over a period t'. ε'' is known as the dielectric loss factor, whereas ε' is generally referred to as the dielectric constant.

Polarization Mechanisms

There are a number of charge separation mechanisms within a dielectric which can cause the formation of dipoles. These are the electronic-, ionic displacement-, orientational or dipolar-, interfacial-, and space charge polarization. Each mechanism is associated with a characteristic signature, the dispersion curve, which occurs only in a particular frequency range. Therefore, the main topic of this section is centered around the identification of the various polarization sources. The optical region (~ 10^{15} Hz) is used as the starting point, because due to the large inertia of ionic charges only the electronic polarization can contribute significantly to ε' and ε''. Electronic charge separation refers to an elastic displacement of the electron cloud with respect to the nucleus. The motion of a particle of mass m and charge ne in an electric field $E_{0z}\, e^{i\omega t}$ is given by

$$\frac{d^2 z}{dt^2} + \Gamma\frac{dz}{dt} + \omega_0{}^2 Z = \frac{ne}{m} E_{0z} e^{i\omega t} \qquad (A.23)$$

Equation A-23 represents a damped harmonic oscillator with a sinusoidal forcing function. The solution is

$$Z(t) = \frac{(1/m)\ (ne\ E_0 e^{i\omega t})}{\omega_0{}^2 - \omega^2 + i\ \omega\ \Gamma}$$

The frequency dependence of ε' and ε'' can be obtained as follows[85]. The polarization $\vec{P}$ is given by

$$\vec{P} = N\ \vec{p}$$

where $\vec{p}$ is the dipole moment per unit volume and N is the total number

of dipoles. For an applied electric field along the z direction

$$\vec{P} = \varepsilon_0 \chi \vec{E} = N \vec{p}$$

and $$\chi^* = \frac{N \vec{p}}{\varepsilon_0 \vec{E}} = \frac{Ne\ Z(t)}{\varepsilon_0 |\vec{E}_0|\ e^{i\omega t}} = \frac{1}{m}\left[\frac{Nne^2}{\omega_0^2 - \omega^2 + i\Gamma\omega}\right]$$

but $$\varepsilon^* = \chi^* + 1$$

hence,

$$\varepsilon^* = 1 + \frac{1}{m}\left[\frac{Nne^2}{\omega_0^2 - \omega^2 + i\,\Gamma m}\right]$$

Separating the real and imaginary components yields

$$\varepsilon' = 1 + \frac{Nne}{m}^2\left[\frac{\omega_0^2 - \omega^2}{(\omega_0^2 - \omega^2) + \Gamma^2\omega^2}\right] \tag{A.24}$$

$$\varepsilon'' = \frac{Ne^2 n}{m}\left[\frac{\omega}{(\omega_0^2 - \omega^2) + \Gamma^2\omega^2}\right] \tag{A.25}$$

Equations A.24 and A.25 are plotted in Figure 47. The equation for ε' and ε'' are also valid for the ionic displacement polarization when the ions are removed a small amount from their equilibrium positions. Ionic absorption occurs at lower frequencies, the infrared region ($\sim 10^{13} - 10^{15}$ Hz). At frequencies less than 10^{12} Hz, the ionic and electronic polarization will be in phase with the electric field. The phase angle ϕ is negligible and the losses are very small! Materials which exhibit only electronic polarization satisfy the relationship $\varepsilon' \sim n^2$ for all frequencies, where n is the index of refraction. Some are shown in Table 4.

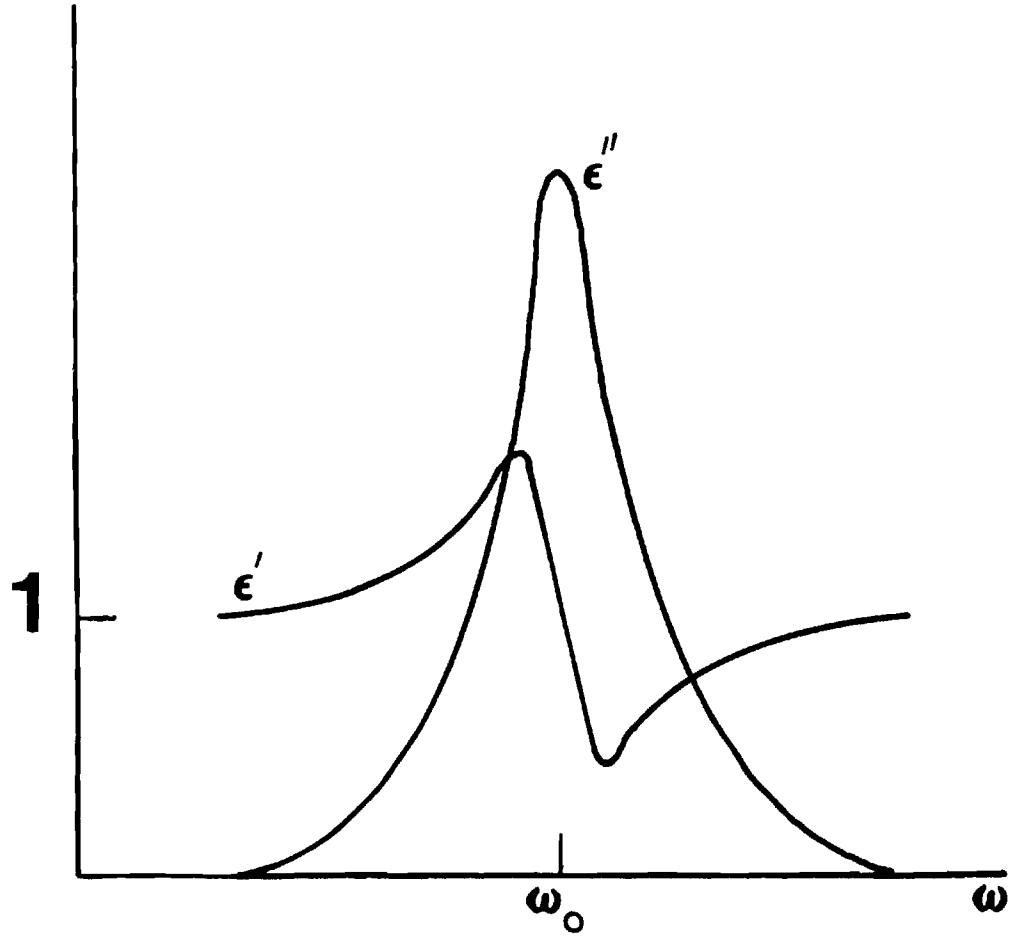

Figure 47. Behavior of Real and Imaginary Parts of Dielectric Constant Near Atomic or Electronic Resonance.

Table 4. Real Part of Dielectric Constants of Materials which Exhibit only Electronic Polarization. n is the refractive index

Material	ε' (at 25°C)	n^2	Frequency (Hz)
Naphthalene	2.50	2.50	60
Polystyrene	2.50	2.40	60
Polyethylene	2.30	2.30	60
Diamond	5.68	5.66	500

Table 5. Real Part of Dielectric Constants of Materials which Exhibit only Electronic and Ionic Polarization. n is the refractive index

Material	ε' (at 22°C)	n^2	Frequency (Hz)
NaCl	6.12	2.25	10^4
K Cl	5.03	2.30	10^4
K I	5.60	2.69	6×10^7

Materials which exhibit only electronic and ionic polarization are found in crystals with predominantly ionic bonding (see Table 5). In the case of ClAp with the field E parallel to $\bar{c}$, $\varepsilon'_{\parallel_c}$ is of the order of 10,000 (n^2 = 2.782 at 25°C) at a frequency of 10^3 Hz. Evidently, the permittivity which arises from the electronic and atomic polarization constitutes an insignificant fraction of the total dielectric constant ($\varepsilon'_{\parallel_c}$) of ClAp at that frequency. For this reason, the low frequency absorption phenomena should be dealt with in detail. Each absorption phenomena within the dielectric may be associated with an equivalent electrical circuit. For resonance absorption, the capacitor can be represented by a parallel L-C-R circuit, which is covered so well in elementary physics that any further discussion is unnecessary. The advantage of using the electrical circuit representation lies in the fact that dispersion equations for ε' and ε'' may be readily obtained through simple calculations. Some insight into the nature of the materials is gained by relating the components of the electrical model to physical phenomena within the dielectric.

The Debye and the Cole-Cole Relaxation

In the audio and radio frequency range the relaxation absorption is often the experimentally observed physical phenomenon. If the applied electric field is oscillating at sufficiently low frequencies, the polarization will be in phase and obtain its full value. With increasing frequency, the polarization amplitude will decrease and eventually will not be able to follow the field giving rise to a relaxation of the measured permittivity. The dispersion equations of

ε' and ε'' at the relaxation frequencies were developed first by Debye[86]. A different approach used by Frohlich[87] leads to both the Debye and the resonance equations. Frolich[88] derived a macroscopic equation for the complex permittivity given by

$$\varepsilon^* (\omega) = \varepsilon'_\infty + \int_0^\infty \alpha (t)\, e^{i\omega t}\, d t \qquad (A.26)$$

where ε'_∞ is the value of $\varepsilon' (\omega)$ when $\omega = \infty$. The function $\alpha (t)$ describes the decay of the polarization of a dielectric with time if the external field $\bar{E}$ is suddenly removed. $\alpha (t)$ has the constraint

$$\alpha (t) \to 0 \text{ as } \omega \to \infty$$

Let
$$\alpha (t) = \alpha (0)\, e^{-t/\tau} \qquad (A.27)$$

Where τ is a relaxation time, characteristic of the dielectric. τ may be a function of temperature, but not of time. Substitution of equation A.27 into A.26 and integrating yields

$$\varepsilon^* (\omega) = \varepsilon_\infty + \frac{\alpha (0)}{\frac{1}{\tau} - i\omega} \qquad (A.28)$$

When $\omega = 0$, $\varepsilon^* (\omega) = \varepsilon_s$. ε_s is, of course, the static dielectric constant. Therefore,

$$\varepsilon_s = \varepsilon_\infty + \tau\, [\alpha (0)]$$

or
$$\alpha (0) = \frac{\varepsilon_s - \varepsilon_\infty}{\tau} \qquad (A.29)$$

and
$$\alpha (t) = \frac{\varepsilon_s - \varepsilon_\infty}{\tau}\, e^{-t/\tau}$$

Again substituting equation A.29 into A.28 yields

$$\varepsilon^{*}(\omega) = \varepsilon' - i\,\varepsilon'' = \varepsilon_{\infty} + \frac{\varepsilon_s - \varepsilon_{\infty}}{1 - i\omega\tau} \tag{A.30}$$

The real and imaginary components are

$$\varepsilon' = \varepsilon_{\infty} + \frac{\varepsilon_s - \varepsilon_{\infty}}{1 + \omega^2 \tau^2} \tag{A.31}$$

$$\varepsilon' = \frac{(\varepsilon_s - \varepsilon_{\infty})\,\omega\,\tau}{1 + \omega^2 \tau^2} \tag{A.32}$$

Equations A.30 and A.31 are known as the Debye relaxation equations and are plotted in Figure 48. At a constant temperature, the maximum of ε'' is given by

$$\left.\frac{\partial\,\varepsilon''}{\partial\,\omega}\right|_{\omega\,=\,\omega_m} = 0$$

$$\left.\frac{\partial\,\varepsilon''}{\partial\,\omega}\right|_{\omega\,=\,\omega_m} = \frac{(\varepsilon_s - \varepsilon_{\infty})\,(\omega_m\,\tau)\,(2\omega_m\,\tau^2)}{(1 + \omega_m^2\tau^2)^2} + \frac{(\varepsilon_s - \varepsilon_{\infty})\,\tau}{(1 + \omega_m^2\,\tau^2)} = 0 \tag{A.33}$$

which yields

$$\omega_{max} = \frac{1}{\tau}$$

at a constant temperature

For atomic and electronic polarization one would expect the function α (t) to undergo damped oscillations with frequency $\frac{\omega_0}{2\pi}$ such that

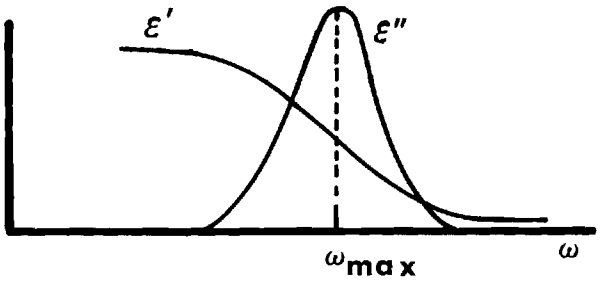

Figure 48. Behavior of Real and Imaginary Parts of Dielectric Constant for a Debye Relaxation.

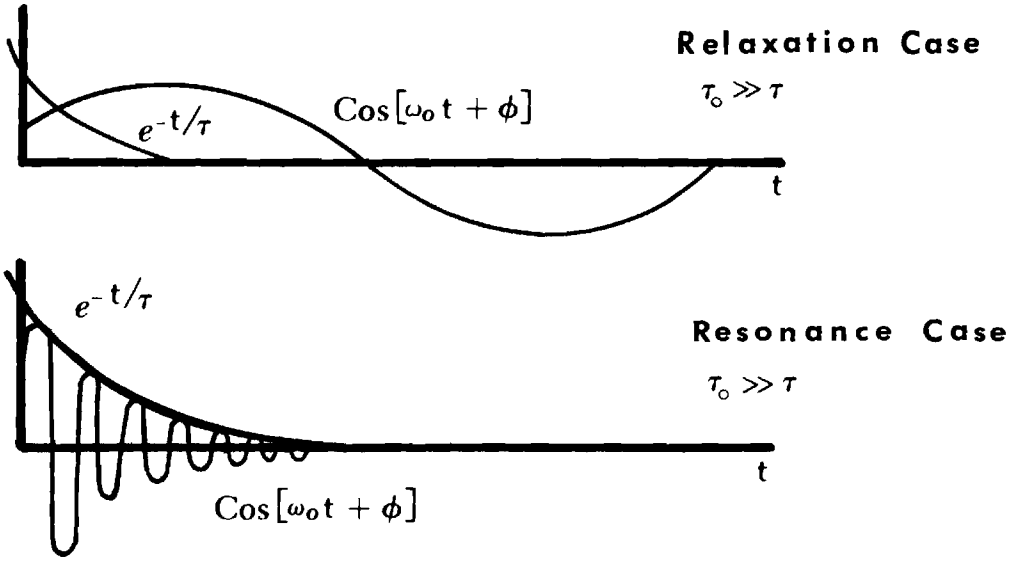

Figure 49. Comparison of Relaxation and Resonance Case. Case (a) shows the time dependence of the components of the polarization decay function $\alpha(t)$ after the applied field is turned off. Case (b) shows the resultant oscillatory behavior of the decay function.

$$\alpha\ (t) = \alpha\ (0)\ e^{-t/\tau}\ (\cos\ \omega_0\ t + \phi) \qquad (A.34)$$

where ϕ is again the phase shift between the field and the polarization. Substituting Equation A.34 into A.26 yields the resonance equations

$$\varepsilon' - \varepsilon_\infty = \frac{\varepsilon_s - \varepsilon_\infty}{2}\left[\frac{1 + \omega_0\ (\omega + \omega_0)\ \tau^2}{1 + (\omega + \omega_0)^2\ \tau^2} + \frac{1 - \omega_0\ (\omega - \omega_0)\ \tau^2}{1 + (\omega - \omega_0)^2\ \tau^2}\right] \qquad (A.35)$$

$$\varepsilon'' = \frac{\varepsilon_s - \varepsilon_\infty}{2}\left[\frac{\omega\ \tau}{1 + (\omega + \omega_0)^2\ \tau^2} + \frac{\omega\ \tau}{1 + (\omega - \omega_0)^2\ \tau^2}\right] \qquad (A.36)$$

A plot of equations A.35 and A.36 is identical with Figure 47 except here ε' is superimposed on the residual permittivity ε_∞.

Notice that the condition $\omega_0\ \tau << 1$ reduces the resonance equations to the Debye relaxation equation. $\frac{\omega_0}{2\pi}$ is the frequency of the polarization oscillation. τ is the characteristic damping constant. For example, if $\omega_0\ \tau << 1$, then $\omega_0 << \frac{1}{\tau}$ and $\tau_0 >> \tau$, i.e., the period of the polarization oscillation is greater than the damping constant τ. Figure 49 shows the function $e^{-t/\tau}$ and $\cos\ (\omega_0\ t + \phi)$ for the resonance case where $\tau_0 << \tau$ and the relaxation case where $\tau_0 >> \tau$.

Suppose a set of experimental data displays a typical relaxation curve. A possible clue to the physical mechanism underlying the relaxation absorption may be acquired if it can be shown that the data represents a Debye dispersion (several mechanisms which are characterized by a Debye dispersion will be discussed later). The easiest method is to plot ε' vs ε''. The equation for this curve is a semi-circle.

Rewriting Equation A.31 and A.32 yields

$$\left[(\varepsilon_s - \varepsilon_\infty)/(\varepsilon' - \varepsilon_\infty)\right] - 1 = \alpha^2 \tag{A.37}$$

where $\alpha = \omega \tau$

$$\varepsilon''^2/(\varepsilon_s - \varepsilon_\infty)^2 = \alpha^2/(1 + \alpha^2)^2 \tag{A.38}$$

Substitution of Equation A.37 into Equation A.38 yields

$$\frac{\varepsilon''^2}{(\varepsilon_s - \varepsilon_\infty)^2} = \frac{\left[\frac{\varepsilon_s - \varepsilon_\infty}{\varepsilon' - \varepsilon_\infty} - 1\right]}{\left[\frac{\varepsilon_s - \varepsilon_\infty}{\varepsilon' - \varepsilon_\infty}\right]^2}$$

$$\varepsilon''^2 = \left[\left(\frac{\varepsilon_s - \varepsilon_\infty}{\varepsilon' - \varepsilon_\infty}\right) - 1\right] (\varepsilon' - \varepsilon_\infty)^2$$

$$\varepsilon''^2 = (\varepsilon_s - \varepsilon_\infty)(\varepsilon' - \varepsilon_\infty) - (\varepsilon' - \varepsilon_\infty)^2$$

$$\varepsilon''^2 = \varepsilon' \varepsilon_s - \varepsilon_s \varepsilon_\infty - \varepsilon' \varepsilon_\infty - \varepsilon'^2 + 2 \varepsilon' \varepsilon_\infty$$

$$\varepsilon''^2 = -\varepsilon'^2 + \varepsilon' (\varepsilon_s + \varepsilon_\infty) - \varepsilon_s \varepsilon_\infty$$

$$\varepsilon''^2 = -\left[\varepsilon' - \frac{(\varepsilon_s + \varepsilon_\infty)}{2}\right]^2 + \left(\frac{\varepsilon_s - \varepsilon_\infty}{2}\right)^2$$

$$\left[\varepsilon' - \frac{(\varepsilon_s - \varepsilon_\infty)}{2}\right]^2 + \varepsilon''^2 = \left(\frac{\varepsilon_s - \varepsilon_\infty}{2}\right)^2 \tag{A.39}$$

This is the equation of a circle, with center at $\frac{\varepsilon_s + \varepsilon_\infty}{2}$, 0 and radius $\frac{\varepsilon_s - \varepsilon_\infty}{2}$ as shown in Figure 50. Only the semicircle where ε'' is positive is usually plotted.

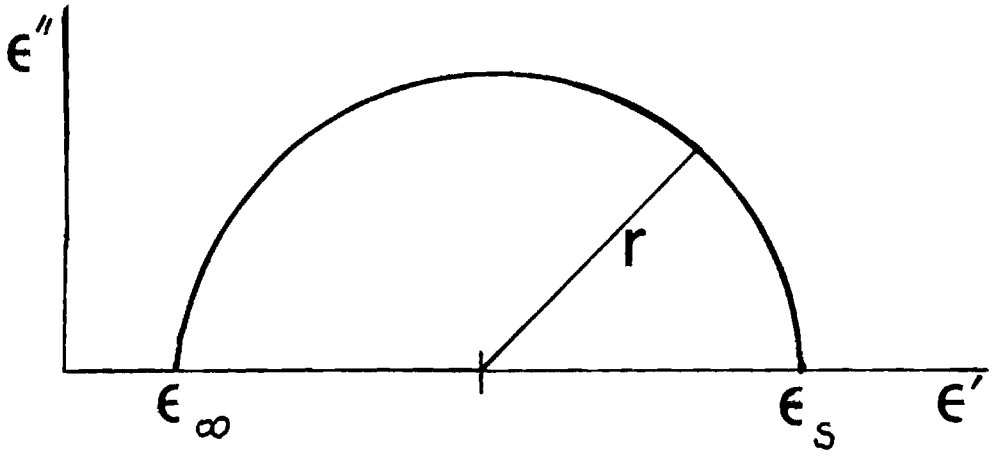

Figure 50. Complex Dielectric Constant for a Debye Relaxation. ε_∞ and ε_s are the dielectric constants at $\omega = \infty$ and $\omega = 0$ respectively. r is the radius of the circle.

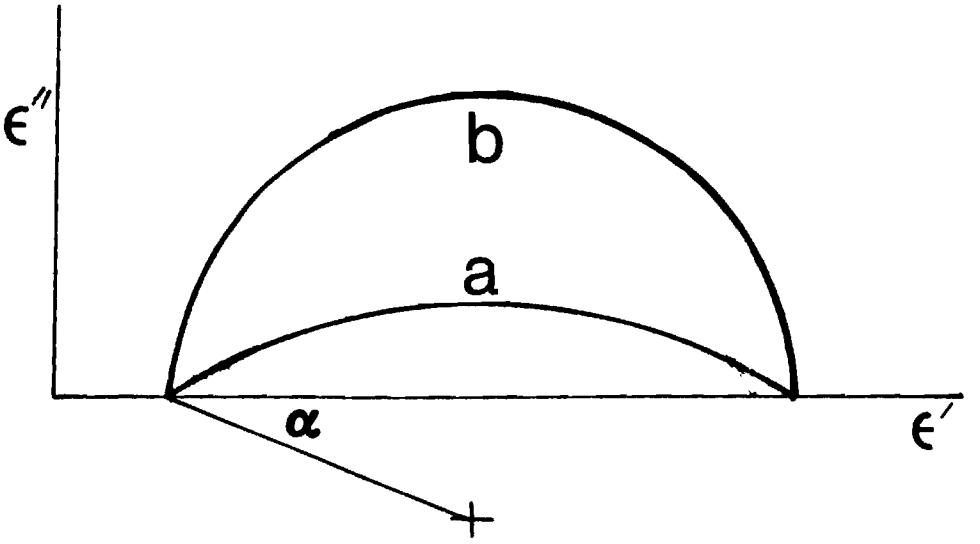

Figure 51. Comparison of Complex Dielectric Constant for a Debye Relaxation with a Single Relaxation Time and a Spread of Relaxation Times. (a), Spread of relaxation times; (b), Single relaxation time.

Many materials show broader ε'' dispersion curves and lower maximum loss which is not expected from the Debye relationships (see Figure 51). This case arises from a spread of relaxation times d τ about a characteristic relaxation time τ. K. S. Cole and R. H. Cole[60] suggested that in this situation the complex dielectric constant might follow the empirical equation

$$\varepsilon^* - \varepsilon_\infty = \frac{\varepsilon_0 - \varepsilon_\infty}{(1 + (i\omega\tau)^{1 - \alpha}} \tag{A.40}$$

where α is the spread parameter ($0 \leq \alpha \leq 1$). The separation of the real and imaginary parts yields

$$\frac{\varepsilon' - \varepsilon_\infty}{\varepsilon_s - \varepsilon_\infty} = \frac{1 + (\omega\tau)^{1 - \alpha} \sin(\pi\alpha/2)}{1 + (\omega\tau)^{2(1 - \alpha)} + 2(\omega\tau)^{1 - \alpha} \sin(\pi\alpha/2)} \tag{A.41}$$

$$\frac{\varepsilon''}{\varepsilon_s - \varepsilon_\infty} = \frac{(\omega\tau)^{1 - \alpha} \cos(\pi\alpha/2)}{1 + (\omega\tau)^{2(1 - \alpha)} + 2(\omega\tau)^{1 - \alpha} \sin(\pi\alpha/2)} \tag{A.42}$$

So far, nothing has been said about the limitations or applications of the Debye theory. One condition which must be satisfied in order to use the Debye theory is Equation A.27. Other conditions may arise depending on the chosen model. The particular model reproduced in this report was first established by Fröhlich[88] and fortunately is also applicable to ClAp.

Double Well Model

Consider a collection of particles, each of which has two possible equilibrium positions A and B, a distance d apart as shown

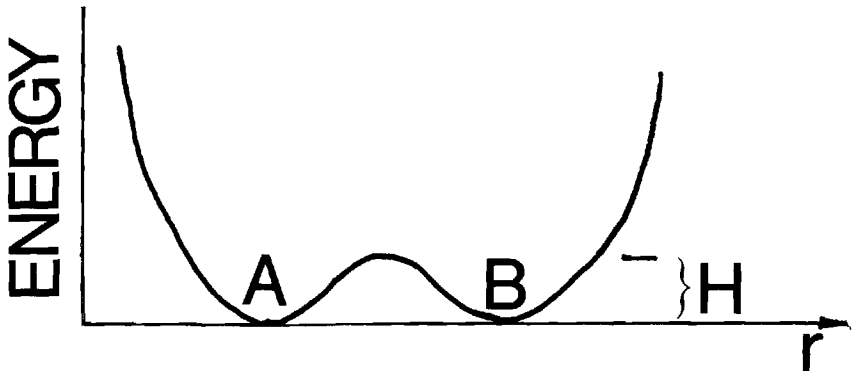

No Electric Field Applied

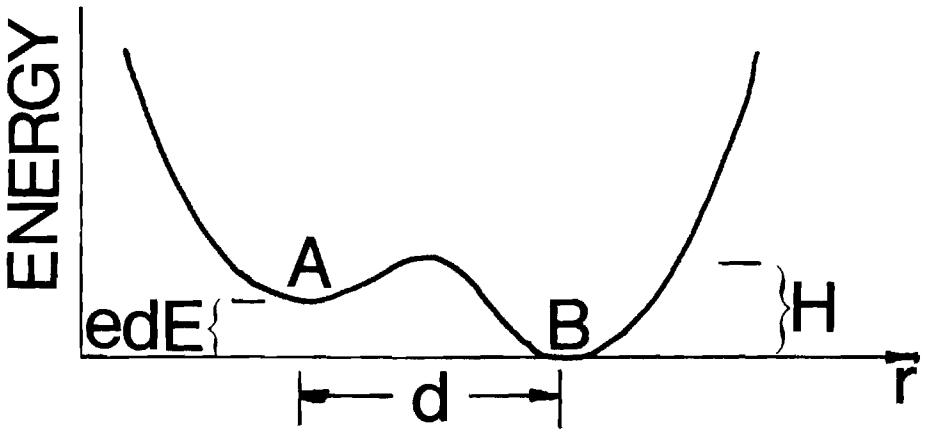

Electric Field Applied

Figure 52. Effect of Electric Field on a Double Potential Well. H represents the potential barrier; d is the distance between the wells; edE is the increase in energy due to the applied field E.

in Figure 52a. The potential barrier is given by H > KT, where KT is the thermal energy of the particle. Occasionally, due to some fluctuation in KT, the particle acquires sufficient energy to jump over the barrier into the other equilibrium position. For conditions of thermal equilibrium, the probability of finding the particle in A or B is 1/2. An electric field E applied in the direction from A to B will raise the potential well by an amount eEd as shown in Figure 52b. e is the charge of the particle, d, the distance between A and B, and E, the magnitude of the electric field. There is now a greater probability of finding the particle in position B. In the absence of the barrier the probability per second of a particle moving from A to B or B to A is $\frac{\omega_0}{2\pi}$. With the barrier present, the probability per second from A to B becomes

$$P_{AB} = \frac{\omega_0}{2\pi} e^{-(H - eEd)/KT} \tag{A.43}$$

and the probability per second from B to A is

$$P_{BA} = \frac{\omega_0}{2\pi} e^{-H/KT} \tag{A.44}$$

Let eEd << KT. A quick calculation shows this approximation to be valid. Let E ~ 300 V/cm, d ~ 1 Å, T ~ 300°K and e is the electronic charge. Then,

$$\frac{eEd}{KT} = \frac{(1.6 \times 10^{-19}\ C)\ (3 \times 10^{4}\ V/m)\ (10^{-10}\ m)}{(1.4 \times 10^{-23}\ J/deg)\ (300°K)} \simeq 10^{-4}$$

At any instant, if N_2 (t) particles are at A and N_2 (t) particles at B, a number $N_1 P_{AB}$ will move per second from A to B and N_2 (t) P_{BA} from B to A. So that

$$\frac{d N_1 (t)}{d t} = -N_1 (t) P_{AB} + N_2 (t) P_{BA} \tag{A.45}$$

$$\frac{d N_2 (t)}{d t} = -N_2 (t) P_{BA} + N_1 (t) P_{AB} \tag{A.46}$$

Subtracting equation A.46 from A.45 yields

$$\frac{d (N_2 - N_1)}{d t} = -N_2 P_{BA} + N_1 P_{AB} + N_1 P_{AB} - N_2 P_{BA} \tag{A.47}$$

In order to solve equation A.47 we must have the variable $N_2 - N_1$ on the right hand side. By adding to and subtracting from the right hand side the two terms $P_{AB} N_2$ and $P_{BA} N_1$ we obtain

$$\frac{d (N_2 - N_1)}{d t} = -(P_{AB} + P_{BA}) (N_2 - N_1) + (P_{AB} - P_{BA}) (N_2 + N_1)$$

But

$$P_{AB} + P_{BA} = P_{BA} (1 + eEd/KT) + P_{BA}$$

$$= P_{BA} (2 + eEd/KT)$$

and because

$$eEd/KT << 1$$

$$P_{AB} + P_{BA} \simeq 2 P_{BA}$$

and

$$P_{AB} - P_{BA} = 0$$

By substitution

$$\frac{d}{dt} (N_2 - N_1) = -2 P_{BA} (N_2 - N_1)$$

Assume that the field is removed at $t = 0$ and at $t \leq 0$, $N_2 - N_1 = N$

The solution is

$$N_2 - N_1 = N e^{-2 P_{BA} t}$$

The polarization is given by

$$P = (N_2 - N_1) e d = Ned e^{-2 P_{BA} t} \qquad (A.48)$$

and decays according to

$$P = P_0 (e^{-t/\tau}) \qquad (A.49)$$

where $P_0 = Ned$

and $$\tau = \frac{1}{2 P_{BA}}$$

or $$\tau = \frac{\pi}{\omega_0} e^{H/KT}$$

or $$\tau = \tau_0 e^{H/KT} \qquad (A.50)$$

where τ_0 is the mean period of vibration of the particle in the absence of the barrier H. The model discussed above will lead to the Debye

equations for ε' and ε'', because the requirement $\alpha(t) = (0)\, e^{-t/\tau}$ (after the field is turned off) is satisfied.

There is another requirement. The particles must be noninteracting. Any interaction between the particles would mean that the transition probabilities depend on the positions of the neighbors, and equation A.47 could not be solved with exponential functions.

Conductivity

The effects of a finite d.c. conductivity on the dielectric loss of a real capacitor can best be illustrated by considering the equivalent electrical model of a pure capacitor in parallel with a pure resistor. The admittance, Y, of this combination is given by

$$Y = i\,\omega\, C_p + \frac{1}{R_p}$$

The admittance of an equivalent capacitor, C_0, which is filled with a dielectric having a complex dielectric constant, is given by

$$Y_0 = i\,(\varepsilon' - i\,\varepsilon'')\,\omega\, C_0$$

Setting $Y = Y_0$ and equating the real and imaginary components yields

$$\varepsilon' = \frac{C_p}{C_0}$$

and

$$\varepsilon'' = \frac{1}{\omega\, R_p\, C_0}$$

If the area of the capacitor C_0 is represented as A and its thickness as d, then the resistivity, ρ, is

$$\rho = \frac{\varepsilon_0 R A}{d}$$

and C_0 is given by

$$C_0 = \frac{\varepsilon_0 A}{d}$$

Hence, the dielectric loss becomes

$$\varepsilon'' = \frac{\sigma}{\omega \varepsilon_0}$$

where the conductivity, σ is the reciprocal of ρ.

In this model σ increases the dielectric loss. However, real capacitors, which do exhibit a large conductivity, also show an apparent increase in the dielectric constant. The observed experimental increase in ε' due to d.c. conductivity can usually be explained on the basis that not all charge carriers are neutralized, but some accumulate near the electrodes to form a space charge. The equivalent electrical circuit for this configuration is represented in Figure 53, where C_1 and R_1 denote the space charge capacitance and resistance, respectively and C_2 and R_2 represent the dielectric itself. d_1 is an effective thickness associated with C_1 and d_2 is the thickness of the dielectric. The admittance is given by

$$Y = \frac{Y_1 Y_2}{Y_1 + Y_2}$$

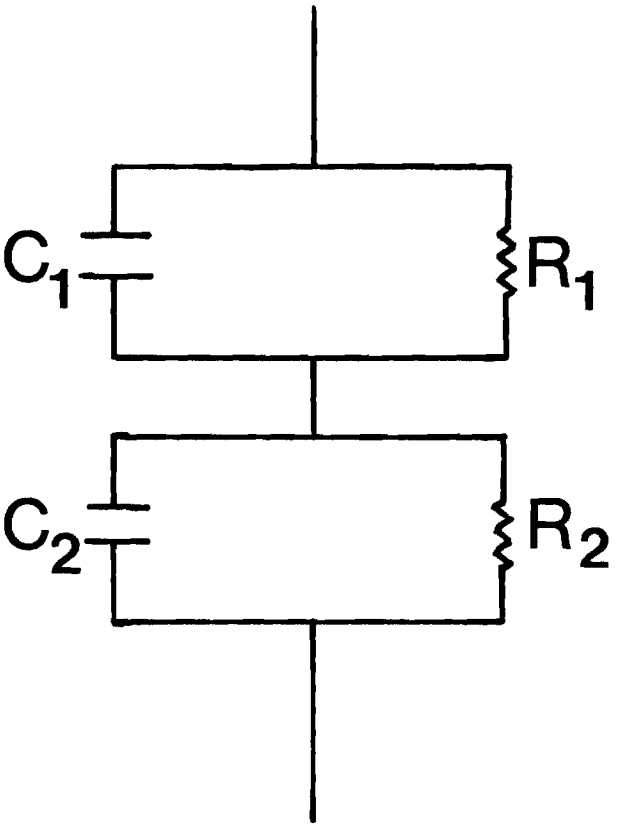

Figure 53. Equivalent Electric Circuit for a Two-Layer Dielectric.

$$Y = \frac{\frac{1}{R_1} + i\omega C_1 \quad \frac{1}{R_2} + i\omega C_2}{\frac{1}{R_1} + \frac{1}{R_2} + i\omega (C_1 + C_2)} = \frac{1}{R_1 + R_2} \frac{(1 + i\omega \tau_1)(1 + i\omega \tau_2)}{1 + i\omega \tau}$$

where

$$\tau_1 = C_1 R_1, \quad \tau_2 = C_2 R_2$$

It can be shown that the circuit acts as a capacitor filled with a homogeneous dielectric with a relaxation time τ given by

$$\tau = \frac{R_2 \tau_1 + R_1 \tau_2}{R_1 + R_2}$$

Thus,

$$Y = \frac{1}{R_1 + R_2}$$

$$\left[\frac{1 - \omega^2 \tau_1 \tau_2 + \omega^2 \tau (\tau_1 + \tau_2) - i\omega \tau (1 - \omega^2 \tau_1 \tau_2) + i\omega (\tau_1 + \tau_2)}{1 + \omega^2 \tau^2} \right]$$

The admittance of an equivalent condensor is

$$Y_0 = i\omega (\varepsilon' - i\varepsilon'') C_0$$

Equating Y with Y_0 and equating the real and imaginary terms yields

$$\varepsilon'_{\text{apparent}} = \frac{1}{C_0 (R_1 + R_2)} \left[\frac{\tau_1 + \tau_2 - \tau + \omega^2 \tau_1 \tau_2 \tau}{1 + \omega^2 \tau^2} \right] \quad \text{(A.51)}$$

$$\varepsilon''_{apparent} = \frac{1}{C_0 (R_1 + R_2)} \quad \frac{1 - \omega^2 \tau_1 \tau_2 + \omega^2 \tau (\tau_1 + \tau_2)}{1 + \omega^2 \tau^2} \qquad (A.52)$$

$$\text{At } \omega = 0,\ \varepsilon' = \varepsilon_s = (\tau_1 + \tau_2 - \tau)/[C_0 (R_1 + R_2)] \qquad (A.53)$$

$$\text{At } \omega = \infty \quad \varepsilon' = \varepsilon_\infty = \frac{\tau_1 \tau_2}{\tau} [1/[C_0 (R_1 + R_2)]] \qquad (A.54)$$

Substituting A.53 and A.54 into A.51 and A.52 yields

$$\varepsilon'_{apparent} = \varepsilon_\infty + \frac{\varepsilon_s - \varepsilon_\infty}{1 + \omega^2 \tau^2}$$

and

$$\varepsilon''_{apparent} = \frac{1}{\omega C_0 (R_1 + R_2)} + \frac{(\varepsilon_s - \varepsilon_\infty)(\omega \tau)}{1 + \omega^2 \tau^2}$$

Note that ε_∞ and ε_s are functions of the conductivity. Table 6 shows $\varepsilon'_{apparent}$ and $\varepsilon''_{apparent}$ at 1000 Hz as a function of ρ_1 and ρ_2. Resistances R_1 and R_2 were replaced by resistivities ρ_1 and ρ_2. It is to be noted that only if C_1, R_1, C_2 and R_2 are independent of the frequency will the two layer model result in a Debye dispersion.

Although the space charge model predicts a Debye dispersion and a dielectric constant and loss similar to that observed for ClAp it is not the correct model for this material. For example, it can not explain the drastic reduction in ε' and ε'' when some of the Cl ions are replaced by F nor the observed hysteresis effects.

Clearly, the answer to this problem lies in the investigation of detailed atomic scale mechanisms, not equivalent electrical models of the dielectric.

Table 6. Dielectric Constant and Loss Tangent for the Two-Layer Dielectric as a Function of Dielectric Thicknesses. ρ_1, ρ_2, d_1, and d_2 are the resistivities and thicknesses of dielectric 1 and 2, respectively. The dielectric constants ε_1 and ε_2 were arbitrarily set equal to 1.

ρ_1 (Ω-cm)	ρ_2 (Ω-cm)	d_1/d_2	$\varepsilon'_{apparent}$	$\varepsilon''_{apparent}$	tan δ
10^{14}	10^{14}	1	1	0.00011	0.00011
10^{14}	10^{14}	10^{-5}	1	0.00011	0.00011
10^{14}	10^{5}	1	2.0	0.0002	0.00012
10^{14}	10^{5}	10^{-5}	56072.4	49630	0.885
10^{5}	10^{14}	1	2.0	0.0002	0.0012
10^{5}	10^{14}	10^{-5}	0.999	0.0001	0.0001
10^{5}	10^{5}	1	1.0	112994	112994
10^{5}	10^{5}	10^{-5}	0.999	112994	112994

APPENDIX B

DATA CORRECTIONS

The Interdependence of Series and Parallel Capacitance

With the GR 1650 B bridge measurements can be made by using either the series or parallel bridge. The difference between the two lies in the representation of the sample in terms of electrical components (see Figure 54). The question which bridge should be used is determined by the operating frequency and the properties of the sample. If the series bridge is required, the series capacitances C_s must then be converted to parallel capacitances C_p because, the ideal capacitor C_p in parallel with an ideal resistor R_p is the model normally used to represent a lossy capacitor. The relationship is derived as follows. The impedance diagrams for the parallel and series components are shown in Figure 55. The impedance for the series components is

$$Z_s = R_s - iX_s$$

and the impedance for the parallel components is given by

$$Z_p = \frac{X_p R_p}{X_p + iR_p} = \frac{X_p^2 R_p}{X_p^2 + R_p^2} - \frac{iX_p R_p^2}{X_p^2 + R_p^2}$$

In order to find the relationship between C_p and C_s and R_p and R_s we set

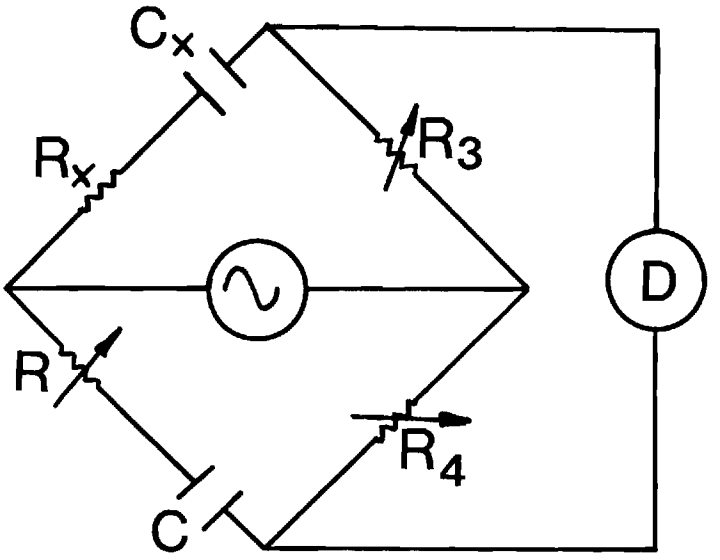

SERIES COMBINATION

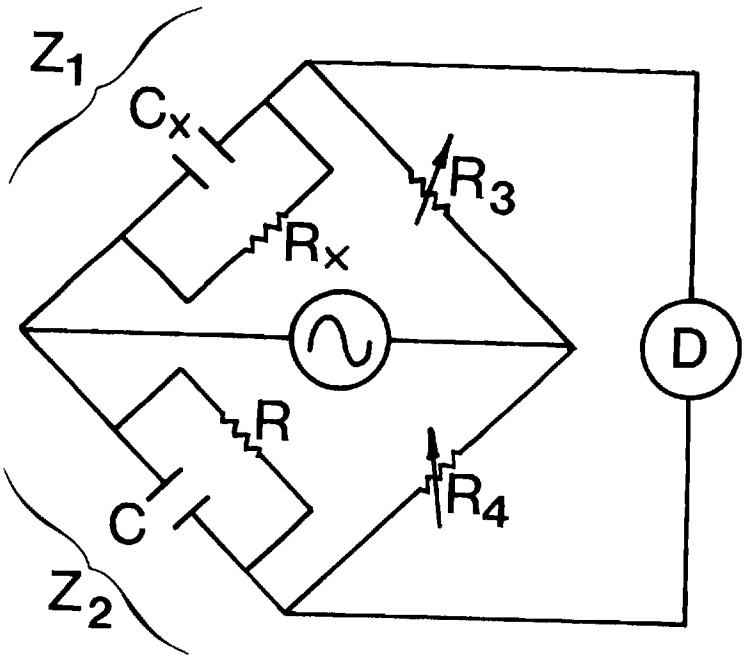

PARALLEL COMBINATION

Figure 54. Schematic Diagrams of a Series and of a Parallel Capacitance Bridge.

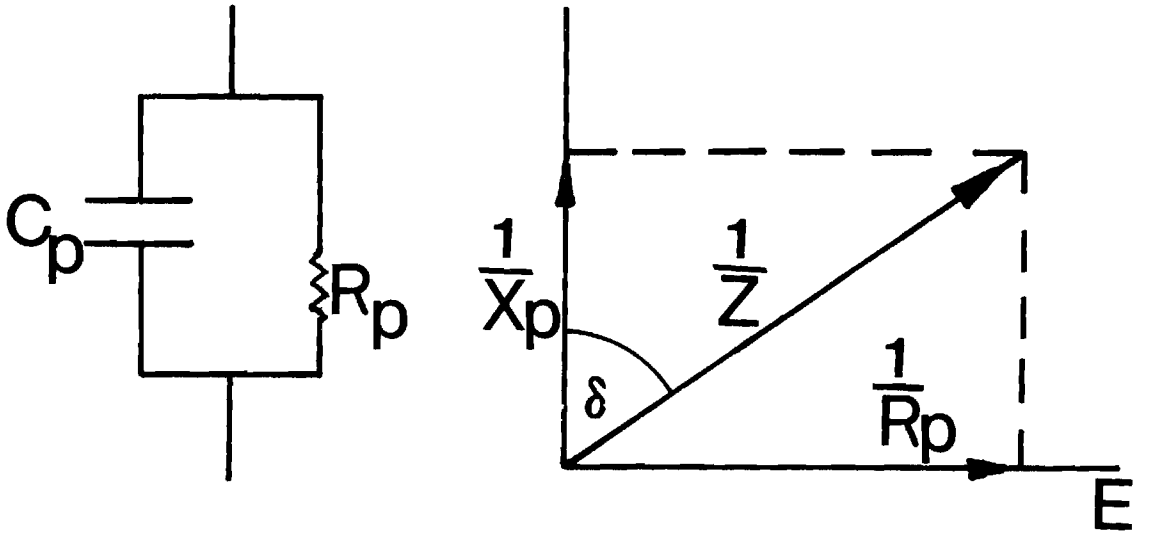

PARALLEL COMBINATION

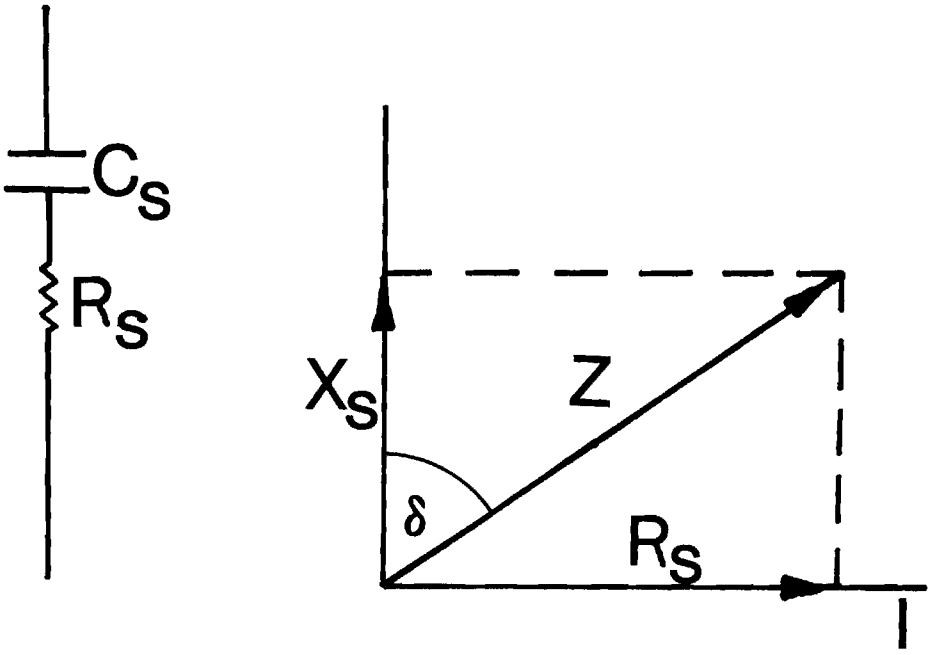

SERIES COMBINATION

Figure 55. Impedance Diagram for a Series or Parallel C, R Combination.

$$Z_s = Z_p \tag{B.1}$$

or

$$R_s - iX_s = \frac{X_p^2 R_p}{X_p^2 + R_p^2} - \frac{iX_p R_p^2}{X_p^2 + R_p^2}$$

Equating the real and imaginary components gives

$$R_s = \frac{X_p^2 R_p}{X_p^2 + R_p^2} \tag{B.2}$$

and

$$X_s = \frac{X_p R_p^2}{X_p^2 + R_p^2} \tag{B.3}$$

It is preferrable to replace the reactances and resistances with capacitances and tan δ, because the latter quantities are measured directly with an audio bridge. Tan δ for the parallel components is given by

$$\tan \delta = \frac{X_p}{R_p} \tag{B.4}$$

when $R_p \to \infty$, tan $\delta \to 0$ as it should be for a pure capacitance given by

$$C = \frac{1}{\omega X} \tag{B.5}$$

Hence, using equation B.4 in B.2 and B.3 yields

$$R_s = \frac{R_p}{1 + \frac{1}{\tan \delta}^2} \tag{B.6}$$

and

$$X_s = \frac{X_p}{1 + \tan \delta^2}$$

and using equation B.5 gives

$$C_s = C_p \ (1 + \tan \delta^2) \qquad (B.7)$$

Of course, the tan δ used in equation B.2 and B.3 (which temporarily will be referred to as tan δ_p) was obtained from the parallel components. However, the measured values sometimes yield tan δ_s by treating the sample as series components. Therefore, we will now prove that

$$\tan \delta_p = \tan \delta_s$$

tan δ_s is given by

$$\tan \delta_s = \frac{R_s}{X_s}$$

which is correct, because as $R_s \to 0$, tan $\delta \to 0$. Substituting equation B.6 and $X_s = X_p/(1 + \tan \delta_p^2)$ and using eq. B.4 gives

$$\tan \delta_s = \left(\frac{R_p}{1 + \frac{1}{\tan \delta_p^2}}\right) \Bigg/ \left(\frac{X_p}{1 + \tan \delta_p^2}\right)$$

or

$$\tan \delta_s = \tan \delta_p$$

Influence of Stray Capacitance and Resistance on Audio Bridge Measurements

The next step is to determine how stray resistances and capacitances, which are always present in any actual circuit, can influence the bridge balancing mechanism. Figure 56 represents the electrical schematic of the C_p bridge-lead-cell system. The various symbols are defined as follows:

C_x and R_x - the unknown capacitance and shunt resistance

C_s and R_s - the stray capacitance and stray resistance in parallel with the unknown

C_L and R_L - the stray capacitance and resistance from the low terminal to ground

C_H and R_H - the stray capacitance and resistance from the high terminal to ground

Z_3 - a discret variable resistance determining the capacitance range (pf, μf x 1, μf x 10, etc. - has the corresponding values 1M, 100K, 10K, etc.)

Z_4 - a continuous variable resistor (0-10K) determining the capacitance labeled as the CGRL dial

C - A fixed 0.1 μf capacitor

R - a (0-16K) resistor determining the tan δ, labeled as the DQ dial.

When a bridge is balanced no current will flow between the low terminal and ground. Therefore, no errors are caused by stray components from the low terminal to ground. To develop the mathematical correction terms for the above system we must start with the balancing equation of the simple C_p bridge (Figure 54b) with no stray components, because this formula is needed for the more complex case.

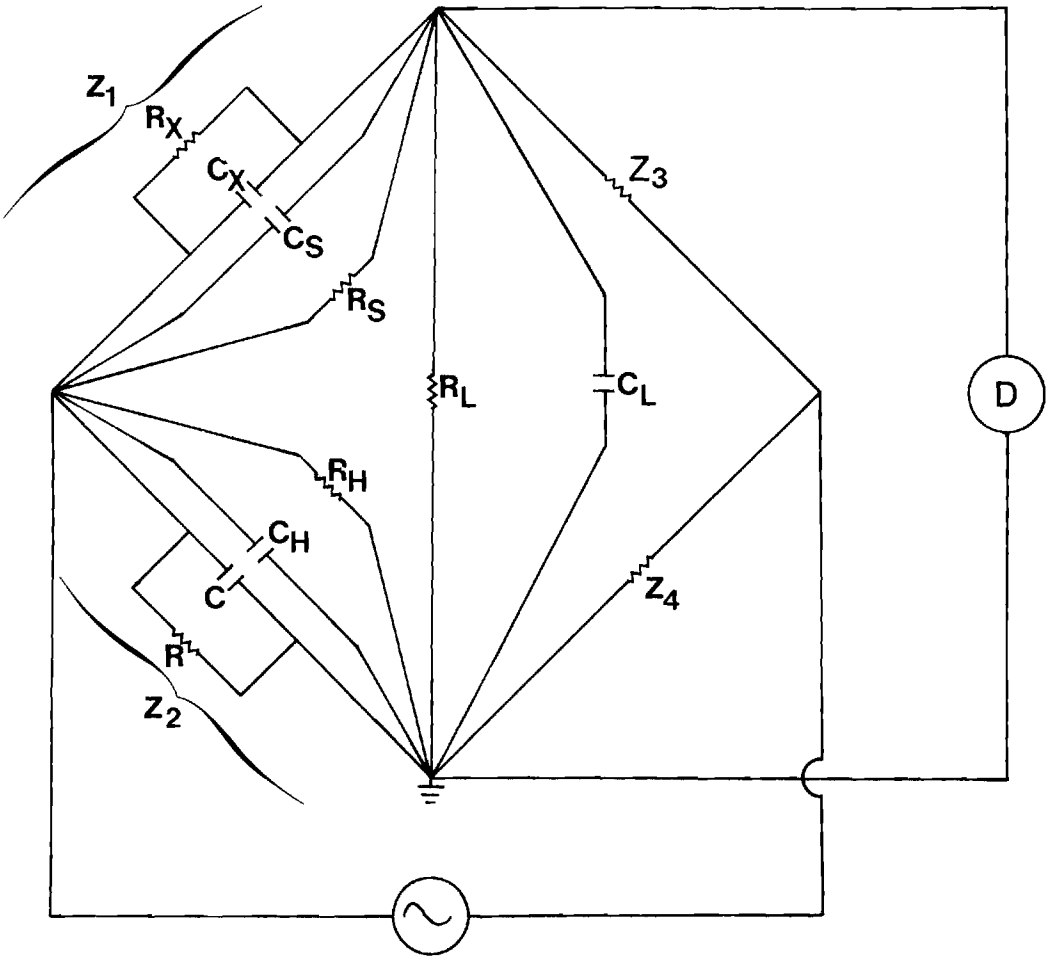

Figure 56. Schematic Diagram of a Parallel Capacitance Bridge-Lead-Cell System at Audio Frequencies. R_X and C_X are the sample's resistance and capacitance. R_S and C_S are a stray resistance and capacitance, in parallel with the sample. R_H and C_H are the stray resistance and capacitance from the high terminal to ground. R_L and C_L are the stray resistance and capacitance from the low terminal to ground. Z_3 and Z_4 are resistors used to balance the sample's capacitance C_X. C and R represent a capacitor and resistor used to balance R_X.

When balanced, the impedance equation is

$$\frac{Z_1}{Z_2} = \frac{Z_3}{Z_4} = \frac{R_3}{R_4}$$

where

$$Z_1 = \frac{1}{\frac{1}{iX_x} + \frac{1}{R_x}}$$

$$Z_2 = \frac{1}{\frac{1}{iX_c} + \frac{1}{R}}$$

or

$$\left(\frac{1}{iX_c} + \frac{1}{R}\right) R_4 = \left(\frac{1}{iX_x} + \frac{1}{R_x}\right) R_3$$

Equating the real and imaginary components yields

$$\frac{R_4}{R} = \frac{R_3}{R_x} \qquad \text{and} \qquad \frac{R_4}{X_c} = \frac{R_3}{X_x}$$

which can be written

$$C\,R_4 = C_x\,R_3 \qquad \text{and} \qquad CR = C_x\,R_x \tag{B.8}$$

where

$$C = \frac{1}{\omega X_x}$$

The same outline above is followed to solve the complex cases. For the C_p bridge (refer to Figure 56) the balance equation is

$$\left(\frac{1}{iX_c} + \frac{1}{R_{err}} + \frac{1}{iX_H} + \frac{1}{R_H}\right) R_{4err} = \left(\frac{1}{iX_x} + \frac{1}{R_x} + \frac{1}{iX_s} + \frac{1}{R_s}\right) R_3 \qquad (B.9)$$

where

$$\frac{1}{Z_1} = \frac{1}{iX_x} + \frac{1}{R_x} + \frac{1}{iX_s} + \frac{1}{R_s} \quad \text{and} \quad \frac{1}{Z_2} = \frac{1}{iX_c} + \frac{1}{R_{err}} + \frac{1}{iX_s} + \frac{1}{R_s} \qquad (B.10)$$

where

X_x is the reactance of C_x, X_s is the reactance of C_s, X_H is the reactance of C_H and X_c is the reactance of C. We assume that the errors are small so that R_3 is not affected. Equating imaginary components yields

$$\frac{R_3}{\omega X_x} + \frac{R_3}{\omega X_s} = \frac{R_{4err}}{\omega X_c} + \frac{R_{4err}}{\omega X_H} \qquad (B.11)$$

R_4 and C_x contain errors. Therefore, the notation "R_{4err}" and "C_{xerr}" were chosen. Variables with the subscript "C_{corr}" denote corrected values.

$$C_x R_3 + C_s R_3 = C R_{4err} + C_H R_{4err} \qquad (B.12)$$

where

$$C = \frac{1}{\omega X_c} \quad , \quad C_x = \frac{1}{\omega X_x} \quad , \quad \text{etc.}$$

using equation B.8

$$R_{4err} = \frac{R_3}{C} \; C_{xerr}$$

equation B.12 becomes

$$C_x \, R_3 + C_s \, R_3 = \left(\frac{C \, R_3}{C}\right) C_{xerr} + \left(\frac{C_H \, R_3}{C}\right) C_{xerr} \qquad (B.13)$$

or

$$C_x = C_{xerr} \left[1 + \frac{C_H}{C}\right] - C_s \qquad (B.14)$$

C_{xerr} is the measured capacitance value. Equating the real components yields

$$\frac{R_3}{R_x} + \frac{R_3}{R_s} = \frac{R_{4err}}{R_{err}} + \frac{R_{4err}}{R_4} \qquad (B.15)$$

To eliminate R_{4err} and R_3 in B.15 we use equation B.11.

$$\frac{\frac{1}{R_{err}} + \frac{1}{R_H}}{\frac{1}{R_x} + \frac{1}{R_s}} = \frac{\frac{1}{X_c} + \frac{1}{X_H}}{\frac{1}{X_x} + \frac{1}{X_s}} \qquad (B.16)$$

Multiplying by $\frac{1}{\omega}$ yields

$$\left[\frac{1}{\omega R_x} + \frac{1}{\omega R_s}\right] \left[C + C_H\right] = \left[C_x + C_s\right] \left[\frac{1}{\omega R_{err}} + \frac{1}{\omega R_H}\right] \qquad (B.17)$$

For the C_p circuit $\tan \delta_{err} = \frac{1}{\omega C R_{err}}$ and $\tan \delta_{corr} = \frac{X_x}{R_x}$. Therefore,

B.17 becomes

$$\left[C_x \tan \delta_{corr} + \frac{1}{\omega R_s}\right]\left[C + C_H\right] = \left[C_x + C_s\right]\left[C \tan \delta_{err} + \frac{1}{\omega R_H}\right] \quad \text{(B.18)}$$

where $\tan \delta_{err}$ is the measured value. Substituting equation B.14 into B.18 yields

$$\left[C_{xerr}\left(1 + \frac{C_H}{C}\right) - C_s\right]\tan \delta_{corr} + \frac{1}{R_s} = \frac{\left[C_{xerr}\left(1 + \frac{C_H}{C}\right) C\right]}{\left[C\left(1 + \frac{C_H}{C}\right)\right]}\left[\tan \delta_{err} + \frac{1}{\omega C R_H}\right] \quad \text{(B.19)}$$

Finally, solving for $\tan \delta_{corr}$, the correct value, yields

$$\tan \delta_{corr} = \left\{\frac{1}{C_{xerr}\left(1 + \frac{C_H}{C}\right) - C_s}\right\}\left[C_{xerr}\left(\tan \delta_{err} + \frac{1}{\omega C R_H}\right) - \frac{1}{\omega R_s}\right] \quad \text{(B.20)}$$

Corrections for the C_s bridge are similar (refer to Figure 57). For the simple C_s bridge (without stray components) the balancing equations are again B.8 to be used in order to solve the complex case in Figure 57. The balance equation for Figure 57 is given by

$$\left(\frac{1}{i_X + R_{err}} + \frac{1}{R_H} + \frac{1}{iX_H}\right)R_{4err} = \left(\frac{1}{iX_x + R_x} + \frac{1}{R_s} + \frac{1}{iX_s}\right)R_3 \quad \text{(B.21)}$$

where

$$\frac{1}{Z_1} = \frac{1}{iX_x + R_x} + \frac{1}{R_s} + \frac{1}{iX_s}$$

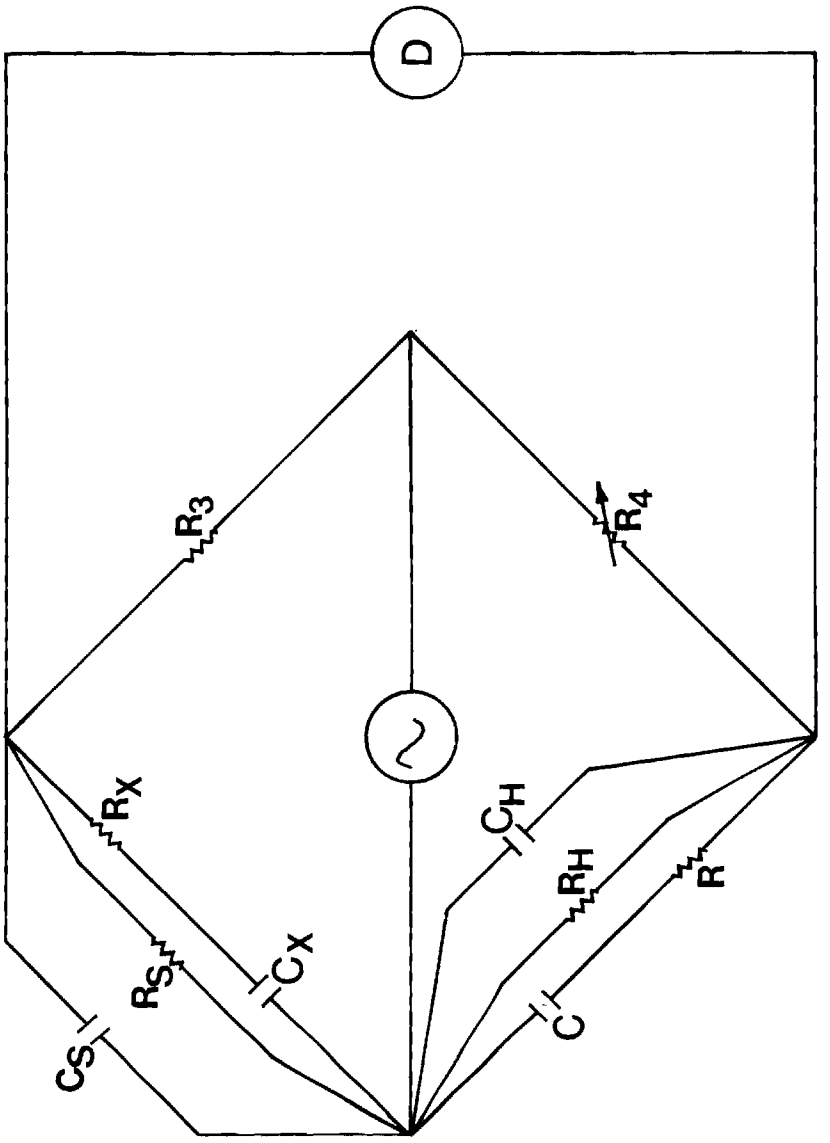

Figure 57. Schematic Diagram of a Series Capacitance Bridge-Lead-Cell System at Audio Frequencies. C_X and R_X are the sample's capacitance and resistance. C_S and R_S are a stray capacitance and resistance in parallel with the sample. C_H and R_H are the stray capacitance and resistance from the high terminal to ground. C and R represent a capacitor and resistor used to balance R_X. R_3 and R_4 are resistors used to balance C_X.

and

$$\frac{1}{Z_2} = \frac{1}{iX_x + R_{err}} + \frac{1}{R_H} + \frac{1}{iX_H}$$

or

$$\frac{R_{err}\, R_{4err}}{X_c^{\,2} + R_{err}^{\,2}} - \frac{iX\, R_{4err}}{X_c^{\,2} + R_{err}^{\,2}} + \frac{R_{4err}}{R_H} - \frac{iR_{4err}}{X_H} =$$

$$\frac{R_x\, R_3}{X_x^{\,2} + R_x^{\,2}} - \frac{iX_x\, R_3}{X_x^{\,2} + R_x^{\,2}} + \frac{R_3}{R_s} - \frac{iR_3}{X_s} \qquad \text{(B.22)}$$

Equating the imaginary components yields

$$\frac{X\, R_{4err}}{X^2 + R_{err}^{\,2}} + \frac{R_{4err}}{X_H} = \frac{X_x\, R_3}{X_x^{\,2} + R_x^{\,2}} + \frac{R_3}{X_s} \qquad \text{(B.23)}$$

Multiplying through by ω yields

$$\left[\frac{R_{4err}}{\omega C\,(X_c^{\,2} + R_{err}^{\,2})}\right] + \omega\, C_H\, R_{4err} = \left[\frac{R_3}{\omega C_x\,(X_x^{\,2} + R_x^{\,2})}\right] + R_3\, \omega\, C_s \qquad \text{(B.24)}$$

or

$$\left[\frac{C\, R_{4err}}{\omega^2\, C^2\, X_c^{\,2} + \omega^2\, C^2\, R_{err}^{\,2}}\right] + C_H\, R_{4err} = \left[\frac{C_x\, R_3}{\omega^2\, C_x^{\,2}\, X_x^{\,2} + \omega^2\, C_x^{\,2}\, R_x^{\,2}}\right]$$

$$+ R_3\, C_s \qquad \text{(B.25)}$$

$$\left[\frac{C\, R_{4err}}{1 + \tan \delta^2_{err}}\right] + C_H\, R_{4err} = \frac{C_x\, R_3}{1 + \tan \delta^2_{corr}} + R_3\, C_s \qquad \text{(B.26)}$$

where $R_x/X_x = \tan \delta_{corr}$ and $R_{err}/X_c = \tan \delta_{err}$

Substituting B.8 into B.26 yields

$$\left[\frac{\frac{C\ R_3}{C}\ C_{xerr}}{1 + \tan \delta^2_{err}}\right] + \left[\frac{C_H\ R_3\ C_{xerr}}{C}\right] = \left[\frac{C_x\ R_3}{1 + \tan \delta^2_{corr}}\right] + R_3\ C_s \qquad (B.27)$$

Using equation B.7 in B.27 where C_{px} is the equivalent correct C_x converted to a parallel capacitance, we have

$$C_{px} = \left[\frac{1}{1 + \tan \delta^2_{err}} + \frac{C_H}{C}\right] C_{xerr} - C_s \qquad (B.28)$$

$\tan \delta_{err}$ and C_{xerr} are the measured $\tan \delta$ and C_x. Equating the real components yields

$$\frac{R_{err}R_{4err}}{X_c^2 + R_{err}^2} + \frac{R_{4err}}{R_H} = \frac{R_x\ R_3}{X_x^2 + R_x^2} + \frac{R_3}{R_s} \qquad (B.29)$$

Equation B.29 can be written as

$$\frac{\frac{X_C}{X_c^2 + R_{err}^2} + \frac{1}{X_H}}{\frac{X_x}{X_x^2 + R_x^2} + \frac{1}{X_s}} = \frac{R_3}{R_{4err}} \qquad (B.30)$$

Equating equation B.30 with B.23 yields

$$\frac{\dfrac{Xc}{X_c^{\,2} + R_{err}^{\,2}} + \dfrac{1}{X_H}}{\dfrac{X_x}{X_x^{\,2} + R_x^{\,2}} + \dfrac{1}{X_3}} = \frac{\dfrac{R_{err}}{X_c^{\,2} + R_{err}^{\,2}} + \dfrac{1}{R_H}}{\dfrac{R_x}{X_x^{\,2} + R_x^{\,2}} + \dfrac{1}{R_s}} \qquad \text{(B.31)}$$

Multiplying through by $\frac{1}{\omega}$ gives

$$\left[\frac{Xc}{\omega(X_c^{\,2} + R_{err}^{\,2})} + C_H\right]\left[\frac{R_x}{\omega(X_x^{\,2} + R_x^{\,2})} + \frac{1}{\omega R_s}\right] = \left[\frac{X_x}{\omega(X_x^{\,2} + R_x^{\,2})} + C_s\right]\left[\frac{R_{err}}{\omega(X_c^{2} + R_{err}^{\,2})} + \frac{1}{\omega R_H}\right] \qquad \text{(B.32)}$$

or

$$\left[\frac{C}{\omega^2\, C^2(X_c^{\,2} + R_{err}^{\,2})} + C_H\right]\left[\frac{\omega\, C_x^{\,2}\, R_x}{\omega^2\, C_x^{\,2}(X_x^{\,2} + R_x^{\,2})} + \frac{1}{\omega R_s}\right] = \left[\frac{C_x}{\omega^2\, C_x^{\,2}(X_x^{\,2} + R_x^{\,2})} + C_s\right]\left[\frac{\omega\, C^2\, R_{err}}{\omega^2\, C^2(X_c^{2} + R_{err}^{\,2})} + \frac{1}{\omega R_H}\right] \qquad \text{(B.33)}$$

$$\left[\frac{C}{1 + (\tan\delta_{err})^2} + C_H\right]\left[\frac{C_x \tan}{1 + (\tan\delta_{corr})^2} + \frac{1}{\omega R_s}\right] = \left[\frac{C_x}{1 + (\tan\delta_{corr})^2} + C_s\right]\left[\frac{C \tan\delta_{err}}{1 + (\tan\delta_{err})^2} + \frac{1}{\omega R_H}\right] \qquad \text{(B.34)}$$

Using Equation B.28 yields

$$\left[\left(\frac{1}{1 + \tan \delta_{err}^2} + \frac{C_H}{C}\right) C_{xerr} - C_s\right] \tan \delta_{corr} + \frac{1}{\omega R_s} = \left(\frac{C}{1 + \tan \delta_{err}^2}\right) \tan \delta_{err} + \frac{1}{\omega R_H} \tag{B.35}$$

Finally,

$$\tan \delta_{corr} = \left[\left\{C_{xerr}\left(\frac{\tan \delta_{err}}{1 + \left(\tan \delta_{err}\right)^2} + \frac{1}{\omega C R_s}\right)\right\} - \frac{1}{\omega R_s}\right] \left[\frac{1}{\frac{1}{1 + \tan \delta_{err}^2} + \frac{C_H}{C}\left(C_{xerr} - C_s\right)}\right] \tag{B.36}$$

The four main equations are summarized below.

For the C_p bridge:

$$C_{px} = C_{xerr}\left[1 + \frac{C_H}{C}\right] - C_s \qquad (C_{px} = C_x) \tag{B.37}$$

$$\tan \delta = \frac{C_{xerr}}{\left[C_{xerr}\left(1 + \frac{C_H}{C}\right) - C_s\right]} \left[\tan \delta_{err} + \frac{1}{\omega C R_H} - \frac{1}{\omega C_{xerr} R_s}\right] \tag{B.38}$$

For the C_s bridge:

$$C_{px} = C_{xerr}\left[\frac{1}{1+\left(\tan\delta_{err}\right)^2} + \frac{C_H}{C}\right] - C_s \qquad (B.39)$$

$$\tan\delta = \left[\frac{C_{xerr}}{\left(\frac{1}{1+\left(\tan\delta_{err}\right)^2} + \frac{C_H}{C}\right)C_{xerr} - C_s}\right]$$

$$\left[\frac{\tan\delta_{err}}{1+\left(\tan\delta_{err}\right)^2} + \frac{1}{\omega C R_H} - \frac{1}{\omega C_{xerr} R_s}\right] \qquad (B.40)$$

When $R_s = \infty$, $R_H = \infty$, $C_H = 0$, $C_s = 0$, equations B.37, B.38, B.39 and B.40 reduce to

$$C_x = C_{xerr}$$

$$\tan\delta = \tan\delta_{err}$$

$$C_{px} = \frac{C_{xerr}}{1+\tan\delta_{err}^2}$$

$$\tan\delta = \tan\delta_{err}$$

Evaluation of Corrections for Audio Bridge Measurements

Table 7 shows the observed and corrected values (using the above equations) of various commercial standard capacitors used as unknown with $R_H \neq \infty$ and $C_H \neq 0$.

Table 7. Corrected Capacitances and Loss Tangent as a Function of Stray Capacitance and Resistance for Both a Series and Parallel Bridge at 1000 Hz.

Series Bridge

C_{px} (pf) (Calc. from equ. B-39)	tan δ (Calc. from equ. B-40)	C_{xerr} (pf) (Measured value)	$\tan\delta_{err}$ (Measured value)	C_H (pf)	R_H (Ω)	R_x (Ω)
945	0.178	977	0.178	0	∞	952 K
948	0.178	972	0.179	661	5MΩ	952 K
948	0.178	972	0.178	661	802 K	952 K
949	0.178	972	0.176	661	404 K	952 K
947	0.178	965	0.160	661	84 K	952 K
945	0.178	950	0.122	992	28 K	952 K

Parallel Bridge

C_{px} (pf) (Calc. from equ. B-37)	tan δ (Calc. from equ. B-38)	C_{xerr} (pf) (Measured value)	$\tan\delta_{err}$ (Measured value)	C_H (pf)	R_H (Ω)	R_x (Ω)
945	1.73	945	1.73	0	∞	952 K
951	1.72	945	1.73	661	5M	952 K
947	1.74	941	1.73	661	802 K	952 K
949	1.74	943	1.71	661	402 K	952 K
949	1.73	943	1.55	661	84 K	952 K

Table 8. Temperature Dependence of R_S and R_L Resistances in the Bridge-Lead-Cell Circuit. R_H was approximately equal to R_L

Temp. (°C)	R_S (Ω)	R_L (Ω)
25	17×10^9	8×10^9
50	17×10^9	8×10^9
100	17×10^9	8×10^9
150	17×10^9	8×10^9
200	13×10^9	7×10^9
250	8×10^9	4×10^9
300	3×10^9	1×10^9

C_H was easily measured with the bridge. Its value is 166 pf. Almost all of this capacitance is due to coaxial cables used as connecting leads between the cell and the bridge. R_S and R_H were first determined with a Keithley 610 electrometer. The d. c. resistances were approximately 10^{10} Ω at 25°C, but did fall below this value at temperatures greater than 200°C (see Table 8). Later, the a. c. conductance between the high terminal to ground and between the high and low terminals were measured with the bridge at frequencies between 100 and 100 K Hz and temperatures between 23°C and 300°C. The a. c. conductance was always less than 10^{-9} Ω^{-1} (the resistance > 10^9 Ω). 10^{-9} Ω^{-1} is the low conductance limit of the bridge. Although a null was not obtained, rotation of the range dial to higher or lower magnitudes produced a clear indication on the detector if one is approaching or receeding from the null.

The substitution of the available numbers into equations B.37 through B.40 yields the following information. The bridge accuracy for the capacitance is given by the General Radio Company as $\pm$ 1% $\pm$ 1 pf. Rewriting equation B.37 yields

$$C_x = C_{xerr} + C_{xerr} \frac{C_H}{C} - C_s$$

C is a standard, fixed capacitor with a value of 10^{-7} fd. Thus,

$$C_{xerr} \frac{C_H}{C} = C_{xerr} \left[\frac{1.66 \times 10^{-10}}{10^{-7}} \right] = C_{xerr} (.00166)$$

This term is always much less than the accuracy of the instrument (< 1%), hence it can be ignored. The importance of C_s is relative depending on the magnitude of C_{xerr}. For chlorapatite with $E \| \bar{c}$, $C_{xerr} \sim 1{,}000$ pf and $C_s \sim 4$ pf for a 0.5 mm electrode separation. Now consider the term $\frac{1}{\omega C R_H}$ in equations B.38 and B.40. This term could be important at low frequencies when $\omega \leq 100$ Hz. Then,

$$\frac{1}{\omega C R_H} \simeq \frac{1}{(100)\ (10^9 \Omega)\ (10^{-7} \text{fd})} = 0.001$$

Again, the loss tangent accuracy for the 1650B GR bridge is never less than $\pm$ 5% $\pm$ .001. Thus, this correction can also be ignored. However, the term $\frac{1}{C_{xerr} R_s}$ may be very large whenever $C_{xerr} \sim 10^{-11}$ fd or less. The actual a. c. R_s value is probably higher than the assumed value of 10^9 Ω. In order to determine the a. c. R_s more accurately, low loss alumina samples (ALSIMAG 772, 99.5% A_2O_3) were requested from the American Lava Corporation. Because the loss tangent is known to be below 0.001 for frequencies $\geq$ 1,000 hz at 25°C, any losses measured with the 1650B GR bridge are most likely due to the $\frac{1}{\omega C_{xerr} R_s}$ correction term. The results with the alumina at 25°C and frequencies $\geq$ 100 hz indicated the residual loss to be $\leq \pm$ 0.001. For the loss correction to be no greater than 0.001, R_s must have a minimum value of

$$R_s = \frac{1}{C_{xerr} \tan \delta} = \frac{1}{2\pi\ (10^3 \text{sec}^{-1})\ (10^{-11} \text{fd})\ (10^{-3})} \simeq 10^{10} \Omega$$

where C_{xerr} is of the order of 10 pf. This value is in agreement with the electrometer measurements. Again, for ClAp with $E \parallel \bar{c}$, $C_{xerr} \sim 10^{-9}$ fd and using the value $10^{10}\Omega$

$$\frac{1}{\omega C_{xerr} R_s} = \frac{1}{2\pi\ (10^3 \text{sec}^{-1})\ (10^{-9}\text{fd})\ (10^{10}\Omega)} \simeq 0.0001$$

This term may, however, be important when C_{xerr} is small (~ few pf). The lowest possible capacitance obtainable with this cell is 4 pf. Using $R_s = 10^{10}\Omega$

$$\frac{1}{\omega C_{xerr} R_x} = \frac{1}{2\pi\ (4 \times 10^{-2}\text{fd})\ (10^3 \text{sec}^{-1}\ (10^{10}\Omega)} \simeq 0.004$$

Which is probably too large an error, because 10^{10} is a low estimate for R_s. Typical FAp samples had a capacitance of about 4 pf and a low measured loss tangent (about 0.001). Clearly, the $\frac{1}{C_x R_s}$ correction would have resulted in a corrected negative loss tangent which is physically impossible. Thus, it must be concluded that the value of R_s is greater than the $10^{10}\Omega$ value given previously. It is seen that all correction terms are negligible.

However, a residual error in tan δ intrinsic to the bridge appeared at frequencies greater than 5,000 Hz (see Figures 58 and 59). The tan δ accuracy above 1,000 Hz and with the CGRL dial setting below 1 as given by the General Radio Corporation is $\pm$ 0.0001 ($\frac{1}{\text{CGRL}}$ dial setting) (f/1 K Hz) $\pm$ 5%. Suppose the CGRL dial is set to 1, the loss tangent accuracy at 10 K hz is then $\pm$ 0.001 (10) $\pm$ 5% or $\pm$ 0.01 $\pm$ 5%.

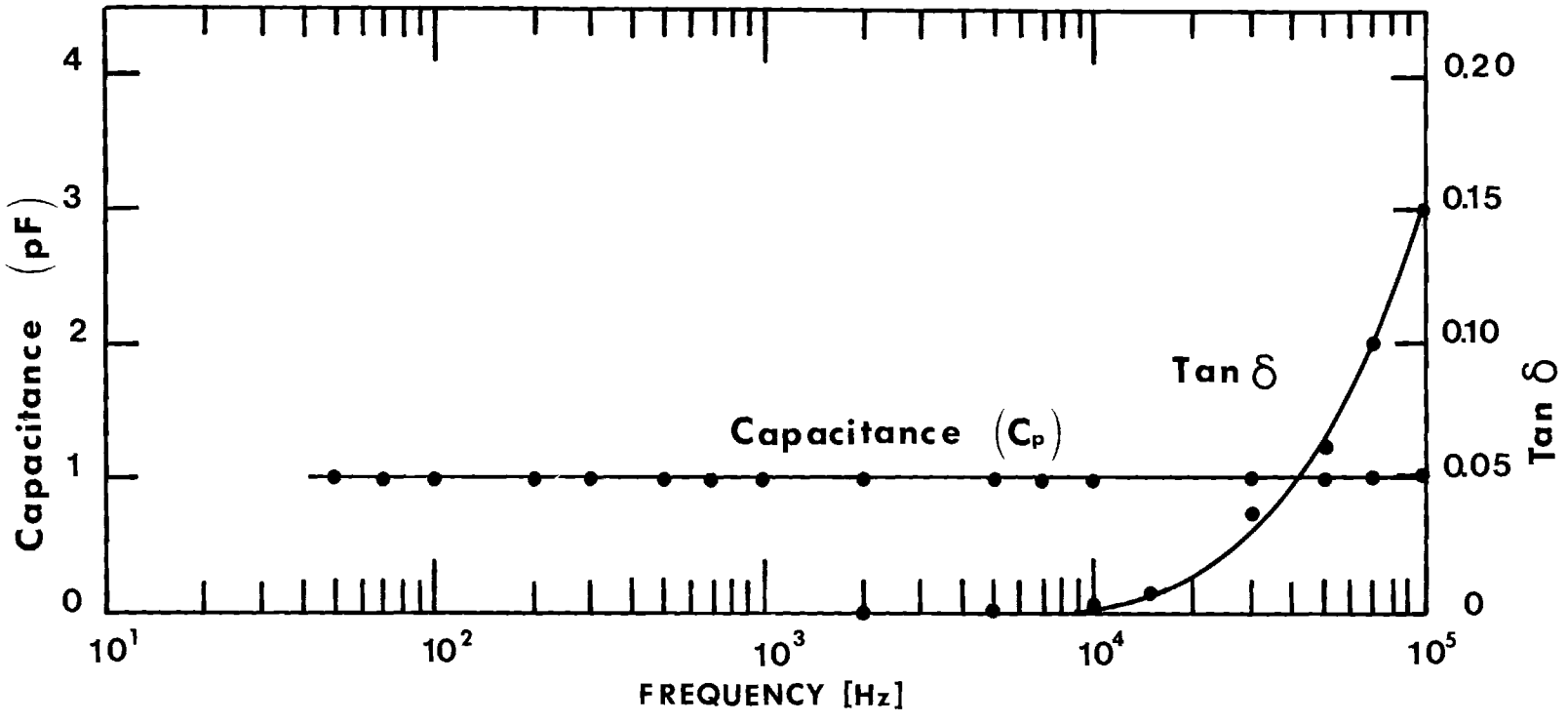

Figure 58. Frequency Dependence of Cell Capacitance and Loss Tangent Without a Dielectric Sample at Audio Frequencies.

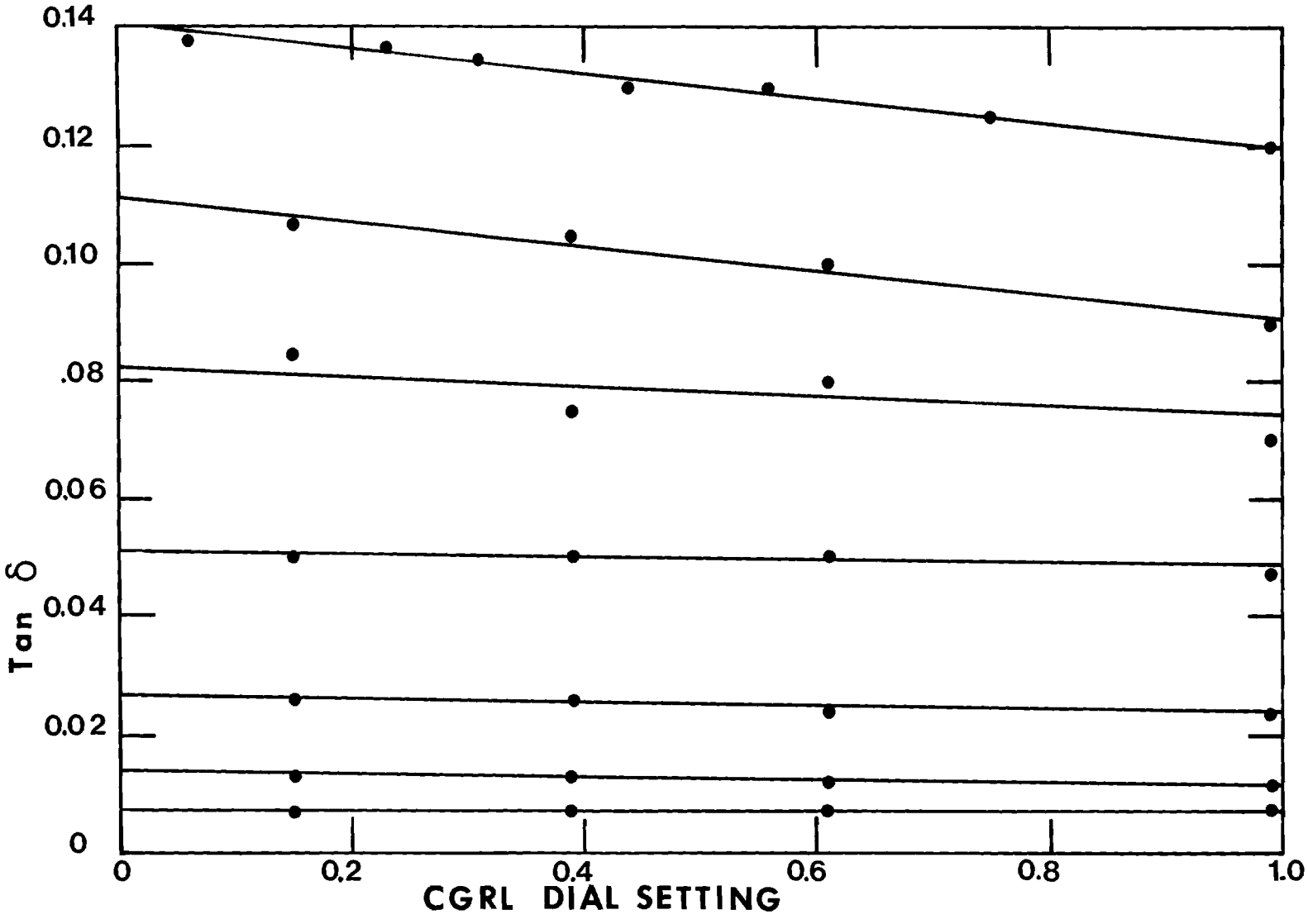

Figure 59. Residual Loss Tangent of Audio Bridge in the KHz Region.

Therefore, for example, the observed increase in tan δ for ClAp with $E \perp C$ may not be real and solely due to this residual bridge error (compare Figure 58 with Figure 60). It was found that (by using $Al_2 O_3$ samples) this correction is only valid when using the picofarad range. Therefore, to improve the accuracy of the loss tangent data for small capacitors (~ 1,000 pf) at frequencies ~ 1,000 hz to $\pm$ 5% $\pm$ 0.001, the corrections shown in Figure 59 were taken in account. These corrections were used for ClAp, with $E \parallel C$, but only when the capacitance was less than 1,000 pf.

Influence of Stray Capacitance and Inductance on R. F. Bridge Measurements

The r. f. bridge measures the reactive and resistive component of the sample by the direct substitution method (the bridge is balanced with and without the sample). The capacitance and loss tangent are obtained with the aid of equations B.41 and B.42

$$C = \frac{1}{2\pi f x_c} \tag{B.41}$$

$$\tan \delta = \frac{X_c}{R} \tag{B.42}$$

where X_c is the capacitive series reactance of the sample, R is the a. c. resistance of the sample and f is the frequency. Only series capacitances are obtained which must be converted to the equivalent parallel capacitance.

Under certain circumstances, either the reactance or the resistance or both fell outside the accessible range of the bridge.

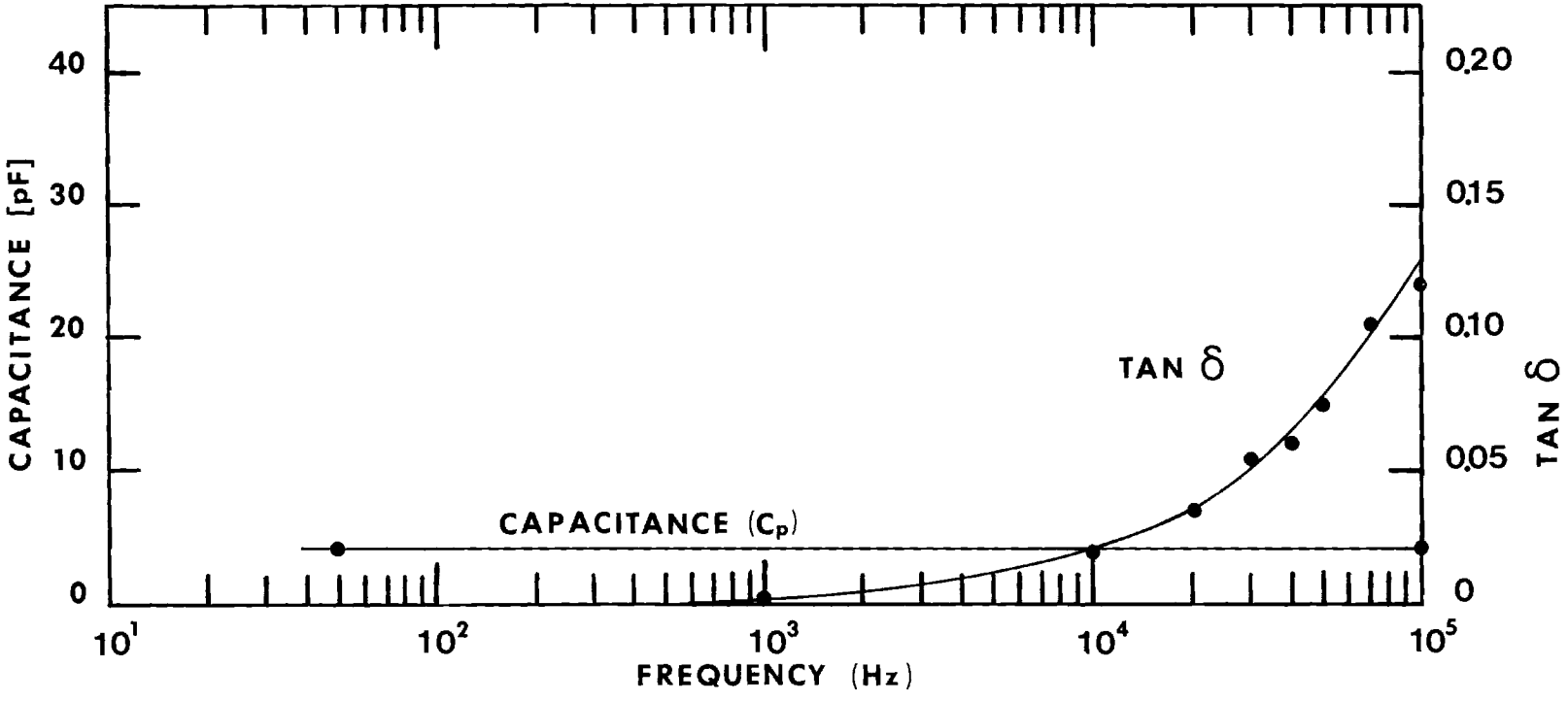

Figure 60. Uncorrected Frequency Dependence of Capacitance and tanδ of a ClAp Sample in the Audio Frequency Range with the Applied E Field Perpendicular to the c Axis.

In this case, measurements could still be made by shunting the sample with a small known capacitor (approximately 40 pf). X_M and R_M are the measured reactance and resistance of the circuit. X_s and R_s are the impedance components of the standard capacitor ($R_s \sim 0$). X_x and R_x, the sample reactance and resistance, are obtained from equations B.43 and B.44

$$R_x = \frac{R_M'}{A} \tag{B.43}$$

$$X_x = \frac{X_M - \frac{R_M'^2}{X_s} - \frac{X_M^2}{X_s}}{A} \tag{B.44}$$

where

$$A = \left(1 - \frac{X_M}{X_s}\right)^2 + \left(\frac{R_M}{X_s}\right)^2$$

and

$$R_M' = R_M - \left[R_s\left(\frac{X_M^2 + R_M^2}{X_s^2}\right)\right]$$

The inductive reactance of the cell leads given by

$$X_L = 2\pi fL \tag{B.45}$$

influenced the measurements considerably at high frequencies (between 1 Mhz and 10 Mhz). In order to find the necessarv corrections for the lead inductance and the cell capacitance, the lead-cell system

was represented by the circuit shown in Figure 61. Z_L is the inductive impedance. Z_{C1} is the residual capacitive cell impedance due to BNC plugs etc. and Z_{C2} is the capacitive electrode impedance. As a result, it was possible to determine the individual impedance components. By shorting the electrodes Z_{C2}, Z_{C1} was effectively eliminated and Z_L could be measured directly. Table 9 shows X_L and R_L as a function of the frequency.

The next step required Z_{C2} to be infinite to be able to measure Z_L and Z_{C1}. Physically, this was accomplished by separating the electrodes as far as possible. Z_{C1} was obtained by subtracting Z_L from the measured impedance Z_M.

Because the reactive and resistive component of Z_M fell outside the direct-reading range of the bridge, indirect measurements were made through the use of an auxillary parallel capacitor. The impedance diagram of Z_{C1}, Z_L and Z_M is shown in Figure 62. Z_M was at all frequencies a capacitive reactance. Let

$$Z_M = Z_{C1} + Z_L \tag{B.46}$$

$$Z_L = iX_L + R_L \tag{B.47}$$

$$Z_{C1} = -iX_{C1} + R_{C1} \tag{B.48}$$

$$Z_M = -iX_{CM} + R_{CM} \tag{B.49}$$

We have from equation B.46

$$Z_{C1} = Z_M - Z_L$$

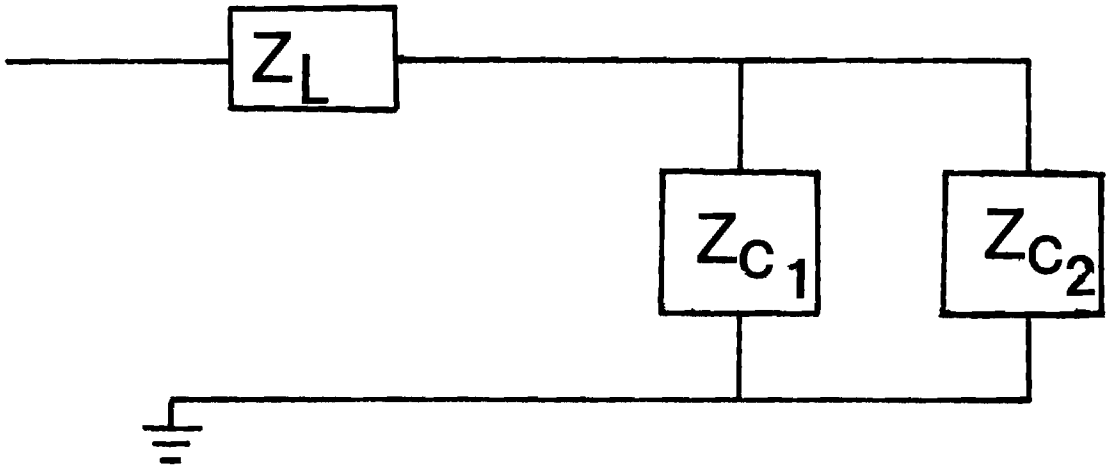

Figure 61. Schematic Representation of Cell Impedances at Radio Frequencies. Z_L is the inductive cell impedance. Z_{C1} is the residual cell capacitive impedance in parallel with the sample. Z_{C2} is the capacitive impedance of the cell electrodes.

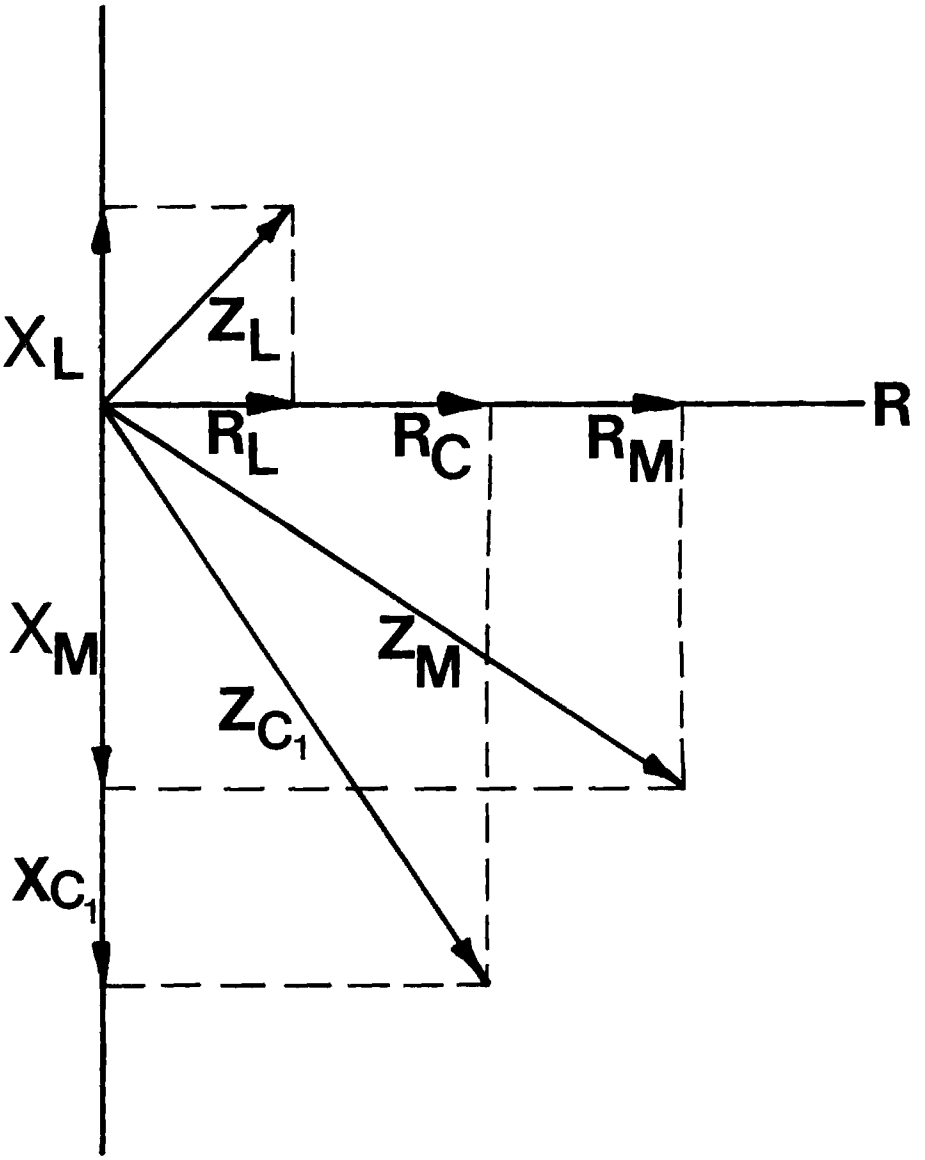

Figure 62. Resolution of the Measured Stray R.F. Impedance, Z_M, into Capacitive and Inductive Impedance Components. Z_L is the inductive cell impedance. X_L and R_L are the inductive and resistive components of Z_L. Z_{C1} is a residual cell capacitive impedance. X_{C1} and R_{C1} are the capacitive and resistive components of Z_{C1}. Z_M is the measured impedance. X_M and R_M are the capacitive and resistive components of Z_M.

Substituting equations B.47, B.48 and B.49 into B.46 yields

$$-iX_{C1} + R_{C2} = -iX_{CM} + R_{CM} - (iX_L + R_L)$$

By separating the real and imaginary parts we obtain

$$X_{C1} = X_{CM} + X_L$$

$$R_{C1} = R_{CM} - R_L$$

Table 9 shows X_{C1} and R_{C1} as a function of the frequency. Figure 63 clearly shows the importance of these corrections within the megacycle range. The last impedance to be determined was Z_{C2}. It was calculated, because the area of and the distance between the electrodes was known. Z_{C2} is given by

$$Z_{C2} = \frac{1}{\omega C_e}$$

where C_e is the capacitance of the cell electrodes without a sample. Of course, C_e changed with the sample thickness, but was usually within the range of a few picofarads.

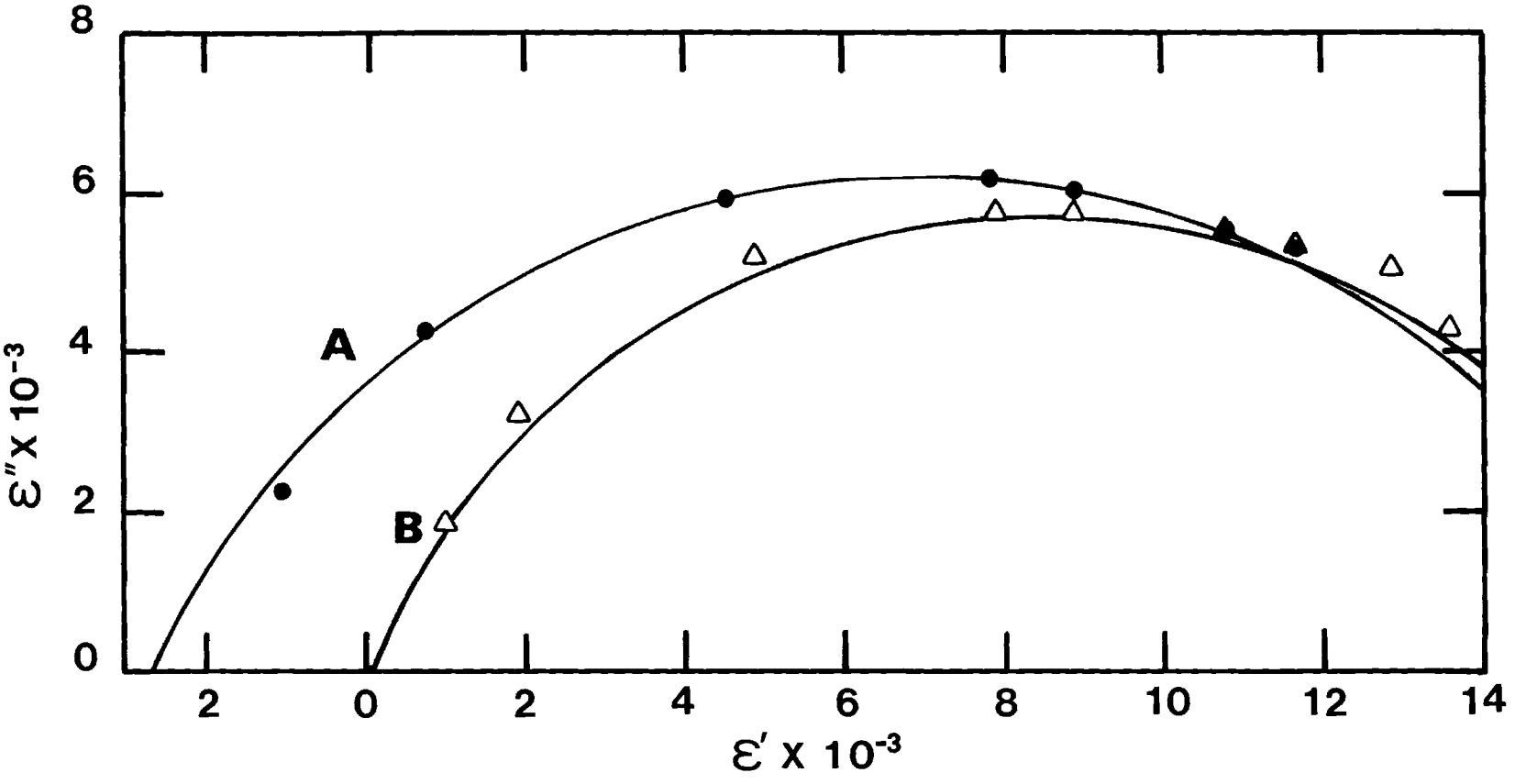

Figure 63. Complex Dielectric Constant of a ClAp Sample at R.F. Frequencies (A) With and (B) Without Inductive Impedance Corrections.

Table 9. Inductive and Capacitive Impedance Corrections for R. F. Bridge Measurements as a Function of Frequency. x_{C_1}, x_L, R_{C_1} and R_L are capacitive and inductive reactances and capacitive and inductive resistances, respectively.

Frequency (Hz)	x_{C_1} (Ω)	x_L (Ω)	R_{C_1} (Ω)	R_L (Ω)
100 K	72555	0	0	0
150 K	48751	0	0	0
200 K	36618	0	0	0
300 K	24375	0	0	0
400 K	18194	2.5	0	0
500 K	14627	2.0	3.2	1
800 K	9087	5.0	8.0	2
1 M	7311	6.0	18.5	2.5
2 M	3655	12.0	38.4	3.4
5 M	1480	30.4	84.4	3.7
10 M	811	65.2	179.8	6.2

APPENDIX C

THE ELECTRIC DISPLACEMENT VECTOR IN AN ANISOTROPIC MEDIUM

The most general equation relating $\bar{D}$ with $\bar{E}$ in any dielectric is given by

$$D_i = \varepsilon_o \sum_j \varepsilon'_{ij} E_j \tag{C.1}$$

where

$$i = j = x, y, z \text{ and } \varepsilon'_{ij} \text{ is a tensor}$$

But $\bar{D}$ is also related to $\bar{P}$ by

$$D_i = \varepsilon_o E_i + P_i \tag{C.2}$$

Combining equation C-1 with C-2 gives

$$\varepsilon_o E_i + P_i = \varepsilon_o \sum_j \varepsilon'_{ij} E_j$$

or

$$\varepsilon_o \begin{pmatrix} E_x \\ E_y \\ E_z \end{pmatrix} + \begin{pmatrix} P_x \\ P_y \\ P_z \end{pmatrix} = \varepsilon_o \begin{pmatrix} \varepsilon'_{xx} & \varepsilon'_{xy} & \varepsilon'_{xz} \\ \varepsilon'_{yx} & \varepsilon'_{yy} & \varepsilon'_{yz} \\ \varepsilon'_{zx} & \varepsilon'_{zy} & \varepsilon'_{zz} \end{pmatrix} \begin{pmatrix} E_x \\ E_y \\ E_z \end{pmatrix}$$

let the E field direction coincide with Z axis. Then,

$$\varepsilon_o \begin{pmatrix} 0 \\ 0 \\ E_z \end{pmatrix} + \begin{pmatrix} P_x \\ P_y \\ P_z \end{pmatrix} = \varepsilon_o \begin{pmatrix} 0 & 0 & \varepsilon'_{xz} E_z \\ 0 & 0 & \varepsilon'_{yz} E_z \\ 0 & 0 & \varepsilon'_{zz} E_z \end{pmatrix}$$

Three equations are obtained.

$$P_x = \varepsilon_o \varepsilon'_{xz} E_z$$

$$P_y = \varepsilon_o \varepsilon'_{yz} E_z$$

$$\varepsilon_o E_z + P_z = \varepsilon_o \varepsilon'_{zz} E_z$$

ε'_{zz} is the dielectric constant along the Z direction due to the electric field component E_z. Hence

$$\varepsilon'_{zz} = 1 + \frac{P_z}{\varepsilon_o E_z}$$

Let the Z direction coincide with the c axis in ClAp. Then, the dielectric constant along the c axis is

$$\varepsilon' = 1 + \frac{P}{\varepsilon_o E} \qquad \text{(C.3)}$$

The subscripts were dropped. If $\varepsilon' \gg 1$, then

$$\varepsilon' \approx \frac{P}{\varepsilon_o E}$$

and if the assumption is made that $P = np$, where n is the dipole density and p, the dipole moment, then n is given by

$$n = \frac{\varepsilon_o \varepsilon' E}{P}$$

APPENDIX D

DEPENDENCE OF CAPACITANCE ON A DIELECTRIC IMPURITY LAYER

Actual capacitors may be represented as two conductors having an area A, separated by a distance d and filled with 3 different dielectrics ε_1', ε_2', and ε_3' having a thickness d_1, d_2, and d_3 respectively such that $d_1 + d_2 + d_3 = d$ (see Figure 64). The displacement field D is everywhere the same between the two conducting plates. From Maxwell's first equation $\int_S \bar{D} \cdot d\bar{a} = \int_V \rho d\tau$, we obtain for a parallel plate capacitor $|\bar{D}| = \frac{Q}{A} = \sigma$ where σ is the free charge density on either conducting plate. For a class A dielectric the folowing equation is correct.

$$\bar{D} = \varepsilon' \varepsilon_o \bar{E}$$

or

$$|\bar{E}| = \frac{|\bar{D}|}{\varepsilon_o \varepsilon'} = \frac{\sigma}{\varepsilon_o \varepsilon'}$$

and the potential differences across each dielectric medium is

$$\Delta V_1 = \frac{Qd_1}{A \varepsilon_o \varepsilon_1'}$$

$$\Delta V_2 = \frac{Qd_2}{A \varepsilon_o \varepsilon_2'}$$

$$\Delta V_3 = \frac{Qd_3}{A \varepsilon_o \varepsilon_3'}$$

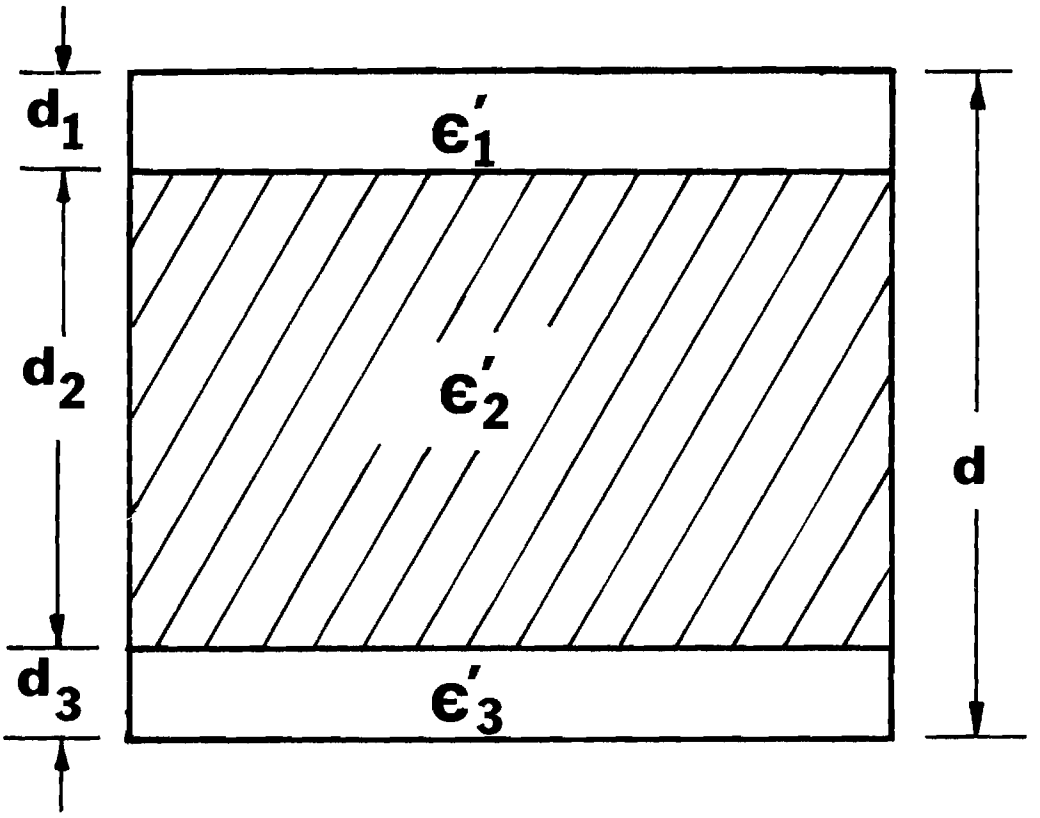

Figure 64. Capacitor Filled with a Three-Layer Dielectric.

The potential difference between the two conducting plates is

$$\Delta V = \Delta V_1 = \Delta V_2 = \Delta V_3 = \frac{Qd_1}{A\,\varepsilon_o\,\varepsilon_1'} + \frac{Qd_2}{A\,\varepsilon_o\,\varepsilon_2'} + \frac{Qd_3}{A\,\varepsilon_o\,\varepsilon_3'}$$

and

$$\frac{1}{C} = \frac{\Delta V}{Q} = \frac{d_1}{A\,\varepsilon_o\,\varepsilon_1'} + \frac{d_2}{A\,\varepsilon_o\,\varepsilon_2'} + \frac{d_3}{A\,\varepsilon_o\,\varepsilon_3'} \geq \frac{I}{C_1} + \frac{1}{C_2} + \frac{1}{C_3}$$

let $\varepsilon_1' = \varepsilon_3'$ and $d_1 = d_3$

then

$$\frac{1}{C} = \frac{2d_1}{A\,\varepsilon_o\,\varepsilon_1'} + \frac{d_2}{A\,\varepsilon_o\,\varepsilon_2'}$$

and

$$C = \frac{\varepsilon_1'\,\varepsilon_2'\,\varepsilon_o\,A}{\varepsilon_2'\,\Delta t + \varepsilon_1' d_2}$$

where $\Delta t = 2d_1 = 2d_3$

If the capacitance is to be known exactly to within a 1% error, assuming A and d can be measured with negligible error, we must have

$$1 \geq \left(\frac{\varepsilon_1'\,\varepsilon_2'\,\varepsilon_o\,A}{\varepsilon_2'\,\Delta t + \varepsilon_1'\,d_2}\right) \Big/ \left(\frac{\varepsilon_o\,\varepsilon_2'\,A}{d_2}\right) \geq .99$$

or

$$1 \geq \frac{\varepsilon_1'\,d_2}{\varepsilon_2'\,\Delta t + \varepsilon_1' d_2} \geq .99$$

or

$$0 \leq \Delta t \leq \frac{1}{\varepsilon_2'}\left(\frac{\varepsilon_1' d_2}{99} - \varepsilon_1' d_2\right)$$

of course, if ε_1' does not exist, then $d = d_2$, $\Delta t = 0$ and $C = \dfrac{\varepsilon_2'\,\varepsilon_o\,A}{d_2}$

which is the desired capacitance. A layer of any dielectric material

between the ClAp surface and the electrodes (especially air, when silver epoxy electrodes are applied) will reduce C. Obviously, large errors are introduced in capacitance measurements, whenever ε_1' is small and ε_2' is large.

APPENDIX E

OPTICAL DATA ON PHASE TRANSITION

Figure 65 shows the intensity variation of the strong 0 3 4 "monoclinic" reflection of a Clap specimen. The same specimen was photographed through a microscope between crossed polaroids while being heated with a hot stage (Figure 66). The x-ray data clearly show that residual monoclinic regions are present above 200° C although the optical data indicate that the crystal has apparently become uniaxial, which is associated with hexagonal symmetry, near 195° C.

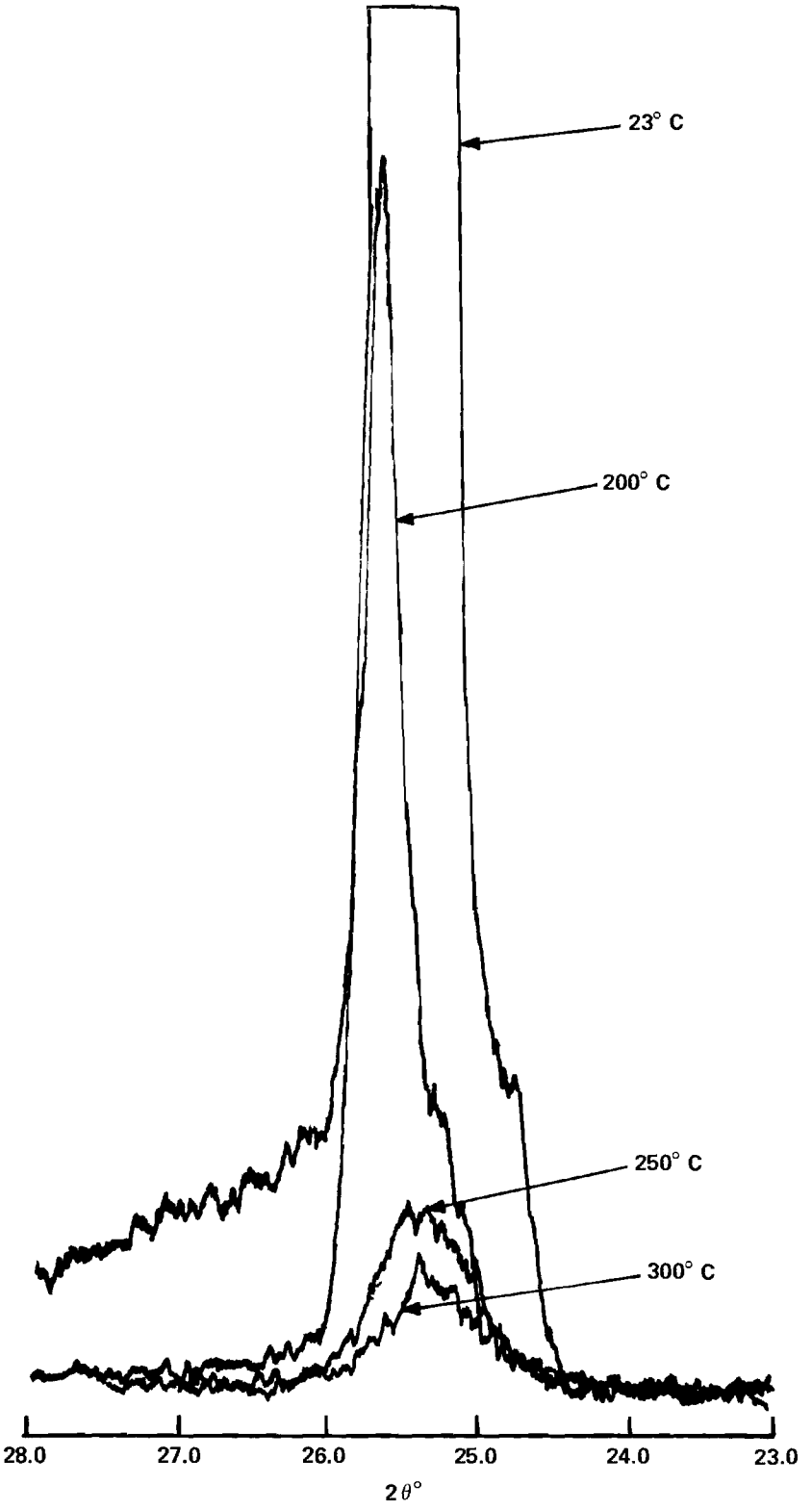

Figure 65. Temperature Dependence of the 0 3 4 X-Ray Reflection of Sample C6PE.

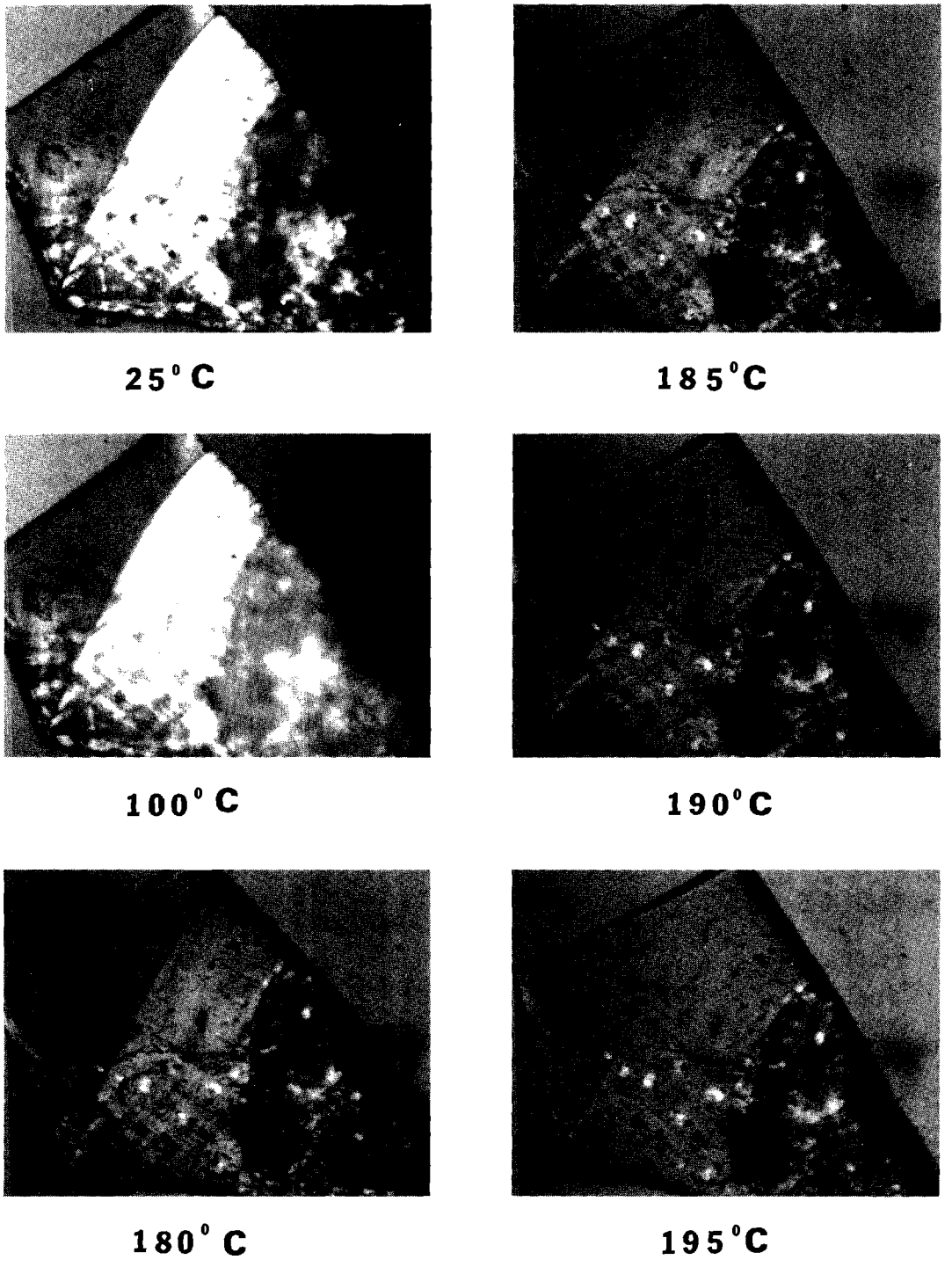

Figure 66. Development of Optically Uniaxial Character with Increasing Temperature in ClAp Sample of Figure 65. The c axis is perpendicular to the paper.

APPENDIX F

DERIVATION OF THE RELATION BETWEEN THE THERMAL VIBRATIONAL AMPLITUDE OF THE CHLORINE ION AND THE β_{33} PARAMETER

The proper form factor for an atom is not simply f_o, but rather the combined expression

$$f = f_o \, e^{-(8\pi^2 \, \overline{u^2} \, \sin^2 \theta)/\lambda^2} \qquad (F.1)$$

Where the exponential factor is the effect of the atom's thermal motion on f_o. $\overline{u^2}$ is the mean-square thermal vibrational amplitude. λ is the x-ray wavelength and 2θ the Bragg reflection angle. Bragg's law states

$$\frac{\sin \theta}{\lambda} = \frac{1}{2d} = \frac{d^*}{2}$$

where d^* is a general vector in reciprocal space given by

$$d^*_{hk\ell}{}^2 = h^2a^{*2} + k^2b^{*2} + \ell^2c^{*2} + 2hka^*b^* \cos \gamma^* + 2h\ell a^*c^* \cos \beta^* + 2k\ell b^*c^* \cos \alpha^*$$

This expression represents a series of vector components which are all perpendicular to a set of equally spaced planes. The thermal vibrational amplitudes along each base vector in reciprocal space have analogous components perpendicular to the set of planes. If

$\frac{d^{*2}}{4}$ is substituted for $\frac{\sin^2 \Theta}{\lambda^2}$ in equation F.1 with each d^{*2} component preceeded by the corresponding anisotropic thermal vibrational amplitude parameter, then the exponential factor becomes

$$\exp[-(8\pi^2 \overline{u^2} \sin^2 \Theta)/\lambda^2] = \exp[-2\pi^2(\overline{u_{11}^2} h^2 a^{*2} + \overline{u_{22}^2} k^2 b^{*2} + \overline{u_{33}^2} \ell^2 c^{*2} + 2 \overline{u_{12}^2} hkz^* b^* + 2\overline{u_{13}^2} h\ell a^* c^* + 2\overline{u_{23}^2} k\ell b^* c^*)]$$

which can be written in the short notation

$$\exp[-(8\pi^2 \overline{u^2} \sin^2 \Theta)/\lambda^2] = \exp[-(\sum_i \sum_j \beta_{ij} \xi_i \xi_j)]$$

where $i = j = 1, 2, 3$, and $\xi_i = h$, $\xi_2 = k$, $\xi_3 = 1$

β_{ij}, the thermal parameter obtained from least squares refinements can now be identified as

$$\beta_{ij} = 2\pi^2 \overline{u_{ij}^2} \int_i \int_j$$

where $$\int_1 = a^*, \int_2 = b^*, \int_3 = c^*$$

In this thesis we are only interested in $\beta_{33}(C\ell)$, the thermal parameter of the Cl ion along the c* axis. Thus,

$$\beta_{33}(C\ell) = 2\pi^2 \overline{u_{33}^2} c^{*2} = \frac{2\pi^2 \overline{u_{33}^2}}{c^2}$$

where $c^* = \frac{1}{c}$.

APPENDIX G

DIELECTRIC DATA FOR SAMPLES CN7PE, C23PE, and CN15PE

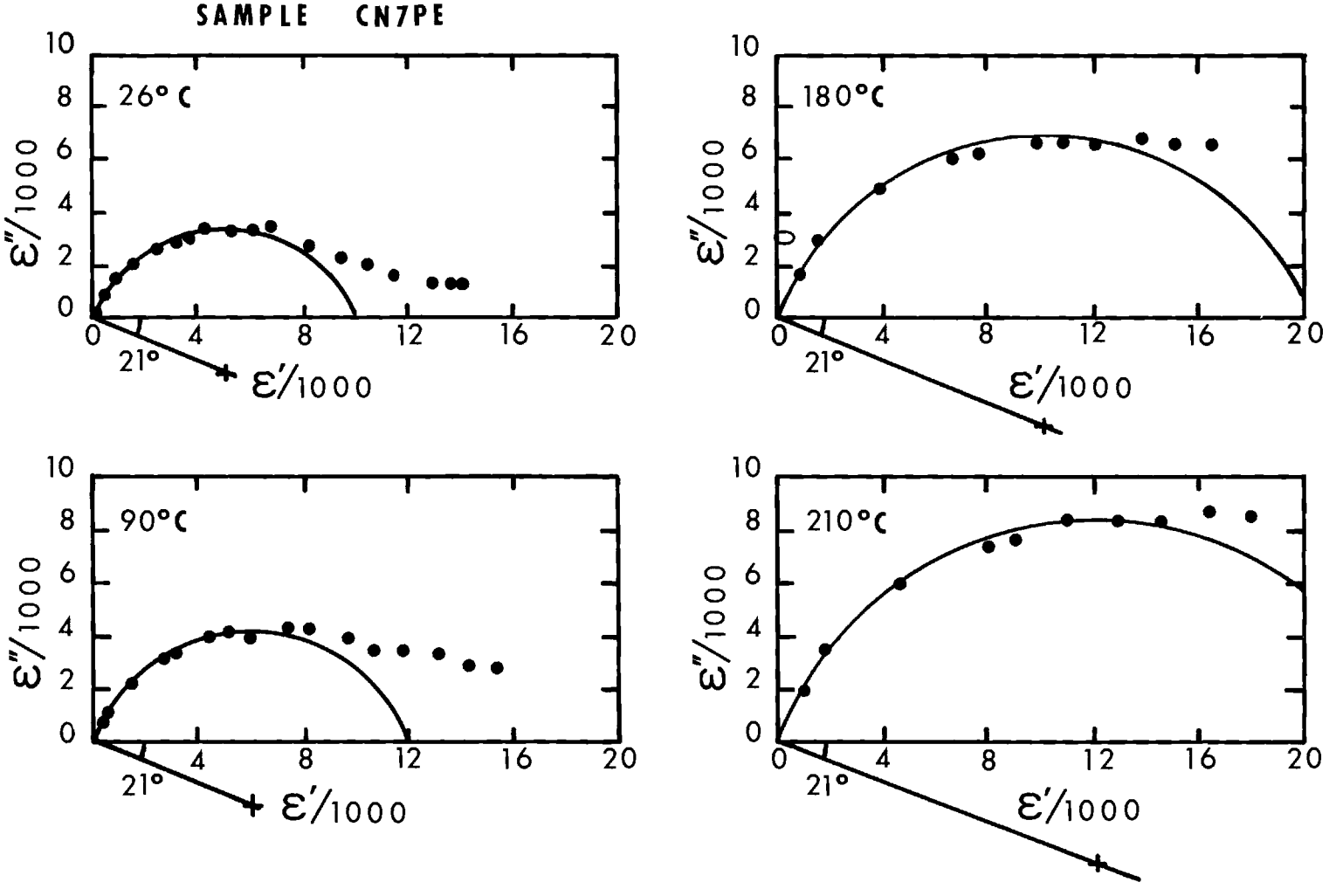

Figure 67. Dielectric Constants of ClAp Sample CN7PE at Four Temperatures Plotted in the Complex Plane.

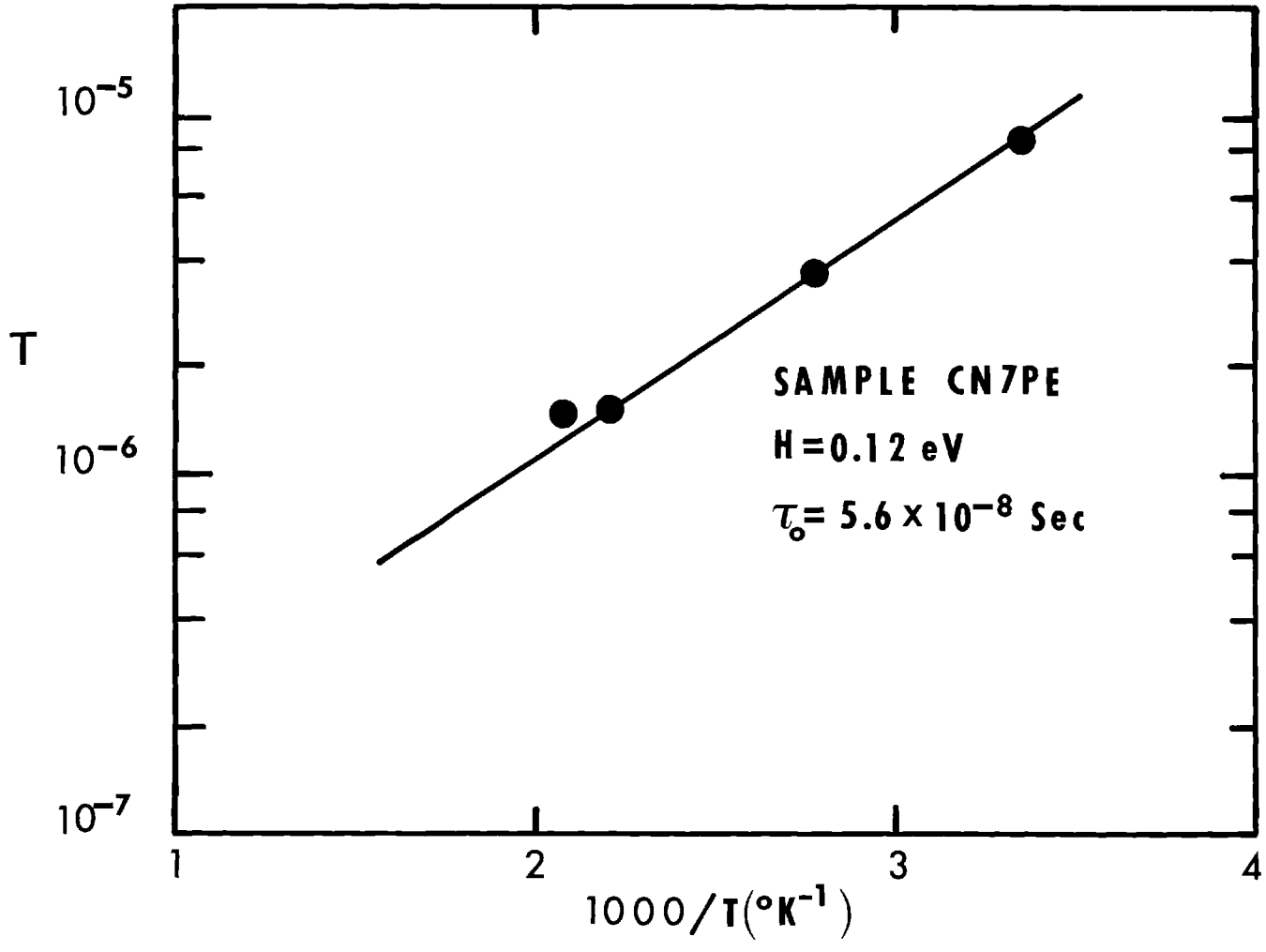

Figure 68. Relaxation Times of ClAp Sample CN7PE as a Function of Reciprocal of Absolute Temperature.

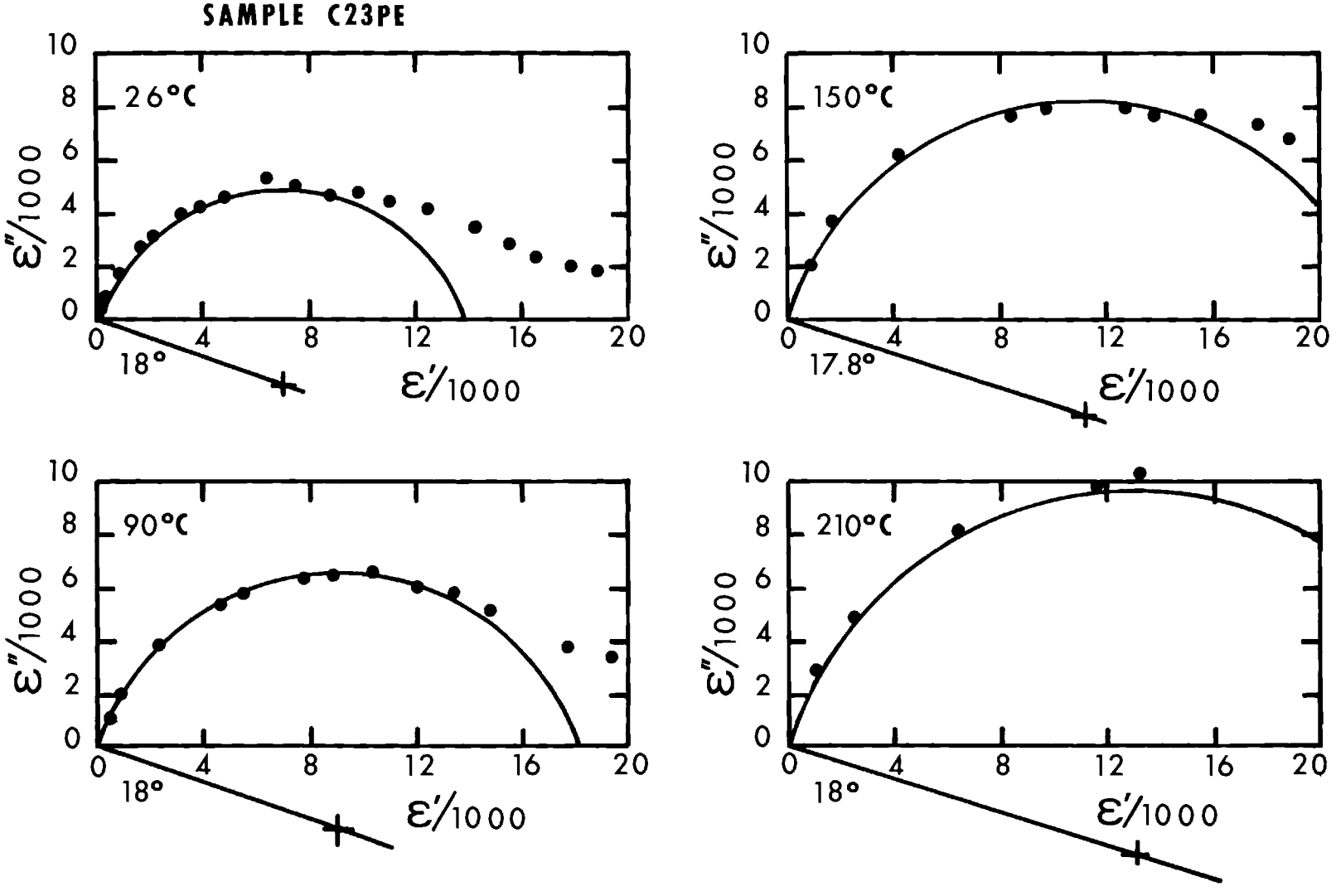

Figure 69. Dielectric Constants of ClAp Sample C23PE at Four Temperatures Plotted in the Complex Plane.

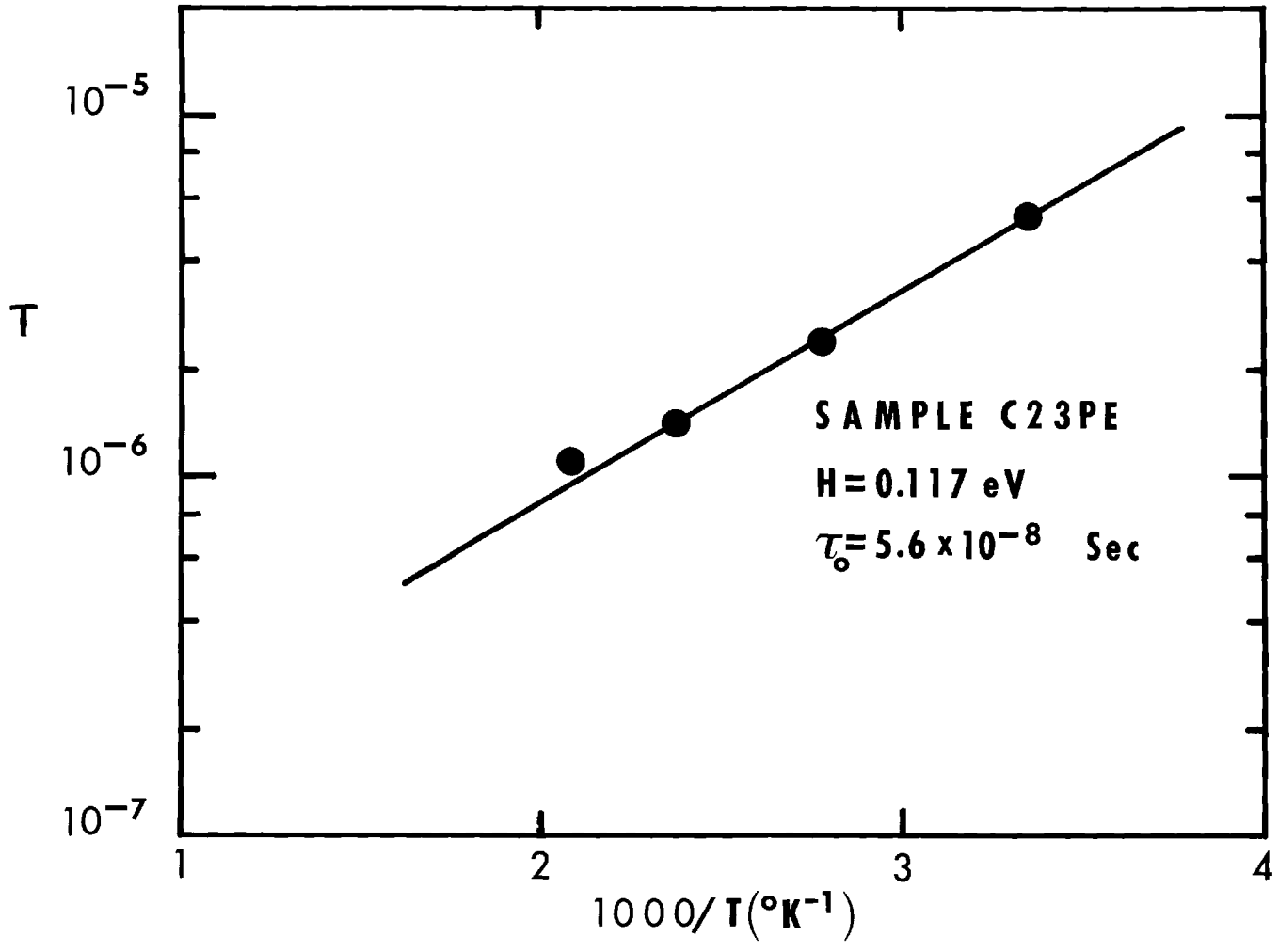

Figure 70. Relaxation Times of ClAp Sample C23PE as a Function of Reciprocal of Absolute Temperature.

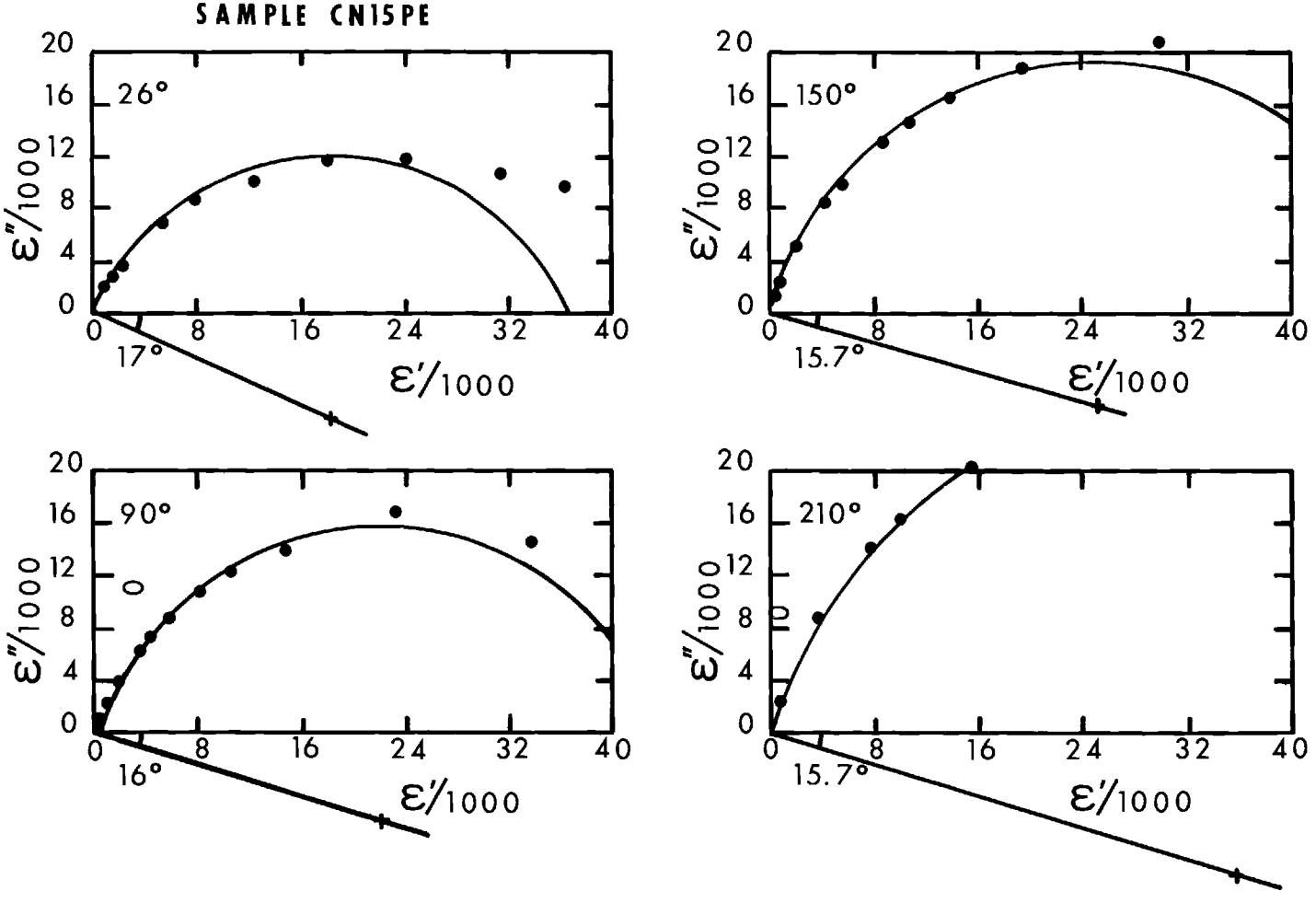

Figure 71. Dielectric Constants of ClAp Sample CN15PE at Four Temperatures Plotted in the Complex Plane.

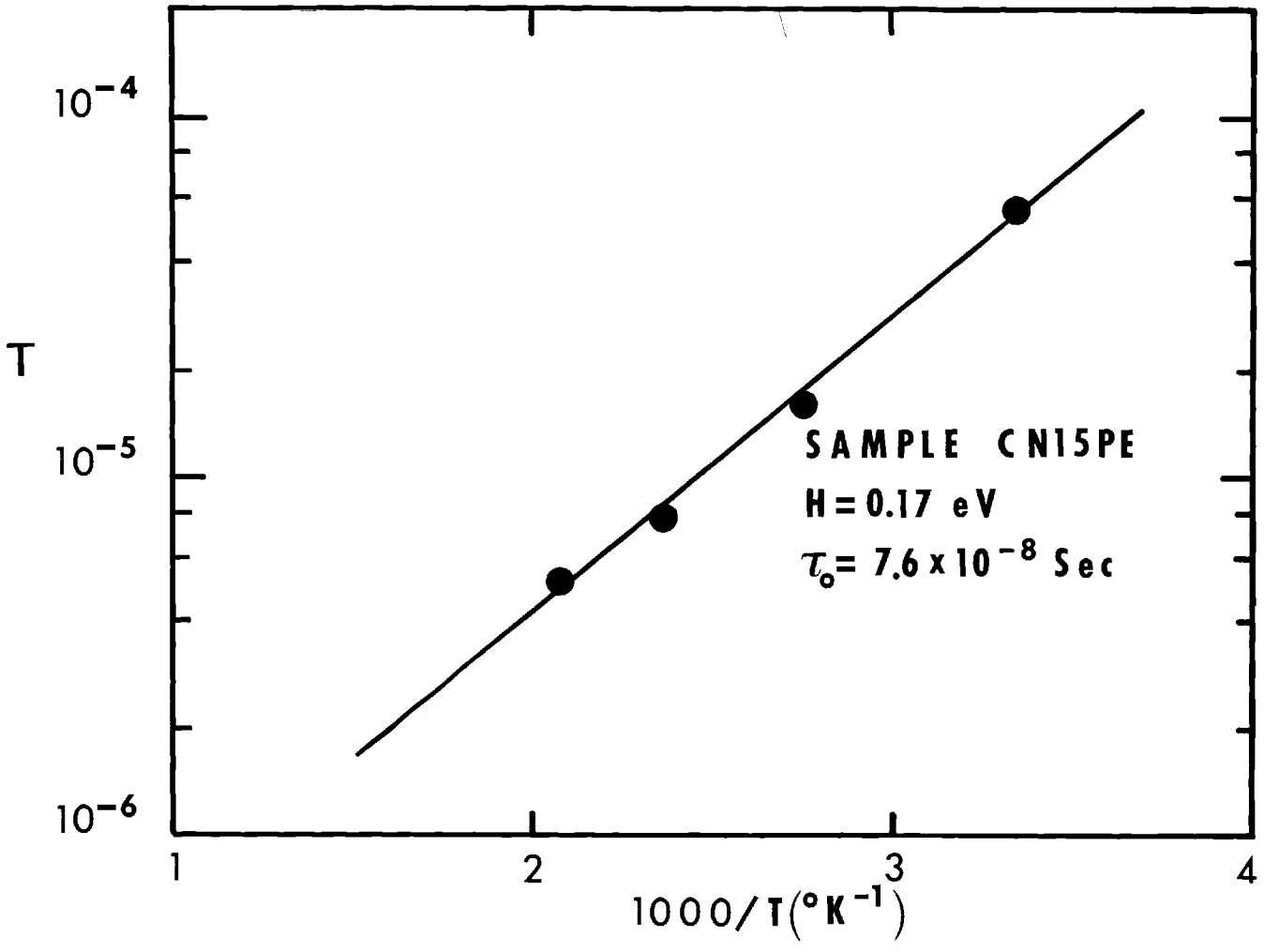

Figure 72. Relaxation Times of ClAp Sample CN15PE as a Function of Reciprocal of Absolute Temperature.

APPENDIX H

STRUCTURE FACTOR TABLES FOR CHLORAPATITE

The values in the columns Y(OBS) and Y(CALC) are the observed ($|F|^2_{obs}$) and calculated ($|F|^2_{calc}$) structure amplitudes squared respectively.

Table 10. Structure Factors for Chlorapatite at 25°C

H	K	L	Y(OBS)	Y(CALC)
-1	0	2	16.0334	17.8685
-2	1	3	2094.0344	2071.7455
0	1	3	26.1080	25.7142
-2	0	4	37.5417	42.1487
1	0	4	727.3363	753.8904
-2	1	4	62.7196	51.9843
0	1	4	728.3211	753.8916
1	1	4	64.9200	51.9843
0	2	4	40.8288	42.1487
-3	0	5	141.7824	136.3539
-2	0	5	524.9401	556.0312
-1	1	5	70.3987	75.1304
0	1	5	71.5572	75.1302
-2	2	5	517.2455	556.0317
0	2	5	532.0547	556.0312
0	3	5	142.4446	136.3539
-3	0	6	201.5973	199.6865
-2	0	6	640.8433	636.0124
1	0	6	563.2930	551.9154
2	0	6	642.6656	636.0132
-4	1	6	2788.1444	2776.4640
-3	1	6	359.2421	374.6480
-1	1	6	559.0319	551.9154
0	1	6	561.5521	551.9172
-3	2	6	3.2148	2.2885
-2	2	6	643.1499	636.0132
0	2	6	643.2472	636.0124
-4	3	6	363.8282	360.2534
-3	3	6	202.2987	199.6862
1	3	6	2801.6979	2776.4639
-3	4	6	2780.5489	2776.4702
-1	4	6	363.1942	360.2523
-2	0	7	9.0451	3.9173
2	0	7	5.1602	3.9173
-4	1	7	1013.9773	998.1566
-1	1	7	43.5601	40.0380
1	1	7	29.6452	24.7653
-4	2	7	12.8165	11.8457
-3	2	7	1944.3871	1912.7492
-1	2	7	23.9859	24.7649
1	2	7	1778.5079	1740.2014
2	2	7	12.4092	11.8457
-3	3	7	125.7014	123.3986
0	3	7	127.1385	123.3981
1	3	7	1031.8503	998.1566
-3	4	7	1014.8392	998.1556
0	4	7	157.1036	151.4908
-4	0	8	42.9442	46.8378
-3	0	8	1709.1067	1716.4467
-1	0	8	461.6578	454.6231
2	0	8	132.5410	144.7065
-4	1	8	374.5675	370.6009
-3	1	8	1728.1206	1746.1848
-1	1	8	462.2168	454.6218
2	1	8	783.7981	808.3371
-4	2	8	28.9408	25.3153
-3	2	8	790.2774	808.3371
2	2	8	30.5354	25.3153
-5	3	8	6.8477	.4800
-3	3	8	1718.4155	1716.4457
-1	3	8	789.8251	808.3423
0	3	8	1713.1122	1716.4467
1	3	8	383.8478	370.6009
-2	4	8	28.8608	25.3153
1	4	8	1103.0578	1087.5314
-4	5	8	1099.2360	1087.5323
-3	5	8	892.9001	910.7799
-2	5	8	3.7098	.4800
-5	0	9	18.9435	14.8635
-3	0	9	50.8301	50.0521
2	0	9	11.0525	7.6831
-5	1	9	57.0749	54.0841
-4	1	9	316.0538	302.6503
-3	1	9	777.0866	769.1749
-1	1	9	18.7780	15.3666
0	1	9	17.2365	15.3666
1	1	9	73.4538	76.4691
2	1	9	2037.6087	2048.0948
-3	2	9	2016.0357	2048.0947
0	2	9	10.0934	7.6831
1	2	9	778.3231	769.1749
2	2	9	1.6345	.0292
3	2	9	482.2501	477.0644
-6	3	9	177.2706	189.6729
-5	3	9	479.0059	477.0644
-4	3	9	373.0685	367.0793
-2	3	9	773.0166	769.1736
-1	3	9	2014.9098	2048.0928
0	3	9	52.0861	50.0521
1	3	9	314.3274	302.6503
-5	4	9	3.2381	.7295
-4	4	9	25.7520	21.0375
-3	4	9	308.3442	302.6505
-1	4	9	369.7730	367.0788
0	4	9	25.7728	21.0372
1	4	9	57.5654	54.0841
-5	5	9	16.8772	14.8637
-4	5	9	58.2499	54.0837
-1	5	9	5.1672	.7295
-4	6	9	891.9924	902.4497
-2	6	9	102.3598	102.2222
-6	0	10	702.2986	706.8543
-4	0	10	989.1726	1036.2240
-3	0	10	44.8855	43.2692
-1	0	10	282.9995	301.4641

Table 10. (Continued)

H	K	L	Y(OBS)	Y(CALC)
2	0	10	289.3129	289.9826
3	0	10	50.1408	43.2691
-6	1	10	172.8305	165.3349
-5	1	10	132.9310	124.6273
-4	1	10	636.7226	639.1232
-3	1	10	139.6640	130.0854
-1	1	10	279.4111	301.4629
0	1	10	280.9403	301.4641
1	1	10	1712.6662	1766.0618
3	1	10	277.4938	286.0771
-6	2	10	42.1582	40.7239
-5	2	10	5.1602	2.8207
-4	2	10	1303.1134	1325.0244
-3	2	10	9.8283	9.5701
-2	2	10	285.8491	289.9826
-1	2	10	1702.6600	1766.0621
0	2	10	289.9769	289.9820
1	2	10	132.2802	130.0854
2	2	10	1318.5114	1325.0244
3	2	10	735.8792	722.2207
-6	3	10	548.0760	538.4713
-4	3	10	279.9211	286.0771
-2	3	10	131.0408	130.0838
-1	3	10	11.5802	9.5699
1	3	10	635.3578	639.1232
2	3	10	5.4328	2.8207
3	3	10	562.0048	538.4713
-7	4	10	82.6436	78.0832
-5	4	10	72.5425	71.1138
-4	4	10	993.6723	1036.2210
-2	4	10	1299.1812	1325.0248
-1	4	10	271.8098	286.0764
0	4	10	995.5001	1036.2239
1	4	10	135.3377	124.6273
2	4	10	44.0742	40.7239
-6	5	10	61.4948	65.4662
-5	5	10	911.0355	916.8581
-4	5	10	133.2350	124.6273
-2	5	10	726.8495	722.2241
-1	5	10	76.7668	71.1139
1	5	10	172.8275	165.3349
-5	6	10	169.0194	165.3336
-4	6	10	40.0270	40.7239
-2	6	10	7.1931	3.2770
0	6	10	690.6602	706.8543
-5	0	11	61.5425	64.9766
1	0	11	71.6096	66.2678
2	0	11	21.2799	15.6835
3	0	11	16.0802	11.3143
-7	1	11	9.5649	6.5956
-6	1	11	383.2273	382.2977
-4	1	11	399.6501	406.3556
2	1	11	598.1853	584.3566
-7	2	11	59.3519	58.3614
-5	2	11	527.4294	517.8260
-2	2	11	16.9720	15.6835
-1	2	11	12.9379	11.6315
0	2	11	18.4434	15.6834
1	2	11	779.4377	773.0787
-7	3	11	74.3281	73.2410
-6	3	11	350.1859	359.3303
-4	3	11	40.9569	37.5761
-2	3	11	765.4596	773.0789
-1	3	11	578.8340	584.3560
0	3	11	12.9612	11.3140
1	3	11	402.8242	406.3556
3	3	11	350.3870	359.3303
-6	4	11	189.9772	188.1248
-5	4	11	8.5660	5.7244
-4	4	11	184.4566	182.0271
-2	4	11	22.1137	18.9481
-1	4	11	41.8771	37.5762
0	4	11	183.3395	182.0260
3	4	11	75.7045	73.2410
-7	5	11	230.4497	234.3874
-6	5	11	742.4914	742.6250
-4	5	11	1.4872	.4365
0	5	11	64.5067	64.9766
1	5	11	383.8229	382.2977
2	5	11	61.3400	58.3614
-7	6	11	120.2682	124.6521
-6	6	11	44.1389	45.2991
-2	6	11	188.2930	188.1246
-1	6	11	734.4531	742.6239
0	6	11	44.1118	45.2994
-6	7	11	8.2424	6.5955
-5	7	11	65.7291	58.3612
-2	7	11	223.5723	234.3877
-1	7	11	122.8762	124.6519
-6	0	12	46.7536	51.9153
-5	0	12	12.1021	11.9267
-1	0	12	63.3867	59.4084
1	0	12	58.9995	59.4080
2	0	12	104.5481	101.4652
3	0	12	1190.6171	1206.1283
4	0	12	58.8706	54.0976
-7	1	12	348.4345	350.0742
-6	1	12	182.2225	181.9847
-5	1	12	465.6941	458.2545
-1	1	12	64.1627	59.4080
0	1	12	61.1712	59.4084
2	1	12	352.6745	354.3428
4	1	12	367.5117	364.7914
-8	2	12	215.5908	214.3906
-7	2	12	64.6480	66.5012
-5	2	12	382.8420	377.4328
-4	2	12	9.7471	9.7013
-2	2	12	104.1466	101.4652
-1	2	12	2.4012	.1591
0	2	12	103.9221	101.4644

Table 10. (Continued)

H	K	L	Y(OBS)	Y(CALC)
2	2	12	10.7629	9.7013
3	2	12	5.6786	4.0521
4	2	12	371.9760	375.7494
-8	3	12	125.8864	131.7971
-7	3	12	107.3585	106.7066
-6	3	12	92.7688	87.6125
-5	3	12	3.7765	4.0521
-4	3	12	47.2371	47.6267
-2	3	12	236.9228	237.4956
0	3	12	1215.1911	1206.1288
1	3	12	2.8182	.2511
2	3	12	371.2924	377.4328
3	3	12	88.0181	87.6125
-7	4	12	64.3195	65.9940
0	4	12	53.7997	54.0973
3	4	12	110.0572	106.7066
-8	5	12	25.8016	29.4922
-5	5	12	13.2026	11.9263
-2	5	12	6.6187	4.0521
-1	5	12	366.2656	364.7913
0	5	12	18.6841	11.9267
1	5	12	178.8657	181.9847
3	5	12	129.3131	131.7971
-8	6	12	47.7407	46.4647
-6	6	12	41.4543	51.9150
-5	6	12	178.0287	181.9847
1	6	12	345.0124	350.0742
2	6	12	226.0368	214.3906
-6	7	12	345.7457	350.0755
-5	7	12	64.9776	66.5010
-2	7	12	439.7286	442.0320
-1	7	12	224.2837	217.9408
-6	8	12	215.1243	214.3900
-8	0	13	4.8661	4.3647
-7	0	13	6.2693	4.2289
-6	0	13	155.2839	148.6362
-5	0	13	18.9181	17.4950
-1	0	13	23.2416	22.8392
2	0	13	12.2109	10.1529
3	0	13	18.5402	15.5047
4	0	13	3.6642	.1756
-8	1	13	85.5397	87.6226
-7	1	13	69.8588	66.0938
-6	1	13	52.1426	42.5367
-5	1	13	24.0174	22.7616
0	1	13	23.0106	22.8392
1	1	13	51.5453	46.5505
2	1	13	646.7219	644.7187
4	1	13	4.9992	3.4001
-8	2	13	15.5871	10.4310
-7	2	13	41.4696	36.6841
-6	2	13	268.5261	274.1270
-5	2	13	232.1191	214.6813
-1	2	13	50.1058	46.5502
0	2	13	13.5011	10.1529
1	2	13	228.0725	231.0886
2	2	13	3.3105	.5204
3	2	13	92.7509	89.4057
-8	3	13	4.8812	3.2665
-6	3	13	97.1991	93.1326
-5	3	13	87.7730	89.4057
-2	3	13	230.8739	231.0877
-1	3	13	638.0926	644.7175
1	3	13	62.8693	62.8268
2	3	13	219.7875	214.6814
3	3	13	97.8026	93.1326
4	3	13	116.8381	125.4489
-8	4	13	26.2308	27.1513
-7	4	13	125.2550	125.4489
-6	4	13	13.5105	12.6596
-2	4	13	1.8802	.5204
-1	4	13	158.4682	158.3643
1	4	13	21.8717	22.7616
2	4	13	264.5418	274.1270
3	4	13	35.4538	34.9430
-8	5	13	4.7110	5.8402
-7	5	13	235.6495	225.3962
-6	5	13	650.6900	641.7582
-2	5	13	89.5721	89.4056
2	5	13	38.1669	36.6841
3	5	13	4.8859	3.2665
4	5	13	46.3009	54.7977
-8	6	13	13.7576	12.4571
-7	6	13	2.8436	4.7040
-1	6	13	648.2682	641.7559
0	6	13	152.2870	148.6362
1	6	13	71.1081	66.0938
2	6	13	11.7299	10.4310
3	6	13	19.8612	16.7647
-8	7	13	42.8224	40.6941
-7	7	13	11.3750	4.2289
-2	7	13	237.9584	225.3966
-1	7	13	2.9029	4.7040
0	7	13	4.0734	4.2289
1	7	13	85.5507	87.6226
-8	8	13	2.3255	4.3649
-7	8	13	85.0711	87.6218
-6	8	13	15.2974	10.4312
-2	8	13	11.8499	12.4571
0	8	13	5.1621	4.3647
-6	0	14	252.1342	242.1495
1	0	14	65.7370	55.2871
2	0	14	68.1720	68.7274
3	0	14	10.7213	10.8080
4	0	14	368.2700	355.9649
-8	1	14	1.0603	3.7762
-7	1	14	34.7727	40.1570
-6	1	14	5.2390	3.0611
-1	1	14	61.6905	55.2871
0	1	14	63.0491	55.2875

Table 10. (Concluded)

H	K	L	Y(OBS)	Y(CALC)
1	1	14	576.6784	545.6595
2	1	14	6.1489	3.9849
3	1	14	139.6816	134.3502
4	1	14	101.9194	94.9464
-7	2	14	539.7169	535.7489
-6	2	14	30.4601	25.7785
-1	2	14	576.0978	545.6602
0	2	14	71.0941	68.7269
1	2	14	4.8091	3.6745
2	2	14	619.4697	585.6978
3	2	14	184.5691	183.5268
4	2	14	56.6183	64.4258
-8	3	14	377.4746	381.9664
-7	3	14	427.4856	438.9401
-1	3	14	7.2589	3.9848
0	3	14	16.7745	10.8080
1	3	14	41.9635	33.6859
2	3	14	3.3739	.0358
3	3	14	252.8927	239.6252
4	3	14	32.5009	28.6327
-8	4	14	16.6470	18.8604
-7	4	14	29.8120	28.6327
-6	4	14	54.3066	64.4258
-1	4	14	137.3751	134.3501
0	4	14	375.4697	355.9663
1	4	14	48.9967	42.5090
2	4	14	26.7109	25.7784
3	4	14	431.3967	438.9401
4	4	14	17.4215	18.8604
-8	5	14	91.2826	101.7862
-7	5	14	146.2349	145.7308
-1	5	14	104.8446	94.9465
0	5	14	320.8644	333.8024
1	5	14	3.9047	3.0611
3	5	14	365.0507	381.9664
-8	6	14	78.2330	81.2101
-1	6	14	91.8350	93.3787
0	6	14	251.3054	242.1495
1	6	14	36.2169	40.1570
2	6	14	12.2379	12.0517
3	6	14	321.5920	313.9366
-8	7	14	100.3779	104.2585
-1	7	14	4.8947	6.9984
1	7	14	.2588	3.7762
2	7	14	3.5486	2.7658
0	8	14	460.9164	478.6988
3	0	15	3.2251	2.1740
4	0	15	72.8119	71.9516
5	0	15	2.3545	2.2240
0	1	15	20.5899	16.3662
1	1	15	7.4012	7.5629
2	1	15	184.2447	185.7936
3	1	15	1.1905	.0100
4	1	15	1.4342	.2330
5	1	15	223.3040	228.3202
0	2	15	10.0437	5.3247
1	2	15	317.8935	321.2850
2	2	15	.5972	.0232
3	2	15	209.0030	209.1625
4	2	15	63.7320	67.7755
5	2	15	80.3175	81.0314
1	3	15	142.1798	142.6437
2	3	15	81.7414	77.1250
3	3	15	57.0119	49.8111
4	3	15	105.2875	114.4995
2	4	15	39.1611	38.9919

Table 11. Structure Factors for Chlorapatite at 50°C

H	K	L	Y(OBS)	Y(CALC)
0	1	3	27.5906	26.4266
-2	0	4	33.3626	37.9549
-2	1	4	68.5418	60.1258
0	1	4	698.2634	728.6985
-2	1	5	217.1141	223.9266
-1	1	5	70.9905	77.7876
-1	2	5	214.3629	223.9274
0	2	5	524.0556	543.0873
1	2	5	1859.6941	1796.9146
-2	0	6	600.5750	594.4210
1	0	6	529.2733	513.3500
2	0	6	596.7219	594.4218
-1	1	6	520.4152	513.3500
0	1	6	523.2395	513.3517
2	1	6	2.5738	1.1460
-3	2	6	2.0094	1.1460
0	3	6	183.7047	176.8837
-3	0	7	115.7840	113.4297
-2	1	7	21.2011	21.5060
-1	1	7	42.1263	39.8900
0	1	7	40.6550	39.8901
1	1	7	24.5051	21.5060
0	2	7	9.6764	3.5720
1	2	7	1697.8459	1689.5851
2	2	7	12.5013	14.1289
-4	3	7	105.1408	94.2298
-3	3	7	122.9259	113.4303
-1	3	7	1842.9448	1829.2307
0	3	7	123.5017	113.4297
1	3	7	988.1466	969.5511
-3	0	8	1693.6855	1705.0174
-1	0	8	419.0646	413.2469
1	0	8	420.3400	413.2457
2	0	8	118.8585	128.0024
2	1	8	727.6930	757.2143
-4	2	8	22.0431	19.7938
0	2	8	121.4061	128.0019
1	2	8	1642.7547	1620.0291
2	2	8	23.9095	19.7938
-5	3	8	7.3045	2.7488
-1	3	8	735.6137	757.2189
0	3	8	1698.1744	1705.0175
-4	4	8	49.6961	55.9024
-2	4	8	22.0484	19.7938
-2	5	8	5.9002	2.7488
-4	0	9	34.8392	22.0550
-5	1	9	56.4936	51.1923
-4	1	9	300.0318	290.2320
-3	1	9	726.3861	722.4993
1	1	9	68.6315	67.6394
-4	2	9	3.8900	.1177
-3	2	9	1911.6197	1907.3141
1	2	9	725.3178	722.4993
2	2	9	2.0530	.1177
-4	3	9	357.9578	356.3951
-2	3	9	718.5207	722.4983
-1	3	9	1885.3139	1907.3124
0	3	9	48.1125	45.4125
1	3	9	302.7630	290.2321
2	3	9	602.6145	616.9926
-5	4	9	1.4451	.6314
-2	4	9	5.7894	.1176
-1	4	9	354.8177	356.3947
0	4	9	23.3881	22.0550
1	4	9	53.6332	51.1923
-5	5	9	12.9478	13.1475
-4	5	9	52.7976	51.1920
-2	5	9	440.4011	430.4375
-1	5	9	1.1514	.6314
-3	0	10	38.2850	33.9449
-1	0	10	256.9402	274.0499
0	0	10	2728.7052	2728.8355
2	0	10	264.3004	267.0503
-6	1	10	154.3193	146.0688
-4	1	10	569.7277	562.6908
-1	1	10	253.3377	274.0486
0	1	10	254.5699	274.0499
1	1	10	1618.2214	1658.9365
3	1	10	242.5414	248.2994
-6	2	10	44.2063	39.8132
-5	2	10	4.7473	3.0105
-4	2	10	1234.0536	1242.6608
-3	2	10	7.9542	7.7754
-2	2	10	263.4723	267.0503
-1	2	10	1588.5390	1658.9365
1	2	10	124.7007	116.8804
2	2	10	1246.3439	1242.6608
3	2	10	681.8111	686.0906
-4	3	10	254.3744	248.2994
-2	3	10	122.3856	116.8787
-1	3	10	8.2425	7.7753
1	3	10	561.6655	562.6908
2	3	10	3.3578	3.0105
3	3	10	534.5312	524.4763
-5	4	10	78.6341	72.5721
-4	4	10	907.6015	933.3165
-2	4	10	1218.9029	1242.6612
-1	4	10	244.3623	248.2986
0	4	10	896.2563	933.3195
1	4	10	128.7877	124.8414
-6	5	10	65.0599	64.2286
-5	5	10	850.4188	860.5316
-4	5	10	129.4129	124.8413
-1	5	10	80.0264	72.5722
1	5	10	162.3023	146.0688

Table 11. (Continued)

H	K	L	Y(OBS)	Y(CALC)
-5	6	10	152.6654	146.0676
-4	6	10	41.2735	39.8133
-1	0	11	64.4727	61.6489
1	0	11	64.8701	61.6491
-5	1	11	1.3733	.2002
-4	1	11	373.2838	373.0614
-1	1	11	68.6286	61.6491
1	1	11	13.0840	9.4245
3	1	11	37.2739	29.0832
-6	2	11	66.0006	67.0189
-5	2	11	478.5418	468.3842
-2	2	11	15.0227	13.5571
-1	2	11	16.8144	9.4248
0	2	11	16.1721	13.5570
1	2	11	712.3818	703.0889
2	2	11	21.7313	19.1783
-7	3	11	72.0955	63.1241
-5	3	11	411.0381	409.5009
-4	3	11	35.8463	29.0832
-2	3	11	705.6958	703.0891
-1	3	11	544.7509	535.0090
0	3	11	10.5825	9.7593
2	3	11	476.8112	468.3842
3	3	11	323.8347	324.3500
-7	4	11	238.3548	227.2344
-5	4	11	4.4561	5.0666
-4	4	11	175.8468	161.3179
-2	4	11	21.7867	19.1780
-1	4	11	33.7063	29.0832
0	4	11	175.6531	161.3169
1	4	11	4.6521	.2002
3	4	11	68.1504	63.1241
-5	5	11	63.0349	56.3142
-2	5	11	410.0643	409.4999
-1	5	11	8.2959	5.0666
0	5	11	52.8168	56.3137
1	5	11	336.9885	335.9907
-6	6	11	38.6722	39.8640
-2	6	11	168.3761	160.7672
-1	6	11	670.3531	697.0081
-6	0	12	50.9234	51.0412
-5	0	12	11.7156	11.8657
-4	0	12	45.7873	44.1034
-1	0	12	57.0825	55.5418
1	0	12	53.4604	55.5414
2	0	12	94.0135	92.3708
3	0	12	1087.4161	1085.4523
-6	1	12	165.2022	162.4553
-5	1	12	427.4767	406.1581
-4	1	12	3.5462	.3799
-1	1	12	59.3919	55.5414
0	1	12	55.6389	55.5418
2	1	12	325.7203	323.9772
3	1	12	44.3979	47.0100
4	1	12	320.2544	323.4650
-7	2	12	58.9909	62.8026
-5	2	12	329.9789	333.6556
-4	2	12	12.2193	10.8090
-2	2	12	93.1882	92.3708
-1	2	12	2.1229	.0473
0	2	12	92.8385	92.3700
2	2	12	11.6586	10.8090
3	2	12	4.4971	2.6587
4	2	12	331.5740	333.3471
-7	3	12	92.1273	91.7663
-6	3	12	80.9503	76.6131
-5	3	12	6.0168	2.6587
-2	3	12	210.0445	214.1116
-1	3	12	319.5252	323.9799
0	3	12	1095.2820	1085.4528
1	3	12	4.2566	.3799
2	3	12	328.0576	333.6556
3	3	12	82.4356	76.6131
-7	4	12	56.0873	62.8193
-6	4	12	327.7912	333.3471
-5	4	12	329.6031	323.4650
-2	4	12	15.1460	10.8090
-1	4	12	48.5568	47.0096
0	4	12	45.4548	44.1034
1	4	12	420.0441	406.1581
2	4	12	624.2971	649.6964
3	4	12	96.7571	91.7663
-7	5	12	397.4568	403.4975
-6	5	12	535.2097	534.2197
-5	5	12	12.7732	11.8654
-2	5	12	5.0953	2.6587
-1	5	12	324.5481	323.4649
0	5	12	15.2920	11.8657
1	5	12	162.5589	162.4553
2	5	12	59.7286	62.8026
-7	6	12	199.7644	198.0453
-6	6	12	52.2095	51.0409
-5	6	12	163.8597	162.4553
-2	6	12	326.3230	333.3468
0	6	12	49.9616	51.0412
1	6	12	305.1382	311.3606
-6	7	12	313.9207	311.3617
-5	7	12	60.4388	62.8024
-2	7	12	395.3263	403.4964
-1	7	12	196.9878	198.0449
-7	0	13	4.4320	5.4570
-6	0	13	134.4227	133.1779
-5	0	13	17.6199	15.3501
-1	0	13	22.5541	18.1711
1	0	13	23.3716	18.1712
2	0	13	13.6054	9.3656
4	0	13	1.8799	.0954
-7	1	13	55.3797	52.0662
-6	1	13	44.8567	35.2930
-5	1	13	21.3479	19.7275

Table 11. (Concluded)

H	K	L	Y(OBS)	Y(CALC)
-1	1	13	21.2880	18.1712
0	1	13	18.9867	18.1711
2	1	13	565.5634	559.4237
4	1	13	6.7539	2.9522
-8	2	13	12.9801	8.1199
-7	2	13	36.5096	32.9199
-6	2	13	243.6373	233.9025
-5	2	13	202.0038	189.3361
-2	2	13	10.8537	9.3656
-1	2	13	40.1172	38.0997
0	2	13	11.3118	9.3656
1	2	13	203.0618	197.6507
3	2	13	81.1226	73.7167
4	2	13	12.7437	10.9598
-8	3	13	5.0566	3.3508
-7	3	13	30.8734	32.6038
-6	3	13	88.3508	80.6148
-5	3	13	80.5723	73.7167
-1	3	13	557.9145	559.4227
1	3	13	57.0321	55.9860
2	3	13	198.7601	189.3361
4	3	13	105.5057	114.0241
-8	4	13	20.7741	26.3691
-7	4	13	110.7067	114.0241
-6	4	13	11.2715	10.9598
-5	4	13	4.3048	2.9522
-2	4	13	.9416	.1053
-1	4	13	141.1122	139.2012
0	4	13	1.1232	.0954
1	4	13	22.2839	19.7275
2	4	13	235.6449	233.9025
3	4	13	32.9550	32.6038
4	4	13	22.9671	26.3691
-8	5	13	5.3579	7.1305
-6	5	13	566.7457	555.2052
-5	5	13	18.0162	15.3503
-2	5	13	77.6549	73.7166
-1	5	13	4.3670	2.9523
0	5	13	15.7453	15.3501
1	5	13	41.0067	35.2930
-8	6	13	11.7939	11.4436
-7	6	13	2.9545	4.2000
-6	6	13	136.9830	133.1778
-2	6	13	12.1571	10.9595
-1	6	13	564.3342	555.2032
0	6	13	134.6068	133.1779
1	6	13	53.1925	52.0662
2	6	13	10.0837	8.1199
-6	7	13	56.7683	52.0658
-1	7	13	5.7023	4.2001
-6	8	13	12.3349	8.1200
-2	8	13	10.6531	11.4436
-7	0	14	198.1222	206.7080
-1	0	14	55.8616	52.5892
0	0	14	244.0364	227.4470
1	0	14	57.1476	52.5889
2	0	14	59.2107	63.4001
3	0	14	9.9424	8.6884
4	0	14	309.9393	313.3874
-8	1	14	3.6120	5.9614
-7	1	14	30.9744	30.3930
-6	1	14	5.8787	3.6926
-1	1	14	55.2591	52.5889
1	1	14	498.7253	474.2924
2	1	14	5.7295	3.6640
3	1	14	116.8466	116.3149
4	1	14	92.4392	82.9112
-8	2	14	10.0808	8.9159
-6	2	14	27.0104	20.4620
-1	2	14	498.0089	474.2929
1	2	14	1.9899	1.7447
2	2	14	516.8202	501.7008
3	2	14	161.5686	166.6451
-8	3	14	323.2945	330.1787
-7	3	14	367.1417	370.0791
-6	3	14	215.4620	206.2302
-1	3	14	4.9923	3.6639
0	3	14	9.7197	8.6884
1	3	14	35.5836	32.2460
2	3	14	1.2244	.2311
3	3	14	215.1179	206.2302
4	3	14	28.3197	27.1050
-8	4	14	14.9994	14.2094
-7	4	14	25.8964	27.1050
-6	4	14	46.4931	49.5860
-1	4	14	116.5821	116.3149
0	4	14	316.0154	313.3885
1	4	14	42.7485	36.9493
2	4	14	22.6848	20.4620
3	4	14	361.0206	370.0791
4	4	14	14.5185	14.2094
-7	5	14	117.4593	116.6749
-1	5	14	96.0921	82.9112
0	5	14	284.2918	295.7687
1	5	14	5.2395	3.6926
2	5	14	438.3773	453.7475
3	5	14	314.8135	330.1787
4	5	14	17.4710	14.8771
-8	6	14	70.2582	76.8152
-7	6	14	7.7287	5.8792
-1	6	14	71.9826	77.8004
0	6	14	210.5715	207.5729
1	6	14	25.5079	30.3929
2	6	14	9.9684	8.9159
-8	7	14	88.2736	89.6414
-1	7	14	7.1258	5.8791
0	7	14	196.9149	206.7080
1	7	14	1.7987	5.9614
1	0	15	19.5540	14.7791
2	0	15	5.1717	4.6591

Table 12. Structure Factors for Chlorapatite at 100°C

H	K	L	Y(OBS)	Y(CALC)
0	1	3	27.6589	26.2630
-2	0	4	23.7391	25.8488
-2	1	4	77.6304	70.4187
0	1	4	653.8496	680.7809
1	1	5	204.0056	215.8676
-1	2	5	204.8797	215.8684
0	2	5	492.1540	512.4896
1	2	5	1815.6483	1757.2086
-1	0	6	472.0647	458.6058
2	0	6	534.5941	537.8214
-1	1	6	466.4389	458.6042
0	1	6	466.6915	458.6058
2	1	6	2.0657	.0813
-3	2	6	.8743	.0813
-2	2	6	540.9906	537.8214
0	2	6	538.3606	537.8208
1	2	6	301.4179	313.5992
-2	1	7	17.8172	19.1215
0	1	7	38.2449	37.9043
0	2	7	8.2122	3.7208
1	2	7	1611.7034	1607.0765
-4	3	7	100.9068	96.3195
-3	3	7	111.0644	102.9038
-1	3	7	1753.6146	1738.0600
0	3	7	108.2087	102.9033
1	3	7	946.7004	917.6144
-4	0	8	50.4293	59.8397
-2	0	8	98.8890	99.3921
1	0	8	360.0828	352.5782
2	0	8	96.4443	99.3925
-4	1	8	291.3023	290.7425
-1	1	8	363.8376	352.5782
0	1	8	362.6964	352.5794
-5	2	8	717.6777	724.1812
-4	2	8	13.4409	9.2018
-1	2	8	7.5370	1.9948
2	2	8	12.7929	9.2018
-5	3	8	9.9349	5.1973
0	3	8	1681.1360	1704.3758
1	3	8	299.5531	290.7425
-4	0	9	33.6435	23.8007
-3	0	9	41.6252	39.0132
-1	0	9	14.0431	11.3321
3	0	9	43.9928	39.0137
-4	1	9	282.0150	271.7748
1	1	9	58.3311	58.7970
2	1	9	1771.9867	1766.2421
1	2	9	664.3419	670.5424
2	2	9	1.1589	.1757
-5	3	9	405.0522	393.8806

H	K	L	Y(OBS)	Y(CALC)
-1	3	9	1751.3952	1766.2403
0	3	9	43.4664	39.0132
1	3	9	277.8477	271.7748
2	3	9	543.5922	556.6244
-5	4	9	2.6917	1.0370
-4	4	9	23.1747	23.8009
-2	4	9	2.7470	.1757
-1	4	9	335.3364	337.7262
0	4	9	24.8615	23.8007
1	4	9	47.6691	44.4753
-5	5	9	10.7629	9.3661
-2	5	9	399.3082	393.8797
-1	5	9	2.4000	1.0370
-3	0	10	31.8655	25.3992
0	0	10	2368.5365	2368.5371
2	0	10	233.2203	237.5075
-6	1	10	136.5643	126.0566
-5	1	10	120.0188	120.9555
-4	1	10	485.1106	479.4368
-1	1	10	212.4475	240.1406
0	1	10	220.2483	240.1418
3	1	10	196.5586	207.8927
-6	2	10	42.4268	39.8397
-4	2	10	1144.0157	1151.0516
-3	2	10	5.1269	3.7745
-2	2	10	232.7523	237.5075
0	2	10	239.0165	237.5068
1	2	10	109.3846	105.6333
2	2	10	1149.0484	1151.0516
-2	3	10	109.2439	105.6318
-1	3	10	4.1448	3.7744
0	3	10	32.7137	25.3992
1	3	10	479.0161	479.4368
2	3	10	3.8406	3.0715
3	3	10	496.7467	493.4570
-5	4	10	82.6863	78.5315
-2	4	10	1111.2184	1151.0520
-1	4	10	199.5785	207.8921
0	4	10	770.8254	821.7419
1	4	10	121.8531	120.9555
2	4	10	42.3777	39.8397
-6	5	10	61.8487	62.6621
-5	5	10	751.9531	769.5886
-4	5	10	124.9724	120.9555
-2	5	10	597.2660	604.9953
-1	5	10	84.7900	78.5315
1	5	10	134.6166	126.0566
-5	6	10	135.8220	126.0545
-4	6	10	39.3726	39.8397
-2	6	10	8.2905	2.2336
-1	6	10	62.0583	62.6627
-6	0	11	37.9913	37.1756
-4	0	11	160.2407	147.3377
-3	0	11	10.4455	7.6849
-1	0	11	56.5792	55.2126

Table 12. (Continued)

H	K	L	Y(OBS)	Y(CALC)
1	0	11	57.7914	55.2127
-5	1	11	1.3939	.0893
-4	1	11	326.3668	333.9514
0	1	11	58.9798	55.2126
1	1	11	12.0869	8.8132
-2	2	11	11.4336	11.1046
-1	2	11	15.8516	8.8134
0	2	11	12.7371	11.1045
1	2	11	632.4482	624.3450
2	2	11	17.8626	17.6615
3	2	11	362.2739	358.5647
-7	3	11	59.2229	53.9135
-6	3	11	270.7076	282.5703
-5	3	11	360.4908	358.5647
-2	3	11	621.9307	624.3451
-1	3	11	482.0108	479.4014
0	3	11	9.0972	7.6849
2	3	11	412.9661	402.3873
3	3	11	274.1536	282.5703
-7	4	11	189.9258	193.0994
0	4	11	160.8769	147.3377
1	4	11	3.2901	.0893
3	4	11	63.4757	53.9135
-5	5	11	47.5191	44.2080
-2	5	11	357.3208	358.5637
-1	5	11	8.8115	5.5753
0	5	11	43.1273	44.2076
1	5	11	290.8561	278.5428
-6	6	11	36.0412	37.1753
-5	6	11	288.1367	278.5429
-1	6	11	591.0057	614.1605
0	6	11	36.7044	37.1756
-6	0	12	40.9022	42.3866
-5	0	12	10.9161	10.9182
0	0	12	3841.6341	3884.3066
1	0	12	50.9647	49.8432
2	0	12	79.9927	80.8360
3	0	12	976.4187	975.0156
4	0	12	40.7962	35.6318
-7	1	12	249.3566	252.7836
-6	1	12	139.9356	141.7964
-5	1	12	376.7022	363.5061
-4	1	12	2.6762	.9028
-1	1	12	49.9841	49.8432
0	1	12	50.1890	49.8435
2	1	12	289.5220	299.9137
4	1	12	280.8384	274.6043
-7	2	12	55.6709	52.3967
-6	2	12	541.9867	573.1145
-5	2	12	283.4886	287.0575
-4	2	12	11.3097	12.5650
-2	2	12	83.5430	80.8360
0	2	12	81.4247	80.8354
1	2	12	183.0019	182.5740
2	2	12	10.8396	12.5650
3	2	12	4.1795	2.4799
4	2	12	282.4036	282.1575
-7	3	12	75.8485	74.4030
-6	3	12	76.1170	67.2423
-5	3	12	6.6403	2.4799
-1	3	12	288.3307	299.9160
0	3	12	981.6369	975.0159
1	3	12	3.0886	.9028
2	3	12	284.0308	287.0576
3	3	12	72.1092	67.2423
-7	4	12	47.4751	51.8531
-6	4	12	273.1973	282.1575
-5	4	12	281.9674	274.6043
-2	4	12	15.6301	12.5650
-1	4	12	44.9154	45.7975
0	4	12	36.5224	35.6317
1	4	12	374.7123	363.5061
3	4	12	76.8173	74.4030
-6	5	12	465.3182	463.9714
-5	5	12	11.3687	10.9180
-2	5	12	3.6764	2.4799
0	5	12	14.8896	10.9182
1	5	12	139.7723	141.7964
2	5	12	51.4675	52.3967
-7	6	12	174.6682	172.6248
-6	6	12	44.9258	42.3864
-5	6	12	137.7705	141.7964
-2	6	12	269.7567	282.1572
-1	6	12	454.4985	463.9744
0	6	12	45.1452	42.3866
1	6	12	254.6316	252.7836
-5	7	12	54.1534	52.3965
-2	7	12	349.5787	363.1383
-1	7	12	177.3410	172.6245
-7	0	13	3.8546	5.5773
-6	0	13	113.7649	114.1145
-5	0	13	11.9139	11.3123
-4	0	13	1.5989	.0104
-1	0	13	19.9732	14.8033
1	0	13	18.2862	14.8034
2	0	13	7.8097	8.3716
4	0	13	1.2972	.0104
-7	1	13	40.6690	38.1251
-6	1	13	35.6277	27.7983
-1	1	13	16.5703	14.8034
0	1	13	18.6492	14.8033
1	1	13	31.9034	29.2230
2	1	13	480.5395	480.7746
4	1	13	5.2429	3.1881
-8	2	13	8.0000	5.5050
-7	2	13	29.2536	26.5040
-6	2	13	205.6520	204.0935
-5	2	13	164.7586	160.0886
-2	2	13	9.8317	8.3716
-1	2	13	33.4440	29.2228

Table 12. (Concluded)

H	K	L	Y(OBS)	Y(CALC)
0	2	13	8.8365	8.3716
1	2	13	166.0483	166.8687
2	2	13	3.9543	.0176
3	2	13	63.0334	60.7085
4	2	13	10.3045	7.0251
-7	3	13	26.3273	26.2022
-6	3	13	75.3874	68.3878
-5	3	13	61.4095	60.7085
-2	3	13	171.9282	166.8681
-1	3	13	479.2250	480.7737
1	3	13	47.8143	50.0022
2	3	13	163.4133	160.0886
3	3	13	75.5380	68.3878
4	3	13	89.0208	94.6066
-8	4	13	19.7529	22.3334
-7	4	13	90.6719	94.6066
-6	4	13	7.9326	7.0251
-1	4	13	127.6262	122.7178
0	4	13	1.9619	.0104
1	4	13	16.9128	15.8481
2	4	13	207.1531	204.0935
3	4	13	29.0787	26.2022
4	4	13	21.4943	22.3334
-8	5	13	6.4473	7.0352
-7	5	13	163.6874	150.8744
-6	5	13	476.0893	471.4009
-5	5	13	12.8836	11.3125
-2	5	13	63.4790	60.7084
-1	5	13	4.0998	3.1881
0	5	13	15.3819	11.3123
1	5	13	32.6433	27.7983
2	5	13	30.9035	26.5040
3	5	13	3.6801	2.0007
-8	6	13	8.7663	8.1190
-7	6	13	4.0052	3.0992
-1	6	13	479.0297	471.3992
0	6	13	112.7293	114.1145
1	6	13	40.7505	38.1251
-6	7	13	41.9377	38.1248
-1	7	13	5.4891	3.0993
0	7	13	4.7116	5.5773
-6	8	13	9.3239	5.5051
-2	8	13	8.8551	8.1190
-7	0	14	166.7988	172.7918
-6	0	14	172.2192	175.1388
-1	0	14	50.2801	50.0042
0	0	14	198.4359	187.1848
1	0	14	50.2504	50.0039
2	0	14	54.6694	59.9082
3	0	14	7.4386	5.9852
4	0	14	260.6452	264.7790
-8	1	14	3.8540	5.6476
-7	1	14	20.6105	19.0679
-6	1	14	5.9834	4.7172
-1	1	14	50.5528	50.0039

H	K	L	Y(OBS)	Y(CALC)
0	1	14	51.5037	50.0042
1	1	14	420.0016	406.2850
2	1	14	7.3425	3.0140
4	1	14	83.1151	73.7253
-8	2	14	7.9413	6.6491
-7	2	14	367.5353	371.7343
-6	2	14	20.5787	15.6355
0	2	14	58.7455	59.9078
2	2	14	442.2557	410.1123
3	2	14	143.3232	148.3750
4	2	14	34.5737	33.3037
-8	3	14	266.7235	271.5885
-6	3	14	180.0084	171.2113
-1	3	14	4.3943	3.0139
0	3	14	9.1478	5.9852
1	3	14	31.6136	27.9243
2	3	14	2.1705	.7316
3	3	14	180.2559	171.2113
4	3	14	26.9920	25.3729
-8	4	14	8.7699	11.0412
-7	4	14	23.8197	25.3729
-6	4	14	35.0893	33.3037
-1	4	14	99.1111	97.7690
0	4	14	266.3604	264.7799
1	4	14	34.8451	30.2554
2	4	14	21.5239	15.6355
3	4	14	301.8194	302.6002
4	4	14	11.8760	11.0412
-8	5	14	67.0711	77.4527
-7	5	14	91.9784	90.0260
-1	5	14	83.8744	73.7253
0	5	14	246.2689	257.4110
1	5	14	4.1794	4.7172
2	5	14	365.9784	371.7343
3	5	14	260.9879	271.5885
4	5	14	15.1402	12.9454
-8	6	14	64.2923	65.9460
-7	6	14	4.8193	5.7881
-1	6	14	60.1081	58.9154
0	6	14	174.7026	175.1388
1	6	14	20.8437	19.0679
2	6	14	6.9859	6.6491
-8	7	14	77.9278	77.7179
-1	7	14	5.9976	5.7880
0	7	14	164.9935	172.7918
1	0	15	13.3392	12.8606
2	0	15	3.8044	3.9522
3	0	15	2.0722	1.3567
4	0	15	53.1385	51.7962
5	0	15	2.5632	2.5029
0	1	15	12.4409	12.8605
1	1	15	5.8184	4.2995
2	1	15	126.1396	125.7484
3	1	15	.3933	.2322
4	1	15	.7397	.2511

Table 13. Structure Factors for Chlorapatite at 150°C

H	K	L	Y(OBS)	Y(CALC)
0	1	3	29.0041	28.0586
-2	0	4	14.6024	18.3967
1	1	4	98.5719	99.5782
0	2	4	15.9680	18.3967
1	0	5	60.1464	66.4804
-1	1	5	65.3753	66.4804
1	1	5	205.7534	214.3079
-1	2	5	201.1219	213.3087
0	2	5	471.6969	485.8791
1	2	5	1731.6545	1709.4628
-2	3	5	1710.7224	1706.4631
-3	0	6	126.7340	125.3041
-1	0	6	413.1322	406.2217
1	0	6	420.4273	406.2202
2	0	6	481.4699	481.4512
-1	1	6	411.3653	406.2203
0	1	6	413.8822	406.2217
2	1	6	3.5487	2.5292
-3	2	6	4.7376	2.5292
-2	2	6	478.9717	481.4512
1	2	6	272.1815	274.2881
-1	3	6	6.8230	2.5292
0	3	6	125.9701	125.3041
-3	0	7	101.8981	99.5422
-2	0	7	-7.0641	-3.2631
1	0	7	36.2543	35.6126
2	0	7	5.1854	-3.2631
-1	1	7	37.9115	35.6126
1	1	7	14.6690	14.0752
2	1	7	1683.9022	1658.0873
0	2	7	4.6853	-3.2631
1	2	7	1541.4478	1546.2422
2	2	7	12.5002	11.8629
-3	3	7	104.7141	99.5426
-1	3	7	1675.3399	1658.0857
0	3	7	103.7721	99.5422
1	3	7	902.0954	869.8922
-4	0	8	56.7778	64.0758
-1	0	8	329.2592	312.5759
1	0	8	316.0369	312.5750
2	0	8	75.2388	78.6163
-4	1	8	259.8533	256.4295
-1	1	8	311.0030	312.5758
0	1	8	310.6672	312.5760
1	1	8	7.1107	6.3032
2	1	8	592.3464	617.2846
-4	2	6	7.3067	3.1817
-3	2	8	603.1388	617.2846
-1	2	8	-12.2559	6.3031
1	2	8	1293.9494	1284.7992
0	3	8	1659.5766	1689.5090
1	3	8	266.8583	256.4295
2	3	8	618.8956	626.9031
-4	4	8	57.1319	64.0761
-2	4	8	4.5474	3.1817
0	4	8	59.4540	64.0758
-2	5	8	9.3864	9.5982
-4	0	9	25.2856	21.0225
3	0	9	36.3308	35.9866
-1	1	9	16.3699	13.4814
0	1	9	15.3326	13.4814
1	1	9	47.9067	53.8026
2	1	9	1652.2325	1677.6087
3	1	9	319.2847	323.0272
0	2	9	6.5604	4.8609
2	2	9	2.0246	.0319
-4	3	9	324.0249	323.0272
-2	3	9	628.3667	627.6319
-1	3	9	1639.0910	1677.6072
1	3	9	266.9583	256.5422
2	3	9	499.8483	494.2647
-5	4	9	.9900	.5556
-4	4	9	27.6240	21.0228
-3	4	9	279.2756	256.5422
-2	4	9	1.1895	.0319
-5	5	9	7.9970	7.7014
-2	5	9	373.9185	372.7888
0	5	9	15.3272	7.7012
-1	0	10	196.7669	204.9428
0	0	10	2090.2113	2098.5217
1	0	10	192.8535	204.9419
2	0	10	216.2808	216.6956
-3	1	10	103.6015	89.1244
-1	1	10	190.3664	204.9419
0	1	10	193.5148	204.9428
1	1	10	1436.7138	1492.1102
3	1	10	172.3419	183.1324
-5	2	10	5.5783	3.0113
-3	2	10	3.8941	2.5895
-1	2	10	1436.0800	1492.1103
0	2	10	216.8467	216.6949
1	2	10	99.2936	89.1244
3	2	10	552.7689	552.2464
0	3	10	26.4111	17.3186
1	3	10	413.4293	403.7505
2	3	10	5.9960	3.0113
3	3	10	473.8995	471.2428
-6	4	10	3.0143	.3326
-5	4	10	93.8522	90.1268
-2	4	10	1090.0914	1102.6778
0	4	10	698.3575	721.4649
1	4	10	123.9445	117.3873
2	4	10	44.6391	38.1582
-6	5	10	65.2230	65.8835
-2	5	10	553.8695	552.2490

Table 13. (Continued)

H	K	L	Y(OBS)	Y(CALC)
-1	5	10	93.3940	90.1268
0	5	10	719.9727	718.9675
-4	6	10	39.7801	38.1583
-2	6	10	3.8731	.3326
-4	0	11	152.2678	140.9196
-3	0	11	10.1354	6.9453
-1	0	11	55.3799	49.5140
-2	0	11	9.2157	9.1541
-5	1	11	.6329	.3556
-1	1	11	57.6157	49.5141
1	1	11	13.5974	11.1756
-2	1	11	450.2288	438.1797
3	1	11	25.9850	20.8180
-6	2	11	62.4903	60.6688
-4	2	11	24.8155	15.3022
-1	2	11	13.8161	11.1758
0	2	11	10.6543	9.1541
-2	2	11	16.6467	15.3022
3	2	11	321.6981	319.7432
-7	3	11	55.7268	47.6037
-6	3	11	247.1021	255.9205
-5	3	11	333.5773	319.7432
-2	3	11	584.8089	570.8735
0	3	11	10.1247	6.9453
1	3	11	312.2992	311.9531
-3	3	11	244.6589	255.9205
-7	4	11	180.6048	183.4361
-6	4	11	127.7026	121.3181
-5	4	11	3.4000	4.4758
-4	4	11	152.5846	140.9204
-2	4	11	17.0579	15.3019
-1	4	11	23.7117	20.8180
0	4	11	146.9651	140.9196
1	4	11	5.3330	.3555
3	4	11	56.4412	47.6037
-6	5	11	545.5779	548.7079
-5	5	11	46.7262	38.8341
-4	5	11	1.2108	.3555
-2	5	11	327.0271	319.7425
-1	5	11	3.6901	4.4758
0	5	11	34.1942	38.8338
1	5	11	252.3624	240.5911
-6	6	11	33.1581	36.6564
-5	6	11	254.4897	240.5911
0	6	11	34.3508	36.6567
-6	0	12	42.6603	35.3498
-4	0	12	32.3075	28.8324
-1	0	12	44.4218	47.8247
1	0	12	45.4373	47.0294
2	0	12	75.0112	71.5993
3	0	12	898.6805	889.3738
-7	1	12	218.8757	222.8933
-4	1	12	4.2019	.7373
-1	1	12	45.1254	47.0294
0	1	12	47.2445	47.0297

H	K	L	Y(OBS)	Y(CALC)
1	1	12	5.9304	.1650
2	1	12	259.8548	269.0045
3	1	12	42.6978	44.6461
4	1	12	243.8617	236.3611
-7	2	12	48.9509	52.8351
-5	2	12	256.8023	249.0262
-4	2	12	13.6878	12.9478
-2	2	12	76.4780	71.5998
-1	2	12	1.7379	.1650
0	2	12	68.7611	71.5993
1	2	12	161.0408	158.3826
2	2	12	17.3982	12.9478
3	2	12	3.3155	1.7718
4	2	12	246.3308	247.4254
-7	3	12	64.8581	61.2077
-5	3	12	4.0228	1.7718
-2	3	12	157.5274	158.3831
-1	3	12	264.8946	269.0065
0	3	12	893.5490	889.3742
1	3	12	1.6453	.7373
2	3	12	238.7774	249.0262
3	3	12	67.1741	60.3759
-7	4	12	43.5701	45.8981
-2	4	12	13.2091	12.9478
-1	4	12	43.2871	44.6458
1	4	12	346.7184	331.7162
2	4	12	480.3219	501.4310
3	4	12	63.3479	61.2077
-5	5	12	11.6888	11.6338
-2	5	12	3.6869	1.7718
-1	5	12	241.7477	236.3610
0	5	12	13.6061	11.6340
1	5	12	125.3736	129.1315
2	5	12	47.5871	52.8351
-7	6	12	158.8465	152.6917
-6	6	12	40.6966	35.3496
-5	6	12	127.1413	129.1315
-2	6	12	242.9926	247.4252
0	6	12	42.1947	35.3493
1	6	12	221.5163	222.8933
-6	7	12	223.9011	222.8940
-5	7	12	50.9693	52.8349
-2	7	12	327.5692	338.7714
-1	7	12	158.1582	152.6913
-7	0	13	5.1911	2.0845
-5	0	13	11.1401	11.4560
-1	0	13	18.3021	14.9767
1	0	13	15.5225	14.9767
2	0	13	8.5040	8.4373
4	0	13	2.0024	.0115
-7	1	13	30.9881	28.3569
-6	1	13	29.2707	22.6593
-5	1	13	15.1903	14.3589
-1	1	13	17.2738	14.9767
0	1	13	14.8062	14.9767

Table 13. (Concluded)

H	K	L	Y(OBS)	Y(CALC)
2	1	13	418.3776	420.4979
3	1	13	111.4278	106.6265
4	1	13	3.8756	2.7338
-8	2	13	7.6338	3.2926
-7	2	13	22.6841	21.8945
-6	2	13	189.0669	186.0162
-1	2	13	22.0098	21.1471
1	2	13	144.0711	142.4648
3	2	13	49.4898	49.6939
4	2	13	8.2273	5.8670
-8	3	13	4.3679	1.9416
-7	3	13	23.8430	24.1544
-6	3	13	66.4365	63.0728
-5	3	13	53.7477	49.6939
-2	3	13	150.3119	142.4644
-1	3	13	417.7240	420.4972
0	3	13	14.7765	9.1137
1	3	13	44.9680	43.8752
2	3	13	143.9374	134.4021
3	3	13	66.4383	63.0728
4	3	13	76.0399	81.9855
-8	4	13	20.3728	22.4771
-7	4	13	81.7081	81.9855
-6	4	13	6.2334	5.8670
-5	4	13	2.5007	2.7338
-2	4	13	1.7221	.0231
-1	4	13	112.8890	106.6264
0	4	13	1.1267	.0115
2	4	13	189.7430	186.0162
3	4	13	23.3790	24.1544
4	4	13	17.0689	22.4771
-8	5	13	3.6960	5.2925
-7	5	13	140.6564	131.0397
-5	5	13	11.8923	11.4562
-2	5	13	51.5563	49.6937
-1	5	13	4.8450	2.7339
0	5	13	9.1142	11.4560
1	5	13	26.5059	22.6593
2	5	13	21.5413	21.8945
3	5	13	5.1314	1.9416
-6	6	13	7.4208	7.2151
-7	6	13	2.7387	4.2842
-6	6	13	107.7839	100.7730
-1	6	13	410.0967	410.8480
0	6	13	98.7941	100.7730
1	6	13	32.8361	28.3569
2	6	13	8.1809	3.2926
-7	7	13	4.8557	2.0845
-2	7	13	142.8849	131.0400
-1	7	13	5.6304	4.2842
0	7	13	3.7257	2.0845
-2	8	13	6.6292	7.2151
-7	0	14	144.7463	149.6795
-6	0	14	152.6581	147.1882
-1	0	14	46.3898	43.4913

H	K	L	Y(OBS)	Y(CALC)
0	0	14	175.4707	153.3183
1	0	14	46.8755	43.4910
2	0	14	55.4336	57.3600
3	0	14	7.1646	6.1157
4	0	14	224.8143	221.8780
-8	1	14	3.1844	5.5272
-7	1	14	16.3022	17.1068
-6	1	14	5.2705	3.9467
0	1	14	45.7272	43.4913
1	1	14	372.8140	347.0127
2	1	14	3.7288	3.9428
3	1	14	84.6009	84.8259
-8	2	14	6.4981	5.1563
-7	2	14	313.9933	310.0059
-6	2	14	17.0907	11.4337
-1	2	14	372.3302	347.0131
0	2	14	54.3060	57.3596
1	2	14	1.2223	.1935
2	2	14	367.5162	350.5554
3	2	14	128.2273	136.6092
4	2	14	27.3473	29.1387
-8	3	14	232.9346	237.1446
-7	3	14	251.3824	260.2939
-6	3	14	157.3795	146.8070
-1	3	14	3.3300	3.9428
0	3	14	8.3480	6.1157
1	3	14	27.6846	23.1968
2	3	14	1.9490	1.4129
3	3	14	148.9609	146.8070
4	3	14	23.2154	29.8673
-8	4	14	8.4490	8.8671
-7	4	14	22.1417	29.8679
-6	4	14	28.5395	29.1387
0	4	14	230.4744	221.8788
1	4	14	27.8076	25.4136
2	4	14	15.4024	11.4387
3	4	14	240.9393	260.2939
4	4	14	7.7752	8.8671
-8	5	14	63.8510	68.8819
-7	5	14	76.5424	72.7072
-1	5	14	75.8839	68.0540
1	5	14	4.8541	3.9467
2	5	14	306.0623	310.0060
3	5	14	219.7505	237.1446
4	5	14	11.5585	9.7681
-7	6	14	6.3792	5.5952
-1	6	14	50.1689	46.4908
0	6	14	147.2629	147.1882
1	6	14	16.5300	17.1068
-8	7	14	70.3648	67.7662
-1	7	14	6.0365	5.5951
0	7	14	139.5422	149.6795
1	7	14	3.8567	5.5272
1	0	15	12.7893	10.6239
2	0	15	3.3231	4.2792

Table 14. Structure Factors for Chlorapatite at 200°C

H	K	L	Y(OBS)	Y(CALC)
-1	0	3	28.0643	29.1828
0	1	3	30.1121	29.1828
-2	0	4	7.4638	7.8320
-2	1	4	128.0400	120.1488
-2	2	4	7.7353	7.8322
-1	2	4	121.9764	120.1486
0	2	4	5.7252	7.8320
-1	1	5	56.8708	64.4638
-1	2	5	192.0192	207.0798
1	2	5	1659.0069	1622.0180
1	0	6	322.9992	318.6947
2	0	6	385.5624	382.8860
-3	1	6	204.7582	213.4081
-1	1	6	319.9775	318.6947
0	1	6	326.7071	318.6960
0	2	6	382.9262	382.8853
1	2	6	216.3367	213.4081
-3	3	6	83.7281	84.8480
0	3	6	88.4730	84.8481
-3	0	7	92.9739	89.9030
-2	0	7	5.1666	3.3282
2	0	7	5.7746	3.3282
1	1	7	11.5716	13.2293
2	1	7	1538.3770	1525.0924
-4	2	7	12.7963	13.7532
-3	2	7	1501.7587	1525.0924
-1	2	7	10.8055	13.2290
1	2	7	1428.9984	1437.4244
-4	3	7	84.9269	79.0851
-3	3	7	92.6208	89.9034
-1	3	7	1534.2317	1525.0910
0	3	7	91.9695	89.9030
-4	0	8	64.9743	71.6302
-1	0	8	243.0613	239.7250
1	0	8	246.3080	239.7241
2	0	8	51.6482	52.8621
-1	1	8	243.3725	239.7241
0	1	8	245.4941	239.7250
2	1	8	488.7694	510.3076
-5	2	8	496.6458	511.9286
-4	2	8	3.6089	.2813
0	2	8	55.8187	52.8618
1	2	8	1078.2713	1080.2601
2	2	8	1.2151	.2813
1	3	8	212.4604	204.0588
2	3	8	513.9631	511.9286
-4	4	8	66.2290	71.6305
-3	4	8	207.9336	204.0588
-1	4	8	20.3484	18.5190
0	4	8	67.1249	71.6302

H	K	L	Y(OBS)	Y(CALC)
-5	0	9	8.9052	4.5475
-4	0	9	24.4344	21.7807
2	0	9	9.0447	4.9071
-5	1	9	41.7389	40.4358
-1	1	9	12.4016	11.5868
3	1	9	291.8410	291.5610
-1	2	9	41.6519	43.2630
1	2	9	560.1167	559.3661
2	2	9	2.6885	.2343
-3	3	9	33.3326	30.5436
-2	3	9	559.8444	559.3653
-1	3	9	1499.3774	1499.4496
0	3	9	34.6362	30.5432
1	3	9	240.1513	228.5868
2	3	9	445.7845	453.2292
-5	4	9	1.4486	.4016
-4	4	9	23.9458	21.7810
-3	4	9	242.1263	228.5868
-2	4	9	6.0884	.2343
-1	4	9	287.8584	291.5607
0	4	9	21.8830	21.7807
-5	5	9	5.8121	4.5476
-2	5	9	328.1444	327.1105
-3	0	10	17.3948	12.8100
-1	0	10	157.2027	165.9323
0	0	10	1794.5837	1796.1561
-6	1	10	95.4143	92.5289
-3	1	10	81.1701	75.3671
-1	1	10	154.8171	165.9316
0	1	10	157.2260	165.9323
1	1	10	1311.5119	1378.3453
3	1	10	132.2595	141.4236
-6	2	10	41.2555	37.1387
-2	2	10	172.8643	177.3691
0	2	10	175.4663	177.3685
1	2	10	78.7432	75.3671
2	2	10	986.0146	998.0869
3	2	10	465.5638	474.8326
-5	3	10	471.5715	474.8326
-4	3	10	140.6339	141.4236
-2	3	10	80.9018	75.3660
-1	3	10	1.3350	.7604
1	3	10	331.7776	330.3987
3	3	10	417.7349	422.0577
-6	4	10	1.8233	.6750
-2	4	10	973.3401	998.0873
-1	4	10	137.1162	141.4232
0	4	10	561.4508	594.0368
1	4	10	114.7511	114.8521
2	4	10	40.3011	37.1387
-6	5	10	65.0478	62.2247
-4	5	10	118.6195	114.8521
-2	5	10	471.3865	474.8348
-1	5	10	94.3937	86.3213
0	5	10	613.4833	607.5034

Table 14. (Continued)

H	K	L	Y(OBS)	Y(CALC)
1	5	10	96.5420	92.5289
-5	6	10	100.5400	92.5282
-4	6	10	40.8508	37.1387
-2	6	10	4.3288	.6749
-1	6	10	63.3174	62.2251
-6	0	11	26.1277	29.5953
-5	0	11	30.9700	28.9941
-4	0	11	133.5316	125.7582
-3	0	11	9.0993	5.5729
-1	0	11	46.6462	42.5984
1	0	11	43.8387	42.5985
2	0	11	10.3661	7.3651
3	0	11	7.5167	5.5730
-6	1	11	206.5949	204.5971
-5	1	11	.5720	.3737
0	1	11	47.7450	42.5984
1	1	11	14.9940	10.3596
2	1	11	380.5395	368.7171
-6	2	11	55.5657	56.8796
-5	2	11	310.8631	299.3064
-4	2	11	16.9709	15.1706
-2	2	11	9.9469	7.3651
-1	2	11	10.9005	10.3598
0	2	11	8.3886	7.3650
1	2	11	482.3946	487.8586
3	2	11	269.8921	268.9836
-7	3	11	47.5152	41.6251
-6	3	11	204.4727	211.3587
-5	3	11	283.0710	268.9836
-2	3	11	486.3154	487.8586
-1	3	11	378.7691	368.7166
0	3	11	6.2211	5.5729
1	3	11	265.6067	269.5588
2	3	11	304.6431	299.3064
3	3	11	201.8077	211.3587
-7	4	11	146.4862	150.0082
-5	4	11	3.6212	3.6547
-4	4	11	130.2310	125.7588
-2	4	11	16.1940	15.1703
-1	4	11	19.5998	15.8251
0	4	11	131.6060	125.7582
1	4	11	1.4974	.3737
3	4	11	44.9669	41.6251
-6	5	11	449.3549	452.1350
-5	5	11	30.1734	28.9944
-4	5	11	1.7966	.3737
-2	5	11	279.5170	268.9830
-1	5	11	4.3013	3.6547
0	5	11	26.0752	28.9941
1	5	11	201.1928	204.5971
-5	6	11	209.3631	204.5971
-2	6	11	102.5492	100.6326
-1	6	11	436.5609	452.1341
0	6	11	26.3267	29.5953
-6	0	12	35.6205	29.4101
-5	0	12	10.8969	10.0589
-4	0	12	26.3677	21.7485
-1	0	12	40.3873	38.5883
1	0	12	40.3309	38.5880
2	0	12	59.3065	57.4724
3	0	12	749.8322	753.5875
4	0	12	25.2137	21.7486
-7	1	12	181.4802	179.6348
-6	1	12	104.4927	102.9701
-5	1	12	293.8293	274.7355
-1	1	12	38.1284	38.5880
0	1	12	37.7341	38.5883
1	1	12	2.6263	.1671
2	1	12	216.7800	225.4015
3	1	12	38.4519	39.1122
4	1	12	197.4903	192.8075
-7	2	12	43.5036	44.9598
-6	2	12	400.9808	419.9481
-4	2	12	11.0683	12.1735
-2	2	12	58.7227	57.4724
-1	2	12	1.2423	.1671
1	2	12	124.2379	127.7609
2	2	12	11.7836	12.1735
3	2	12	1.3308	1.1183
4	2	12	191.2479	198.5900
-7	3	12	50.5426	43.8378
-2	3	12	125.2767	127.7610
0	3	12	739.0009	753.5878
1	3	12	1.9517	1.1219
2	3	12	192.9496	200.1681
3	3	12	55.8645	52.2858
-7	4	12	37.2430	38.3317
-2	4	12	13.5576	12.1735
-1	4	12	35.0132	39.1118
0	4	12	26.4361	21.7485
1	4	12	283.5761	274.7355
-7	5	12	277.5636	285.3678
-6	5	12	327.4495	333.9389
-2	5	12	1.7062	1.1183
-1	5	12	198.1172	192.8074
0	5	12	11.0918	10.0589
1	5	12	96.4770	102.9701
2	5	12	39.3331	44.9598
-7	6	12	128.0024	124.3823
-6	6	12	34.3289	29.4100
-5	6	12	100.4945	102.9701
-2	6	12	195.8950	198.5897
-1	6	12	324.8444	333.9412
0	6	12	34.9416	29.4101
-6	7	12	184.6195	179.6355
-5	7	12	41.7112	44.9597
-2	7	12	269.4812	285.3671
-1	7	12	126.3941	124.3819
-7	0	13	2.6447	2.0254
-6	0	13	81.5337	82.1050

Table 14. (Continued)

H	K	L	Y(OBS)	Y(CALC)
-5	0	13	8.3414	7.6374
-4	0	13	3.2683	.0172
-1	0	13	13.4622	11.6454
1	0	13	14.4305	11.6454
2	0	13	6.0603	7.1662
4	0	13	.8833	.0172
-7	1	13	20.1330	19.4184
-5	1	13	12.7935	11.8039
-1	1	13	13.2829	11.6454
1	1	13	16.6764	14.9675
2	1	13	333.0882	340.1637
3	1	13	90.9407	88.7651
4	1	13	2.7346	2.2269
-8	2	13	4.7223	2.3643
-7	2	13	19.3678	15.7504
-2	2	13	6.1767	7.1662
-1	2	13	18.1746	14.9674
1	2	13	114.8154	113.7208
2	2	13	1.4722	.0473
3	2	13	38.6589	38.3771
4	2	13	3.0782	4.4387
-7	3	13	20.4820	20.1724
-6	3	13	53.9618	48.9026
-5	3	13	41.7171	38.3771
-2	3	13	119.9387	113.7205
-1	3	13	336.1397	340.1631
0	3	13	9.6860	7.0563
1	3	13	37.4802	36.4436
2	3	13	111.3483	109.0319
3	3	13	54.4902	48.9026
4	3	13	58.9118	64.5851
-8	4	13	13.9871	16.4605
-7	4	13	66.0514	64.5851
-6	4	13	3.5467	4.4387
-5	4	13	2.5868	2.2269
-2	4	13	.7654	.0473
-1	4	13	96.6970	88.7650
0	4	13	.7357	.0172
1	4	13	12.9654	11.8039
2	4	13	154.5492	155.6974
3	4	13	18.8762	20.1724
4	4	13	13.5831	16.4605
-8	5	13	4.3097	4.3231
-7	5	13	108.6271	102.8763
-5	5	13	7.9837	7.6375
-2	5	13	39.4111	38.3770
0	5	13	7.6902	7.6374
1	5	13	19.6635	16.4911
2	5	13	15.6402	15.7504
3	5	13	3.1601	1.7830
-8	6	13	6.8377	6.3062
-7	6	13	2.1126	4.0691
-6	6	13	85.2698	82.1049
-2	6	13	6.8572	4.4386
-1	6	13	325.7686	318.4053
0	6	13	82.9345	82.1050
1	6	13	21.6260	19.4184
2	6	13	2.8606	2.3643
-7	7	13	5.5441	2.0254
-6	7	13	21.8866	19.4182
-2	7	13	109.9217	102.8765
-1	7	13	4.7170	4.0691
0	7	13	3.4757	2.0254
-6	8	13	5.1486	2.3643
-2	8	13	5.5495	6.3062
-6	0	14	122.9978	114.3528
-1	0	14	37.2781	35.7252
0	0	14	129.5495	126.7521
1	0	14	37.7419	35.7249
2	0	14	46.3779	47.0992
3	0	14	5.4495	3.6008
4	0	14	166.1000	170.3932
-8	1	14	4.0226	4.4230
-7	1	14	11.6824	11.8681
-6	1	14	4.3534	4.1639
-1	1	14	38.6651	35.7249
0	1	14	38.3172	35.7252
1	1	14	294.1259	277.3916
2	1	14	4.0258	2.8547
3	1	14	67.2606	64.3319
4	1	14	61.2959	54.0114
-8	2	14	2.8895	2.8205
-6	2	14	13.7023	8.6528
-1	2	14	296.3223	277.3918
0	2	14	45.2724	47.0989
1	2	14	.6614	.1304
3	2	14	103.1841	111.6265
4	2	14	17.0346	19.4169
-8	3	14	187.7358	183.4763
-6	3	14	123.5980	111.2332
-1	3	14	3.8528	2.8547
0	3	14	5.0756	3.6008
1	3	14	21.9295	17.9966
2	3	14	3.3022	1.5530
3	3	14	114.6284	111.2332
4	3	14	16.2687	16.7687
-8	4	14	6.4285	6.0372
-7	4	14	18.9568	16.7687
-6	4	14	22.1377	19.4169
0	4	14	181.2066	170.3939
1	4	14	22.1114	19.8976
2	4	14	11.5932	8.6528
4	4	14	6.0332	6.0372
-7	5	14	58.2170	53.6708
-1	5	14	63.7070	54.0115
0	5	14	178.7586	186.3581
1	5	14	4.6278	4.1639
3	5	14	173.3804	183.4763
4	5	14	9.0235	7.4225
-8	6	14	46.8634	45.8474

Table 14. (Concluded)

H	K	L	Y(OBS)	Y(CALC)
-7	6	14	4.8902	5.0109
-1	6	14	36.2190	34.6200
1	6	14	11.2787	11.8681
2	6	14	4.0341	2.8205
-8	7	14	57.2062	54.6983
-1	7	14	4.6764	5.0108
0	7	14	112.7563	116.0801
1	7	14	3.4323	4.4230
1	0	15	10.0675	8.5615
2	0	15	2.2117	3.0508
3	0	15	.8039	.7625
4	0	15	33.1241	36.7793
5	0	15	3.8291	2.6502
0	1	15	8.5001	8.5615
1	1	15	1.7164	1.3544
2	1	15	80.5470	78.5890
3	1	15	1.0496	.2393
4	1	15	1.8928	.0972
0	2	15	3.8705	3.0508
1	2	15	134.9362	135.4654
2	2	15	.1028	.1748
3	2	15	86.2576	84.7003
4	2	15	24.4018	26.8466
5	2	15	23.8642	27.2795
0	3	15	1.4781	.7624
1	3	15	69.0358	68.7966
2	3	15	29.8394	27.7694
3	3	15	19.3488	18.2298
4	3	15	46.7653	50.5911
0	4	15	38.0941	36.7791
1	4	15	1.7184	1.8954
2	4	15	20.4663	22.2327
3	4	15	8.9000	8.4638

Table 15. Structure Factors for Chlorapatite at 250°C

H	K	L	Y(OBS)	Y(CALC)
-1	1	3	30.0005	29.1830
0	1	3	31.4797	29.1828
1	0	4	505.7807	521.0716
2	0	4	4.3586	5.7133
0	1	4	505.7416	521.0725
-1	2	4	144.4497	135.3934
2	0	5	433.2321	444.4427
-1	1	5	58.0929	62.6703
1	1	5	202.5202	214.6262
-1	2	5	203.1791	214.6270
0	2	5	433.0048	444.4423
1	2	5	1653.0350	1606.2162
1	0	6	312.0879	291.6199
2	0	6	360.9402	356.4161
3	0	6	73.2969	70.1019
-3	1	6	188.9730	196.4044
-1	1	6	308.0674	291.6199
0	1	6	309.0787	291.6210
2	1	6	21.1058	15.2489
0	2	6	364.3153	356.4155
1	2	6	195.2753	196.4044
0	3	6	75.7535	70.1020
-1	0	7	32.5058	32.5982
2	0	7	4.7073	3.6365
3	0	7	90.7911	83.7222
-2	1	7	10.6718	10.5213
0	1	7	34.1798	32.5982
2	1	7	1507.5880	1490.0760
3	1	7	88.9256	80.7816
-4	2	7	15.4236	15.0915
-1	2	7	11.2024	10.5210
1	2	7	1414.9893	1399.2344
2	2	7	13.5667	15.0915
-3	3	7	87.9619	83.7222
-1	3	7	1508.2268	1490.0744
1	3	7	837.7478	808.0558
-4	0	8	71.2831	76.8532
-1	0	8	228.9107	219.3186
1	0	8	228.7915	219.3178
2	0	8	40.3489	44.2161
3	0	8	1639.3563	1649.2087
4	0	8	72.3898	76.8535
-4	1	8	180.7475	178.4628
-1	1	8	225.0518	219.3178
1	1	8	22.3953	17.7689
2	1	8	472.7680	477.7962
3	1	8	17.7913	16.2686
-4	2	8	1.6835	.7013
-1	2	8	20.0151	17.7688
0	2	8	40.2256	44.2158
3	2	8	25.0736	24.3882
-4	3	8	17.8120	16.2686
-3	3	8	1625.4839	1649.2087
-1	3	8	463.7935	477.7995
0	3	8	1639.9226	1649.2095
1	3	8	181.1652	178.4628
2	3	8	454.4903	450.4270
-4	4	8	74.0763	76.8535
-2	4	8	1.1862	.7013
0	4	8	76.8654	76.8532
-2	5	8	25.4371	24.3882
-4	0	9	24.2215	20.3767
-3	0	9	31.3242	28.3498
1	0	9	12.7562	11.0863
3	0	9	30.7143	28.3502
5	0	9	4.0625	3.7822
-5	1	9	38.3398	37.8139
-3	1	9	532.4566	532.7581
-1	1	9	11.6270	11.0863
0	1	9	13.5091	11.0863
2	1	9	1417.8168	1437.0485
4	1	9	1.0897	.5130
-4	2	9	.3770	.3930
-1	2	9	36.3839	38.8693
0	2	9	5.3368	4.5557
1	2	9	531.5917	532.7581
2	2	9	.8651	.3930
3	2	9	302.6825	307.0214
-4	3	9	282.2142	285.9257
-2	3	9	537.7606	532.7575
-1	3	9	1432.8741	1437.0473
0	3	9	31.4816	28.3498
1	3	9	230.4665	222.6705
2	3	9	420.1218	414.8125
-3	4	9	228.4160	222.6705
-2	4	9	8.2747	.3930
-1	4	9	286.4929	285.9254
1	4	9	39.7126	37.8139
-5	5	9	5.3385	3.7822
-4	5	9	43.3311	37.8136
-2	5	9	302.3092	307.0206
-5	0	10	540.9246	554.6143
-1	0	10	140.9700	154.0308
0	0	10	1676.2968	1646.8132
1	0	10	139.5194	154.0301
2	0	10	166.1394	166.6312
3	0	10	13.1588	8.6983
4	0	10	508.3974	538.3104
5	0	10	542.7909	554.6150
-6	1	10	86.8028	77.8217
-3	1	10	75.9806	69.8575
-1	1	10	142.5903	154.0301
0	1	10	139.2051	154.0308
1	1	10	1293.6186	1328.7688
3	1	10	118.3851	121.6411

Table 15. (Continued)

H	K	L	Y(OBS)	Y(CALC)
4	1	10	100.2986	97.4404
5	1	10	59.1234	63.6000
-5	2	10	5.4240	4.0913
-3	2	10	1.4115	.2764
-1	2	10	1281.3867	1328.7688
0	2	10	166.3080	166.6307
1	2	10	74.9142	69.8575
3	2	10	444.7926	446.2346
-5	3	10	450.8305	446.2346
-4	3	10	119.8543	121.6411
-1	3	10	.5696	.2763
1	3	10	289.3315	291.4815
2	3	10	6.6175	4.0913
3	3	10	409.6776	413.0865
-6	4	10	4.2856	.0098
-5	4	10	99.4546	97.4404
-4	4	10	502.1722	538.3104
-2	4	10	946.1734	964.9472
-1	4	10	115.7867	121.6407
0	4	10	516.5430	538.3122
1	4	10	116.7683	112.7998
-6	5	10	62.7711	63.6000
-5	5	10	540.2523	554.6150
-4	5	10	115.0098	112.7998
-2	5	10	444.4096	446.2369
-1	5	10	102.4853	97.4404
0	5	10	542.1376	554.6143
-5	6	10	87.7948	77.8211
-4	6	10	40.0841	38.9302
-2	6	10	1.7678	.0098
-1	6	10	62.7441	63.6004
-6	0	11	25.4934	26.0485
-4	0	11	125.8707	120.4269
-3	0	11	6.2220	4.7702
-1	0	11	43.8156	40.7565
1	0	11	44.2240	40.7566
3	0	11	7.5614	4.7703
4	0	11	121.9391	120.4274
5	0	11	27.5155	24.7071
-6	1	11	180.7300	176.6785
-5	1	11	.8072	.5144
0	1	11	47.5975	40.7565
-6	2	11	58.2649	53.3729
-5	2	11	277.6802	265.8135
-4	2	11	16.0981	15.6468
-1	2	11	13.9433	11.0353
0	2	11	6.8695	5.9841
1	2	11	453.3578	452.4322
2	2	11	15.3101	15.6468
3	2	11	254.7142	246.8491
4	2	11	89.3492	88.2309
-7	3	11	43.3691	35.9635
-6	3	11	186.5359	185.2987
-4	3	11	13.2068	13.0025
-2	3	11	454.7382	452.4322
-1	3	11	358.8403	346.8477
0	3	11	4.4912	4.7702
1	3	11	253.2685	255.1038
2	3	11	271.3579	265.8135
3	3	11	181.6156	185.2987
4	3	11	140.1407	141.0375
-7	4	11	138.1831	141.0375
-6	4	11	90.2997	88.2309
-5	4	11	4.6111	2.7326
-4	4	11	127.8786	120.4274
-2	4	11	16.8547	15.6466
-1	4	11	16.6478	13.0025
0	4	11	122.4672	120.4269
1	4	11	1.8733	.5144
3	4	11	42.0208	35.9635
-6	5	11	402.7353	410.8485
-5	5	11	22.4391	24.7071
-4	5	11	1.4695	.5144
-2	5	11	254.0610	246.8484
-1	5	11	3.4579	2.7326
0	5	11	20.6055	24.7069
1	5	11	178.9761	176.6785
-6	6	11	23.9874	26.0483
-5	6	11	183.0887	176.6786
-2	6	11	92.1253	88.2307
-1	6	11	401.5291	410.8477
0	6	11	24.1363	26.0485
-6	0	12	33.5145	29.9022
-5	0	12	12.3102	10.7146
-4	0	12	18.9032	19.1365
-1	0	12	37.4883	36.5830
0	0	12	2727.4673	2746.9382
1	0	12	37.5777	36.5827
2	0	12	54.2227	52.2161
3	0	12	703.2284	708.8942
4	0	12	20.7662	19.1366
5	0	12	10.4901	10.7144
6	0	12	29.0023	29.9020
-5	1	12	272.5457	263.3472
-4	1	12	1.6721	1.3464
-1	1	12	34.5930	36.5827
0	1	12	36.2019	36.5830
1	1	12	3.2287	.3973
2	1	12	202.7336	211.7540
3	1	12	36.0653	38.0705
4	1	12	174.3154	176.6988
6	1	12	111.4751	111.9264
-7	2	12	42.3772	43.2536
-6	2	12	355.4065	376.1069
-5	2	12	181.8050	179.5752
-4	2	12	12.2017	13.2605
-2	2	12	56.1760	52.2161
-1	2	12	.6875	.3973
0	2	12	52.0116	52.2157
1	2	12	115.6737	114.1611

Table 15. (Continued)

H	K	L	Y(OBS)	Y(CALC)
2	2	12	14.6300	13.2605
3	2	12	1.3173	.4789
4	2	12	177.2429	179.8934
5	2	12	259.4423	271.2111
-7	3	12	44.2510	39.8037
-6	3	12	56.5854	51.4067
-5	3	12	2.8793	.4789
-4	3	12	41.4949	38.0705
-2	3	12	115.2922	114.1614
-1	3	12	209.0615	211.7557
0	3	12	713.4092	708.8944
1	3	12	1.4890	1.3464
2	3	12	178.1827	179.5752
3	3	12	57.7597	51.4067
4	3	12	32.8597	34.3408
-7	4	12	34.5027	34.3408
-6	4	12	182.4443	179.8934
-5	4	12	188.6171	176.6988
-2	4	12	16.2329	13.2604
-1	4	12	36.2901	38.0701
0	4	12	25.2045	19.1365
2	4	12	361.0613	376.1069
3	4	12	42.6250	39.8037
-7	5	12	267.1638	271.2111
-6	5	12	302.2905	294.4636
-5	5	12	12.2980	10.7144
-2	5	12	2.3883	.4789
-1	5	12	181.7547	176.6987
0	5	12	11.9898	10.7146
1	5	12	91.0620	88.4683
-7	6	12	116.3651	111.9264
-6	6	12	34.6244	29.9020
-5	6	12	90.2684	88.4683
-2	6	12	180.8853	179.8932
-1	6	12	293.8115	294.4656
0	6	12	33.7535	29.9022
1	6	12	158.6773	158.1209
-6	7	12	160.2066	158.1215
-5	7	12	42.6499	43.2535
-2	7	12	263.1529	271.2104
-1	7	12	116.8701	111.9260
-7	0	13	.9747	1.6399
-6	0	13	71.6836	71.8091
-5	0	13	6.2832	6.7292
-4	0	13	.7795	.0227
-1	0	13	11.6992	10.5829
1	0	13	14.1884	10.5829
2	0	13	7.1643	6.8162
3	0	13	8.3573	6.2208
4	0	13	.9978	.0227
5	0	13	7.8697	6.7293
6	0	13	71.9927	71.8091
7	0	13	2.3454	1.6399
-7	1	13	17.9475	14.0758
-6	1	13	17.6089	13.9298
-5	1	13	10.5264	10.4399
-1	1	13	12.2877	10.5829
1	1	13	14.6014	12.1391
2	1	13	315.4253	312.0096
3	1	13	89.7305	82.3241
4	1	13	2.1483	1.9715
5	1	13	288.0286	286.0484
6	1	13	2.5456	4.5099
-8	2	13	3.0623	1.8118
-7	2	13	14.2286	13.7218
-6	2	13	150.7662	143.6224
-5	2	13	103.2088	96.6893
-1	2	13	14.7498	12.1391
0	2	13	8.0618	6.8162
1	2	13	98.5598	100.5625
2	2	13	1.6830	.1422
3	2	13	36.8534	33.3120
4	2	13	3.2900	3.0697
5	2	13	92.7429	87.9153
6	2	13	3.3648	4.8756
-8	3	13	3.7126	2.1197
-7	3	13	17.6093	18.8787
-6	3	13	47.7354	43.4248
-2	3	13	102.6173	100.5622
-1	3	13	310.7655	312.0091
0	3	13	6.1061	6.2206
1	3	13	34.8782	34.0402
2	3	13	97.9151	96.6893
3	3	13	47.6422	43.4248
4	3	13	57.2905	59.0801
-8	4	13	12.4606	15.4444
-7	4	13	58.4777	59.0801
-6	4	13	5.1494	3.0697
-5	4	13	3.9508	1.9715
-2	4	13	.6853	.1422
0	4	13	1.3080	.0227
1	4	13	10.6370	10.4399
2	4	13	147.1335	143.6224
3	4	13	18.4317	18.8787
4	4	13	14.3758	15.4444
-8	5	13	3.7714	5.5747
-7	5	13	94.7295	87.9153
-6	5	13	289.3336	286.0484
-5	5	13	8.1657	6.7293
-2	5	13	34.1049	33.3119
-1	5	13	2.5183	1.9715
0	5	13	7.5757	6.7292
1	5	13	16.6520	13.9298
2	5	13	16.3005	13.7218
3	5	13	1.8852	2.1197
-8	6	13	5.4200	4.8756
-7	6	13	2.7863	4.5099
-6	6	13	74.4296	71.8091
-2	6	13	5.8578	3.0696
-1	6	13	284.9401	286.0474

Table 15. (Concluded)

H	K	L	Y(OBS)	Y(CALC)
0	6	13	73.9669	71.8091
1	6	13	14.8205	14.0758
2	6	13	1.9372	1.8118
-7	7	13	3.4955	1.6399
-6	7	13	17.6376	14.0757
-2	7	13	90.4878	87.9156
-1	7	13	4.4703	4.5099
-6	8	13	4.3573	1.8118
-2	8	13	5.7495	4.8756
-7	0	14	92.5209	93.0392
-5	0	14	163.5039	168.9657
-1	0	14	35.3673	33.3059
0	0	14	101.5260	107.3573
2	0	14	43.8975	44.3304
3	0	14	4.1873	3.9016
4	0	14	155.0145	148.8842
5	0	14	158.3857	168.9661
6	0	14	106.2993	102.6056
7	0	14	89.3747	93.0387
-8	1	14	2.6856	4.3313
-7	1	14	10.5250	10.8748
-6	1	14	5.8310	4.0761
0	1	14	34.4861	33.3059
1	1	14	271.9327	254.9776
3	1	14	56.1615	55.8422
4	1	14	62.9994	53.1894
5	1	14	31.3379	28.1148
6	1	14	4.3554	4.7145
7	1	14	49.9187	51.8651
-8	2	14	3.3599	1.9571
-7	2	14	216.6424	208.1285
-6	2	14	9.8838	7.6705
-1	2	14	268.8065	254.9778
0	2	14	43.0286	44.3301
1	2	14	1.7019	.2894
2	2	14	257.5947	241.6240
3	2	14	99.5243	104.3211
4	2	14	15.9562	17.4750
5	2	14	46.1356	44.9859
6	2	14	40.7750	41.4764
-8	3	14	158.4157	164.8207
-7	3	14	169.4021	166.6700
-6	3	14	109.5311	102.1738
-1	3	14	2.8254	2.5083
0	3	14	4.3028	3.9016
2	3	14	1.2529	1.9441
3	3	14	106.7378	102.1738
4	3	14	15.5620	13.4384
5	3	14	46.4807	49.5648
-8	4	14	3.6489	3.6951
-7	4	14	13.9866	13.4384
-6	4	14	14.1566	17.4750
-1	4	14	57.4559	55.8421
1	4	14	18.3579	18.0850
2	4	14	8.7301	7.6705
3	4	14	159.7645	166.6700
4	4	14	3.7588	3.6951
5	4	14	.4008	1.1615
-8	5	14	45.1019	49.5648
-7	5	14	48.6248	44.9859
-1	5	14	59.4663	53.1894
0	5	14	159.3397	168.9657
1	5	14	4.1599	4.0761
2	5	14	210.4243	208.1285
3	5	14	147.7833	164.8207
4	5	14	6.7040	5.6859
-8	6	14	44.0140	41.4764
-7	6	14	4.5994	4.7145
-1	6	14	28.5034	28.1150
0	6	14	102.6778	102.6053
1	6	14	9.4533	10.8748
-8	7	14	53.2423	51.8651
-1	7	14	4.7688	4.7145
0	7	14	94.6677	93.0392
1	7	14	3.7863	4.3313
1	0	15	8.8893	8.1056
2	0	15	2.3352	2.9745
3	0	15	1.5060	.6639
4	0	15	34.2448	33.1328
5	0	15	3.1633	2.8543
6	0	15	8.8954	9.5617
0	1	15	8.0165	8.1056
1	1	15	1.9787	.9505
2	1	15	71.7007	68.7459
3	1	15	.5135	.2867
4	1	15	.3156	.0740
0	2	15	3.5568	2.9745
1	2	15	122.8433	118.6636
2	2	15	2.1147	.2620
4	2	15	23.2636	22.7474
5	2	15	22.9558	22.5326
0	3	15	.8481	.6638
1	3	15	63.9703	62.4043
2	3	15	28.7519	22.5389
3	3	15	17.8986	15.3990
4	3	15	45.6326	46.4733
2	4	15	19.8979	20.3575

Table 16. Structure Factors for Chlorapatite at 300°C

H	K	L	Y(OBS)	Y(CALC)
1	-1	3	29.2535	29.4711
1	0	3	31.1790	29.4712
0	-2	4	2.9823	4.1802
1	1	4	148.0795	134.0186
2	-1	4	146.8600	134.0185
2	0	4	4.2712	4.1802
0	-1	5	51.7898	56.4930
0	1	5	50.6191	56.4929
1	0	5	52.4068	56.4930
1	2	5	1630.7072	1574.2719
2	-2	5	393.3307	404.9309
2	0	5	399.8438	404.9312
0	-3	6	65.3065	61.0555
0	-1	6	277.7715	263.7070
0	1	6	274.4769	263.7079
0	2	6	327.7605	318.1479
0	3	6	62.6374	61.0557
1	-3	6	22.2396	23.1950
1	0	6	275.6692	263.7070
2	-3	6	172.7897	180.5703
2	-2	6	325.7700	318.1479
2	1	6	23.0851	23.1950
3	-3	6	63.6081	61.0557
3	-2	6	23.0342	23.1952
3	-1	6	173.6655	180.5746
3	0	6	62.8795	61.0555
0	-2	7	2.8209	4.1667
0	3	7	78.0896	73.3898
1	-4	7	81.6898	79.6304
1	-2	7	8.8317	8.1348
1	0	7	30.6556	31.3531
1	3	7	771.4103	771.5793
2	-4	7	17.5575	8.6308
2	-1	7	8.3434	8.1345
2	0	7	3.8875	4.1667
2	2	7	13.6903	8.6308
3	-3	7	79.5512	73.3898
3	-1	7	1323.8354	1337.3266
3	0	7	81.1928	73.3902
3	1	7	80.5703	79.6304
0	-1	8	198.7300	197.3210
0	1	8	195.7478	197.3217
0	3	8	1605.4373	1602.4404
0	4	8	68.7680	88.1860
1	-3	8	426.2135	412.3594
1	-2	8	13.3354	17.5196
1	-1	8	195.8552	197.3217
1	0	8	192.6318	197.3210
1	1	8	20.0309	17.5196
1	3	8	161.5977	151.0730
2	-4	8	1.5200	5.0859
2	-2	8	35.7233	40.9372
2	-1	8	24.0977	17.5196
2	0	8	34.5965	40.9375
2	1	8	428.7090	412.3594
3	-5	8	402.0738	411.2549
3	-4	8	161.9545	151.0730
3	-1	8	878.8717	848.7628
3	1	8	17.5712	16.8705
3	2	8	24.2967	28.2822
4	-3	8	15.7246	16.8701
4	-1	8	160.0531	151.0730
5	-2	8	396.1596	411.2532
0	-4	9	26.1523	18.0207
0	3	9	26.7955	21.3861
0	4	9	23.6051	18.0205
0	5	9	4.2758	4.6657
1	-5	9	1.3462	.0912
1	-2	9	29.7512	29.3027
1	-1	9	13.0333	10.2130
1	0	9	11.9202	10.2130
1	1	9	29.9150	29.3027
1	2	9	483.1008	487.8216
1	4	9	36.4514	36.1890
2	-5	9	279.7079	292.0618
2	-4	9	3.1549	.0494
2	-3	9	492.5964	487.8216
2	-2	9	7.9614	4.7177
2	-1	9	30.0536	29.3025
2	0	9	4.7726	4.7177
2	1	9	1329.9350	1336.9861
3	-5	9	371.0754	369.3949
3	-4	9	217.9474	206.9024
3	-3	9	24.7747	21.3861
3	0	9	26.7371	21.3864
3	1	9	264.8392	262.9410
3	2	9	278.6252	292.0618
4	-5	9	35.8521	36.1890
4	-4	9	22.4493	18.0205
4	-3	9	265.4605	262.9407
4	-2	9	1.4803	.0494
4	-1	9	217.6784	206.9025
4	0	9	23.2378	18.0207
5	-5	9	3.2445	4.6657
5	-4	9	2.9375	.0912
5	-3	9	275.1618	292.0612
5	-2	9	374.9383	369.3955
5	-1	9	35.3057	36.1888
5	0	9	7.0367	4.6658
0	-1	10	119.5889	129.5544
0	0	10	1484.7441	1478.1181
0	1	10	118.2903	129.5551
0	4	10	438.4366	464.0237
0	5	10	483.6580	383.3187
1	-6	10	56.7272	61.3259

Table 16. (Continued)

H	K	L	Y(OBS)	Y(CALC)
1	-4	10	96.9534	98.4588
1	-2	10	1165.7299	1238.0597
1	-1	10	122.7073	129.5551
1	0	10	119.7801	129.5544
1	1	10	1189.2267	1238.0597
1	2	10	68.0682	68.8777
1	4	10	103.7903	107.0505
2	-6	10	.9065	.0617
2	-5	10	403.0514	415.1443
2	-4	10	863.0165	875.6328
2	-3	10	68.6875	68.8777
2	-1	10	1182.4999	1238.0596
2	0	10	147.7202	147.9128
2	1	10	.5028	.0297
2	4	10	35.2493	29.1211
3	-6	10	368.8527	374.9163
3	-5	10	3.4126	6.6772
3	-4	10	245.9849	242.1887
3	-2	10	.8619	.0297
3	-1	10	70.1446	68.8767
3	0	10	9.8012	8.4145
3	1	10	97.3572	98.4588
3	2	10	401.0909	415.1443
4	-6	10	37.2429	29.1211
4	-5	10	102.6073	107.0505
4	-4	10	448.4215	464.0237
4	-2	10	871.9398	875.6332
4	-1	10	245.0905	242.1902
4	0	10	444.4053	464.0220
4	1	10	102.2543	97.9513
4	2	10	1.9423	.0617
5	-6	10	77.2980	69.3803
5	-5	10	485.4000	383.3187
5	-3	10	401.3598	415.1463
5	-2	10	4.2657	6.6771
5	-1	10	103.8234	107.0504
5	0	10	178.9267	383.3192
5	1	10	54.3861	61.3259
6	-5	10	58.9443	61.3263
6	-4	10	3.0042	.0617
6	-3	10	370.0496	374.9157
6	-2	10	35.4812	29.1211
6	-1	10	74.9679	69.3797
0	-6	11	22.2096	18.4549
0	-5	11	17.6892	21.3073
0	-4	11	118.7390	111.1161
0	-2	11	5.7931	3.6063
0	-1	11	39.5679	36.8408
0	0	11	1.2854	.0000
0	1	11	35.4584	36.8407
0	2	11	6.2449	3.6063
0	4	11	113.2514	111.1156
0	5	11	16.4504	21.3071
0	6	11	21.5758	18.4551
1	-6	11	351.4243	355.4667
1	-4	11	12.0120	9.6854
1	-3	11	313.2720	299.2717
1	-2	11	11.3672	10.6108
1	-1	11	37.3580	36.8407
1	0	11	35.2766	36.8408
1	1	11	12.0562	10.6108
1	2	11	399.2448	401.5714
1	5	11	158.1419	147.7891
2	-6	11	77.1442	72.1596
2	-5	11	223.8293	206.9041
2	-4	11	12.1151	10.2402
2	-3	11	401.8972	401.5714
2	1	11	318.9610	299.2717
3	-7	11	122.1033	112.3506
3	-6	11	159.4718	117.6879
3	-4	11	230.8079	235.2152
3	-3	11	5.8568	4.5948
3	-2	11	318.6369	299.2713
3	-1	11	403.2352	401.5714
3	0	11	3.1308	4.5949
3	1	11	10.5127	9.6854
3	2	11	224.5626	206.9041
4	-7	11	37.7087	27.8488
4	-6	11	56.5491	40.0332
4	-5	11	.7809	.9166
4	-3	11	10.9507	9.6854
4	-2	11	13.6720	10.2400
4	-1	11	228.6607	235.2146
4	0	11	112.6981	111.1161
4	1	11	5.2162	2.1545
4	2	11	74.1041	72.1595
5	-6	11	152.4703	147.7891
5	-5	11	17.4467	21.3071
5	-3	11	217.8876	206.9035
5	-2	11	233.3000	223.4523
5	-1	11	1.6738	.9166
5	0	11	18.9407	21.3073
5	1	11	356.8625	355.4667
6	-5	11	350.2001	355.4660
6	-4	11	75.4028	72.1594
6	-2	11	55.2075	40.0329
6	-1	11	154.6656	147.7892
6	0	11	19.6896	18.4549
7	-4	11	120.3831	112.3506
7	-3	11	37.1502	27.8490
0	-6	12	28.6576	27.6675
0	-4	12	17.0456	18.7085
0	-2	12	43.8743	45.4490
0	-1	12	30.9599	31.4909
0	0	12	2433.5951	2414.6965
0	1	12	31.4798	31.4911
0	2	12	45.6758	45.4486
0	5	12	11.6601	4.0406
0	6	12	26.5806	27.6677
1	-7	12	98.3152	81.5497

Table 16. (Continued)

H	K	L	Y(OBS)	Y(CALC)
1	-6	12	258.2697	237.6879
1	-5	12	149.4917	137.6596
1	-4	12	33.6203	34.7082
1	-3	12	176.6558	181.4509
1	-1	12	34.2875	31.4911
1	0	12	29.8159	31.4909
1	1	12	2.3183	.3702
1	2	12	96.1145	94.7326
1	5	12	77.5574	76.9960
1	6	12	132.3278	113.9442
2	-7	12	231.1485	234.1920
2	-6	12	146.4268	147.4062
2	-5	12	1.6938	.2018
2	-4	12	16.3126	14.2634
2	-3	12	93.7347	94.7326
2	-2	12	45.3535	45.4486
2	-1	12	2.0290	.3702
2	0	12	43.2603	45.4490
2	1	12	177.1962	181.4509
2	2	12	16.5812	14.2634
3	-7	12	29.5511	23.8619
3	-6	12	47.7853	45.2093
3	-5	12	146.0096	144.2051
3	-3	12	621.0975	625.5553
3	-2	12	175.2239	181.4523
3	-1	12	92.7820	94.7328
3	0	12	618.0036	625.5550
3	1	12	35.8040	34.7082
3	2	12	.4459	.2018
4	-7	12	33.8555	30.3347
4	-6	12	307.3416	305.1148
4	-5	12	231.2130	227.4079
4	-4	12	15.4996	18.7085
4	-3	12	34.8182	34.7079
4	-2	12	15.6505	14.2634
4	-1	12	1.0033	.7392
4	0	12	16.6302	18.7085
4	1	12	144.9990	137.6596
4	2	12	146.8695	147.4062
5	-6	12	75.8902	76.9960
5	-5	12	8.4165	4.0406
5	-4	12	147.9411	137.6596
5	-3	12	1.6066	.2018
5	-2	12	145.6466	144.2041
5	-1	12	235.4531	227.4081
5	0	12	10.3065	4.0405
5	1	12	243.9262	237.6879
5	2	12	222.8895	234.1920
6	-7	12	127.1870	113.9442
6	-6	12	26.6448	27.6677
6	-5	12	244.8188	237.6894
6	-4	12	147.2686	147.4061
6	-3	12	48.1517	45.2096
6	-1	12	74.7279	76.9960
6	0	12	26.6041	27.6675
6	1	12	95.5584	81.5497
7	-6	12	94.7682	81.5495
7	-5	12	225.8905	234.1915
7	-4	12	26.9680	23.8619
7	-3	12	37.0830	30.3349
7	-2	12	35.0656	38.5436
7	-1	12	127.6835	113.9446
0	-7	13	.5935	1.8799
0	-6	13	62.6931	55.0855
0	-5	13	6.0893	6.6223
0	-4	13	2.0647	.0247
0	-3	13	7.4696	4.8701
0	-2	13	4.5797	7.0041
0	-1	13	8.2403	9.1761
0	1	13	10.3948	9.1761
0	6	13	62.1721	55.0854
0	7	13	2.5826	1.8799
1	-7	13	2.3931	6.8742
1	-6	13	243.9476	237.0271
1	-5	13	2.9443	1.1205
1	-4	13	73.5198	71.4472
1	-3	13	260.9499	261.5240
1	-2	13	9.3145	8.1975
1	-1	13	10.3075	9.1761
1	1	13	11.2867	8.1975
1	2	13	85.5738	81.9909
2	-8	13	3.7882	1.2127
2	-7	13	77.7021	75.3929
2	-5	13	26.8233	27.2939
2	-4	13	.9733	.0495
2	-3	13	82.5918	81.9909
2	-2	13	4.8597	7.0041
2	-1	13	10.2932	8.1974
2	0	13	4.9508	7.0041
2	1	13	257.5983	261.5240
2	2	13	1.8856	.0495
3	-8	13	4.4619	6.5712
3	-7	13	45.8741	42.4732
3	-6	13	39.6403	28.3533
3	-5	13	81.2734	77.9817
3	-4	13	30.3683	29.3439
3	-3	13	5.9953	4.8700
3	-2	13	260.0112	261.5236
3	-1	13	81.8967	81.9907
3	0	13	6.9691	4.8701
3	1	13	73.8483	71.4472
3	2	13	27.2104	27.2939
4	-8	13	11.2933	7.9965
4	-7	13	14.7524	16.8193
4	-6	13	125.7660	120.0465
4	-5	13	10.1342	8.7745
4	-3	13	70.7079	71.4471
4	-2	13	.2741	.0495
4	-1	13	29.7848	29.3440
4	0	13	.5787	.0247

Table 16. (Concluded)

H	K	L	Y(OBS)	Y(CALC)
4	1	13	3.0733	1.1205
4	2	13	4.2483	1.9951
5	-8	13	3.0675	2.8881
5	-7	13	12.0564	15.0946
5	-5	13	7.2699	6.6222
5	-4	13	2.2232	1.1205
5	-3	13	25.2771	27.2938
5	-2	13	83.2503	77.9819
5	-1	13	10.5700	8.7744
5	0	13	6.4485	6.6223
5	1	13	235.2527	237.0271
5	2	13	73.6481	75.3929
6	-8	13	2.8798	3.4421
6	-7	13	13.0692	8.1409
6	-6	13	58.3762	55.0854
6	-5	13	239.1753	237.0263
6	-4	13	3.9219	1.9950
6	-3	13	39.6280	28.3533
6	-2	13	124.8460	120.0460
6	-1	13	14.0847	9.1621
6	0	13	58.9212	55.0855
6	1	13	5.2575	6.8742
6	2	13	3.5642	1.2127
7	-7	13	.9549	1.8799
7	-6	13	3.6371	6.8742
7	-5	13	75.4198	75.3932
7	-4	13	47.1078	42.4732
7	-3	13	16.2782	16.8191
7	-2	13	11.0235	15.0946
7	-1	13	11.8796	8.1408
7	0	13	2.4779	1.8799
8	-6	13	2.1716	1.2127
8	-5	13	2.7484	6.5713
8	-4	13	9.6024	7.9967
8	-3	13	2.8080	2.8882
8	-2	13	2.3502	3.4421
0	-7	14	73.6941	59.8883
0	-6	14	92.0807	72.8909
0	-5	14	138.4127	121.8554
0	-4	14	129.2907	116.1741
0	-3	14	4.8327	2.3708
0	-2	14	37.8847	36.3706
0	-1	14	30.9067	26.9635
0	0	14	87.8323	97.6636
0	1	14	29.9721	26.9636
1	-8	14	44.2236	40.5358
1	-7	14	3.9859	4.7840
1	-6	14	25.8847	20.9913
1	-5	14	53.6183	46.1799
1	-4	14	47.4663	42.7043
1	-3	14	2.6050	1.9460
1	-2	14	227.3488	221.2723
1	-1	14	29.9588	26.9636
1	0	14	27.6055	26.9635
2	-8	14	37.7637	35.4896
2	-7	14	37.0591	40.6623
2	-6	14	12.3309	13.3941
2	-5	14	84.3671	88.3698
2	-4	14	212.9591	195.5075
2	-3	14	.5696	.8799
2	-2	14	39.5370	36.3704
2	-1	14	229.4621	221.2724
2	0	14	36.8872	36.3706
2	1	14	2.6980	1.9460
3	-8	14	37.6898	41.1440
3	-7	14	12.3471	11.2531
3	-6	14	89.8688	78.5559
3	-5	14	2.2992	1.2989
3	-4	14	16.1965	12.9098
3	-3	14	4.0414	2.3708
3	-1	14	.5103	.8798
3	0	14	4.6701	2.3708
3	1	14	43.8857	42.7043
4	-8	14	1.6825	1.4167
4	-7	14	125.9359	135.0704
4	-6	14	7.4274	5.6300
4	-5	14	17.9757	16.9274
4	-3	14	41.3168	42.7043
4	-1	14	15.7701	12.9100
4	0	14	119.7991	116.1741
4	1	14	51.6961	46.1799
5	-6	14	4.1561	3.3093
5	-5	14	129.3870	121.8550
5	-4	14	52.1191	46.1799
5	-3	14	78.3549	88.3704
5	-2	14	2.3348	1.2989
5	-1	14	15.6431	16.9274
5	0	14	126.8667	121.8554
5	1	14	22.0015	20.9913
6	-8	14	2.5416	1.1752
6	-7	14	5.7511	7.3651
6	-6	14	80.9607	72.8907
6	-5	14	21.8586	20.9914
6	-4	14	11.9300	13.3943
6	-3	14	81.9372	78.5558
6	-2	14	8.4950	5.6300
6	-1	14	3.0926	3.3092
6	1	14	2.7771	4.7840
7	-8	14	2.7731	4.5118
7	-7	14	66.2282	59.8846
7	-6	14	5.0005	4.7839
7	-5	14	35.5462	40.6625
7	-4	14	12.6716	11.2533
7	-3	14	121.1695	135.0701
7	-1	14	7.4451	7.3651
8	-7	14	41.6913	40.5359
8	-6	14	31.8234	35.4897
8	-5	14	33.1114	41.1437
8	-4	14	2.0511	1.4167
8	-2	14	2.3299	1.1753

APPENDIX I

X-RAY DATA ON TRANSITION NEAR 200°C

I_I, I_P and R are the integrated intensity, the peak intensity and the ratio of I_I/I_P, of the corresponding h k ℓ reflection, respectively. To obtain I_I and I_P divide $I_I \cdot N$ and $I_P \cdot N$ by the scale factor N.

Table 17. X-ray Reflection Data for Chlorapatite at 25°C

Temperature 25°C N = 1.0

h	k	l	$N \cdot I_I$	$N \cdot I_P$	R
$\bar{2}$	1	3	30980	4224	7.33
$\bar{4}$	1	4	95059	12455	7.58
0	1	4	44175	5696	7.76
2	1	4	53349	6657	8.01
0	3	4	86104	11137	7.73
2	3	4	84186	10371	8.12
$\bar{2}$	5	4	45268	5632	8.04
$\bar{6}$	1	6	41808	4547	9.19
0	1	6	39844	4544	8.77
4	1	6	33715	3457	9.75
2	5	6	30488	3200	9.53
$\bar{6}$	7	6	30950	3209	9.64
1	3	4	85834	9482	9.05
$\bar{3}$	3	4	75665	9472	7.99
$\bar{3}$	5	4	72155	8960	8.05
1	5	6	37267	3776	9.87
$\bar{3}$	4	4	64506	8192	7.87
$\bar{3}$	0	4	56017	7168	7.81
$\bar{5}$	2	4	53510	6528	8.20
$\bar{5}$	6	6	28891	3073	9.40

Table 18. X-ray Reflection Data for Chlorapatite at 100°C

Temperature 100°C N = 1.06

h	k	l	$N \cdot I_I$	$N \cdot I_P$	R
$\bar{2}$	1	3	29407	4032	7.29
$\bar{4}$	1	4	80766	10496	7.69
0	1	4	39570	4928	8.03
2	1	4	45263	5376	8.42
0	3	4	73401	8579	8.56
2	3	4	71300	7813	9.13
$\bar{2}$	5	4	38437	4417	8.70
$\bar{6}$	1	6	35545	4035	8.81
0	1	6	33740	3723	9.06
4	1	6	28823	2954	9.76
2	5	6	26436	2678	9.87
$\bar{6}$	7	6	26703	2792	9.56
1	3	4	73136	9345	7.83
$\bar{3}$	3	4	64307	8193	7.85
$\bar{3}$	5	4	60827	7168	8.48
1	5	6	31752	3407	9.32
$\bar{3}$	4	4	54777	6657	8.23
$\bar{3}$	0	4	48032	5824	8.25
$\bar{5}$	2	4	45113	5632	8.01
$\bar{5}$	6	6	19442	2017	9.64

Table 19. X-ray Reflection for Chlorapatite at 150°C

Temperature 150°C N = 1.11

h	k	l	$N \cdot I_I$	$N \cdot I_P$	R
$\bar{2}$	1	3	26372	3328	7.92
$\bar{4}$	1	4	64702	8064	8.02
0	1	4	32718	3522	9.29
2	1	4	36917	4099	9.01
0	3	4	59950	6405	8.93
2	3	4	57871	5408	10.70
$\bar{2}$	5	4	31367	3396	9.24
$\bar{6}$	1	6	29503	3269	9.02
0	1	6	27671	2517	10.99
4	1	6	24443	2215	11.04
2	5	6	21482	2045	10.50
$\bar{6}$	7	6	22234	2234	9.95
1	3	4	58335	6913	8.44
$\bar{3}$	3	4	52162	6336	8.23
$\bar{3}$	5	4	49577	5699	8.70
1	5	6	24850	2423	10.26
$\bar{3}$	4	4	44612	5058	8.82
$\bar{3}$	0	4	37282	4672	7.98
$\bar{5}$	2	4	36327	4480	8.11
$\bar{5}$	6	6	19501	1998	9.76

Table 20. X-ray Reflection Data for Chlorapatite at 170°C

Temperature 170°C N = 1.13

h	k	l	$N \cdot I_I$	$N \cdot I_P$	R
$\bar{2}$	1	3	22415	2816	7.96
$\bar{4}$	1	4	54144	6656	8.13
0	1	4	27630	3106	8.89
2	1	4	31087	3329	9.34
0	3	4	49665	5251	9.46
2	3	4	48609	4561	10.657
$\bar{2}$	5	4	25696	2818	9.12
$\bar{6}$	1	6	24351	2628	9.27
0	1	6	22308	2131	10.46
4	1	6	20115	1762	11.42
2	5	6	17512	1624	10.79
$\bar{6}$	7	6	18511	1968	9.41
1	3	4	48423	5570	8.69
$\bar{3}$	3	4	42593	4992	8.53
$\bar{3}$	5	4	40682	4672	8.71
1	5	6	20567	1914	10.74
$\bar{3}$	4	4	36911	4418	8.36
$\bar{3}$	0	4	30221	3712	8.14
$\bar{5}$	2	4	29479	3712	7.94
$\bar{5}$	6	6	16269	1672	9.73

Table 21. X-ray Reflection Data for Chlorapatite at 180°C

Temperature 180°C N = 1.14

h	k	l	$N \cdot I_I$	$N \cdot I_P$	R
$\bar{2}$	1	3	18072	2400	7.53
$\bar{4}$	1	4	45329	5696	7.96
0	1	4	23497	2560	9.18
2	1	4	25296	2754	9.18
0	3	4	42565	4293	9.92
2	3	4	39377	3672	10.72
$\bar{2}$	5	4	22246	2434	9.14
$\bar{6}$	1	6	20659	2147	9.62
0	1	6	19446	1873	10.38
4	1	6	16497	1565	10.54
2	5	6	14526	1249	11.63
$\bar{6}$	7	6	15610	1512	10.32
1	3	4	39136	4419	8.86
$\bar{3}$	3	4	35621	4224	8.43
$\bar{3}$	5	4	34472	3968	8.69
1	5	6	18282	16291	11.22
$\bar{3}$	4	4	30680	3520	8.71
$\bar{3}$	0	4	26855	3201	8.39
$\bar{5}$	2	4	24921	3104	8.03
$\bar{5}$	6	6	14100	1318	10.69

Table 22. X-ray Reflection Data for Chlorapatite at 196°C

Temperature 196°C N = 1.16

h	k	l	$N \cdot I_I$	$N \cdot I_P$	R
$\bar{2}$	1	3	13895	1760	7.89
$\bar{4}$	1	4	33669	3776	8.92
0	1	4	16552	1600	10.34
2	1	4	17277	1857	9.31
0	3	4	26147	2594	10.08
2	3	4	25114	2248	11.17
$\bar{2}$	5	4	13214	1281	10.31
$\bar{6}$	1	6	12679	1219	10.41
0	1	6	13674	1212	11.28
4	1	6	11256	1010	11.14
2	5	6	10093	8577	11.77
$\bar{6}$	7	6	11151	9633	11.58
1	3	4	24638	2432	10.13
$\bar{3}$	3	4	19399	1952	9.94
$\bar{3}$	5	4	17622	1696	10.39
1	5	6	13225	1064	12.43
$\bar{3}$	4	4	18977	1888	10.05
$\bar{3}$	0	4	14781	1536	9.62
$\bar{5}$	2	4	13320	1328	10.03
$\bar{5}$	6	6	7637	562	13.59

Table 23. X-ray Reflection Data for Chlorapatite at 203°C

Temperature 203°C N = 1.17

h	k	l	$N \cdot I_I$	$N \cdot I_P$	R
$\bar{2}$	1	3	3870	296	13.07
$\bar{4}$	1	4	12475	8004	15.71
0	1	4	7470	480	15.56
2	1	4	7014	536	13.09
0	3	4	13032	946	13.77
2	3	4	9819	592	16.57
$\bar{2}$	5	4	6302	376	16.74
$\bar{6}$	1	6	6209	393	15.78
0	1	6	5961	353	16.86
4	1	6	5334	313	17.01
2	5	6	4969	278	17.84
$\bar{6}$	7	6	4732	281	16.82
1	3	4	11552	752	15.36
$\bar{3}$	3	4	11469	784	14.63
$\bar{3}$	5	4	10891	736	14.79
1	5	6	6602	394	16.75
$\bar{3}$	4	4	10222	625	16.36
$\bar{3}$	0	4	9431	608	15.51
$\bar{5}$	2	4	8982	624	14.39
$\bar{5}$	6	6	5714	312	18.27

Table 24. X-ray Reflection Data for Chlorapatite at 210°C

Temperature 210°C N = 1.17

h	k	l	$N \cdot I_I$	$N \cdot I_p$	R
$\bar{2}$	1	3	2594	177	14.63
$\bar{4}$	1	4	9476	545	17.38
0	1	4	5717	328	17.42
2	1	4	4959	264	18.79
0	3	4	8586	480	17.88
2	3	4	8638	466	18.51
$\bar{2}$	5	4	4714	240	19.61
$\bar{6}$	1	6	5226	282	18.52
0	1	6	5445	289	18.81
4	1	6	4525	210	21.50
2	5	6	4175	224	18.62
$\bar{6}$	7	6	4510	232	19.41
1	3	4	9209	496	18.56
$\bar{3}$	3	4	8049	467	17.24
$\bar{3}$	5	4	8242	417	19.75
1	5	6	5386	274	19.66
$\bar{3}$	4	4	8159	482	16.94
$\bar{3}$	0	4	8174	400	20.41
$\bar{5}$	2	4	7803	384	20.32
$\bar{5}$	6	6	4854	248	19.52

Table 25. X-ray Reflection Data for Chlorapatite at 220°C

Temperature 220°C N = 1.19

h	k	l	$N \cdot I_I$	$N \cdot I_P$	R
$\bar{2}$	1	3	2288	140	16.32
$\bar{4}$	1	4	7789	417	18.68
0	1	4	4851	240	20.21
2	1	4	4638	232	19.99
0	3	4	6583	369	17.84
2	3	4	6417	369	17.35
$\bar{2}$	5	4	3596	192	18.73
$\bar{6}$	1	6	4179	200	20.88
0	1	6	3940	209	18.89
4	1	6	3601	184	19.56
2	5	6	3715	192	19.34
$\bar{6}$	7	6	3611	186	19.56
1	3	4	8149	480	16.97
$\bar{3}$	3	4	6934	336	20.62
$\bar{3}$	5	4	6995	304	22.99
1	5	6	--	--	--
$\bar{3}$	4	4	6908	370	18.66
$\bar{3}$	0	4	5783	304	19.00
$\bar{5}$	2	4	5911	320	18.47
$\bar{5}$	6	6	4179	208	20.05

Table 26. X-ray Reflection Data for Chlorapatite at 230°C

Temperature 230°C N = 1.20

h	k	l	$N \cdot I_I$	$N \cdot I_P$	R
$\bar{2}$	1	3	2301	129	17.83
$\bar{4}$	1	4	6555	319	20.57
0	1	4	4557	228	20.00
2	1	4	4191	225	18.66
0	3	4	6339	340	18.62
2	3	4	6479	309	20.98
$\bar{2}$	5	4	3541	164	21.56
$\bar{6}$	1	6	3970	209	19.02
0	1	6	4263	216	19.69
4	1	6	3223	160	20.11
2	5	6	3068	165	18.65
$\bar{6}$	7	6	3554	171	20.72
1	3	4	6978	360	19.38
$\bar{3}$	3	4	6035	354	17.05
$\bar{3}$	5	4	5951	298	19.99
1	5	6	4036	201	20.12
$\bar{3}$	4	4	6176	330	18.72
$\bar{3}$	0	4	5439	284	19.18
$\bar{5}$	2	4	5674	306	18.55
$\bar{5}$	6	6	3722	184	20.22

Table 27. X-ray Reflection Data for Chlorapatite at 250°C

Temperature 250°C N = 1.22

h	k	l	$N \cdot I_I$	$N \cdot I_P$	R
$\bar{2}$	1	3	1632	103	15.81
$\bar{4}$	1	4	5596	270	20.72
0	1	4	4365	189	23.15
2	1	4	3725	171	21.75
0	3	4	6048	290	20.82
2	3	4	5322	278	19.14
$\bar{2}$	5	4	3456	187	18.44
$\bar{6}$	1	6	3315	154	21.58
0	1	6	3691	176	20.92
4	1	6	3136	144	21.74
2	5	6	2595	130	19.92
$\bar{6}$	7	6	2865	137	20.89
1	3	4	6160	309	19.92
$\bar{3}$	3	4	4928	249	19.82
$\bar{3}$	5	4	5023	240	20.90
1	5	6	3930	184	21.36
$\bar{3}$	4	4	5229	274	19.11
$\bar{3}$	0	4	4769	266	17.94
$\bar{5}$	2	4	4562	225	20.31
$\bar{5}$	6	6	3506	148	23.64

Table 28. X-ray Reflection Data for Chlorapatite at 300°C

Temperature 300°C N = 1.27

h	k	l	$N \cdot I_I$	$N \cdot I_P$	R
$\bar{2}$	1	3	1535	802	19.13
$\bar{4}$	1	4	4501	227	19.80
0	1	4	3793	148	25.63
2	1	4	2948	123	23.78
0	3	4	4102	201	20.36
2	3	4	4314	193	22.34
$\bar{2}$	5	4	1997	96	20.79
$\bar{6}$	1	6	2727	132	20.65
0	1	6	3357	148	22.65
4	1	6	2181	108	20.13
2	5	6	2099	99	21.14
$\bar{6}$	7	6	2266	96	23.41
1	3	4	4913	208	23.57
$\bar{3}$	3	4	3987	169	23.60
$\bar{3}$	5	4	3808	177	21.52
1	5	6	2939	133	22.15
$\bar{3}$	4	4	4363	189	23.06
$\bar{3}$	0	4	4267	208	20.51
$\bar{5}$	2	4	4045	168	24.06
$\bar{5}$	6	6	3018	133	22.74

Table 29. X-ray Reflection Data for Chlorapatite at 350°C

Temperature 350°C N = 1.33

h	k	l	$N \cdot I_I$	$N \cdot I_P$	R
$\bar{2}$	1	3	--	--	--
$\bar{4}$	1	4	3292	149	22.12
0	1	4	3040	144	21.07
2	1	4	2701	116	23.26
0	3	4	3406	160	21.26
2	3	4	3679	147	25.08
$\bar{2}$	5	4	2023	98	20.58
$\bar{6}$	1	6	1709	96	17.80
0	1	6	2770	113	24.51
4	1	6	2033	75	27.10
2	5	6	1148	56	20.43
$\bar{6}$	7	6	1849	72	25.38
1	3	4	4610	200	23.05
$\bar{3}$	3	4	3358	160	20.95
$\bar{3}$	5	4	3669	252	19.89
1	5	6	2290	112	20.41
$\bar{3}$	4	4	3327	176	18.90
$\bar{3}$	0	4	2720	149	18.31
$\bar{5}$	2	4	3067	133	23.12
$\bar{5}$	6	6	1757	88	19.90

Table 30. X-ray Reflection Data for Chlorapatite at 408°C

Temperature 408°C N = 1.40

h	k	l	$N \cdot I_I$	$N \cdot I_P$	R
$\bar{2}$	1	3	--	--	--
$\bar{4}$	1	4	3544	156	22.64
0	1	4	3065	131	23.43
2	1	4	1669	84	19.80
0	3	4	3382	144	23.43
2	3	4	2791	129	21.76
$\bar{2}$	5	4	1567	64	24.37
$\bar{6}$	1	6	1894	100	18.91
0	1	6	1965	94	20.75
4	1	6	1601	71	22.65
2	5	6	1726	70	24.56
$\bar{6}$	7	6	1424	60	23.79
1	3	4	3234	160	20.18
$\bar{3}$	3	4	2809	140	20.06
$\bar{3}$	5	4	2760	108	25.46
1	5	6	1727	86	20.08
$\bar{3}$	4	4	2997	137	21.82
$\bar{3}$	0	4	3659	152	24.03
$\bar{5}$	2	4	2151	108	19.90
$\bar{5}$	6	6	1686	90	18.82

Table 31. Integral Breadth of 008 Reflection from 100°C to 408°C

Temperature (°C)	R
100	10.4
150	10.4
170	10.3
180	10.3
196	10.3
203	10.2
210	10.4
220	10.3
230	10.4
250	10.3
300	10.4
350	10.3
408	10.5

REFERENCES

1. Young, R. A., "Biological Apatite versus Hydroxapatite at the Atomic Level," Clin. Orthop. 113, 249 (1975).

2. Posner, A. S., "Crystal Chemistry of Bone Mineral," Physiol. Rev. 4, 760 (1969).

3. Elliot, J. C., "The Problems of the Composition and Structure of the Mineral Components of the Hard Tissues," Clin. Orthop. 93, 313 (1973).

4. Carlström, D., "Advances in Oral Biology," Staple, P.H., Ed., Academic Press, London, p. 255 (1964).

5. Young, R. A., "Some Aspects of Crystal Structural Modeling of Biological Apatite," N° 230, Colloque Internationaux C.N.R.S. (1975).

6. Trautz, O. R., "Crystalline Organization of Dental Mineral" in "Structural and Chemical Organization of Teeth," Miles, A. E. W., Ed., Vol. 2, p. 165 (1976).

7. Termine, J. D., "Mineral Chemistry and Skeletal Biology," Clin. Orthop. 85, 207 (1972).

8. Zipkin, I., "Biological Mineralization," J. Wiley and Sons, p. 487 (1973).

9. Kay, M. I., Young, R. A., and Posner, A. S., "Crystal Structure of Hydroxyapatite," Nature 204, 1050 (1964).

10. Sudarsanan, K., and Young, R. A., "Significant Precision in Crystal Structural Details: Holly Springs Hydroxyapatite, "Acta. Cryst. B 25, 1534 (1969).

11. Elliott, J.C., Mackie, P. E. and Young, R. A., "Monoclinic Hydroxyapatite," Science 180, 1055 (1973).

12. Young, R. A., Van Der Lugt, W. and Elliott, J. C., "Mechanism for Flourine Inhibition of Diffusion in Hydroxyapatite," Nature 223, 729 (1969).

13. Van Der Lugt, W., Knottnerus, D. I. M. and Young, R. A.," NMR Determination of Flourine Position in Mineral Hydroxyapatite," Caries Res. 4, 89 (1970).

14. Tse, C., "Point Defect Formation and Migration in Apatite, "Ph.D. Thesis, Princeton University (1972).

15. Tse, C., Welch, D. O. and Royce, B. S. H., "The Migration of F^-, OH^-, and O^{2-} Ions in Apatites," Calc. Tiss. Res. 13, 47 (1973).

16. Gottschal, A. J., J. S. Afr. Chem. Inst. XI, 45 (1958).

17. Handbook of Chemistry and Physics, Editor, Weast, R. C., 51st Edition, Chemical Rubber Publishing Co., Cleveland, Ohio, p. E-73 (1971).

18. Wolff, J., "Das Gesetz der Transformation der Knochen, Hirschwald, A., Berlin (1892).

19. Fukada, E. and Yasuda, I., "On the Piezoelectric Effect of Bone," J. Physiol Soc. Jap. 12, 1159 (1956).

20. Bassett, C. A. L., "Biological Significance of Piezoelectricity," Calc. Tiss. Res. 1, 252 (1968).

21. Bassett, C. A. L., Pauluk, R. J. and Becker, R. D., "Effects of Electric Currents on Bone in Vivo," Nature 204, 652 (1964).

22. Jahn, T. L., "A Possible Mechanism for the Effect of Electrical Potentials on Apatite Formation in Bone," Clin. Orthop. 56, 261 (1968).

23. Lavine, S. L. and Lustrin, I., "Electric Enhancement of Bone Healing," Science 175, 1118 (1971).

24. Williams, W. S., "Sources of Piezoelectricity in Tendon and Bone," CRC Critical Review Bioengineering, p. 95 (1974).

25. Shamos, M. H. and Lavine, L. S., "Physical Bases for Bioelectric Effects in Mineralized Tissues," Clin. Orthop. 35, 177 (1964).

26. Cochran, G. V. B., Pawlak, R. J. and Bassett, C. A. L., "Electromechanical Characteristics of Bone Under Physiologic Moisture Condition," Clin. Orthop. 58, 249 (1968).

27. Mackie, P. E., Elliott, J. C. and Young, R. A., "Monoclinic Structure of Synthetic $Ca_5(PO_4)_3Cl$, Chlorapatite, Acta Cryst. B 28, 1840 (1972).

28. Young, R. A., "Dependence of Apatite Properties on Crystal Structural Details," Trans. N. Y. Acad. Sci. 29, 949 (1967).

29. Seigel, J., "Point Defects and the Electrical Properties of Apatite," Ph.D. Thesis, Princeton University (1970).

30. Elliott, J. C. and Young, R. A., "Dielectric Measurements on Single Crystals of Synthetic Chlorapatite," Bull. Soc. Chim. Fr., n° Spécial: 1973 (1968).

31. Young, R. A. and Elliott, J. C., "Atomic-Scale Bases for Several Properties of Apatites," Arch. Oral. Biol. 11, 699 (1966).

32. Kittel, C., "Theory of Antiferroelectric Crystals," Phys. Rev., 82, 729 (1951).

33. Elliott, J. C., Priv. Comm. (1973).

34. Arends, J., Royce, B. S. H., Siegel, J., and Smoluchowski, R., "Dielectric Relaxation in Hydroxyapatite," Phys. Lett., 27 A, 720 (1968).

35. Tse, C., Welch D. O. and Royce, B. S. H., "Calculation of Anion Migration Energy in the Calcium Apatites," Bull. Amer. Phys. Soc. 17, 265 (1972).

36. Tse, C. Welch, D. O. Royce, B. S. H., "Dielectric Relaxation in Fluorapatite," Bull. Amer. Phys. Soc. 17, 265 (1972).

37. Pollard, C. O., Jr., "Dielectric Properties of Hydroxyapatites," Min. Mag., 36, 1169 (1968).

38. Kautz, H. E., "Dielectric Loss in Fluorapatite Crystals of Various Fluoride Vacancy Concentration," J. Electrochem. Soc., 120, 84 (1973).

39. Prener, J. S., "The Growth and Crystalographic Properties of Calcium Fluor- and Chlorapatite Crystals, J. Electrochem. Soc, 114, 77 (1967).

40. Elliott, J. C. and Young, R. A., "Conversion of Single Crystals of Chlorapatite into Single Crystals of Hydroxyapatite," Nature 214, 904 (1967).

41. Prener, J. S., "Nonstoichiometry in Calcium Chlorapatite," J. Solid State Chem. 3, 49 (1971).

42. Gravel, R. L. and Kestigian, M., "Low Terminal Capacitance Dielectric Sample Holder," Rev. Sci. Inst., 36, 1264 (1965).

43. Sawyer, C. B. and Tower, C. H., "Rochelle Salt as a Dielectric," Phys. Rev. 35, 269 (1930).

44. Roctschi, H., "New Type of Loop Tracer for Ferroelectrics," J. Sci. Inst. 39, 152 (1962).

45. Schubring, N. W., Nolta, J. P. and Dork, R. A., "Ferroelectric Hysteresis Tracer Featuring Compensation and Sample Grounding," Rev. Sci. Inst., 35, 1517 (1964).

46. Tsui, Y. T., Hinderaker, P. D. and McFadden, F. J., "New Ferroelectric Hysteresis Curve Tracer Featuring Compensation and Virtual Sample Grounding," Rev. Sci. Inst. 39, 1423 (1968).

47. Mackie, P. E., "Precision Single Crystal X-ray Diffractometry," Ph.D. Thesis, Georgia Institute of Technology (1972).

48. Young, R. A., Goodman, M. R., Jr., and Kay, M. I., "Goniostats for Siemens and Phillips Diffractometers," ACA Abstracts, p. 18, July 1964.

49. Young, R. A., "X-ray Specimen Temperature Control with Gas Streams," J. Sci. Inst., 34, 449 (1966).

50. Bond, W. L., "Precision Lattice Constant Determination," Acta Cryst. 13, 814 (1960).

51. Ida, M., Hirata, M. and Kawada, S., "The Changes in Dielectric Properties of Water during Adsorption by Solids," J. Phys. Soc. Japan 19, 417 (1964).

52. McIntosh, R. L. "Dielectric Behavior of Physically Adsorbed Gases," Marcell Dekker, New York, N. Y. (1966).

53. Zech, B. and Wittmann, F., "Studium des Dielektrischen Verhaltens von dünnen adsorbierten Wasserfilmen," Z. Physik. Chem. New Folge 92, 45 (1974).

54. Busing, W. R., Johnson, C. R., Thiessen, W. E. and Levy, H. A., "ORXFLS3 Accession #84, World List of Crystallographic Computer Programs," 3rd ed., J. App. Cryst. 6, 309 (1973).

55. General Radio Co., Instruction Manual for Type 1650-B Impedance Bridge (1968).

56. Zachariasen, W. H., Acta Cryst., 23, 558 (1967).

57. Cromer, D. T. and Waber, J. T., Acta Cryst., 18, 104 (1965).

58. Cromer, D. T., Acta Cryst., 18, 17 (1965).

59. Granicher, H., Jaccard, C., Scherrer, P. and Steinemann, A., "Dielectric Relaxation and the Electrical Conductivity of Ice Crystals," Discuss. Faraday Soc., 23, 50 (1957).

60. Cole, K. S. and Cole, R. H., J. Chem. Phys. 9, 341 (1941).

61. Mackie, P. E. and Young, R. A., "Fluorine-Chlorine Interaction in Fluor-Chlorapatite," J. Solid State Chem. 11, 319 (1974).

62. The chemical analysis was carried out by N.V. Braun of the Quality Assurance Division at General Electric Co. in 1970. The fluoride was separated by using the Williard-Winter Steam distillation method and then filtrating with thorium nitrate.

63. Johnson, P. D., "Some Optical Properties of Powder and Crystal Halophosphate Phosphors," J. Electrochem. Soc. 108, 159 (1961).

64. Mengeot, M. Harvill, M. L. and Gilliam, O. R., "Hydrothermal Growth of Calcium Hydroxyapatite," J. Crystal Growth, 19, 199 (1973).

65. Roy, D. M., "Crystal Growth of Hydroxyapatite," Mat. Res. Bull., 6, 1337 (1971).

66. Walder, V. and Burke, J., J. Appl. Cryst., 4, 337 (1971).

67. Burke, J. and Tomkeieff, M. V., Acta Cryst., A 24, 683 (1968).

68. Burke, J. and Tomkeieff, M. V., J. Appl. Cryst. 2, 247 (1969).

69. A-C Loss Characteristics and Dielectric Constant (Permittivity) of Solid Electrical Insulating Materials," ASTM D-150-64T, 28 (1965).

70. Merz, W. J., "The Electric and Optical Behavior of $BaTiO_3$ Single Domain Crystals," Phys. Rev. 76, 1221 (1949).

71. Cross, L. E., "Antiferroelectric-Ferroelectric Switching in a Simple Kittel Antiferroelectric," J. Phys. Soc. Japan 23, 77 (1967).

72. Fatuzzo, E. and Merz, W. J., "Ferroelectricity," Vol. 7, John Wiley and Sons, New York, N. Y. (1967).

73. Megaw, H. D., "Ferroelectricity in Crystals," Methuen Co., London (1957).

74. Sutton, L. E., "Interatomic Distances and Configuration in Molecules and Ions," London: The Chemical Society (1958).

75. MacDonald, J. R., "Theory of AC Space-Charge Polarization Effects in Photoconductors, Semiconductors, and Electrolytes," Phys. Rev. 92, 41 (1953).

76. MacDonald, J. R., "Electrical Response of Materials Containing Space Charge with Discharge at the Electrodes," J. Chem. Phys. 54, 2026 (1971).

77. Jaffe, G., Ann. Physik 16, 217 (1933).

78. Jaffe, G., Phys. Rev. 85, 354 (1952).

79. Azaroff, L. V., "Elements of X-Ray Crystallography," McGraw-Hill Co., New York, p. 551 (1968).

80. Van Rees, H. B., Mengert, M. and Kostiner, E., "Monoclinic-Hexagonal Transition in Hydroxyapatite and Deuterohydroxyapatite Single Crystals," Mat. Res. Bull. 8, 1307 (1973).

81. Cockbain, A. G. and Smith, G. V., Min. Mag. 36, 411 (1967).

82. Roufosse, A., Stapelbrock, M., Bartram, R. H. and Gilliam, O. R., "Oxygen-Associated Holelike Centers in Calcium Chlorapatite," Phys. Rev. B 9, 855 (1974).

83. Tang, H. and Casabella, P. A., "NMR Study of Diffusion in Hydroxyapatite," Bull. Am. Phys. Soc. 19, 252 (1974).

84. Hill, N. E., North, E. V., Price, A. H. and Davies, N., "Dielectric Properties and Molecular Behavior," Van Nostrand Reinhold, Co., London, p. 47 (1969).

85. Azaroff, L. V., "Elements of X-Ray Crystallography," McGraw-Hill Co., New York, p. 165 (1968).

86. Debye, P., "Polar Molecules," Chemical Catalog Co., New York (1929).

87. Fröhlich, H., "Theory of Dielectrics, Oxford University Press, London (1949).

88. Busing, W. R., Ellison, R. D., Levy, H. A., King, S. P., and Roseberry, R. T., "The Oak Ridge Computer - Controlled X-Ray Diffractometer," ORNL - Report 4143, p. 20 (1968).

VITA

Ekkehart Otto Rausch was born in Bamberg, West-Germany on September 28, 1943. He received his elementary education in Munich, West-Germany and then attended the Altsprachliche Gymnasium (a 9 year humanistic, pre-university school) at Kaiserslautern, West-Germany. On November 2, 1958 he emigrated to the United States. For six months he lived in New York City where he attended Cardinal Hays High School. During that time he learned to speak English. He then moved to Huntsville, Alabama and attended Huntsville High School. In 1963 he received his U.S. citizenship and was admitted to the University of Alabama. Upon graduation in 1966 he joined the U.S. Navy as an officer with the rank of Ensign on the aircraft carrier USS Saratoga. Upon completion of his tour of active duty he entered graduate school at the Georgia Institute of Technology. He earned the M.S. degree in Physics from the Georgia Institute of Technology in 1972.